NsG-58
U. Md.

378p.

N O T I C E

THIS DOCUMENT HAS BEEN REPRODUCED FROM THE BEST COPY FURNISHED US BY THE SPONSORING AGENCY. ALTHOUGH IT IS RECOGNIZED THAT CERTAIN PORTIONS ARE ILLEGIBLE, IT IS BEING RELEASED IN THE INTEREST OF MAKING AVAILABLE AS MUCH INFORMATION AS POSSIBLE.

Chapter ...

CRATERING AND THE MOON'S SURFACE*

By E. J. Öpik

Armagh Observatory, Armagh, Northern Ireland

and

Department of Physics and Astronomy, University of Maryland, College Park, Maryland

* Supported by National Aeronautics and Space Administration Fund NsG-58-60.

Introduction*

This monographic Chapter has grown out of a planned much less expanded review article on the moon's surface, solicited for the end of 1966. Instead, a complete mechanical and statistical analysis of the lunar surface has been drawn along new quantitative lines, without however attempting anything like a complete review of the existing literature. Also, during the two years which have passed since the above-mentioned provisional deadline, much new factual material has been provided by the American Ranger, Surveyor and Orbiter, as well as by Russian spacecrafts; some of these data have been incorporated into the framework of this analysis, incompletely however. The material is too voluminous and still increasing, awaiting exhaustive treatment at a later date. Yet, as things stand now, the selected data used here appear to be sufficient in characterizing the mechanical and other properties of the lunar soil and surface, so that not much substantial change except in some details can be expected from a comprehensive discussion of the entire material. The success in predicting statistically from first principles the observed distribution of crater numbers over a wide range of sizes, from 3 cm to 5 km, lends support to the reliability of the theoretical basis of cratering and erosion which forms the backbone of this chapter.

---

* In the tables, abbreviated numerals are often used, substituting for powers of ten: $1.58^{-10} = 1.58 \times 10^{-10}$; $6.0^{3} = 6.0 \times 10^{3}$.

The phenomenal growth of lunar literature, while contributing to the knowledge of our satellite, has not removed the occurrence of contradictory interpretations even in such basic questions as the origin of lunar craters. In this respect an old tendency manifests itself: to make hypotheses about astronomical objects which are based on only one aspect of the problem, while overlooking or ignoring contradictory evidence. Hence an impression is created that astronomers always disagree between themselves, an impression that transpires even by reading the best review articles on the moon (Baldwin, 1964a)*.

Undoubtedly, difficulty of a direct proof and impossibility of experimentation were conducive to such a state of affairs; surprisingly even in the case of the nearest of all celestial bodies. Also, lunar physical study has for too long been neglected by professional astronomers and left in the hands of amateurs---whose merits, however, are by no means to be underestimated.

At present space research has brought the moon so-to--speak within an arm's length, and many theories can be proved

*Symbolically in this context, there exists a purely formal ambiguity in defining selenographic directions. In this article the directions are reckoned "astronomically" as for the terrestrial telescopic observer. When South is above, West is to the left, so that Mare Crisium is in the western hemisphere. In the "astronautical" reckoning, the directions are inverted as for an observer standing on the moon.

or disproved as in a laboratory; and the moon is increasingly becoming the object of professional study. Yet a new source of misinterpretations is becoming troublesome. In the old days, the astronomer had time for the study of all the relevant literature and for a critical assessment of the available evidence. Nowadays, with the enormous supply of scientific publications, it becomes progressively more difficult to master the entire literature, or even the details of one narrow branch of science. This has led to an ever increasing habit of trusting authority, second- and even third-hand. Statements are repeated which never would have been made upon critical study of the evidence. Erring is in human nature, but too much reliance on unchecked authority may lead to unwarranted perpetuation of error, as has happened with the much publicized so-called gaseous eruption from the crater Alphonsus. The spectrogram was not studied properly, or it would have become obvious that no gas was emitted, but that luminescence of the solid peak of the crater was responsible for the phenomenon. As a classical case of repeated misinterpretation, the Alphonsus "eruption" is specially dealt with in Section I.

When this, and similar unfounded or one-sided interpretations are discarded, the picture of the lunar surface becomes much less controversial. As a powerful instrument of interpretation, too little used until now, the quantitative theory (and experiment) of solid-body impact (hypervelocity and low-velocity) helps to resolve the most relevant problems of crater formation and erosion, dust formation and transport, bearing on the strength of lunar soil and rock and the mechanical structure of the upper few kilometers of the lunar crust. The quantitative approximation is of the order of 10-20 per cent in absolute linear measure, thus far better than an order-of-magnitude approach. With another little used instrument, the theory of planetary encounters as developed by the author, it is possible to remove much (if not all) of the ambiguity relating to the origin and internal structure of the moon, which is also directly related to the present structure and properties of the lunar surface.

I. The Alphonsus Event and Fluorescence on the Lunar Surface

Instigated by some observations of Dinsmore Alter in California, the Russian astronomer Kozyrev kept under observation the crater Alphonsus in October and November, 1958. As stated in his report (Kozyrev, 1959a), he was intentionally in search of volcanic phenomena on the moon. In the early morning of November 3, 1958, he noticed an unusual brightening on the peak of the crater and, while the brightening lasted, a spectrogram taken with the 50-inch Crimean reflector (linear scale 10 seconds of arc or 18.4 km to the mm, dispersion 23 Å/mm at $H\gamma$, exposure 30 min) showed strong banded emission over the peak. The emission no longer was visible on the next spectrogram, nor was it visible in previously taken spectra. The moon was one day before last quarter, the altitude of the sun over Alphonsus was 18°, and about 31° over the illuminated slope of the peak. Reproductions of the spectrograms, with photographs of the crater itself, were published repeatedly (Kozyrev, 1959b, 1962) but no essential points were added to the first discussion (Kozyrev, 1959a) which ~~was~~ appeared under the challenging title of "Volcanic Activity on the Moon". Essentially Kozyrev--and others--identified the band structure of the observed emission with that of the cometary radical C_2 as fluorescent in sunlight.

Yet the details of the spectrum along the slit, or at right angles to the dispersion, show without the least trace of doubt that the luminescence was strictly confined to the illuminated portion of the peak, and that therefore no eruption of gas did ever take place. This has been pointed out by Öpik (1962a, p. 252 and b, p. 218; 1963b) but somehow overlooked. Distinguished authors, trusting Kozyrev's announcement and without taking a critical look at the published spectrograms, have been led to discussions of the "gaseous eruption" (e.g. Baldwin, 1963, pp. 415-419). Actually, Kozyrev did measure the distribution of monochromatical brightness of the spectrum along the slit and his measurements did show indeed--what was also obvious from a direct inspection of the spectrograms--that the increase in brightness did not affect the shadow of the peak (Kozyrev, 1962, Fig.2; obviously the linear scale there should be kilometers, not seconds of arc, and the orientation is inverted relative to the spectrogram). However, he did not see the consequences of this fact; everybody else accepted then Kozyrev's interpretation on his authority.

Kozyrev's announcement was hailed as the first definite proof of gaseous phenomena on the moon. After some doubts and questioning, chiefly concerned with the band structure of the spectrum, the astronomical community seems to have accepted this interpretation. Nobody seems to have worried about the second dimension of the spectrogram which reproduced the surface features and showed a puzzling detail. The emission was spatially restricted to the bright peak about 4--5 km wide, without trespassing into the shadow of about the same width. The transition was abrupt at the border of the shadow and took place over a distance of about 1 km which corresponds to the resolving power of the photograph. The neutral C_2 gas could not have been restricted by a magnetic field and, with a molecular velocity in excess of 0.5 km/sec, the gas would have spread over a radius of some 900 km during the exposure, covering both the peak and its shadow. Gases emitted from a point source (the peak) would have formed something similar to a comet's head (coma), with a strong central condensation and an intensity decreasing inversely as the first power of distance. The average intensity over the shadow would then have been equal to about one-half the average intensity over the peak. Nothing of this sort was shown in the spectrogram.

There nevertheless appears to be some similarity between the emission from Alphonsus' peak and the cometary or Swan bands of C_2. In this respect Kozyrev (1959a, p.87) points out a strange detail (translation from Russian): " The Swan bands should be completely sharp on the long-wave side, yet they turned out to be washed out over about 5 Å." Here seems to be the clue to the interpretation : bands originating in a solid lattice must be washed out, on account of perturbation by nearby other atoms. Kozyrev proposes another interpretation, to fit into his concept of a gas, namely that the radiation was created <u>in statu nascendi</u> when C_2 was produced from its parent molecules. However, this would mean that each C_2 molecule was radiating only once, not being repeatedly (5-10 times per second) fluorescent in sunlight (what could have prevented it from doing so?), and the brightness could then never have been "10^4 times as intense as in comets" (Kozyrev's estimate).

Clearly, Kozyrev's phenomenon can be interpreted only as emission, probably fluorescent, from a solid surface, and not from an expanding gas. Most that has been written about this event is, therefore, not valid; also, the identification of the emitting molecules can hardly be made with any degree of reliability, although there may have been blurred emission from C_2 somehow present in the solid lattice.

Experimentally it has been shown that meteoritic enstatite ($MgSiO_3$, $FeSiO_3$, as distinct from the more usual olivines, Mg_2SiO_4, Fe_2SiO_4, $MgFeSiO_4$) emits fluorescent light under proton bombardment (40 Kev), and also that certain regions on the moon, around Aristarchus and Kepler in particular, may become fluorescent, apparently in response to bursts of corpusculer radiation from solar flares (Kopal, 1966a). There is a grave difficulty in describing the source of the observed lunar fluorescence in terms of the energy of the proton stream which falls short by many orders of magnitude, as follows from the observed intensities of solar wind. Focusing effects of the earth's magnetosphere have been suggested which would hardly work. It seems that the only explanation is to ascribe the fluorescent radiation to direct sunlight (as for C_2 in comets), whereas the role of the corpuscular bursts would be to raise the molecules to a metastable state capable of fluorescence. The ground state of the C_2 molecule is a singlet, while the lowest level of the Swan bands is a triplet state, only about 0.09 ev above the ground state. The transition from triplet to singlet is forbidden and can be efficiently achieved only by collisions. A similar situation may obtain in the case of lunar luminescence; the emission from the metastable state would then derive from direct sunlight, which is amply sufficient as it is in comets, and not from the inadequate energy of the corpuscular stream acting only as a trigger.

II. Cratering Relationships

A. Destructive Impact and Volcanism

There are no signs of continuing volcanism on the moon. Extensive lava flows as witnessed by the maria, flooded craters and small "domes" must have happened early in the history of the moon, during the first one million, even the first 20,000 years of its existence. On earth, volcanism is related to mountain building and this in turn is the consequence of powerful erosion cycles leading to recurrent imbalance in the earth's crust. On the moon erosion from interplanetary dust is about 2000 times less efficient than in terrestrial deserts (Öpik, 1962a); if on earth the major orogenic cycles followed at intervals of the order of 2×10^8 years, on the moon the interval should be of the order of 10^{12} years: it never could happen.

The lunar surface markings, from craters down to the compacted dust layer, are undoubtedly produced or evolved under the bombardment of interplanetary bodies and particles, as well as of the secondary ejecta from the surface itself. The quantitative study of cratering contains therefore the most important clue to the structure and history of the lunar surface.

Usually, the term "hypervelocity" is applied to cratering impacts. This refers either to the case when the initial velocity of the projectile exceeds the velocity of sound in the target, and/or when the frontal pressures at penetration exceed the strength of both the projectile and the target, so that the projectile itself is destroyed and flattened while entering the target.

Actually, cratering is not a purely hypervelocity phenomenon when the whole of the crater volume is considered. Hypervelocity phenomena may occur only in the heart of the crater. Destruction and ejection of the target ~~materiak~~ material takes place over most of the crater volume when the shock front velocity is less than the velocity of sound yet when the shock pressure still exceeds the strength of the material, or when the energy density of vibration is more than can be borne out by the elastic forces in the target. From this standpoint, a uniform quantitative theory of destructive cratering, applicable also to low-velocity impact, has been worked out by Öpik (1936, 1958a, 1961a). The theory, based on the consideration of <u>average</u> pressure and momentum transfer over shock fronts, from first principles and without experimental adjustment of the parameters gives an approximation to experiment within 10-20 per cent in linear dimensions and can effectively substitute for the huge amount of experimental material accumulated and not yet properly systematized.

B. <u>Destructive Impact; Mechanical Theory</u>

Full or mutually destructive impact is the common "hypervelocity" case when both the target and the projectile are destroyed during the penetration. Formulae for direct application to lunar or similar cases are given below; they are partly new developments, as a sequel to the latest published paper (Öpik, 1961a).

In Fig. 1 a schematic half-section of a cratering event is represented. The relative dimensions are partly kept to scale of the "Teapot" nuclear crater in the desert alluvium of Nevada (Shoemaker, 1963). A meteorite of "equant shape" (whose linear dimensions in different directions do not differ more than in a ratio of about 2 to 1), mass μ, density δ and initial velocity w_0 normal to the target surface ISLS penetrates into target and, while itself flattened and deformed or broken up, stops at I_1 with its front surface reaching a depth x_0 below the surface. If the velocity was sufficiently high, the meteorite with a "central funnel" Q (20-25 times the mass of the meteorite) may be completely or partly vaporized and backfired. The forward passage of the meteorite combined with the backfiring create a destructive shock wave which stops at A, at a depth x_p in the frontal direction and propagates laterally as a <u>radial momentum</u> (Rad.) either with the shock velocity u, or the sound velocity, whichever is greater. In the crater bowl the material is crushed, pulverized, or even melted (near Q) and, after stopped at a bedrock surface AAL as conditioned by a limiting "crushing" value of $u = u_s$, is partly ejected upwards (velocity vector v inside, v_0 at the surface under an angle β to the normal). The bedrock surface AAL is itself displaced outwards, producing a raised lip LL_oN, with the underlying strata L_1, L_2, L_3 characteristically bent over into the lip. Part of the debris falls back into the crater, part is thrown out over the lip, forming the apparent crater and surrounding surface BCB with the rim at C and an apparent depth x' (as distinct from x_o and x_p). The volume of the crater bowl, $AALL_o$, below the bedrock rim level, L_o, is close to

$$V = 0.363\, x_p\, B_o^2 \ , \qquad (1)$$

where B_o is the rim to rim diameter of the crater.

The "mass affected" is assumed equal to

$$M = \rho V \ , \qquad (2)$$

where ρ is the original target density; it depends on the radial momentum,

$$M = k\, \mu w_o / u_s \ , \qquad (3)$$

where

$$u_s^2 = s/\rho \qquad (4)$$

Here s(dyne/cm^2) is the lateral crushing strength of the target, and k a coefficient of radial momentum varying between 2 and 5 as depending on the degree of vaporization and backfiring, defined by the quadratic equation (Öpik, 1961a)

$$k = mw_o^2(1 - 0.04k^2)^{\frac{1}{2}} + 2 \ , \qquad (5)$$

where $m = 3.5 \times 10^{-13}$ for iron impact into stone, and 4.2×10^{-13} for stone impact into stone when w_o is in cm/sec.

From numerical integrations (Öpik, 1936) an interpolation formula for the relative depth of penetration can be set up:

$$p = x_p/d = 1.785(\delta/\rho)^{\frac{1}{2}} (w_0{}^2/s_p)^{1/30}\cos\gamma , \tag{6}$$

and from equations (1), (2), (3), and (4) the relative crater diameter results as

$$D = B_0/d = 1.20\left[(kw_0\delta)/p\right]^{\frac{1}{2}}/(\rho s)^{\frac{1}{4}} \tag{7}$$

Here the non-dimensional numerical factor, 1.20, allows for the funnel-shaped crater profile and differs from the factor of unity formerly used (Öpik, 1961a). Equation (6) tentatively allows for oblique incidence, γ being the angle of incidence relative to the normal to SS, and s_p is the compressive strength or frontal resistance (dyne/cm^2) of the target material (usually an order of magnitude greater than s). The reduced spherical equivalent diameter of the projectile is

$$d = (6\mu/\pi\delta)^{1/3} = 1.241(\mu/\delta)^{1/3} \tag{8}$$

and p and D are the depth and diameter of the crater in units of d.

The ratio of depth to diameter becomes

$$x_p/B_0 = p/D = 1.99(\cos\gamma)^{1.5}(s\delta)^{\frac{1}{4}}/\left[(k\rho)^{\frac{1}{2}}w_0{}^{0.4}s_p{}^{0.05}\right]. \tag{9}$$

The numerical coefficients in (6) and (9) are dimensionally adapted to c.g.s * units [in (9) the dimension of the coefficient is cm$^{0.15}$ g$^{-0.05}$, and in (6) it is cm$^{0.1}$ g$^{-1/30}$].

Typical parameters can be assumed: silicate stone of a planetary upper crust, $\rho = 2.6$, $s = 3 \times 10^8$, $s_p = 2 \times 10^9$; nickel iron, $\delta = 7.8$; $s_p = 2 \times 10^{10}$. Table I contains some relative crater dimensions calculated with these constants.

R

TABLE I

Relative Crater Dimensions for Vertical Impact into Solid Rock; $\gamma = 0°$

w_0, km/sec	3	6	10	15	20	25	30	35	40	50	75
					Stone impact into stone, $\delta/\rho = 1$						
k	2.03	2.14	2.36	2.78	3.31	3.79	4.18	4.44	4.44	4.44	4.44
p	2.03	2.12	2.20	2.26	2.30	2.33	2.37	2.39	2.41	2.45	2.51
D	4.82	6.36	9.12	12.0	14.9	17.8	20.3	22.4	23.9	26.5	32.1
					Iron impact into stone						
k	2.05	2.32	2.56	3.12	3.75	4.21	4.52	4.70	4.70	4.70	4.70
p	3.25	3.69	3.82	3.93	4.00	4.05	4.11	4.15	4.19	4.26	4.37
D	6.63	9.17	12.5	16.7	20.9	24.6	28.2	30.4	32.4	35.9	43.4

TABLE II

Comparison with Experiment : Aluminum → Aluminum, $\rho = \delta = 2.7$

μ, gram	1.265	0.378	0.158	0.047	0.376	0.376	*...
w_0, km/sec	5.22	6.87	8.63	9.05	7.80	6.58	...
s_t, 10^9 dyne/cm^2	1.01	1.01	1.01	1.01	5.07	2.84	...
k, calc.	2.11	2.19	2.28	2.30	2.23	2.17	...
x_p lip, obs., cm	2.36	1.86	1.58	1.04	1.50	1.41	...
$1.16x_p$, calc., cm	2.40	1.65	1.24	0.84	1.56	1.57	Aver.
x_p, ratio calc./obs.	1.02	0.89	0.79	0.81	1.04	1.11	0.94
B_0, obs., cm	4.44	3.32	2.76	1.82	2.71	2.68	...
B_0, ratio calc./obs.	1.06	1.09	1.12	1.16	0.93	1.04	1.08
B_0, calc., cm	4.71	3.62	3.10	2.12	2.67	2.78	...

The equations are supposed to be valid when the aerodynamic pressure, $K_a \rho w_o^2$ with the drag coefficient $K_a \sim 0.5$, greatly exceeds s_p, the compressive strength of both the target and the projectile. For a sixfold safety margin, $w_o > 3$ km/sec for iron impact into stone, and $w_o > 1$ km/sec for a hard stone projectile impact into stone. In such a case, aside from backfiring, a radial momentum equal to μw_o is generated both in the target and the projectile, adding up in k as a component equal to 2; backfiring due to explosive vaporization increases the value of k as the velocity increases [cf. equation (5)].

Only the aerodynamic component of frontal pressure generates radial momentum, whereas the "dead resistance", s_p, does not participate. Hence at smaller velocities k further decreases, (5) being no longer valid, in proportion to the ratio of aerodynamic to total resistance, and down to a value of unity and even less. This is reached at the lower velocity limit w_m for the applicability of the model when the projectile is no longer subject to lateral expansion, or when

$$\tfrac{1}{2} \rho w_m^2 = s_p \text{ (projectile).} \qquad (10)$$

For hard stone impact into stone, $w_m = 0.39$ km/sec; for iron impact into stone, $w_m = 1.24$ km/sec.

In large-scale phenomena friction generates an additional component of lateral resistance depending on the weight of the overlying mass and the coefficient of friction,

f_s :

$$s = s_c + f_s g \rho x_c \tag{11}$$

Here s_c is the component of lateral strength due to cohesion, g the acceleration of gravity, and x_c the half-depth of radial momentum which approximately can be set equal to

$$x_c = 0.610\ x_0 \tag{12}$$

with

$$x_0 = 0.800\ x_p', \tag{13}$$

these values representing more or less overall averages for destructive impact (cf. Fig.1).

In some cases s_c itself may depend on depth; an effective depth corresponding to x_c is then to be adopted.

To compare the preceding formulae with experiment would require laborious study, on account of the amount and complexity of the experimental material accumulated. It is also unnecessary at this stage because it turns out that the formulae describe the experiments with an accuracy that is not inferior to that of the parameters involved when they are known, such as the strength characteristics of the material; and in many cases the parameters are unknown and only can be derived best from the very formulae as given above. This especially applies to the moon.

A couple of examples may illustrate the approximation to experiment obtained by the application of equations (3), (4), (6) and (7). ~~The latter point referring to the behavior of ductile materials has also been anticipated theoretically (Öpik, 1958a, p. 32).~~ "The discrepancy is shown to be attribut-

Table II summarizes experiments with aluminum spherical pellets, accelerated in vacuo with a light-gas gun and fired into aluminum targets of different tensile strength (s_t) as determined in the laboratory(Rolsten, Hopkins and Hunt, 1966). For ductile metallic solids, $s_p = 5s_t$; $s = 3s_t$ can be assumed, and much of the mass affected will stick to the crater, making its diameter smaller than predicted by equation (7). This expectation is borne out by the last line of the table, although the systematic difference is but slight. The observed penetrations include the height of the lip, and to make the data comparable the calculated penetrations, x_p , were increased by an average factor of 1.16. With this, there is a perfect--and rather unexpected--agreement between theory and observation.

In another set of experiments (Comerford, 1966) the results were compared with Öpik's theory with the conclusion that "theory and experiment agree reasonably well for brittle materials, but there is only partial agreement when theory is compared with measurements on ductile materials". The latter point, refferring to the behavior of ductile materials, has also been anticipated theoretically (Öpik, 1958a, p.32). The discrepancy is shown to be attributable due to the ability of ductile materials to deform plastically without fracturing" (Comerford, 1966). Planetary crustal or surface materials are predominantly of the brittle type and the theory should well apply here.

Not all of the mass affected is demolished; part of it is plastically displaced into the rim or lip (cf. Fig.1, LL_0N). The crushed volume of debris, as contained between the basic rock ($AALL_0NS$) and the apparent surface ($x'BBCB$...) equals 0.669 of the total volume affected, for the typical crater contour. Hence the mass crushed can be assumed equal to

$$M_c = 0.669 k \mu w_0 / u_s \quad , \tag{14}$$

and the volume crushed

$$V_c = 0.244\, x_p\, B_o^2 \quad . \tag{15}$$

Part of it falls back into, or stays in the crater ("fallback", F_b, Fig.1), part is ejected over the rim ("throwout", Tho, Fig. 1).

C. Ejection Velocity, Heating and Crater Ellipticity

The modification of the target in cratering events is basically of two types (apart from the hypervelocity phenomena in and around the central funnel, Q), with possible transitions: the destruction of the target over the volume of the crater bowl (IFLAA, Fig.1); and the plastic compression and deformation of the bedrock surface ($AALL_0N$). Most of the debris of the bowl are fanning out into an expanding volume, being crushed as in one-sided compression. In "normal" fragmentation, for fragments of "finite" dimensions, only moderate heating takes place, because excessive shock required for frictional and compressional heating would pulverize the material. However, some of the target material, especially around the central funnel, may become locked in all-sided compression which, at pressures of $10^5 - 10^6$ atmospheres, may be subject to pressure modifications of its crystal structure (coesite) and to more intense heating without however acquiring considerable ejection velocities. The amount of such material, subject to hyperpressures without ultimate fragmentation, is relatively small. In the following we will concern ourselves only with the massive debris and ejecta of the crater bowl which are the product of crushing, leading to "normal" fragmentation. With a few reservations (central funnel, vaporization) the formulae of this section apply also to semi-destructive impact (cf. next section).

Let P (Fig.1) represent a surface of constant shock velocity u, the mass enclosed in it being yM, so that y is the "fractional mass affected". The shock velocity at P is then

$$u = kw_0\mu/yM = u_s/y \qquad (16)$$

valid outside the central funnel (Q) at which approximately

$$y_Q = 25\,\mu/M \qquad (17)$$

where

$$u_Q = 0.04\ kw_0 \qquad (18)$$

The kinetic energy at P is released and converted

22

mainly into heat, partly into the kinetic energy of ejection. If λ_x is the kinetic efficiency of the shock at depth x, the transversal velocity at the shock front is

$$v = \lambda_x u \quad ; \tag{19}$$

and the heat release in erg per gram of the crater material becomes (Öpik, 1958a)

$$q = \tfrac{1}{2}u^2 \, (1 - \lambda_x^{\,2}) \tag{20}$$

In the central funnel turbulent mixing is supposed to lead to a uniform heating and impulse ejection velocity $0.2\lambda_c w_0$, so that the heat release becomes (Öpik, 1958a, 1961a)

$$q_c = 0.02 w_0^{\,2}(1 - 0.02k^2)(1 - \lambda_c^{\,2}) \tag{21}$$

If leading to vaporization, it increases the velocity of ejection from the central funnel over the value of $0.2\lambda_c w_c$ and increases the recoil momentum; this ghas been taken into account in equation (5). The fraction vaporized in the central funnel is then (Öpik, 1961a)

$$f_g = 3.3 \times 10^{-13}\left[(1 - 0.02k^2)w_0^{\,2} - 10^{12}\right] \leqslant 1 \ . \tag{22}$$

~~f_g = 1 is reached~~ ($k^2 \rightarrow 20$ for high velocities and stone impact into stone). $f_g = 1$ is reached at $w_0 = 24$ km/sec ($k^2 = 15$). For higher velocities, shock vaporization at the expense of released heat (q) becomes possible outside the central funnel. Vaporization can take place only when $w_0 > 10.4$ km/sec, according to this equation.

An element of mass dy between two shock surfaces P and P_1 (Fig.1) is streaming out in a manner analogous to hydrostatic flow of a liquid from the bottom opening of a vessel, the velocity decreasing according to $h^{\frac{1}{2}}$, where h is the fluid level of the vessel. For a vessel of constant width the mass is dh, the kinetic energy $v^2 \sim h$, and the frequency of v^2 to $v^2 + dv^2$ is proportional to dh or to $d(v^2)$: the kinetic energy has a constant frequency law,

$$f(v^2)d(v^2) = d(v^2) \times \text{const.} \qquad (23)$$

We assume the same law for the distribution of v inside dy, the ejection velocity decreasing linearly with depth x. Conventionally, we assume all dy elements to reach to the same depth x_0, so that

$$v^2 = v_0^2(1 - x/x_0) \quad , \qquad (24)$$

also

$$v_0 = \lambda u \quad , \qquad (25)$$

and the relative (normalized) frequency of v^2 or the fraction of v^2 between v^2 and $v^2 + dv^2$ to be

$dn = dv^2/v_0^2 = dx/x_0$

$$dn = \cancel{F(v^2)}\, dv^2 / v_0^2 = dx/x_0 \quad . \qquad (26)$$

Although the hydrostatic analogy is remote, the accepted velocity distribution accounts, qualitatively at least, for loss of kinetic energy in collisions and turbulent friction while a mass element makes its way outwards, so that the loss will be, i.e. greater the deeper it had started. The assumptions are justified by the application to lunar and terrestrial crater profiles (cf. Sections II. F and V. A) and, probably, are not far from reality even quantitatively.

A similar rough assumption is to be made for the distribution of the exit angles, β, of the ejecta (Fig. 1). The condition of continuity and near-incompressibility of the target material over the relevant major fraction of the mass affected requires that the ejection vectors must be all in "meridian" planes directed outwards, and that the exit angles form a continuous sequence from 0° at the center to β_0 at the rim, at $y = 1$, where the direction is tangent to the crater lip at L. An interpolation formula,

$$\sin \beta = y \sin \beta_0 \qquad (27)$$

is here proposed without further justification, to represent the fanning-out of the ejection angles at the original target surface.

Equation (7) defines an average crater diameter which, in the case of ellipticity, can be assumed to be the mean of the maximum and minimum diameters. In a homogeneous target the crater ellipticity, $\varepsilon = (a - b)/a$, in the direction of motion of the projectile, should depend on the angle of incidence, γ, as follows (Öpik, 1961a) :

$$\varepsilon = 2\left[\sec\gamma + (p \tan\gamma)/3 - 1\right]\Big/(3D) \qquad (28)$$

in former notations. The formula should be valid for angles less than $\gamma = 60^{\circ}$, and roughly up to 75°

D. Semi-Destructive Impact

This is the case of a hard projectile entering a softer target with a velocity below w_m [equation (10)]. The projectile essentially retains its shape and, to some extent, also its aspect relative to the direction of motion, while the target yields, being crushed and forced into hydrodynamic flow. The equation of motion (for $\gamma = 0^o$) is

$$m\,dw/dt = -(K_a \rho w^2 + s_p) \qquad (29)$$

in former notations, with the mass load per cm^2 cross section being defined as

$$m = \mu/(\pi R^2) \quad ,$$

where R is the equivalent radius of the cross section (σ) contour at right angles to the direction of motion, $\sigma = \pi R^2$

The drag coefficient depends on the shape of the projectile. For a flattish angular front surface $K_a = 0.75$ can be assumed as an overall mean characteristic value (while a value of 0.5 better suits a hemispherical front, as well as the case of full destructive impact with a hydrostatically deforming projectile).

With

$$dw/dt = w\,dw/dx$$

equation (29) can be integrated for the specific case of s_p = const.,

$$w^2 = (w_1^2 + N)\exp(-Px) - N \quad , \qquad (30)$$

where w_1 is the initial entry ~~wx~~ velocity and

$$N = s_p/(\rho K_a), \quad P = 2K_a \rho/m \quad .$$

For $w = 0$, the depth of penetration x_0 is determined by

$$Px_0 = \ln\,(1 + w_1^2/N) \quad . \qquad (31)$$

Equation 7 remains valid, as well as other equations of Sections II. B and C except (5), (6), (9), (13), (17), and (19) and (22). Instead of (17) and (18) $y_Q = \mu/M$ and $u_Q = kw_0$ can be set.

At first contact of the projectile with the target, there is a shock forcing a hydrodynamic flow pattern on the target; only after the flow is established is equation (29) valid. For an incompressible model with a blunt front the shock momentum transmitted to the target is close to $\rho w_1 \cdot \frac{1}{2} R\sigma$, and this must equal the loss of momentum by the projectile, $(w_0 - w_1)m\sigma$, where w_0 is the initial velocity before contact. Hence the shock ratio of velocities becomes

$$\psi = w_1/w_0 = (1 + \tfrac{1}{2}\rho R/m)^{-1}. \qquad (32)$$

The coefficient of radial momentum is less than unity and is obtained by integrating the first (hydrodynamic) term of (29),

$$k_1 = \int K_a \rho\, w^2 dt \Big/ (2K_a m w_1)$$

(K_a not cancelled with purpose),

$$k = (1-\psi)/2K_a + \psi k_1 \qquad (33)$$

The momentum integral is rather inconvenient for quick use. Instead, the work integral yields the fraction of hydrodynamic work [$\int dx$ of first term in (29), with (30) substituted] to total work as

$$\eta_1 = 1 - (N/w_1^2)\ln(1 + w_1^2/N) \qquad (34)$$

For very varied conditions and parameters an empirical relation has been established by numerical integration,

$$k_1 = \eta_1(0.65 + 0.35\eta_1^6)/2K_a, \qquad (35)$$

which represents the momentum transfer within a few per cent.

Also, instead of equation (13) (which refers to the mutually destructive impact), the effective depth of disturbed material in the target can be assumed equal to

$$x_p = x_o + \tfrac{1}{2}R \tag{35}$$

The above equations are for an idealized case of a flat evenly loaded front surface of the projectile parallel to the target surface and $\gamma = 0°$. The actual shape of the projectile and orientation of the front surface would introduce complications, including rotational couples which here are disregarded. For oblique impact under maderate angles, a symbolical improvement would consist in replacing x by xsecγ in the preceding equations and in taking the encounter cross section at right angles to the direction of motion.

E. Impact of Rigid Projectile into Granular Target

In the preceding the frontal resistance from target cohesion, s_p, was assumed to be constant. On granular surfaces--dust, sand, gravel, including partly consolidated material, the resistance is variable, increasing with the depth of penetration; this is obvious from the experience that a heavy load sinks deeper into sand than a light one. Experiments as reported below have shown that for an upper thin layer of sand (0.5--15 cm) the cohesive frontal resistance can be well represented by a small constant term plus a main quadratic term of the depth x,

$$s_p = S_p\ (x^2 + a^2) \tag{37}$$

Natural sand or gravel containing an unsifted variety of grain sizes, and natural stony projectiles with a flattish bottom were preferred to artificially normalized laboratory conditions. Experiments on a natural beach (Almuñécar, Spain, October 1966 and 1967), though showing considerable local differences, generally were conforming to (37). There were no obvious differences between the static values of s_p (pure pressure without motion) and the dynamic values computed from cratering impact experiments, according to the modified cratering formulae as given below. It was surprising to find that similarly conducted experiments by Surveyor spacecraft yielded even quantitatively similar mechanical characteristics of the lunar top soil.

When (37) is substituted into (29), integration yields, for this particular case of variable resistance,

$$w^2/Q = (w_1^{\ 2}/Q + 2 + a^2P^2)\exp.(-\xi) - (2 - 2\xi + \xi^2 + a^2P^2), \tag{38}$$

with $\xi = Px$, P being the same as in (30), and with

$$Q = S_p m^2 /(4\ K_a^{\ 3}\ \rho^3) \quad (\mathrm{cm/sec})^2\ . \tag{39}$$

The ultimate depth of penetration, $x_o = \xi_o / P$, is obtained from (38) with w = 0, or from

$$\left(2 - 2\xi_o + \xi_o^{\ 2} + a^2P^2\right)\exp \xi_o = (w_1^{\ 2}/Q) + 2 + a^2P^2 \tag{40}$$

Equations (32), (33) and (35) further determine w_1, the entry velocity, and k, the coefficient of radial momentum transfer, but instead of (34) the dynamical work ratio now becomes

$$x_1 = 1 - Q\left(a^2 p^2 \xi_0 + \tfrac{1}{3}\xi_0^{\,3}\right)/w_1^{\,2} \quad . \tag{41}$$

when $\xi_0 \to 0(< 0.20)$, $\frac{1}{3}\xi_0^3 \to (w_1^{\,2}/Q) - a^2 p^2 \xi_0$ and

$x_1 \to (\frac{1}{4}\xi_0^{\,4} + \frac{1}{2}a^2 p^2 \xi_0^{\,2})Q/w_1^{\,2}$.

With the total radial momentum defined as

$$J_r = k\mu w_0$$

and on the provisional assumption that crater volume is determined through dynamical action alone according to (1), (2), (3), and (4), an "apparent" average lateral strength s_a is defined as

$$s > s_a = J_r^{\,2}/(\rho V^2) = 7.59 J_r^2/(\rho\, x_0^{\,8} B_0^{\,4}) \ (\text{dyne/cm}^2). \tag{42}$$

This is an apparent value and a lower limit because, at the low velocities and energies involved, the static work of penetration (against cohesive strength) also appreciably participates in producing a crater as shown by experiments in gravel.

A satisfactory representation of the experiments by a law of cohesive resistance in the form of equation (37) has been arrived at by trial and error. Surprisingly, no dependence of the static or dynamic resistance (bearing strength) on the linear dimension could be detected except the inevitable shock interaction (32). Shape of the contact surface (projectile or slug) is, of course, of decisive importance in the dynamic interaction as it determines K_a and k ; the use of flattish surfaces throughout has given a degree of homogeneity to the experiments which also should correspond to low-velocity impacts of throwout boulders on the moon.

The constant component in (37) was too small and variable for exact determination, but its form as $a^2 S_p$, thus proportional to the strength at greater depth and not an absolute constant, was preferable, with an overall value of the parameter $a^2 = 2 \pm 0.5$ cm^2. (The same constant worked well also in interpreting the Surveyor experiments on the moon. The constant term is, of course, of importance only at small loads and penetrations.

Static tests of cratering interpreted according to a certain rational model gave the clue to the ratio s/s_a, of the true to apparent average lateral strength. If μ is the static mass load, g the acceleration of gravity, σ the frontal cross section (of stone, slug, or rod), x_o the equilibrium depth attained by gradual loading so that the velocity is kept near zero, the maximum resistance equals s_p (max) $= \mu g / \sigma$, and the resistance parameter of equation (37), with $a^2 = 2$ and c.g.s. units becomes

$$\cancel{\bar{s}_p \neq s_p \left(\tfrac{1}{3} x_o^2 + 2\right)}. \quad S_p = \mu g / \sigma (x_o^2 + 2) \text{ (dyne/cm}^4\text{)}$$

The resistance averaged ever x_o, the entire depth of penetration, is then

$$\bar{s}_p = S_p \left(\frac{1}{3} x_o^2 + 2\right)$$

A "pressure crater" is formed, of diameter B_o and depth $x' \ll x_o$ (unlike the impact craters in sand or gravel where $x' = x_o$; invariably reaching the bottom contact surface). The volume displaced by slug and crater then equals cf Equ. 1)

$$V_p = (0.363\, x' B_o^2 - \sigma x') + \sigma x_o = V_1 + V_2$$

The total work of "static" penetration evidently is

$$E_p = \sigma \bar{s}_p \, x_o \quad \text{(erg)},$$

a fraction F of which is assumed to be transmitted at right angles on lateral work of cratering as measured by the product of lateral strength and volume displaced,

$$F \, E_p = sV_p \; .$$

In an incompressible medium the volume displaced is ultimately lifted up, the average lifting height being $\frac{1}{2}(x' + h)$ for V_1 and $\frac{1}{2}(x_o + h)$ for V_2, h denoting the rim elevation of the crater. This involves a work against gravitation,

$$E_g = g\rho \left[V_1 \tfrac{1}{2}(x' + h) + V_2 \tfrac{1}{2}(x_o + h) \right]$$

The work of uplift against gravitation is transmitted at right angles from lateral expansion, in the same manner as the lateral work originated from the downward work of penetration. It is sensible then to assume (and the numerical applications amply support the assumption) that

$$E_g = FsV_p = F^2 E_p \; ; \text{ or } F = (E_g / E_p)^{\frac{1}{2}}$$

whence a value for the average lateral strength in stati penetration results as

$$s = FE_p / V_p = (E_g \, E_p)^{\frac{1}{2}} / V_p \qquad (43)$$

As example, in the "static" Experiment 2 of Table III, Part a, with a round rod of $\sigma = 3.63$ cm^2 and a final load of 7.28×10^4 g, $x_o = 15.0$ cm, $x' = 1.7$ cm, $h = 1.0$ cm, $B_o = 12.6$ cm. Hence $V_1 = 114.0$ cm^3, $V_2 = 53.7$ cm^3, $s_p(\max) = 1.97 \times 10^7$ dyne/cm^2, $S_p = 8.65 \times 10^4$ dyne/cm^4, $\bar{s}_p = 6.66 \times 10^6$ dyne/cm^2; $E_p = 3.62 \times 10^8$ erg, $E_g = 9.73 \times 10^5$ erg, $F = 0.0518$ and

and $s = 1.12 \times 10^5$. With $f_s = 0.63$ (determined from angle of repose), $g = 980$ cm/sec, the contribution from friction becomes [equations (12) and (13)] $640x_o$ dyne/cm^2, and the lateral strength, according to (11), is then $s_c = 1.12 \times 10^5 - 9600 = 1.02 \times 10^5$ dyne/cm^2. Unlike s_p, this is an average or effective value, to be compared with the average bearing strength : $\bar{s}_p / s_c = 65.3$ (an unusually high ratio). Although variable, there did not seem to be a systematic dependence of this ratio on penetration, whence (37), properly modified, can also be adapted to represent the average lateral strength,

$$s_c = S_c\left(\tfrac{1}{3} x_o^2 + a^2\right) \qquad (37a)$$

the value of $a^2 = 2$ cm^2 being used throughout.

In interpreting the dynamic (impact) experiments, it was assumed that the independently calculated dynamic (V_d) and static (V_p) cratering volumes are additive. Let $V = V_d + V_p$ denote the total crater volume, proportional to $x_p B_o^2$ of equation (42). According to this equation, evidently

$$s/s_a = (V/V_d)^2 = V^2/(V - V_p)^2 = \left(1 - \frac{F E_p}{sV}\right)^{-2}.$$

A quadratic equation with respect to s is obtained which ultimately yields

$$s_a / s = A(1 + \tfrac{1}{2}A) - \left(A + \tfrac{1}{4}A^2\right)^{\frac{1}{2}} \qquad (44)$$

where

$$A = s_a V / F E_p.$$

An average value of $F = 0.113$, obtained from the first six static tests [Table III(a)] was used. Table III contains a summary of the experiments. No two experiments (static with gradual loading) were made on the same spot; only the ultimate load and penetration are recorded.

Because of the large dispersion, logarithmic mean values are quoted as being more significant. The "probabl deviation ratio" of a single experiment; corresponding to 0.845 of the absolute deviation in the logarithm, $\sum|\Delta| / [n(n-1)]^{\frac{1}{2}}$, would indicate that 50% of the deviations if Gaussian are expected to be within this ratio of the logarithmic mean and its reciprocal. Experiment (25) was made at oblique incidence, $\gamma = 24\overset{\circ}{.}6$ from the vertical, and is interpreted with corresponding modification, $\xi = Px \sec\gamma$ and using $S_p \cos^2\gamma$ instead of S_p in Equation (39), while S_c remains unaffected. Experiments (30) (31) (32) yield anomalously high frontal resistance while the s_c values are normal despite high s/s_a ratios. These were the only experiments where a longish slug was made to impact on its narrow end, and every time it tilted over and was found lying overturned on ~~x~~ its long side after impact; possibly, in this twisting movement the area of resistance was increased which could account for the abnormal values calculated on the assumption of the small area of encounter. The lateral resistance was not affected, depending on total momentum, actual volume of crater and penetration, without direct intervention of aspect or area of contact.

Although measurements of x_o and B_o on sandcraters cannot be very accurate, the dispersion in the inferred S_p

TABLE III

Mechanical Strength and Cratering in Natural Beach Gravel

Site	I	II	III	IV	V
Average grain size, mm	5	3.5	4	1.5	1.8
State of moisture	dry	dry	dry	wet	moist
Assumed density, g/cm^3	1.7	1.7	1.7	2.0	1.7
Friction, f_s	0.63	0.63	0.63	0.40	0.63

(a) Static Experiments with Craters Measured ($x' = 0.15 x_o$ average)

No	Site	x_o cm	B_o cm	σ cm^2	F	$s_p$max. $dyne/cm^2$	$\bar{s}_p$ $dyne/cm^2$	s_c $dyne/cm^2$	S_p $dyne/cm^4$	S_c $dyne/cm^4$	$\bar{s}_p/s_c$
(1)	I	5.5	11.5	3.63	0.117	1.15×10^6	4.33×10^5	1.96×10^4	35800	1620	22.1
(2)	I	15.0	12.5	3.63	0.052	1.97×10^7	6.66×10^6	1.02×10^5	86500	1330	65.3
(3)	I	1.75	23.5	198	0.094	3.69×10^5	2.20×10^5	1.75×10^4	72800	5800	12.6
(4)	I	8.5	22.5	29.3	0.105	2.42×10^6	3.51×10^5	3.82×10^4	32600	1460	22.3
(5)	I	5.2	10.5	3.25	0.176	6.27×10^5	2.38×10^5	8.9×10^3	21600	810	26.8
(6)	I	6.5	9.9	3.25	0.161	9.02×10^5	3.28×10^5	1.28×10^4	20400	800	25.6
				Mean	0.118						

Logarithmic mean 25.5

Probable deviation ratio 1.36

(2a) The rod of Experiment (2) was excavated in situ and the same load of $s_p = 1.97 \times 10^7$ applied. The additional penetration was $x'_o \approx 5.0$ cm (thus reaching a total of $15.0+5.0 = 20.0$ cm below the undisturbed surface)

(b) Other Static Experiments

No	Site	x_o cm	σ cm^2	s_p max $dyne/cm^2$	S_p $dyne/cm^4$
~~(7)~~	I				
(7)	I	0.9	3.63	2.82×10^5	100 000
(8)	I	1.25	3.63	4.31×10^5	121 000
(9)	I	2.82	3.63	6.16×10^5	61 900
(10)	I	4.9	3.63	1.15×10^6	44 200
(11)	I	17.8	3.63	1.96×10^7	61600
(12)	I	0.28	29.3	1.65×10^5	79 300
(13)	I	1.7	3.25	2.46×10^5	50 400
(14)	I	2.0	3.25	3.50×10^5	58 300

No.	Site	x_o cm	σ cm^2	s_p max $dyne/cm^2$	S_p $dyne/cm^4$
(15)	II	2.5	145	4.76×10^5	57800
(16)	II	4.0	46	1.50×10^6	83300
(17)	III	1.4	140	4.80×10^5	120000
(18)	IV	0.90	140	6.5×10^4	232000
(19)	IV	2.25	140	4.8×10^5	68000

Log. mean of Exper. (1)--(19) 55500

Probable deviation ratio [illegible].46

TABLE III. Continued

(c) Dynamic (Impact) Experiments

No	Site	x_o cm	B_o cm	m gr/cm^2	cm^2	w_o cm/sec	w_1/w_o	k	s/s_a	S_p dyne/cm^4	S_c dyne/cm^4	S_p/S_c
(20)	I	5.8	54	34.5	525	577	0.759	0.253	1.89	31500	3250	9.7
(21)	I	2.6	21	18.4	108	221	0.788	0.211	1.82	19900	2520	7.9
(22)	I	3.9	26	18.4	108	479	0.788	0.250	1.98	32000	2980	10.7
(23)	II	2.3	8.8	8.05	15.8	372	0.809	0.260	1.79	26200	4230	6.2
(24)	II	2.4	10.0	8.05	15.8	525	0.809	0.267	1.96	47000	5400	8.7
(25)	II	2.3	13.0	8.05	15.8	573*	0.809	0.271	2.41	60300	3380	17.9
(26)	III	2.9	14.7	7.55	22.1	1266	0.770	0.317	2.03	132000	9750	13.5
(27)	IV	0.9	20.1	12.93	140	220	0.660	0.257	1.43	59100	3420	7.0
(28)	IV	1.2	20.1	12.93	140	372	0.660	0.268	1.43	112000	14100	7.9
(29)	IV	2.2	23.5	12.93	140	525	0.660	0.300	1.49	70600	8530	5.7
(30)	V	3.2	13.3	10.5	9.0	1266	0.880	0.237	4.31	220000	5210	42.2
(31)	V	2.5	12.5	10.5	9.0	525	0.880	0.205	4.60	73400	1530	48.0
(32)	V	1.8	9.5	10.5	9.0	372	0.880	0.169	3.87	77200	3080	25.1
(33)	V	2.6	12.1	4.87	19.4	1266	0.677	0.397	1.47	63300	9960	6.4
(34)	V	2.1	10.9	4.87	19.4	525	0.677	0.366	1.48	20800	3340	6.2
(35)	V	1.7	10.4	4.87	19.4	372	0.677	0.339	1.53	17700	2610	6.8
(36)	V	3.7	16.1	7.55	22.1	1266	0.770	0.344	2.00	60700	3370	15.7
(37)	V	2.65	12.0	7.55	22.1	525	0.770	0.304	1.78	29300	3580	8.1
(38)	V	2.22	11.4	7.55	22.1	372	0.770	0.281	1.81	23500	2780	8.5
Logarithmic mean, Exper. (20)-(38) ...								...	...	48600	4380	10.9
Probable deviation ratio										1.65	1.54	1.61

* Experiment (25) at oblique incidence.

and S_c values is much greater than could be due to straightforward errors of observation. A natural granular layer possesses an intrinsic non-homogeneity of which the dispersion testifies, and which in particular may depend on accidental configurations of the larger grains or pebbles.

The increase of strength with depth depends on two factors: the tighter packing of the deep layers, and the strengthening effect of the weight of the overlaying layers. In Experiment (2a), when these layers in Experiment (2) were removed, the surface laid bare in such a manner was unable to support a load of $s_p = 1.97 \times 10^7$ dyne/cm^2 which it withstood under the weight of the former layer of 15 cm with $S_p = 8.65 \times 10^4$ dyne/cm^2. With re-application of the former load, a new penetration of $x_0 = 5.0$ cm was achieved, yielding a strength coefficient $S_c = 7.30 \times 10^5$ dyne/cm^2, 8.4 times larger than the former value--a characteristic of the intrinsic tightening of the granular matrix with depth. With unremoved layer, the resistance at $x_0 = 15.0 + 5.0 = 20.0$ cm, according to (37), would have been $s_p = 8.65 \times 10^4 \times 401 = 3.48 \times 10^7$ dyne/cm^2, 1.77 times the value when the layer was removed; this indicates the degree of additional reinforcement below the depth of 15 cm due to the weight of the overlying 15 centimeters.

All these details are brought out because of their close qualitative and quantitative analogy with similar experiments made on the lunar surface by Surveyor spacecrafts, so that the results of these terrestrial experiments can be applied with some confidence, by way of extrapolation, to the mechanical properties of the lunar soil.

Although of good working value, it would be wrong to extrapolate equations (37) and (37a) to greater depths without limitation. The quadratic law of increasing strength can be valid only in a top layer; at greater depth it should merge into a constant value corresponding to compacted granular material. For the "Teapot" nuclear crater in desert alluvium (cf. Shoemaker, 1963), at $x_o = 3150$ cm, $s_c = 4.0 \times 10^7$ dyne/cm^2 (cf. Section II.F); a value of $S_c = 4 \times 10^3$ which is about the mean in Table III(c) for gravel would reach the observed value at x_o . 100 cm, and this shall not be surpassed in a granular matrix except at very much greater depth when plastic compaction into solid rock takes place. The same must be true of the frontal strength; with $s_p < 2 \times 10^8$ as for sandstone and $S_p \approx 5 \times 10^4$ as a mean value in Table III(c) the limiting depth for the quadratic term is only about $x_o \approx 63$ cm. Thus, it can be assumed provisionally that (37) and (37a) are probably valid to a depth of about 60--100 cm, beyond which s_c and s_p assume constant "compacted" values.

The logarithmic mean of the ratio of frontal to lateral cohesive resistance at impact [Table III(c)] is 11. This is about the same as the ratio of compressive to crushing strength of brittle materials.

All experiments were conducted at vertical incidence except one on October 12 with $\gamma = z = 25^{\circ}$, $w_0 = 578$ cm/sec; it gave the crater ellipticity as $\varepsilon = 0.039 \pm 0.008$ (measured), to compare with a theoretical value of 0.046 according to equation (28).

For some of the impact experiments of Table III(c), on Sites II, III, and V, the typical crater characteristics mostly averaged in the form as they occur in equation (7), are collected in Table IV. The second half of the table contains the relative diameter limits to which throwout of the qualitatively described intensity was reaching.

F. Kinetic Efficiency and Throwout

In low velocity collisions of stone or other brittle substances, part of the kinetic energy is lost into heating, destruction or rotation, so that the reflected translational kinetic energy is a fraction λ^2 of the original (see equations (19) and (25)). In the proposed cratering model (Fig. 1) the fraction is assumed to vary uniformly from 0 (at $x = x_0$) to λ^2 (at $x = 0$) at constant u, so that the average translational kinetic energy per gram of the ejecta at $y =$ const is $\frac{1}{4}\lambda^2 u^2$.

Experiments with stony projectiles falling on a massive stony surface from a height of 0.5 - 2 meters and reflected from it gave $\lambda^2 = 0.23$ as an average. If an equal

TABLE IV

Typical Gravel Cratering Parameters

Experiments (23)(24)(36)(37) weighted

	B_o, cm	$s^{\frac{1}{4}}$	s dyne/cm^2	$w_o^{\frac{1}{2}}$	w_o cm/sec	x_o cm	x_o/B_o	Lip height h, cm	h/B_o	x_p/B_o
Average	11.7	12.0	2.07×10^4	25.7	660	2.55	0.226	0.66	0.056	0.286

Throwout Estimated Characteristics, in Units of B_o

Experiment (26) only; $B_o = 14.7$ cm

	Outer Crater wall	Massive throwout	Considerable throwout	Extreme noticeable throwout	s	k	w_o
B/B_o	1.355	1.96	3.9	6.8	4.87×10^4	0.317	1266

TABLE V

"Teapot" Nuclear Crater Ejecta (Fallback Throwout) Distribution

(Ballistic distance)

B/B_o $\leq$	1.000	1.185	1.304	1.414	1.581	1.732	∞
Calculated with $a = 1.92$, $b = 0.80$, $\sin\theta_o = 0.800$ for ballistic distance							
F_B	0.346	0.400	0.426	0.463	0.517	0.561	1.000
Observed, Fig. 1 volume x ~~drag~~ (.85)							
F_B	0.274	0.339	0.490	0.570	0.565	0.731	(1.000)
Calculated distance reduced by atmospheric drag							
B'/B_o	1.000	1.175	1.289	~~1.522~~ 1.386	1.522	1.607	
F_B observed	0.274	0.334	0.477	0.550	0.631	0.676	
F_B calculated	0.346	0.400	0.426	0.468	0.517	0.561	

TABLE VI

Variation of Mass Ratio of Two Accreting Nuclei

μ_1/μ	1.000	0.512	0.216	0.125	0.064	0.027	0.008	10^{-3}	10^{-6}	10^{-9}
μ_1/μ_2	81.5	49.8	27.5	19.0	12.7	8.0	4.6	2.37	1.10	1.01

amount was stored in rotation, the coefficient of elastic reflectivity would be 0.46. The experiments consisted in measuring the length of flight [equation (45)]; on the assumption of $z = 45^0$, the apparent values of λ^2 ranged from 0.08 to 0.43 (n = 26) with an apparent average of 0.180; allowing for a dispersion in z, a correction factor of $4/\pi$ was then applied.

The greater internal friction during cratering is likely to lead to a smaller value of λ than in the simple two-body collision. From Table IV it can be seen that the ejecta spread over an extreme diameter of 6.8 B_o [Experiment (26)], or over a horizontal distance of $L \sim 47$ cm. The flight distance is given by

$$L = (v^2/g) \cdot 2\sin z \cos z \qquad (45)$$

where $z = \beta$ (Fig.1) is the zenith angle of ejection. From equation (4) and $s = 4.87 \times 10^4$, $\rho = 1.7$ and $w_o = 1266$ cm/sec as for this experiment, $u_s = 169$ cm/sec. With the condition $u < w_o$ instead of equation (17), (16) yields $y > y_Q = u_s/w_o = 0.133$ in the present case. Taking $y = 2y_Q = 0.266$ as a middle value for top ejection, $u = 635$ cm/sec, $\sin\beta_o = 0.8$ and $\sin\beta = 0.213$, $\cos\beta = 0.977$ according to (27), the top velocity of ejection according to (45) becomes $v = 333$ cm/sec, Hence $\lambda \cong 333/635 = 0.527$, $\lambda^2 = 0.275$ with a considerable margin of freedom, however. It is perhaps an overestimate, as, for constant λ, u increases with decreasing y and the farthest throwout will come from the innermost portions from $y \sim y_Q$. Taking now $y = 0.15$, $u = 1126$ cm/sec, $\sin\alpha = 0.12$, $v = 440$ cm/sec is obtained whence $\lambda = 0.391$, $\lambda^2 = 0.153$. The grain size (0.4 cm, $m = 0.7$ g/cm^2) was such that over the flight length of 47 cm or through an air mass of about 0.07 g/cm^2, about 5 per cent of the velocity would have been lost at the endpoint through air drag. An increase of λ by 2.5 per cent would be required, making it 0.401 and $\lambda^2 = 0.16$. This latter value is probably the best guess that can be made.

With the adopted cratering model [equations (4), (16), (24), (25), (26) and (27)], the fraction f_b (fallback) of ejecta falling inside a radius $\frac{1}{2}B$ from the center of impact and originating along shock surface P of u = const. (Fig. 1) or y = const. equals

$$f_b = \left[aby^2 + by(B/B_0 - y^{\frac{1}{2}}) / (1 - y^2 \sin^2\beta_0)^{\frac{1}{2}}\right] / (1 + aby^2). \quad (46)$$

The term $y^{\frac{1}{2}}$ represents conventionally the distance IE of the ejection point (Fig. 4) in units of B_0. When $f_b > 1$ is obtained, $f_b = 1$ is to be taken. Here

$$a = 8x_0 \sin\beta_0 / B_0 \quad , \quad (47)$$

so that ab accounts for the work of gravity in lifting the ejecta from the depth of the crater to its surface, and

$$b = gB_0\rho / (4\lambda^2 \cdot \sin\beta_0) \quad . \quad (48)$$

takes care of the horizontal length of the trajectory.

The total deposition of ejecta inside $\frac{1}{2}B$ is obtained by numerical integration.

$$F_B = \int_0^1 f_b dy = y_Q \cdot f_Q + \int_{y_Q}^1 f_b dy \quad (49)$$

Of the two parameters, b is by far the more important one. Fig. 2 represents the function log $(1 - F_B)$ as depending on log b, for four selected values of a and for $\sin \beta_0 = 0.80$. The insert, Fig.2a, valid for a > 0.91, represents log $(1 - F_B)$ as depending on log (ab).

It may be noted that the destructive and ejection phenomena depend primarily on the properties of the rock target (ρ, s, u_s). For a ~~[illegible]~~ crater of given dimensions, the distribution of the ejecta will be practically the same, whatever the velocity of the projectile, or whatever the origin of the crater--meteorite impact, high explosive or nuclear blast if the charge is properly placed (not too deep and not too near the surface) so that a not too abnormal crater profile results. The difference in the origin of the blast, velocity and impacting mass, etc., would reveal itself chiefly in the central funnel, Q while over most of the crater volume this is irrelevant, once the crater size is given (the size, of course, is determined by the conditions around the center of impact).

We chose the "Teapot" nuclear crater (Shoemaker, 1963; Nordyke, 1961) whose profile is reproduced in Fig. 1. The dimensions are : $2(I)L_3 = B_0 = 10500$ cm; of the ground-level bowl, $2IL = 9100$ cm; $x_o = 0.8x_p = 3150$ cm; $x_c = 0.61x_o = 1920$ cm. The target is "a loose sand-gravel mix with a density of 1.5-1.7 and a water content (at depth) of about 10 per cent". We assume $\rho = 1.7$ <u>in situ</u> and $\rho = 1.5$ for the ejecta deposit whose volume is thus to be multiplied by a factor of 1.5/1.7 = 0.883 to reduce it to that of the parent matrix. In similar ground, the "Scooter" TNT explosion indicated a radial stress of 600 psi at a distance of 200 feet (Murphey, 1961) which, at the crater bowl (150 ft) and an inverse-cube law for the stress, would correspond to lateral strength $s = 9.8 \times 10^7$ dyne/cm^2; with a depth $x_c \cong 1800$ cm, $f_s = 0.78$, a small frictional component of 2.1×10^6 would make little difference, $s_c = 9.6 \times 10^7$ dyne/cm^2 according to equation (11). Within +100 to -50 per cent, this should hold also for the "Teapot".

Integrations according to (48) and (49), with $a = 1.92$, $b = 0.80$, $\sin\beta_0 = 0.800$ gave the distribution of the ejecta as shown in Table V. The value for $B/B_0 \leq 1.000$ is the true fall-back (F_b, Fig. 14). There is a systematic difference between the observed and calculated values which cannot be removed by a different set of parameters. Namely, only the choice of b is to some extent free, while a and β_0 are prescribed by the crater profile. With a change in b, all the calculated values of F_B move in the same direction, so that an improvement at one end of the table will be countered by deterioration at the other. Some of the difference may be attributed to air drag which forced the ejecta to deviate from the purely ballistic trajectories and descend at distances smaller than those of equation (45). The air drag on these massive ejecta does not depend on grain size but on the total mass of the stream, m; if m_a is the traversed air mass, the loss in velocity is

$$\Delta v/v = -m_a/m = \Delta L/L$$

The relative loss in the distance is then equal to the average loss $\Delta v^2/v^2$ over the entire trajectory, or to one-half the final loss, $\frac{1}{2}\Delta v^2/v^2$, which is $\Delta v/v$ as indicated. With this, and m determined from the thickness of the deposit (from 4 to 1 meters), the ballistic distances are decreased to B'/B_o as given in the bottom part of the table. The last two lines contain the comparison between observation and calculation with this refinement. The discrepancy is diminished but still persists. Nevertheless, for an a priori approach, the results are quite satisfactory.

With b = 0.80 and the other parameters, equations (47) and (4) yield

$$\lambda^2 u_s^2 = \lambda^2 s/\rho = 4.0 \times 10^6$$

or, with $\rho = 1.7$,

$$\lambda^2 s = 6.8 \times 10^6$$

for the desert alluvium. With s = 5 to 20 x 10^7 as for "Scooter", one would obtain $\lambda^2 = 0.14$ to 0.034. Taking $\lambda^2 = 0.16$ as for the gravel craters, $s_c = 4.2 \times 10^7$ dyne/cm^2 can be conventionally regarded as the best estimate for the "Teapot" alluvium, the gravity friction correction amounting to a mere 2.5×10^6 dyne/cm^2.

III. Planetary Encounters

The surface properties of the moon cannot be well interpreted without its past history, beginning with its origin and followed by further exposure to collisions with interplanetary stray bodies. This purpose is basically served by the theory of interplanetary encounters which in its original "linear" form (Öpik, 1951, 1963a) is concerned with very small collision cross sections as compared to the orbital dimensions. Supplemented by the consideration of acceleration in repeated gravitational "elastic" encounters (Öpik, 1966a), it requires essential modifications when dealing with rings of "planetesimals" orbiting in tightly packed nearly circular orbits. The relative velocities are then small, the cross sections large and the linear approximation (i.e. treating the orbital arc segments near the points of encounter as straight lines) is no longer workable. Appropriate formulae for these cases are for the first time given further below.

The linear approximation formulae for planetary encounters are as follows. In a Jacobian frame of the restricted three-body problem, a smaller body (planet, moon to be called further "satellite") of relative mass μ revolves around a central body (sun, earth to be called "main body"), of mass 1 ($1 - \mu$ more precisely) in a nearly circular orbit of radius 1 and period 2π, so that its orbital velocity is taken as unit, and the gravitational constant is also 1. A stray body (to be called "particle") when at distance A has a velocity U relative to the circular velocity of μ, in the units chosen,

$$U^2 = 3 - 2\left[A(1 - e^2)\right]^{\frac{1}{2}} \cos i - 1/A \qquad (50)$$

and a radial component U_r

$$U_r^2 = 2 - A(1 - e^2) - 1/A \qquad (50)$$

where A = semi-major axis, e = eccentricity, and i = inclination of the orbit of the particle relative to that of the satellite.

A particle which can pass at distance 1 "crosses" the orbit of the satellite without necessarily intersecting. Due to secular perturbations, precession of the node and advance of the periastron of the satellite's orbit, resulting in a secular motion of the argument of periastron (perihelion, perigee) ω, a particle crossing the orbit of the satellite will be intersecting it twice during the period of ω, $t(\omega)$. For the earth in heliocentric orbit the repetition interval is $\frac{1}{2}t(\omega) = 32000$ years. The "probability" P_e (mathematical expectation) of encounter per one revolution of the particle is then

$$P_e = (\sigma_e^2/\pi \sin i)\left(U^2 + 0.44e_0^2\right)^{\frac{1}{2}} \Big/ \left(U_r^2 + 0.44e_0^2\right)^{\frac{1}{2}}, \qquad (52)$$

where e_0 = eccentricity of the satellite's orbit, σ_e = target radius or encounter (collision) parameter in units of the orbital radius of the satellite. For the inclination the average vector sum

$$\sin i = (\sin^2 i_\rho + \sin^2 i_0)^{\frac{1}{2}} \qquad (53)$$

must be taken, where i_p and i_0 are the average orbital inclinations of particle and satellite to the invariable plane of the system. However, when the encounter lifetime [equation (59) below] is shorter than one-half the "synodic" period of orbital precession, the "instantaneous" value of the inclination must be taken : a similar restriction holds for the term $0.44e_0^2$ in equation (52) with respect to the synodic period of the longitude of periastron.

For physical collision with the satellite of radius R_p (in the same relative units),

$$\sigma_e^2 = \sigma_0'^2 = R_p^2 \left[1 + 2\mu / (R_p U^2)\right] \tag{54}$$

where

$$2\mu / R_p = v_\infty^2 \tag{55}$$

is the square of the escape velocity from the surface of the satellite. For a complete gravitational "elastic collision", yielding a mean angular deflection of 90°, the cross section radius is defined through

$$\sigma_e^2 = \sigma_a^2 = T_a \ln \left[(R_a^2 + T_a) / (\sigma_0^2 + T_a)\right], \tag{56}$$

with

$$T_a = 16\mu^2 / (\pi^2 U^4) \tag{57}$$

where

$$R_a = (\tfrac{1}{2}\mu)^{1/3} \tag{58}$$

is the radius of the "sphere of action" upon the particle of the satellite against the main body. This is not a clearcut limit of action, but its use in logarithmic form renders unimportant this uncertainty. The average perturbation vector of the main body on the radial acceleration of the particle relative to the satellite is zero, so that there is no virtual limit of action, only a disarrangement.

by the perturbation.

The lifetime of the particle with respect to a given type of encounter with probability P_e is

$$t(\sigma) = 2\pi A^{1.5}/P_e \quad , \tag{59}$$

and the true probability of encounter during a time interval t is

$$\eta_t = 1 - \exp\left[t/t\ (\sigma)\right] \tag{60}$$

The validity of the linear approximation P_e is restricted to the case when the curvature of the arc of encounter is less than the target radius σ, which for σ_5 as for the earth and near-circular orbits of the particles requires (Öpik, 1951)

$$\epsilon > 0.0063,\ \sin i > 0.0064,\ U > 0.0090 = 0.27\ \text{km/sec}. \tag{61}$$

Further, provided that sin i and e exceed σ, the target radius, the lifetime must exceed one-half the period of the argument of periastron (not the synodic period in this case),

$$t\ (\sigma) > \tfrac{1}{2}t(\omega) \tag{62}$$

If this is not fulfilled,

$$t\ (\sigma) \cong \tfrac{1}{2}t(\omega) \tag{63}$$

must be taken, unless a shorter lifetime not depending on the secular advance of ω is indicated [cf. equations (69)---(73)].

The breakdown of the linear approximation leads to unreasonably high values of P_e in (58). In such a case an upper limit P_m to P_e is set (Öpik, 1966a), still depending on the secular variation of ω yet independent of the orbital elements e and i ,

$$P_e \leq P_m = 2\sigma_e/(3\pi U) \tag{64}$$

When this condition is not fulfilled, $P_e = P_m$ must be taken instead of P_e (unless superseded by another limit).

For small values of U, when $\sigma_a \gg \sigma$, repeated elastic encounters bring the variable sin i and U_r values often near zero, so that partly (64) has to step in instead. The statistical mean probability P_e is then

$$(P_e \text{ aver.} = P_0 = K_p \overline{\sigma^2}/U \quad , \tag{65}$$

where $K_p \cong 3$ for heliocentric encounters with the earth, and $K_p \cong 2$ for those with Jupiter (Öpik, 1966a). Applying equation (64) to $P_e = P_0$ with $K_p = 3$ the condition of validity of (65) becomes

$$\sigma_e < 2/9\pi = 0.0707 \text{ or } \sigma^2 < 0.005 \tag{66}$$

Otherwise P_m as in (64) must be used.

On the other hand, the target radii should not exceed the sphere of action,

$$\sigma_e \leq R_a \tag{67}$$

When equations (54), (56) or (66) exceed this limit, $\sigma_e = R_a$ shall be conventionally taken; although action is not limited to this distance, it cannot be treated by the simple statistical model of two-body encounters; classical perturbational methods must then be used instead.

The preceding equations of encounter apply when the orbital range of the particle comes within the reach of that of the satellite, augmented by the target radius. The range of applicability is defined by the two conditions of full crossing to be fulfilled simultaneously; when $e > e_0$, these conditions are

$$\left.\begin{array}{l} A(1-e) \leq 1-e_0-\sigma_e \\ A(1+e) > 1+e_0+\sigma_e \ldots \end{array}\right\} \tag{68}$$

and when $e < e_0$, the roles of particle and satellite are interchanged.

A fractional factor may sometimes be applied to the P-values allowing for partial crossing (Öpik, 1951, 1963a).

For very small values of U, as those which would occur in pre-planetary rings of planetesimals, an overall upper limit to the probability of encounter evidently is $P_e < 1$. However, two narrower limits exist which cannot be surpassed; the average lifetime for an encounter, whatever its target radius, must be longer than the shorter one of two : either one-half the synodic period of revolution, t_s, of the particle, or the time of unperturbed fall from a distance of $\sqrt{2}$ (middle of circular orbit) under the attraction of the satellite. Thus,

$$t(\sigma) > \tfrac{1}{2} t_s = \pi A^{1.5} / \left| A^{1.5} - 1 \right| \tag{69}$$

or

$$t(\sigma) > t_F = \pi / (2.83\mu)^{\frac{1}{2}} \quad , \tag{70}$$

when 2π is the orbital period of the satellite around the central body.

These cases occur only when the orbital semi-major axis of the particle is close to unity,

$$A = 1 \pm \Delta , \tag{71}$$

so that a linear approximation to (69) can be used,

$$t_s = 4\pi / 3 |\Delta| \tag{72}$$

II 51

$\frac{1}{2}t_S$ is shorter than t_F ; equation (70), when

$$\Delta^2 > 1.26\mu \tag{73}$$

and when $\frac{1}{2}t_S$ is the lower limit to $t(\sigma)$. When (73) is not fulfilled, t_F is the limit. When the lifetime as calculated from (59) comes out shorter than the limit, $\frac{1}{2}t_S$ or t_F must be substituted for it; the equivalent probability P_e can then be calculated from (59).

As can be seen, complications arise when U is small. A "Fermi-type" acceleration of the encounter velocity for a non-circular precessing orbit of the satellite (Öpik, 1965a, 1966a) could increase it sufficiently before a collision takes place, so that equations (65) or (64) could apply. The acceleration is given by

$$d(U^2)/dt = 1.23F(\omega)(0.625e_0^2 + \sin^2 i_0)/t(\sigma_a), \tag{74}$$

in former notations, where $1.23 = \pi^2/8$ and $F(\omega) = 1$ when $t(\sigma_s) > \frac{1}{2}t(\omega)$. When the deflection lifetime is shorter than $t(\omega)$,

$$F(\omega) = 4\left[t(\sigma_a)/t(\omega)\right]^2 \tag{75}$$

While being deflected and accelerated in the elastic gravitational encounters, the particles are removed by physical collisions, so that they virtually disappear before a certain average value of U is reached. The fraction surviving is

$$\mathcal{J}(U)_2 = \exp\left[-\int_0^t (\sigma/\sigma_a)^2 dt / t(\sigma_a)\right] \tag{76}$$

when U is accelerated from U_1 at $t = 0$ to U_2 at t. In this equation $F(\omega)$ does not appear and there is no restriction depending on lifetime which enters, however, implicitly through (74) from which the interval t is to be determined.

When U exceeds the critical value of $\sqrt{2} - 1 = 0.414$, additional depletion of the particle population begins, through ejection out of the system by way of hyperbolic orbits.

For particles encountering the earth with low initial encounter velocities, $U_1 = 0.1$ (3 km/sec), rapid depletion by physical collisions prevents 99.9 per cent of the particles from reaching $U > 0.3$ (9 km/sec). The average encounter velocity of such particles, when captured by the earth or the moon, is then $U = 0.178$ (5.3 km/sec) (Öpik, 1965a, 1966b). Of course, gravitational action will increase this value to a collision velocity of about 12 km/sec for the earth and 5.8 km/sec for the moon. The fraction accelerated above $U = 0.414$ is less than 10^{-13}, so that ejection is negligible, the entire population being removed in collisions. For Jupiter, however, the conditions are very different, and so are those for the moon with respect to earthbound orbiting particles.

The preceding equations apply to free orbiting particles. In a pre-planetary ring mutual collisions and drag will reduce U to very small values and will also prevent the acceleration mechanism from working (Öpik, 1966a), conditions which must have prevailed during the origin of the moon. Also, when the "particle" is no longer of infinitesimal dimensions as compared to the "satellite", the radius $R_p = R_1 + R_2$, and the mass $\mu = \mu_1 + \mu_2$ must be taken as the sum of the values for the two colliding or interacting bodies, the satellite and the particle.

IV The Origin of the Moon

A. Theoretical and Observational Basis; the Alternatives

The events which shaped the present surface of the moon must be traced to the very origin of our satellite as an individual body. Three principal modes of origin have been envisaged.

(a) The fission theory proposed by Sir George Darwin which at present has fallen into disrepute though without convincing reason;

(b) The theory of formation from swarm of planetesimals orbiting the earth, simultaneously with the formation of our planet (Schmidt, 1950; Öpik, 1962a).

(c) The theory of capture, suggested by an extension of Darwin's calculations backwards by Gerstenkorn (1955) (Öpik, 1955, 1962a) and recently sponsored by Urey (1966a) and Alfven (1963, 1965).

As will be seen, there may be more variants of these typical hypotheses.

Hypothesis (b), originated by O.J. Schmidt (1950), has been strongly supported by Russian astrophysicists--Ruskol, Levin and others; Levin (1966a) provides a fair survey not only of the work of O.J. Schmidt's school in this direction, but also on work done elsewhere on hypothesis (c), while (a) he rejects outright because of the impossibility "of the smooth separation of a rotating fluid mass". The objection holds only if a ready-made moon is supposed to be the end-product. However, the products of fission, broken up into numberless fragments inside Roche's limit, could later on gather and recede, leading thus to a variant of hypothesis (b) (Öpik, 1955).

Observational data, based on the statistics of ellipticities of lunar craters and the geometry of tidal deformations (Öpik, 1961b), point with a good (though not overwhelming) probability to the craters in the lunar continentes having formed at a distance from 5 to 8 earth radii, supporting thus hypothesis (b) as outlined by O.J. Schmidt. While the upper limit is uncertain, owing to the statistical error of sampling the lower limit is well determined. It is pretty certain that the lunar craters in the highlands have not been formed at a distance closer than 4 earth radii.

After Gerstenkorn, retrospective calculations of the evolution of the moon's orbit have been made by MacDonald, Slichter, Sorokin, with very different results as depending on the assumed parameters (Levin, 1966a). All these point to a minimum distance somewhere near or inside the present

Roche's limit, 2 - 5 x 10^9 years ago. Yet the history of the moon preceding this minimum distance or "zero hour" cannot be decided mathematically because not only the tidal friction parameters but even the masses of the interacting bodies themselves could have been variable and their identities unknown (there could have existed several moons, of which only one survived; and the moon may never have gone through this stage at all (Öpik, 1955)). It is reasonable to assume that zero hour was some time near the beginning of the solar system, 4.5 x 10^9 years ago. At that time the mass of the earth was accumulating, and capture of the moon could have taken place at close approach into any near-parabolic orbit, and not necessarily into a retrograde one, by non-tidal trapping through increase of the earth's mass and loss of momentum in collisions during the passage.

It must be emphasized that direct condensation of the moon from a gaseous state is a rather incredible proposition. Even if the required extremely low temperature and high density of the gas prevailed, the earth would have profited from it first, turning into a giant planet like Jupiter. Accretion of particulate matter is reasonably the only way the moon could have come into being. The impact velocities must not have exceeded 11 km/sec, otherwise loss of mass instead of accretion would have resulted (Öpik, 1961a) for the present lunar mass; a lower limit down to 2 km/sec and less must be set for a growing smaller mass [cf. equation (22)]. It is therefore imperative that accretion must have taken place from some kind of a ring of solid particles in which the relative velocities were small.

E. Mass Accumulation from Orbiting Debris

Even in the capture hypothesis of the moon, it must have entered the sphere of action of the earth on a near -parabolic relative orbit, or $U \cong 0$. According to equation (50), this requires $A \approx 1$, $e \approx 0$, $i \approx 0$. The moon must have formed on the same circular orbit with the earth inside the pre-planetary ring and from the same material. Any hope to find on the moon cosmic material of different origin than that of terrestrial material is thus not justified. Also, the time scale of the major accumulation, or depletion of the pre-planetary ring, was determined by the earth as the major body.

In the pre-planetary ring, a remnant of the solar nebula the original cosmic distribution of the elements with the predominance of hydrogen must have prevailed. Jupiter and the outer planets apparently have incorporated hydrogen, helium and other volatiles in cosmic proportion, while the terrestrial planets consist to 99.8 per cent of the non--volatile silicates and iron. If in cosmic proportion, the earth would have captured about 100 times its mass in hydrogen, enabling to keep gravitationally this and other volatiles at any imaginable temperature. Therefore, the gaseous constituents of the nebula must have been swept away somehow from terrestrial space before being sucked into the earth, while the refractory materials gathered into a common plane, into a thin sheet similar to Saturn's rings. For a ring spread from 0.9 to 1.1 a.u., over a width of 0.2 a.u., the total mass of the earth--moon system would correspond to a mass load of $m_0 = 21.3$ g/cm^2 over the orbital plane. A spherical planetesimal of density $\delta = 1.3$ (cometary nucleus without the ices) and radius R_c (cm) has a mass load

$$m_c = 4R\delta/3 \qquad (77)$$

or $1.73\ R_c$ g/cm^2. The damping lifetime of the relative velocity U at orbital inclination i of a particle which has to pass through the ring twice during 2π Jacobian units of time or one orbital revolution (a year) is, in the relative units chosen

$$t_z = \pi m_c \sin i / U m_0 \ , \quad t_z / 2\pi = \tfrac{1}{2} m_c \sin i / U m_0 \ \text{(years)} \qquad (78)$$

and the damped value of U after a time interval t is

$$U_2 = U_1 \exp(-t/t_z) \qquad (79)$$

The orbits of the planetesimals when perturbed will rapidly become circles again while the Jacobian velocity decays on a time scale of

$$t_z / 2\pi = 0.02 R_c / \eta_m \ \text{(years)}$$

for a typical case of $\sin i / U = 0.5$. Here η_m is the fraction of the total mass in the ring which has not yet been accreted by the planet. Thus, for a typical projectile producing a crater about 10 km in diameter, $R_c \sim 1$ km, $t_{\frac{1}{2}}/2\pi = 2000/\eta_m$ years, this short by cosmogonic standards.

Damping is even very much greater for $i = o$, when the U vector is in the plane of the ring. In that case, instead of the cross sections the linear encounter diameter $\sim 4R_c/3$ is the sweeping unit (R_c is assumed to be greater than the thickness of the ring, and slightly displaced from its plane); the linear load of the planetesimal is then

$$m'_c = \pi R_c^2 \delta \tag{81}$$

or 4.1 R_c g/cm. Over a path dL it sweeps a mass $\eta_m m_o dL$ per cm. The radial displacement being $dL_r = |U_r| dL/U$, the radial damping length then becomes

$$L_r = |U_r| m_c' / U m_o \eta_m \tag{82}$$

or, with typically $|U_c|/U_o = 0.5$, $m_o = 21.3$,

$$L_r = 0.1 R_c^2/\eta_m \quad \text{(cm)}, \tag{83}$$

and the damping time is (independent of the ratio U_r/U)

$$t_r = 2L_r/(U \cdot 3 \times 10^6)(\text{sec}) = 2 \times 10^{-15} R_c^2/(U\eta_m)(\text{years}). \tag{84}$$

For $R_c = 10^5$ cm as before, $L_r = 10^9/\eta_m$ (cm), $t_r = 2 \times 10^{-5}/U\eta_m$ (years).

The damping is highly efficient and, unless disturbed by the growing earth or other centers of condensation, the particles of the ring will all move in co-planar circular orbits and mutual coagulation would stop when they are touching side by side, as envisaged by Jeffreys for Saturn's rings

(Jeffreys, 1947b). With small particles, an almost continuous disk is thus formed which, from orbital friction and gravitational instability, is then breaking up into larger planetesimals through coagulation of neighboring regions. When their size and damping time are sufficiently large, they can be collected gravitationally by the growing planetary nucleus when planetary perturbations divert them into its path. Also, perturbations will change the orbital elements e and i of the earth's nucleus, thus increasing its range of heliocentric distance and sweeping ability. Encounters with other massive nuclei will also lead to changes in the orbital elements.

Disregarding damping at first, the earth can collect the particles from the ring only when their circular orbits are perturbed so that they can cross the orbit of the earth. An exception are those which lie within a range from $1 + e_0$ to $1 - e_0$ heliocentric distance, where e_0 is the eccentricity of the earth's orbit. From equation (50) it can be shown that, for $A = 1 + \Delta A$, $i = 0$, and $A(1 - e) \simeq 1$ just sufficient for orbital crossing, the encounter velocity becomes (to terms of second order)

$$U^2 \simeq (\Delta A)^2 \quad \text{or} \quad U = |\Delta A| \tag{85}$$

Hence, when perturbations or collisions induce the particles from orbit A to cross and thus subject them to chances of collision, the U-parameter will be close to that of equation (85). For the envisaged ring, U values up to 0.05

are thus expected, with an average about $0.025 \approx 0.75$ km/sec. In such a case, for bodies even much smaller than the earth, with an escape velocity $v_{es} > 1.5$ km/sec, the unity term in equation (54) can be dropped, and the collision cross section of the growing earth then becomes as from (51),

$$\pi\sigma_v^2 = \pi \cdot 2.63 \times 10^{-10}(1 - \eta_m)^{4/3}/U^2 , \qquad (86a)$$

and

$$\sigma_v = 1.62 \times 10^{-5}(1 - \eta_m)^{2/3}/U . \qquad (86b)$$

With the collision probability from equation (65) which holds, the corresponding collision lifetime from (59) results as

$$t(\sigma)/2\pi = 1.27 \times 10^8 U^3/(1 - \eta_m)^{4/3} (\text{years}). \qquad (87)$$

For $U = 0.025$ corresponding to $A = 1.05$ or 0.95 as the median for the ring, and $\eta_m = 0.5$, the lifetime is 50,000 years ; at the outskirts this may attain 400,000 years. The period of ω may set a lower limit of 30,000 years.

Provided perturbations are available soon enough--which may not be the case at all--a minimum time scale of accretion of the earth may be set at 50,000 years. The effective time may be several times longer.

One source of the perturbations is the earth itself which passes the particles at the close range of ΔA during a synodic period

$$t_s/2\pi = (1.5\Delta A)^{-1} \text{ (years)} , \qquad (88)$$

to first-order approximation. During this period the eccentricity is excited by earth's periodic perturbations to a value of about

$$e' \cong 2\mu(1-\eta_m)/\pi(\Delta A)^2, \qquad (89)$$

the perihelion or the direction of the e' vector revolving with the synodic period. To reach the earth's orbit, $e' = |\Delta A|$ is required, which yields

$$|\Delta A| \approx \left[2\mu(1-\eta_m)/\pi\right]^{1/3} = 0.0124(1-\eta_m)^{1/3}, \qquad (90)$$

or practically the radius of the sphere of action of the accumulated nucleus [equation (58)]

$$R_a \approx 0.0115\,(1-\eta_m)^{1/3} \qquad (91)$$

A secular increase of the semi-major axis of the particle's orbit with a time scale of

$$t_A = \Delta A/(dA/dt) \cong (\Delta A)^4/24\mu^2(1-\eta_m)^2 = 5\times10^9(\Delta A)^4/(1-\eta_m)^2 \text{ (yrs)}, \qquad (92)$$

gives $t_A = 3200$ years at $\Delta A = 0.02$, 1.3×10^5 yrs at $\Delta A = 0.05$, 2×10^6 yrs at $\Delta A = 0.10$. This has the effect of moving away the outer portion of the ring and bringing nearer the inner portion.

Of course, with the distribution of masses in the solar system already settled, perturbations by the other planets will add to the effect. The time scale of secular perturbations here is of the order of 50,000 years (half period, quite sufficient except for their small amplitude, only 0.05 in the eccentricity.

To make perturbations (including acceleration) work, damping must be overcome. For the periodic perturbations, $\frac{1}{2}t_s < t_{\psi}$ or t_{ι} is required. From equations (83), (80) and (83) we thus obtain, for $U = 0.025$, $\eta = 0.5$, $\Delta A = 0.05$:

$R_c > 170$ cm from $t_{1/2}$, but $R_c > 65$ km from t_r, moderate clump-will be needed to counteract damping, provided the perturbations include inclination. The case of $i = 0$ (with the sheet of particulate matter thinner than the diameter of the planetesimal) is too extreme, and the clumping limit too high to be considered: there will be always some deviation at right angles to the plane, $i \neq 0$.

For long-period perturbations, including those in i, to be effective, for $t_{1/2} > 50{,}000$ years we find $R_c > 12.5$ km. Below this the particles of the ring must respond to the perturbations somehow in a cooperative way.

It seems that, with a secular amplitude in the eccentricity of the earth of about 0.05, a similar value of e for the larger particles above the damping limit as caused by perturbations of the major planets, and with additional perturbations by the earth in close passages, the particles may be accreted indeed at an average encounter velocity of $U = 0.025$ and a time scale of 50,000 years,

$$\eta_m = \exp(-t/50{,}000) \tag{93}$$

being the unaccreted fraction left in the ring after the lapse of t years.

C. Capture Hypotheses of the Origin of the Moon

a. Moon formed independently and captured by non-tidal process

The increment of mass of two bodies placed in the same medium is proportional to their collisional capture cross section, $\pi\sigma_0^2$. For the low velocities of encounter the unity term in equation (54) can be disregarded; the rate of accretion of two independent nuclei of equal density (for the sake of simplicity) is then proportional to the 4/3 power of mass. The differential equation of growth of two independent centers of accretion can be integrated and the result represented as a variable ration of the masses,

$$\mu_1 / \mu_2 = (1 + C\mu_1^{1/3})^3 . \qquad (94)$$

With the adjustable parameter $C = 3.34$, and ($\mu_1 = 1$) $\mu_1/\mu_2 = 81.5$ is obtained as for the present mass ratio of earth to moon. Table VI then represents the variation of the mass ratio as depending on the value of μ_1 —the variable mass of the earth in the course of accretion.

Thus, going backwards in time during the process of accretion, the mass ratio decreases. At $\mu_1 = 10^{-3}$, when the radius of the earth was one-tenth its present value, the mass ratio was 2.37 only. The initial difference in the size of the nuclei could have been very small, just a matter of chance. Also, in the beginning there could have been many competing nuclei of comparable size.

If J_m is the mass accretion per unit of surface area and time, w the impact velocity, T_0 the original temperature of the accreting material in space, T_a the surface radiation temperature, $\bar{C}_1$ the average specific heat of the solid, $k_s = 5.67 \times 10^{-5}$ Stefan's radiation constant, the subsurface temperature T_s of the accreting material will more or less satisfy the equation

$$J_m\left[\tfrac{1}{2}w^2 - c_1(T_s - T_o)\right] = k_s(T_e^4 - T_o^4) \ . \qquad (95)$$

For silicate material, $c_1 = 9 \times 10^6$ erg/g degK, also $T_o = 300$ degK can be assumed. Because of surface shielding and finite conductivity of the solid,

$$T_s > T_e > T_o \ . \qquad (96)$$

Setting $T_e = T_s = T_o$; in (95), a lower limit for the temperature is obtained for $T_e = T_o$. An upper limit T_s'', corresponding to zero radiation losses, obtains. However, when the temperatures reach above T_m 1800 °K, the temperature of fusion, equation (95) does not apply. When the lower limit, T_s', is below the fusion limit and $w < w_f \cong 1.64$ km/sec, fusion cannot take place even at complete shielding, and the upper limit is then

$$T_s'' = T_o + w^2 / 2c_1 \ . \qquad (97)$$

When $w > w_f$, in the case of extreme shielding partial fusion must take place. Let θ be the melted fraction, and let the same fraction of the surface be unshielded liquid (lava) radiating with the intensity

$$Q_o = k_s(T_m^4 - T_o^4) = 6 \times 10^8 \text{ erg/cm}^2 \text{ sec} \ , \qquad (98)$$

the rest of the surface being completely shielded (e.g. by insulating dust) and at $T = T_o$. The maximum melted fraction (on the surface as well as in the subsurface) is then

$$\theta(\max) = J_m\left(\tfrac{1}{2}w^2 - H_o\right) / (Q_o + H_f J_m) \leq 1 \ , \qquad (99)$$

where $H_o = 1.35 \times 10^{10}$ erg/g is the heat required to raise the temperature from T_o to T_m, and $H_f = 2.7 \times 10^9$ erg/g is the heat of fusion.

When Q exceeds 1, complete fusion takes place. The liquid is assumed to radiate to space unshielded, at $T_e = T_s$, and probable temperature T (not a limit) is then determined by the equation

$$J_m\left[\tfrac{1}{2}w^2 - (H_0 + H_f) - c_2(T - T_m)\right] = k_s(T^4 - T_0^4) \qquad (100)$$

where c_2 is the specific heat of the liquid.

Over the short time scale of accretion, conductive exchange of heat with the interior will not greatly change the results.

For a planet of density δ and radius R_p accreting on a time scale of $t(\sigma)$, the accretion is

$$J_m = \tfrac{4}{3}R_p \eta_m \delta / t(\sigma)(1 - \eta_m) \qquad (101)$$

Neglecting the small role of the independently accreting moon, at $\eta_m = 0.5$, $R_p = 5.1 \times 10^8$ cm, $\delta = 5.5$, $t(\sigma) = 50{,}000$ years, we find $J_m(\text{earth}) = 6.6 \times 10^{-4}$ g/cm^2. sec falling at a velocity of 8.4 km/sec upon the half-mass earth. For the moon of 1/50th the earth's mass (cf. Table VI) the accretion per unit area at constant U, $\sim \sigma_0^2/R_p^2$ [equations (54) and (65)], is 1/14 that for the earth or J_m (moon) $= 4.7 \times 10^{-5}$ g/cm^2. sec. With $w_\infty = 2.0$ km/sec for the moon at that epoch (mass = 0.6 of present moon) and $U = 0.025 \div 0.75$ km/sec, $w^2 = 4.6 \times 10^{10}$ (cm/sec)^2 and $w = 2.1$ km/sec is the velocity of fall.

With these data, for the independently moon at epoch $\eta_m = 0.5$

of accretion and a time scale of 50,000 years, equation (95) yields $T_s > T_s' = 404\ ^{o}K$, thus a low minimum value of the temperature, although heating is not negligible. The true temperature would be near this value for continuous accretion of finely divided material which does not penetrate deep into the surface.

The other extreme, e.g. conditioned by an insulating dust layer of low thermal conductivity covering every bit of a solid area, would allow heating of the bulk of the mass to nearly 1800 ^{o}K. According to equation (99), the fraction melted as well as the fraction of exposed molten silicates would then be

$$\Theta_{(max)} = 1.6 \times 10^{-3}$$

only. A hot solid body with some lava enclosures and exposures, just sufficient to radiate away the extra heat, could be envisaged. The lava exposures act as a thermostat, keeping the mean temperature near the melting point without complete melting.

The craters in the lunar continentes correspond to the accretion of the top fraction of about 3×10^{-5} of the lunar radius or 9×10^{-5} of the mass (Öpik, 1961b). At that stage, the collision cross sections of earth and moon were in a ratio of 280 to 1 [as they are now; cf. equation (54) with $U = 0.025$], so that there was left over unaccreted in the ring a fraction

$$\eta_m = 8 \times 10^{-5} \times 281 / (81.5 + 1) = 3.1 \times 10^{-4}$$

According to (93), this would require a time interval of about 400 000 years for the beginning of the formation of craters which have survived, and 600,000 years for the practical termination of this primeval crater-forming epoch, as reckoned from the epoch of half-accretion ($\eta_m = 0.5$). Accretion must have been slower in the beginning, before sizeable nuclei were formed, and the total length of accretion into the earth-moon system may have lasted about one million years [20 times t(ω), according to a certain model (Öpik, 1961b)].

A non-tidal capture of the moon into a direct orbit could have taken place most probably when accretion was intense, thus not at the very last stage. The craters would then have been formed on a moon in orbit around the earth. Whatever its original distance of closest approach was, in 25000--100,000 years it must have receded tidally to 12--15 earth radii. The majority of the craters could not have been formed at 5--8 earth radii, and their tidal distortions (inversely proportional to the cube of the distance) would have been 10 times smaller than measured (Öpik, 1961b), or entirely negligible.

A stronger objection comes from crater statistics. Boneff and Fielder have shown that the craters are more or less evenly distributed over the moon's surface (continentes and maria taken separately). Contrary to expectation, the western hemisphere which is trailing behind even carries about 10 per cent more craters per unit area than the eastern which is preceding in the orbital motion (Fielder, 1965, 1966). In view of the great differences in crater densities over the moon's surface, the small excess is not very relevant and may be caused by unequal maria flooding. Now, with the craters imprinted when the moon was at about 10 earth radii, at an orbital velocity (full earth mass being attained) of 2.5 km/sec and isotropically distributed hyperbolic velocity of the infalling fragments of 3.5 km/sec, strong aberration and bias toward the eastern hemisphere should have resulted. Under these circumstances, an approximate calculation based on encounter equations and which considers the crater numbers to increase inversely as the square of the limiting diameter or, for fixed crater diameter, as the velocity [equation (7)], indicates that an excess of 74 per cent is expected for the entire eastern over the entire western hemisphere of the moon, instead of a deficiency of 10 per cent as observed. The crater statistics are therefore incompatible with this model of formation of the moon.

For the earth equations (95) and (99), with $t(\sigma) = 50{,}000$ years and a half-mass or $\eta_m = 0.5$, yield

$$T_s > T_s' = 1410\ ^{\circ}K, \quad \theta_{(max)} = 0.373$$

The two extremes are in this case not very different. A partially molten earth is indicated, with oceans of lava that must have considerably influenced the tidal history of the moon (if it was near the earth at that time). Otherwise these figures stand irrespective of the history of the moon; they depend only on the time scale of encounters.

I. Accretion of an Earth-Orbiting Moon from Interplanetary Material

On this model, the overall frame of accretion of the earth-moon mass is the same as in Sections IV. B and C, but the moon is now supposed to have started from a nucleus already placed in orbit around the earth. The moon is now the "satellite", the earth the "main body" of our model, but the particles are now entering in hyperbolic orbits with respect to the earth-moon system and the equations of encounter probability per revolution of the particle are no longer valid. Instead the following obvious equation, an exact equivalent of those for elliptic orbits, applies. The total accretion rate on a moving "satellite" equals

$$A_p = \pi R_p^{\,2} \rho v \left(1 + w_\infty^{\,2}/v^2\right), \tag{102}$$

where ρ is the space density of the particles and v their (average) velocity relative to the satellite (Öpik, 1956). Also

$$J_m = A_p / 4\pi R_p^{\,2} = \tfrac{1}{4} \rho v \left(1 + w_\infty^{\,2}/v^2\right). \tag{103}$$

For accretion by the half-mass earth ($\eta_m = 0.5$), $\rho = \rho_0$

is the average density of matter in the ring, $v = U = 0.75$ km/sec, $w_{\infty} = 8.4$ km/sec. For accretion by the earth-orbiting moon at 10 earth radii, with v as the vector quadratic sum of the moon's orbital velocity (2.5 km/sec) and the velocity of escape from 10 earth radii w_{∞}' (3.5 km/sec) or $v = 4.30$, $\rho = \rho_0\left[1 + (w_{\infty}')^2 / U^2\right]^{\frac{1}{2}}$ (Öpik, 1965b), the new value for accretion on the moon as "helped" by the earth now becomes 5.8 times greater than for the "independent" moon, $J_m = 2.73 \times 10^{-4}$ g/cm$^2\cdot$sec. The impact velocity, with $w_{\infty} = 2.0$ km/sec for the moon, is now $(v^2 + w_{\infty}^{\ 2})^{\frac{1}{2}}$ or $w_0 = 4.79$ km/sec.

With these numerical data, for the "earth monitored" moon at 10 earth radii and $t(\sigma) = 50{,}000$ years,

$$T_s > T_s' = 350\ ^{\circ}K \text{ and } \delta\,(max) = 0.046$$

is obtained. The minimum temperature turns out to be quite high and, if its solid surface is well insulated (or thick enough), 4.6 per cent of melting should occur on the moon kept "thermostatically" close to the temperature of fusion.

Otherwise the two objections pointed out in the preceding section and based on tidal deformations of the craters ~~craters~~ and especially on crater counts, apply here, too, rendering the model highly improbable.

E. Capture into a Retrograde Orbit

Retrospective calculations of the tidal evolution of of the lunar orbit, on the assumption of invariable masses of moon, earth, and sun, and an absence of other relevant interacting bodies, all lead to a minimum distance close to, yet inside Roche's limit, D_r, as given by

$$D_r = 2.46 R_o (\delta_o/\delta_p)^{1/3} \qquad (104)$$

where R_o and δ_o are radius and density of central body(earth) and δ_p is the density of the satellite (moon). For the moon and the present ratio of the densities (5.52/3.34), D_r = 2.88 earth radii. With the effect of solar tides, Gerstenkorn (1955) obtains 2.86, MacDonald (1964) 2.72, and Sorokin (1965) 2.40 earth radii for the minimum distance of the moon as depending on the assumptions. On the assumption of an unbroken moon, the calculations extended further backwards (Gerstenkorn, 1955) indicate capture into a retrograde nearly parabolic orbit at a perigee of 26 earth radii, which then decreases, the orbital eccentricity decreasing and the inclination turning from retrograde over 90° to direct (Öpik, 1955, 1962a). We thus can distinguish an incoming phase, with the moon approaching, and the present outgoing phase, with the moon receding.

It seems now that, if the minimum distance was inside Roche's limit, the moon cannot have existed as an integer body, and that the calculations beyond that point cannot strictly apply. Yet, when a finite number of fragments was formed ~~As~~ (see below), orbital evolution must have been slowed down without the geometry being essentially different. Through collisional damping, the fragments were forced to stay on the same orbit, and the calculations are therefore formally valid except for the time scale. Assume therefore that an independently accreted body of lunar mass was tidally captured by the finally accreted earth into a retrograde orbit and went through Gerstenkorn's incoming phase until it broke up while in a circular direct orbit (as the calculations indicate). At this moment tidal evolution was greatly slowed down (by a factor of $N_f^{\frac{1}{2}}$, where N_f is the number of fragments) yet did not stop completely. The reason for this is the strength of the solid lunar body which must have led to fragments of finite size to be formed in the breakup, as visualized by Jeffreys (1947a). The upper limit of the radius R_f of the fragments, when formed at a distance $D_f < D_r$ inside Roche's limit, is given by (Öpik, 1966c)

$$R_f \leq \left[sD_f^{\,3} \Big/ \left(\pi G \delta_p \delta_o R_o^{\,3} \right) \right]^{\frac{1}{2}} \tag{105}$$

where G is the gravitational constant and s the "lateral" crushing strength as used in equation (7), practically equal to s_c of (11). In c.g.s. units, with $s = 2 \times 10^8$ dyne/cm^2 as for sandstone, and $D_f / R_o = 2.5$, $R_f = 2.86 \times 10^7$ cm or a diameter of 572 km for the surviving fragments, about one-sixth that of the moon. The number of fragments if of equal size would then be $N_f = 224$. At the strength of granite, $s = 9 \times 10^8$, $R_f = 6.07 \times 10^7$ cm, $N_f = 23$. We will further consider only the first case. If released in synchronous rotation from a circular orbit, the fragments will enter elliptical orbits with the encounter velocity ranging from $U=0$ to $U=\left|(1 \pm R_p/D_f)^{1.5}_{-1}\right| \cong 1.5R_p/D_f \cong 0.164$ according to the distance from the center of the parent body. (There is no significant tidal deformation of the brittle solid body before it yields to the ultimate stress.) Fragments released from the earthward side would reach a perigee distance of 1.2 earth radii if the attraction of the moon mass on the released fragments is neglected, but actually farther out and break up to somewhat smaller sizes; similarly those from the far side will have their perigees there and go out in elliptical orbits to apogees of considerably less than 5.9 earth radii, being bent inwards by the attraction of the residual lunar mass.

For free orbiting fragments at 2.5 earth radii, in notations and units of Section III, and for collisions of two equal particles, $R_p = 2R_f = 0.0360$, orbital circular velocity 1 (4.93 km/sec), orbital period 0.23 days, $w_\infty = 0.079$ (0.392 km/sec) equal to average $U = 0.079$, the collision cross section is

$$\pi \sigma_c^2 = 2.6 \times 10^{-3}\pi, \quad \sigma_c = 0.0510 < 0.0707$$

therefore equation (65) applies with $K_p = 2$, yielding

$$P_0 = 0.066, \quad t(\sigma^\circ)/2\pi = 15 \text{ orbital revolutions}$$

or 3.5 days. As to $t(\omega)$, the solar perturbation is insignificant and the only important effect stems from the

74

oblateness of the earth which yields (Öpik, 1958b), at a distance of r_m/R_0 earth radii and for an orbit of small eccentricity and inclination,

$$t(\omega) = 18(r_m/R_0)^{3.5} \text{ (Earth Rot.} / 24^h)^2 \qquad (106)$$

in days; it equals one-half the period of precession of the nodes. With 4.8 hours as the period of rotation of the earth at that epoch, $t(\omega) = 18$ days $> 2t(\sigma)/2\pi$. Hence the collision lifetime of an isolated pair of fragments would equal 9 days. With 100--200 fragments around, in a matter of hours mutual collisions would completely destroy the fragments which originally survived tidal disruption.

Originally, the fragments could be imagined to be injected into a ring about 4000 km wide or thick and 10^5 km circumference. With $N_f = 224$, this yields a number density of $N = 1.8 \times 10^{-10}$ km^{-3}. The collision cross section, $\pi\sigma_0^2$, is 2.1×10^6 km^2. Hence a collisional mean free path results as $(N \cdot \pi\sigma_0^2)^{-1} = 2600$ km. This is of the order of the diameter of the moon and, therefore, collisions are not restricted to particles of neighboring origin; the full variety of encounter velocities and full gravitational interaction will be realized as has been assumed.

With $w = 5 \times 10^4$ cm/sec, $s = 2 \times 10^8$, $\rho = 3.3$, $k = 1$, equations (4) and (14) yield

$$M_c / \mu = 8$$

for the relative mass of secondary fragments when the target is much larger than μ. Here fragments of comparable dimensions are colliding; they will be destroyed completely in the first collision, and subsequent collisions will reduce the entire mass to rubble and dust, collected in a ring whose sections are orbiting separately. Let the equatorial velocity of synchronous rotation of the parent body (0.538 km/sec) be u_o; then the ultimate heating of the mass can be assumed to correspond to the average kinetic energy of rotation, $\frac{1}{5}u_o^2$ erg/g which, at $c_1 = 9 \times 10^6$ erg/g, yields only about 60 °C.

With the proportions approximately as of Saturn's inner ring, extending from 2.25 to 2.75 earth radii, or with a surface of 3.18×10^8 km^2, the average mass load per unit surface of the ring is 2.31×10^7 g/cm^2; at average density $\delta = 2$ for the rubble, the average thickness is 115 km.

Now, even with the low cohesion as of sand, clumps of dimensions smaller than R_f [equation (105)] will be formed again. At incidental contacts, friction at the interfaces of of the independently orbiting sections may force the clumps to rotate in a retrograde direction, with an angular velocity up to

$$\omega_f = \tfrac{1}{2}\omega_o \qquad (107)$$

where ω_o is the orbital angular velocity,

~~The average tensile centrifug~~

$$\omega_o^2 = \frac{4}{3}\pi G \delta_o (R_o / D_f)^3 \qquad (108)$$

The average tensile centrifugal stress in a rotating sphere of radius R_f is (Öpik, 1966c)

$$s_t = -\frac{1}{4}\omega_f^{\,2}\delta R_f^{\,2} \qquad (109)$$

and, after substituting R_f and ω_f from (105), (107) and (108),

$$s_t \simeq s/12 \qquad (110)$$

is obtained. The ratio is of the order of the tolerance of most brittle materials, whence no separate consideration of the survival of the clumps from the standpoint of tensile stresses is needed.

The ring is to stay for several hundred years at least, before it is pulled outwards by the weak tidal acceleration [cf. equations (111)--(113)]. Its separately rotating parts will probably possess the mechanical properties _in vacuo_ similar to, or slightly harder than desert alluvium; from Section II. F we may set $s \doteq 6 \times 10^7$ dyne/cm^2 and $\rho = 2$ g/cm^3 for these "orbiting sand dunes". Equation (105) yields in this case for the newly formed clumps,

$$R_f \sim (s/\delta_p)^{\frac{1}{2}} \text{ or } R_f \leq 286 \text{ km} \times (0.3/0.6)^{\frac{1}{2}} = 202\text{km}.$$

If spherical, the average thickness is (4/3)R or 269 km. This is more than the estimated thickness of the ring and would lead to loss of permanent contact between its parts, a fraction of $115/269 = 0.427$ of the ring area being occupied by the projections of the fragments. This corresponds to an average spacing between the fragments $(\Delta/R_f) = (\pi/0.427)^{\frac{1}{2}} = 2.71$ or 547 km. The total number of fragments or mini-satellites in the middle ring is then $N_r = 10^5/547 = 180$ and, over the width of $0.5R_0 = 3200$ km there will be 6 full rings, the total number of fragments being $N_r = 1080$ in this symmetrically arranged model. Each of the six rings is orbiting independently, small perturbations of individual members being damped in mild collisions inside a ring.

Each of the 1080-odd members or moonlets raises on the rotating earth its own tidal bulge; the instantaneous tidal bulge is the vector sum of the component bulges and, for a precisely symmetrical arrangement of the moonlets, the resultant tidal vector would be zero. However, within each of the six rings there is some freedom of motion for its members; their grouping will be ruled by the law of chance and the ~~resultant~~ average absolute value of the resultant random vector will be proportional to the square root of their number. For a Poisson distribution of N equal mass points this would be exactly true; for finite size members the freedom of re-arrangement is limited, but a dispersion in the masses and radii of individual members would add additional variance. It can therefore be assumed that the tidal acceleration, or the rate of tidally-induced orbital change in one of the six rings is

$$(da/dt)_f = (da/dt)_0 N_r^{\frac{1}{2}} / N_f \qquad (111)$$

or

$$(da/dt)_f / (da/dt)_0 = 0.0124 = 1/80,$$

where $(da/dt)_0$ denotes the rate of orbital evolution ruled by an integer lunar mass. The time scale is thus increased 80 times and, instead of some 5 years sojourn inside Roche's limit, this would take about 400 years.

Neighboring rings will not add to this acceleration (their tidal bulges induced on the earth cannot stay in resonance) except through a periodic term of accidentally fluctuating amplitude of zero expectation over the synodic period (due to "regrouping" of the members of a ring) These terms work in proportion to the square root of time and their contribution is small or negligible (a calculation has been made in this respect). It can be assumed that the contributions from other rings cancel out over one synodic period (5 days or less), and that the residual tidal effect upon one of the six rings is fully accounted for ~~x~~ by the random wanderings of members within the same ring as expressed by equation (111).

For the rate of tidal orbital evolution in the outgoing phase an interpolation formula can be written satisfactorily representing Gerstenkorn's (1955) calculations at geocentric distances smaller than 12 earth radii, giving the time of drift in years for an integer lunar mass as

$$t_a = 0.025(a_2^{5.5} - a_1^{5.5}), \qquad (112)$$

where a_2 and a_1 are the distances in earth radii. (Between 12 and 60 earth radii the average power is 7.1, as compared to an "ideal" value of 6.5 for constant inclination and friction, and the time scale should be adjusted to 4.5×10^{9} years.)

Each of the six rings drifts outward at its own rate, expected to be given by (111) with

$$(da/dt)_0 = da_2 / dt_a \qquad (113)$$

as defined by (112). In the case of overtaking by members inside the same ring, collisional damping will adjust the pace. The outer and inner edges of the ring, at $a_1 = 2.75$ and 2.25, respectively, according to (111) will reach Roche's limit at $a_2 = 2.86$ within 80 times the time given by (112), or within 210 and 560 years, respectively; the interval between the extreme rings is thus 350 years, and between two successive rings 70 years.

As soon as a ring emerges from Roche's limit, its 130-odd components will be drawn together and accrete into a moonlet of one-sixth lunar mass, with a radius of 956 km (density 3.34 assumed for the compressed and heated material), and a velocity of escape of $w_{esc} = 1.31$ km/sec. The ring will collapse in "free fall", the time scale being given by equation (70),

$$t_F / 2\pi = 6.6 \text{ orbital periods or } 1.6 \times 10^{6} \text{ seconds.}$$

The average potential energy $(3/5) \cdot \frac{1}{2} w_{esc}^{2} = 5.07 \times 10^{9}$ erg/g does not suffice for melting. At middle accretion or $\eta_m = 0.5$, the rate of accretion as given by equation (101) is 500 g/cm^{2} · sec. The accretion is so intense that radiation losses are negligible. The minimum and maximum temperatures from equations (95) and (97) are identical and, with $T_o = 300$ °K, yield for the average temperature of the accreted moonlet

$$T_s' \approx T_s'' \approx T_s = 833 \ ^{\circ}K$$

As conditioned by tidal interaction, the moonlets emerge thus at intervals of $350/5 = 70$ years, and with inclinations to the earth's equator decreasing from about 42° for the first to 27° for the sixth moonlet. The compacted moonlets drift outwards on a time scale 14 times faster than the rings [equation (111) with $N_r = 1$, $N_f = 6$ conventionally] yet still six times that of equation (112), so that when one reaches Roche's limit, the preceding one with its faster rate of recession has gone far enough to escape direct contact with the newcomer. The orbits are nearly circular though of considerable inclination (specifically for the capture model), and interaction between two consecutive moonlets begins only when they approach within the gravitational target radius R_a without their orbits intersecting or crossing. This is made possible by the law of tidal evolution as expressed in (112) which brings the two moonlets separated by a time interval $\Delta t = 70$ years the closer together the farther they go ($da/dt \sim a^{-4.5}$, thus rapidly decreasing with distance) When interaction begins, Roche's limit (mutual for the two moonlets) is always reached before physical collision can take place, because

$$D_r > R_p \ .$$

Therefore, the two moonlets first break up into a large number of fragments which then, while mutually colliding, accrete into a moonlet of double mass which begins drifting outwards at double speed.

The time scale of this second accretion is one-half the synodic period of revolution of the two approaching moonlets and runs into a few days The relative orbital inclination may have any value from $i_1 - i_2$ to $i_1 + i_2$, according to the position of the precessing nodes, and will not change much during the process of accretion , the period of precession being (Öpik, 1958b)

$$t(i) = 35.8 \sec i \cdot a^{3.5} \text{ (Earth Rot./24}^h)^2 \qquad (114)$$

the period of the advancing perigee

$$t(\Pi) = 35.8 a^{3.5} \text{(Earth Rot./24}^h)^2/(1.5 \cos^2 i - 0.5), \qquad (115)$$

and the period of the argument of the perigee

$$t(\omega) \doteq \left[1/t_i + 1/t(\Pi)\right]^{-1} \qquad (116)$$

For nearly circular orbits the motion of the perigee is irrelevant and only precession of the nodes matters. The relative inclination of two orbits varies with their synodic period of precession which runs into tens of years in the present case.

For a pair of interacting moonlets, each one-sixth the lunar mass, the sum of the radii is 956 + 956 km=0.300 earth radii, and Roche's limit is about 0.40 earth radii, each of the moonlets breaking up into ν_f = 120 fragments of 194 km radius ($s = 6 \times 10^7$ dyne/cm^2) [equation (105)]. This sets the order of magnitude of how closely interaction begins. The appropriate distance is reached approximately 140 years after the emergence of the preceding and 70 years after the following moonlet. In Table VII the history of accretion of the moon according to this scheme is shown. At t = 140 yrs moonlets I + II are assumed to merge, at 280 yrs--III + IV, at 420 yrs--V + VI. These pairs then may further combine at 490 yrs and after, leading to a complete merger somewhere near $a = 5$ earth radii. On account of the high power of distance in equation (112) this last result is quite stable for widely differing initial assumptions.

The heating of the moon, finally accreted at 5 earth radii, partly depends on the time scale which, for the combination of all the considered phases of accretion, can be set at 350 years, yielding $J_m = 0.0174$ g/cm^2.sec as an overall average [equation (101)]; it chiefly depends on the average encounter velocity U_m which, from equation (50) for $e = 0$ and $A = 1$, conveniently is reduced to

$$U_m{}^2 = 2(1 - \cos i_e) \text{ or } U_m = 2\sin(\tfrac{1}{2}i_e) \qquad (117)$$

where i_e is the average inclination of the combining orbits to the final resultant orbit. Thus, with an average of the component inclinations of 36°, $U_m = 0.62$ is an upper limit when the resultant orbit coincides with the equatorial plane, and will be less for a final inclination different

TABLE VII

Hypothetical History of Accretion of the Moon from

Six Moonlets with High Inclinations

Time, years		0	70	140	210	280	350	420	490	560
		Distance a, Earth Radii								
Moonlet	i									
I	42^{o}	2.86	3.37	3.66	...	...	...	...	...	...
II	39^{o}	...	2.86	3.37	...	...	...	...	...	...
III	36^{o}	...	...	2.86	3.37	3.66	...	...	...	...
IV	33^{o}	...	...	...	2.86	3.37	...	...	...	...
V	30^{o}	...	...	...	...	2.86	3.37	3.66	...	...
VI	27^{o}	...	...	...	...	...	2.86	3.37	...	...
I + II		...	...	3.52	3.96	4.26	4.48	4.66	4.81	4.95
III+IV		...	...	...	...	3.52	3.96	4.26	4.48	4.66
V + VI		...	...	...	...	...	...	3.52	3.96	4.26

84

from zero as depending on the phase of precession. The probable value of U_m^2, calculated as the deviation from a mean of six independent vectors, is $5U_m^2/6$, or $U_m = 0.565 = 2.0$ km/sec at 5 earth radii (orbital velocity $v_o \doteq 3.5$ km/sec). With three-fifths of the final escape energy as an average of the potential energy, $T_o = 863$ °K as from the original formation of one moonlet, the minimum average internal temperature of the moon at formation becomes $T_s' = 1680$ °K [equation (95)] and the maximum fraction of melting is $\theta_{max} = 0.333$. These are probable values; with an improbable combination of the phases of precession at the times of interaction of the six moonlets and their resultants, both T_s' and θ_{max} may be lower, the resultant inclination remaining large in such a case. This, however, is not supported by the majority of calculations (MacDonald, 1964; Sorokin, 1965; Slichter, 1963; Darwin, 1879) which point to a low value of 10-14° at 5 earth radii, a distance to which the retrospective calculations are more reliable. The lower limits of heating are for zero relative inclination at encounter and are identical with those calculated in Section IV. G; they hardly apply to the case of tidal capture in which component inclinations of the order of 36° at encounter must have been reduced to some 12° after completed accretion and must have led thus to intense conversion of kinetic energy and heating. The average encounter velocity in our model exceeds $\sqrt{2}-1$, and ejection of some fragments to interplanetary space becomes possible (Öpik, 1963a). The fraction ejected is

$$f_{\infty}=\left[\sigma_a^2/(\sigma_a^2+\sigma_o^2)\right]\cdot\left[(U^2+2U-1)/4U\right]. \qquad (118)$$

Consider the middle pair of moonlets III + IV (Table VII) whose merger is supposed to take place at $t = 280$ years and $a = 3.52$ (average of 3.37 and 3.66). The orbital periods of revolution of the two before the merger are 0.363 and 0.411 days, respectively, the synodic period 3.11 days; one-half of the latter is the time scale, $t(\sigma)$. The orbital precession periods are 11.0 and 14.6 years, respectively, and the synodic period during which the relative inclination fluctuates between 3° and 72° is 45 years. After merger the combined double mass settles into an intermediary orbit with inclination i_m. Neglecting the small difference between the two original inclinations, we set $i=i_1=i_2=35°$. From spherical geometry we have

$$\sin i_e=\sin i\cdot\sin(\tfrac{1}{2}\alpha), \qquad (119)$$

$$\tan i_m=\tan i\cdot\cos(\tfrac{1}{2}\alpha), \qquad (120)$$

while the relative inclination of the two original orbits is $2i_e$. Here α is the difference in longitude of the two nodes on the equatorial plane. With the assumed inclination, $\alpha = 90°$ or 270° divides the equator into two equal parts, one with $U > \sqrt{2}-1$, the other with smaller U. In the first mentioned high velocity part, $U_{av} \cong 0.52$, $\sigma_o^2 = 2.49 \times 10^{-3}$, $\sigma_a^2 = 1.92 \times 10^{-4}$ and $f_{\infty} = 0.0090$. Completely negligible is also the acceleration, according to equations (74), (75), (76), where $t(i)$ is to stand for $t(\omega)$. The total colliding mass is one-third of the mass of the moon and, thus, in the encounter of only one pair of moonlets in this orbital configuration, 0.003 of the lunar mass is expected to be

II 84

ejected to interplanetary space. From there it returns as considered in Section IV. D and, over a period of over 50,000 years, is captured by earth and moon, the share of the earth-orbiting moon being 60.7 times less than that of the earth. Hence, from the ejected mass the moon will receive a final contribution equal to 0.003/61.7 or 5×10^{-5} of its mass.

The craters on which crater statistics were based, of an average diameter of less than 20 km and a depth (x_p) about 3.2 km, covering about 50 per cent of the continentes area, correspond to a depth of erosion of 1.6 km, involving 9×10^{-4} of the lunar radius or 2.7×10^{-3} of the lunar mass. At $w_o = 3$ km/sec, $s = 2 \times 10^8$, $\rho = 2.6$, $k = 1$, one obtains $M_c / \mu = 34$ [equations (3) and (14)]. The impinging mass that was mainly responsible for shaping the present relief of the continentes would thus equal

$$2.7 \times 10^{-3}/34 = 8 \times 10^{-5}$$

of the lunar mass. The contribution of 5×10^{-5} or 60 per cent of it would suffice to influence the crater statistics in a manner different from that observed: the late interplanetary projectiles would not contribute to a systematically arranged ellipticity of the craters. Hence 20 per cent of interplanetary fragments is, perhaps, the upper limit admissible for shaping the present surface of the continentes. The rest, or all, must be of earth-orbiting origin.

There are, in the scheme as of Table VII, altogether four merger events, each of which would suffice to obliterate the uniformity of crater numbers and the tidal deformations of the craters (imprinted 50,000 years later at a distance where the deformations are negligible) if they happened in the high-velocity configuration. In each case the probability of the configuration is one-half; the probability that it did not take place and that, in the case of the tidal capture theory, no ejection of fragments to interplanetary space did occur, is thus

$$(\tfrac{1}{2})^4 = 1/16$$

a low though not a forbidding value. With such a probability the crater statistics can be reconciled with tidal capture of the moon and an ensuing high inclination of its orbit when at minimum distance from earth.

F. Origin through Fission or from a Ring inside Roche's Limit

The two possibilities are indistinguishable as far as the ultimate consequences are concerned and will be treated together.

The fission theory has been doubted, even rejected (Levin, 1966a), because it is inconceivable that a mass separating from the earth inside Roche's limit and in violent upheaval could have preserved integrity. This, however, is not needed and, with the finite cohesion and clumping mechanism, the ring of debris could slowly recede and emerge from Roche's limit, to form the moon in a manner ~~described~~

described in Section IV. E. There is one important difference: the inclination of the ring to the terrestrial equator would have been near zero in such a case. As compared with the preceding model, the sequence of events would be essentially similar, but the kinetic energy in accretion would be smaller (the encounter velocity of the debris and with U, the moonlets, being near zero. Ejection of fragments to interplanetary space could not then take place, and the last fragments captured from the earth-orbiting cloud would be co-moving with the orbiting moon, descending on it more or less isotropically from all directions. A small preference of impacts from the rear, as revealed by crater counts (Fielder, 1965, 1966), could be expected if the last fragments, were accelerated in encounters with the moon and removed into elliptic orbits with large semi-major axes, so that they were overtaking the moon while indirect motion near their perigees. A similar excess of directly moving meteorites, periodic comets and Apollo-type asteroids is observed in the present terrestrial space of the solar system.

Another objection—that the backward calculation of the tidal evolution, based on the present masses and angular momenta of the earth-moon-sun system does not lead to a solution much closer then Roche's limit—is only of "paper" value in this case, because neither the identity nor the mass and momentum distribution of the bodies or agglomerations can be considered known during this primitive stage.

The parent ring is assumed to be in the earth's equatorial plane, and so will be the component six moonlets of our idealized model. Table VIII shows their calculated hypothetical history as ending in the formation of the moon. Because of the small relative velocity, as conditioned be the small relative inclinations, they combine sooner then in the previous scheme, I+II at t=70 yrs, III+IV after 210 yrs; V+VI after 350 years, but before this happens, at t=280 yrs the first two pairs combine into one containing two-thirds of the lunar mass. This body (I+II+(III+IV), twice the mass of the remaining pair (V+VI), drifts out twice as fast and cannot be easily overtaken by the smaller companion although their separation still decreases at first (compare 3rd and 4th lines from the bottom of the table). Instead the collision target radius, σ_0 [last line of the table, from equation (54)], rapidly increases and when it exceeds the separation between the moonlets, final merger occurs at t=420 or 490 years, at a=4.5 - 5 earth radii. Before this happens, a passage through Roche's limit of the larger body destroys the smaller body (V+VI). The radius of the larger body is then R_p=1519 km=0.243 earth radii, and

$$\sigma_0=0.243(1 + w_\infty^2/U^2)^{\frac{1}{2}} \tag{121}$$

in earth radii is calculated with w_∞=2.08 km/sec for the

TABLE VIII

Idealized History of Accretion of the Moon from Six Moonlets Orbiting in the Earth's Equatorial Plane

Time, years		70	140	210	280	350	420	490
				Geocentric Distance a, Earth Radii				
Moonlet								
I	2.36	3.37	...	...	...	...	...	...
II	...	2.86	...	...	...	...	...	...
III	...	...	2.86	3.37	...	...	...	...
IV	...	...	...	2.86	...	...	...	...
V	...	...	...	....	2.36	3.37	...	...
VI	...	...	...	...	...	2.86	...	...
I + II	...	3.12	3.76	4.11	4.37	...	...	...
III + IV	...	...	...	3.12	3.76	...	...	...
V + VI	...	...	...	...	...	3.12	3.76	4.11
I+II+III+IV	...	...	...	...	4.06	4.54	4.85	5.11
U, km/sec	...	...	...	...	...	0.75	0.43	0.40
σ_0, Earth Radii	...	...	...	...	...	0.72	1.11	1.29

larger body, while U is taken as the difference of the orbital velocities of the two circular orbits (second line from the bottom of the table).

To calculate the heating limits [equations (95) and (99)], we again set J_m=0,0174 g/cm^2. sec as for a time scale of 350 years, T_o=863 °K, and take $\frac{1}{2}w^2$=1.19 x 10^{10} erg/g; this is equal to three-fifth of the kinetic energy at escape velocity of the present moon (2.38 km/sec) less 5.07 x 10^9 erg/g as the potential energy of accretion of the component moonlets. The minimum average internal temperature of the accreted moon is then T_s'=1260 °K, and the upper limit of the melting fraction Θ^*_{max}=0.301. The kinetic energy of U, or the free orbital energy, is neglected; it is nearly compensated by the overestimate in the potential energy.

G. Thermal History and Origin

Table IX contains a summary of the preceding subsections. Although based on numerical data which are inevitably rather rough, the conclusions in each case are comparatively stable and may serve as a basis for judgment which is better than a mere qualitative approach. The following summary can be made.

Hypotheses 1, 2, ~~3~~ and 3 disagree with crater statistics and tidal deformation trends, while 4 and 5 do agree. In Hypothesis 3, the surface during cratering is too

TABLE IX

Synopsis of Origin and Heating

Hypothesis	1	2	3	4	5
Accretion Source	Inter-planetary	Inter-planetary	Inter-planetary	Inter-planetary	Fission or Ring
First Accretion Place	Inter-planetary	In earth-bound orbit	Inter-planetary	Inter-planetary	Inside Roche's limit
Mode of Capture	Non-tidal	Formed in orbit outside Roche's limit	Tidal	Tidal	Formed in place
Final Accretion Place	Inter-planetary	In earth-bound orbit	Earth-bound	Earth-bound	Earth-bound
Distance, Earth Radii	10	10	5	5	5
Inclination	any	any	10°	34°	0°
Time Scale, years	50,000	50,000	350	350	350
Minimum Aver. Temperature, T_s, °K	404	850	1680	1300	1260
Final Cratering Impact Velocity, km/sec	2.5	4.9	3.1	2.4	2.4
Maximum Melted Fraction, δ	0.0016	0.046	0.838	0.355	0.301

hot and too much melted to acount for the regular and dense crater coverage in the continentes (lunar bright regions or highlands). Hypothesis 4 requires an unusual combination of the nodes of the component orbits (the probability is 0.06, or less if there were more than six component bodies); also most retrospective calculations indicate a small inclination at 5 earth radii, contrary to the requirements of this hypothesis.

Only Hypothesis 5 is free from obvious objections and will be considered as the most probable working basis. As to the consequences for the structure of the lunar surface, Hypothesis 4, although much less probable, is almost ~~with~~ identical with Hypothesis 5.

The termal history of the moon has been treated by different authors, mostly on the assumption of an originally cold accreted body heated by radioactive sources. As depending on the assumed amount and radial distribution of the heat sources, opposing conclusions have been reached; either that the melting was essentially complete (Kuiper, 1954), or that there was no substantial melting except in the deep interior (Urey, 1960b, 1966). Most comprehensive calculations have been made by Majeva (1964) and Levin (1966a, containing a review of her work and that of others); radiative transfer as a component of thermal conductivity and different abundances of the radioactive elements were taken into account, as well as differentiation of a lighter sialic crust from the heavier simatic melt; for various initial parameters, the main conclusion is that at present the moon "is solid at least to a depth of 500--700 km. But the central part, embracing 20-40 per cent of its mass, must have been in a molten state up till the present time".

The estimates of initial heating, as originating from gravitational energy, and as for Hypothesis 5, would enhance these conclusions. Initial melting could have occurred on a large scale as the consequence of bombardment, although for the present thermal state the difference in the initial conditions would be essentially obliterated. This is partly due to the nature of the thermal decay by cooling, partly to the sialic differentiation which transports most of the radioactive elements into the granitic-basaltic crust whence the heat easily escapes to space while further heating of the melted interior stops. Thus, melting is a ~~regulater~~ regulator of internal heating that automatically limits itself as soon as it starts. In a solid body of sufficient size radioactive sources sooner or later lead to melting; this causes sialic differentiation, removes the heat sources from the interior, so that a cooling phase starts According to Levin (1956a), after a cool start the lunar interior would have reached maximum heating and melting

"1 - 2 billion years after its accumulation". Levin's assumptions correspond to our Hypothesis 2, yet on a very much longer time scale; with the shorter time scale as follows from the low U-values, the initial average internal temperature of the moon should have exceeded 850 ^{o}K and, with sufficient shielding by a protective crust, may have reached 1800 ^{o}K with about 5 per cent melting on the surface. This no longer is a cold moon for a start, and in Hypothesis 5 an average interior temperature between 1260 and 1800 ^{o}K is indicated with up to 30 per cent surface melting. In such a case the melting of crater bottoms and the lava flows which covered the maria need not be relegated to some later epoch awaiting radioactive heating, but most probably were contemporaneous with the accretion itself and the last cratering. On the continentes, a solid crust of unspecified depth, 10-20 km at least, must have existed, while the maria were overflown by lava.

On a lava sea which is able to form a solid crust, either because of differentiation of lighter minerals, or because the crust is not cracked by impacts, the "bottle-neck" of heat transfer is the conductivity of the solid, radiation from the surface coping with the heat flow at a very small excess of temperature over the equilibrium temperature, $T_o \sim 300$ ^{o}K. With the liquid at melting temperature, conventionally 1800 ^{o}K, an assumed specific heat $\rho c = 2.7 \times 10^7$ erg/cm^3. deg and heat conductivity

$K_t=3.2 \times 10^5$ erg/cm.sec.deg (allowing for the radiative component, the thickness Δh of the crust increases with time (in years) closely as

$$\Delta h=0.018t^{\frac{1}{2}} \quad (km) \tag{122}$$

During an upper limit of time for crater formation on the continentes, t=2100 years during which the moon receded from 5 to 8 earth radii [equation (112)], Δh=0.82 km only. The crust would be too thin for the craters. The process cannot be advocated for the formation of a basis for cratering.

However, as pointed out by Urey (1966), the crust will be battered and cracked by impacts at the outset; the solid fragments, being heavier than the liquid, are sinking to the bottom, leaving the open liquid surface radiating to space at a rate of 6×10^8 erg/cm^2.sec. At 7.3×10^9 erg/cm^3 as the heat of solidification, the solidified layer at the bottom now increases linearly with time,

$$\Delta h/\Delta t=26 \quad km/year . \tag{123}$$

The rate is high enough to overrule all our time scales of accretion. A pressure-dependent melting point will not essentially influence the process, except by providing a "bottom" to a superficial pool. As a result, during accretion that is too rapid to be influenced by radioactive energy release, a solid almost isothermal body is rapidly formed throughout, at a temperature near the melting point, while the excess energy is radiated away from the surface of the liquid. This is exactly the condition on which equation (99) was based. This makes $\beta_e = 0.301$ an upper limit that is close to the real value; it differs from it only in so far as the remaining 70 per cent of the surface, being solid, does participate in radiation to space; the participation must be small indeed. Hence β_s may represent, in fact, the instantaneous surface fraction of transient liquid pools, formed by bombardment and rapidly solidifying at the bottom. The quoted value corresponds, of course, to the middle phase of intense bombardment; at the epoch of crater formation, β_s must have been near zero, incidental melting occurring from the cratering impacts into the hot substratum.

With the rapidity of solidification from the bottom, no large combined lava pools could have been formed, and the melting must have been confined entirely to the surface of the moon. A consolidated, dense and hot body was formed in such a manner. No lava extrusion, caused by rupture of an imaginary crust, could have taken place at this stage. The maria must have been produced superficially and locally, by impacts of a few large planetesimals, soon after the intense bombardment ended but not very much later. from the number of post-mare craters on them, their age cannot differ much from the 4,500 million years of the moon itself (Öpik, 1960).

In the process of surface melting and bottom solidification in small local pools, not much differentiation could have taken place, any difference created in the pool being locally frozen in, without exchange between different depths. Iron phase could have separated into small pockets but prevented from concentrating in the core. (There may be now a few per cent metallic iron in the core.)

After a hot solid moon had accreted, isothermal at the surface melting temperature but about 200 °K below melting point at the central pressure, radioactive heating of the interior and conductive cooling of the outermost few hundred kilometers must have started. From curves of radioactive heating and cooling of an initially cold moon, Levin (1966b) concludes that widespread melting, from a depth of the order of 500 km down to the center, must have occurred about 2.0×10^9 years from the start. This corresponds to a rise of central temperature by about 1600°. With the initially hot moon, the required heating is 8 times less; allowing for exponential decay of the radioactive sources, the melting should have occurred 10 times earlier. Thus, some 200 million years after accretion, a second stage in the internal evolution of the moon must have been reached; in the molten interior, sialic differentiation must have occurred, forming a lighter intermediate layer adjacent to the outer crust. The crust itself, however, must not have been affected, retaining its original composition and cooled by radiation. The basis of the craters--the highlands or continentes--must have been preserved as it was formed. So also must have remained the maria. At the epoch of radioactive melting, the crust was too thick for lava extrusions or for being pierced by an impacting body; the original planetesimals must have been swept absolutely clean from the surrounding space by that time [cf. equation (93)], while stray objects of the required size from other parts of the solar system are too rare to produce one mare-generating collision (not to mention several) on the moon (Öpik, 1958a, 1960) with a reasonable probability. There can be located 8 mare impact areas on the earthward hemisphere of the moon exceeding 500 km across or requiring projectiles larger than 25 km in diameter. For the whole earth, one such impact is expected once in 2×10^9 years (Öpik, 1958a), and for one lunar hemisphere the time scale is 6×10^{10} years, yielding an expectation of 0.075 interplanetary impacts during 4.5×10^9 years. The Poisson formula yields a probability of 2.3×10^{-14} for having 8 such impacts. Clearly, it is reasonable to assume that the maria were generated as an immediate sequel of the events, and from the same source, which finally built the moon.

An idea of how much an initial hot stage could have influenced the present thermal state of the moon can be obtained from the calculations by Allan and Jacobs (1956) who somehow varied their radioactivity parameters more or less as they would be influenced by melting and differentiation. For a lunar size body, Table X shows the change in average temperature over an interval of 4.5×10^9 years, for three selected cases: A, a cold start with strong radioactive sources throughout the body, the concentrations of uranium, potassium and thorium being those for an actual chondritic meteorite; E, a cold start but with about $4\frac{1}{2}$ times less radioactivity, a concentration assumed to hold for the earth as a whole; and G, a hot start, but with still less radioactivity, nearly one-half of that in E and equal to that in dunite, believed to be the main constituent rock of the earth's mantle.

Each of these assumptions has something in its favor. Case A might appear the most probable one, yet meteoritic concentration of radioactivity which may have prevailed at the start must have led to melting even from a cold start, to differentiation and depletion of the internal heat sources; Case G may then represent the continuation (the absolute values of temperature are not relevant; the starting temperature could be that of melting). Case E shows that, with an average concentration of the radioactive nuclides as in the earth, an initially cold moon

TABLE X

Sample Calculations (Allan and Jacobs, 1956) of Thermal Conditions in a Body of Lunar Size

Age, Years	Central Temperature, °K	Average Temperature, °K	Radioactive Heating, Temperature Rise deg C per Million Years
		A	
0	300	300	3.24
4.5×10^9	5300	3750	0.70
		E	
0	300	300	0.74
4.5×10^9	1400	1100	0.18
		G	
0	1600	1600	0.35
4.5×10^9	1670	1260	0.10

may not yet have reached the melting point; however, as shown above, gravitational heating during rapid accretion would have overruled this restriction, too, and with the higher radioactivity as compared to Case G, a molten interior would have been preserved until our time.

A possibility that the maria were formed as the result of

continued p. 104

radioactive heating during the 200 million years following accretion, by complete melting of the mantle underneath and collapse of the solid crust inwards, must be rejected for another reason, besides objections from the standpoint of thermal balance. The non-differentiated base of the continentes would have collapsed also and have become non-existent. Also, deep melting on the maria would have led to differentiation and formation of a light sialic crust in their place, while the continentes, if somehow preserved, would be supported by a heavier base. Isostatic equilibrium would have sunk them deeper, lifting the maria surfaces into uplands, which is the very opposite of the actual state of things. The maria are definitely depressions as shown by Baldwin's (1963) contour maps, 2.52 ± 0.15 km below the average continentes (Öpik, 1962a). Although made of the same material, the top layer of the continentes may be battered into rubble and may be lighter. Melting at impact of the relatively hot substance (cf. below) would favor compaction, but a ratio of about 0.8 of the density of the rubble in the highlands to the solidified rocks of the maria may be a fair estimate. The thickness of the unconsolidated material in the continentes as required by the postulated isostatic equilibrium, would then be 12.5 km or eight times the estimated thickness of the layer eroded during the formation of the presently surviving craters.

As to isostatic adjustment, it must have worked on the primeval hot lunar material as it does now on earth. With cooling of the outer mantle, some rigidity must have developed as witnessed by the earthward bulge of about h = 1.16 km in excess of the equilibrium tidal configuration (Öpik, 1962a) (dynamical value from physical libration). The extra load, supported by the solid mantle whose inner and outer radii are R_i and R_e, respectively, causes a compressive stress S_m in the mantle, without participation of the liquid core,

$$S_m = \tfrac{1}{2}h\rho g/(1 - R_i^2/R_e^2). \qquad (124)$$

With 500 km as the thickness of the mantle at the time of the last adjustment of the bulge (not necessarily now), $\rho = 2.6$, $R_i/R_e \sim 0.7$, $s_c = S_m = 4.6 \times 10^7$ dyne/cm^2 (46 atmospheres pressure) must have been the average compressive strength of the lunar mantle. The excess bulge, not really a "fossil" tidal bulge but raher a lagging behind remnant of it, would indicate also the differences in lunar level which can be supported on a large scale without isostatic adjustment.

H. Crater Statistics and Origin

If the relative equality of the crater densities on the eastern and western hemispheres ("astronomical" terminology of orientation) on lunar continentes, and even a slight excess in the western can be understood, in terms of the tidally directed accretion history of the moon and the co-orbiting swarm (cf. Section IV F)), a similar distribution on the maria may appear more of a puzzle. Unlike the hypothetical primitive projectiles which were bombarding the continentes, those on the maria must have belonged to the known classes of interplanetary stray bodies - comet nuclei, Apollo group "asteroids" (extinct comet nuclei) and true asteroids deflected by Mars perturbations. With respect to this external medium, whatever the distribution of velocities, the preceding hemisphere of the moon is subjected to a greater frequency of impacts than that trailing behind, and an excess, instead of a deficiency of craters on the eastern hemisphere should have been expected.

However, the orbital velocity of the moon is so small as compared to the interplanetary velocities that only a small effect can be expected; this could be easily masked by sampling errors, inhomogeneities in the counts (as an example, for Mare Crisium, Baldwin (1965) finds 62 craters exceeding one mile in diameter, against 40 counted by Shoemaker and Hackman), or even by systematic differences in the mechanical properties of lunar rocks in the two hemispheres which look so different. Also, a distinction between primary and secondary craters must be made when small craters are counted although, for craters exceeding 1.6 km (one mile) in diameter, the number of secondary craters in lunar maria is only 4 per cent according to Shoemaker (1966).

From data by Shoemaker and Hackman (1965) as adjusted by Baldwin (1965), the number density of primary craters in lunar maria in the two hemispheres is as represented in Table XI.

TABLE XI

CUMULATIVE FREQUENCY OF CRATERS IN LUNAR MARIA IN THE TWO HEMISPHERES

		D > 1.6 km		D > 3.2 km	
Hemisphere	Area, km^2	Number	Number per 10^5 km^2	Number	Number per 10^5 km^2
Eastern	1.52×10^6	583	38.5 ± 1.1	275	18.0 ± 0.8
Western	1.29×10^6	555	43.0 ± 1.5	276	21.3 ± 0.9
Ratio E/W	...	...	0.89 ± 0.04	...	0.84 ± 0.06

The purely statistical probable error of sampling is indicated. For the eastern hemisphere, Mare Imbrium, Nubium, Humorum and Epidemiarum, for the western, Mare Serenitatis, Foecunditatis, Tranquillitatis, Nectaris and Crisium were combined. The largest and easternmost area of Oceanus Procellarum is not represented. The average number density in the eastern hemisphere, both at the 1.6 km and 5.2 km crater diameter limit, is found to be markedly smaller than in the western.

For a lunar body orbiting in the ecliptical plane with a circular velocity v_c, and meeting a stream of particles of velocity U relative to the earth of arbitrary direction, integration of the accretion flux, for the linear case of v_c/U being small, yields a hemispheric ratio

$$\text{Eastern/Western} = 1 + 1.9\, v_c/U \; , \qquad (125)$$

practically independent of the inclination of the U vector to the lunar orbit; at zero inclination, the coefficient is $56/3\pi^2 = 1.89$, and at 90° it is $6/\pi = 1.91$. The concentrating factor as represented by the second term in brackets of (54) is not taken into account; it is of the order of $(v_c/U)^4$ and thus negligible for the small lunar escape velocity. For the lunar orbit 2.25×10^9 years ago as the middle interval of bombardment, a = 55 earth radii and $v_c = 1.08$ km/sec can be assumed. For Apollo group objects, U = 0.660 = 19.7 km/sec is an observed average (Öpik, 1965a) whereas for isotropically orbiting objects at heliocentric velocity v_h the average weighted by the square of encounter velocity (stream velocity times cumulative number proportional to $D^2 \sim w$ according to equation (7)), or the average impact velocity square for craters of a fixed size limit, is

$$U^2 = 1 + {v_h}^2 + 2{v_h}^2/3(1 + {v_h}^2) \; . \qquad (126)$$

For parabolic comets, $v_h = \sqrt{2}, U = 1.358 = 55.3$ km/sec.

The two extreme types of objects yield according to equation (125) expected impact ratios for the two lunar hemispheres E/W of 1.10 and 1.04, respectively. For craters of the size limit in question, the average of the two groups may be representative (Öpik, 1958a), or a ratio of 1.07. A difference from the observed values (Table XI) appears to be well established, but it would be rather far-fetched to draw conclusions as to the origin of lunar craters from such slender deviations of the ratios from unity (Fielder, 1965, 1966).

Here it may be pointed out that comet nuclei, carrying a substantial proportion of volatile ices and of higher velocities, will for equal mass produce more violent explosions than the extinct nuclei or asteroidal objects. The effect of volatiles was not considered in connection with the origin of the moon because it may be assumed that, in the terrestrial pre-planetary ring, these volatiles would not be condensable and, apparently, were not massively represented judging from the composition of the earth.

The density of craters in the continentes is estimated to be 19 times that in an average mare — M. Imbrium (Fielder, 1965) — or 15 times (Baldwin, 1964b). It is therefore expected that 5 - 7 per cent of the craters in the continentes are of post-mare origin. These may be difficult to distinguish except for the ray craters which are apparently the result of more violent impacts, perhaps by the high-velocity comet nuclei. Of the 50 ray craters in Baldwin's (1963) list, 32 are on continentes (a few just on the margin), 18 on maria, which more or less corresponds to the ratio of areas on the earthward hemisphere of the moon, 60 - 65 per cent being occupied by continentes (more in the limb areas which, from projection, represent a smaller apparent fraction of the visible hemisphere than occupied by their actual area). The post-mare origin of these features is thus obvious. Between the hemispheres, 26 ray craters are in the western, 24 in the eastern; if polar and centrally placed "indifferent" objects are omitted, 14 are definitely western, 15 eastern. The uniformity of distribution is also apparent, however with a large statistical sampling error implied (about ± 15%), considering the smallness of the numerical sample.

Reverting to the general crater densities in the two hemispheres, the crater numbers seem to be much more influenced by throwout from a few large cratering events than it would appear from Shoemaker's (1966) estimates. In a specially investigated area of Western Mare Imbrium, covering 465,000 km^2, a definite increase in crater numbers is revealed in the southern portion of the mare, in the vicinity of Copernicus and within the reach of its rays (Öpik, 1960). At an effective limit of 1.1 km for crater diameter, the northern half shows a crater density that is uniform within the sampling error, 13.5 ± 0.5 craters per 10^4 km^2. From the middle of the area the densities increase southwards far beyond the sampling error, so that 580 craters counted over 152,500 km^2 yield a density of 25.6 ± 0.9. Assuming 13.5 to be the density of primary craters (a maximum value - some secondaries may be present in the northern half, too), the excess density in the southern half is to be attributed to 185 secondaries - 22.3 per cent of craters in the entire mare; Shoemaker's (1966) graph indicates only 6 per cent at the 1.1 km limit. Moreover, about the same relative excess persists also in Southern Mare Imbrium at the higher diameter limit of 2.5 km. The number of secondaries increases southward as Copernicus is approached, from 52 ± 6 per cent in the northern third, to 62 ± 7 per cent in the middle third and 61 ± 6 per cent in the southern third of the southern half of the mare (Öpik, 1960).

As shown by the Ranger photographs, the rays appear to consist of tightly distributed secondary craters (Shoemaker, 1966). Crater chains belong to the same phenomenon, produced by a salvo of projectiles, or by a spinning larger clump shattered by the shock, which breaks up in flight and sends out fragments with different velocities at different locations along a line.

A different kind of exceptional object are the lava-filled or flooded craters. 42 of them are in the highlands or continentes, and 20 on the marginal regions of the maria, flooded by the latter, (Baldwin 1949); they belong thus all to the pre-mare stage. This is in harmony with the picture of accretion of the moon as drawn above; the continentes base, still hot after intense accretion had subsided, was then receptive to impact melting. In the post-mare period, the crust had cooled and impact melting became much less prominent.

I. Melting of a Mare

Extrusion of lava from an inner molten core to the lunar surface is as difficult to visualize as it is for the earth's core. On earth, lava formation and extrusion is connected with mountain building, folding, subsequent erosion and isostatic depression which leads to the radioactive sources being buried deep and insulated. The rocks are heated beyond melting point in subsurface lava foci. If saturated with water vapor and other gases (water drifting down from the surface), volcanoes are formed. However, more powerful lava extrusions are the plateau basalts, coming through crustal cracks and overflowing vast areas at a time, covering hundreds of thousands of square kilometres.

On the moon the mountain building processes are absent, erosion is too slow and surface stores of water are not available. The lava pools of the period of intense accretion must have completely solidified at its conclusion. At that time, perhaps some 2000 years after the start of final accretion, the subsurface rocks must have been hot, from a depth below some 0.5 km [using equation (122) for a rough estimate]. At a temperature near melting point, the shock energy of a cratering impact then easily caused melting.

Using equation (20) with $\varepsilon_m^2 = 0.5$ as an upper limit and $q = 2.7 \times 10^9$ erg/g as for melting of a solid already heated to the melting point, the shock velocity at the fringe of complete melting becomes $u \geq 1.04$ km/sec. Equation (16) with $k = 2$ then yields the melted mass ratio to that of the projectile as $y_1 M/\mu = k w_o/\mu$ or 5.77 when $s_p = 2 \times 10^8$ dyne/cm^2 and $w_o = 5$ km/sec is assumed as for the low velocity primeval impact into rock softened by heat. Choosing a depth of penetration of $x_o = 100$ km, $\gamma = \psi = 45^\circ$, $\varepsilon = 1.5$ as for a loose sandball, $\delta = 2.6$, the cratering equations yield $p = 1.093$, $d = 114.5$ km for the diameter of the projectile. Further, from (11) with $f_\rho = 0.78$, $s_c = 1.0 \times 10^8$ (cf. Section V), $s = 3.1 \times 10^9$ dyne/cm^2 obtains as chiefly caused by gravity friction. Equations (7), (4) and (14) then yield a crater or mare diameter of $B_c = 424$ km, $u_s = 0.285$ km/sec, $M/\mu = 21.0$ (mass affected), $M_c/\mu = 14.1$ (mass crushed or melted), $y_1 = 5.77/21.0 = 0.375$ (completely melted fraction).

The projectile itself is not here included; its material may be mostly melted, while vaporization, mixing and a distinct "central funnel" do not occur. The volume of the projectile is $V = 7.8 \times 10^5$ km^3, and the volume of completely melted rock results as $(\bar{\rho}/\rho)V \times 5.77 = 2.25 \times 10^6$ km^3 which could cover the crater area of 1.41×10^5 km^2 with a layer of 16 km. The sprayed liquid and the rock debris, ejected with velocities of 0.2 - 6.5 km/sec, are falling back into the crater, little being thrown over the rim.

Outside the completely melted fraction, y_i, partial melting in proportion to the heat release or to $(y_i/y)^2$ will occur [equations (16) and (20)]. The total melted fraction of the mass affected is then

$$f_m = y_i^2 \int_{y_i}^{1} dy/y^2 + y_i = 2y_i - y_i^2 \qquad (127)$$

or $f_m = 0.609$. The unmolten rock debris will settle down, leaving a lava sea of 3.65×10^6 km^3; if spread uniformly over the crater area, a liquid layer 26 km deep would result. According to (123), under bombardment the solidification of this lava mare would take only about a year. On the other hand, if the mare was formed when intense bombardment had subsided the formation of an unbroken solid crust would have become possible; on the linear scale contemplated, this could have happened only through differentiation of the lighter sialic rocks which would float on the simatic melt.

A characteristic trait of the described mare-generating mechanism is the deep penetration of the impacting body, to about one-quarter of the diameter of the mare. The depth of penetration at oblique incidence (100 km) is here less than the diameter of the projectile (114 km). For Mare Imbrium, at $B_o = 1050$ km, the other linear dimensions must be increased somewhat more than in proportion to the crater diameter. Since the lateral strength is in this case closely proportional to crater depth (11), from (9) we have

$$x_o \sim x_p \sim B_o^{4/5} \qquad (123)$$

whence, for Mare Imbrium, at $\gamma = 45^o$, we find x_o = 555 km for the penetration of the front of the projectile whose diameter would then be 384 km (density 1.5). The average depth of the molten layer would be about 87 km. All this is on the assumption that a single event was reponsible for the creation of the mare, an assumption that is difficult to refute in view of the regular, nearly circular outline of its border. A satellite which produced Sinus Iridum may have impacted nearly at the same time.

K. The Date of Closest Approach and Alfven's Model of Lunar Capture

Mathematical attempts to retrace backwards in time the history of the earth-moon system depend, in the first place, on the assumed law of tidal friction, either as it did, or did not vary in the course of time. The different results obtained by different authors (cf. Section IV E) as to the minimum distance and, especially, the time scale, depend mainly on the assumed history of friction. The relatively short time intervals of 2 - 5 billion years obtained for the time of closest distance are undoubtedly due to an overestimate of friction which so fundamentally depends on the distribution of the oceans and continentés, as well as upon the total amount of water in the hydrosphere of the earth. The oldest dated minerals, such as the Zirkons in the gneisses of Minnesota, show an U-Pb age of 3.5 x 10^9 years, equal to the oldest representatives from the Central Ukraine and the Congo, and sedimentary rocks reach down to 3 X 10^9 years (Cloud, 1963). The closest approach of the moon could not have happened later than these dates: ocean tides of up to 10 km height, accompanied by rock tides of similar amplitude (at $\Delta h = 10$ km, rocks become plastic and cohesion no longer can prevent them from following the tidal bulge of the rotating earth, cf. Section V.B), and tidal friction heating of the order of 9×10^9 erg per gram of the <u>entire earth</u> would have evaporated the oceans and melted the upper crust into a lava sea of which no previous extrusive or sedimentary rocks could have survived. Indeed, the heat of tidal friction must have concentrated in the upper portion of the earth's mantle, yielding there well over 1.6×10^{10} erg/g required for raising the temperature to 1800°K and melting (cf. Section IV.C). The history of the earth's present crust must have begun with a completely molten state, synchronous with the time when the moon was closest to earth (either captured, or emerging from inside Roche's limit as described in Sections IV.C-G). With all the uncertainty as to the absolute time scale, it is most natural to adjust it to a more definite event - the origin of the earth itself, 4.5×10^9 years ago. From the theory of planetary encounters (Section III), a lunar body orbiting somewhere near the earth's orbit could not have escaped close approaches to earth for longer than $10^5 - 10^6$ years and, if tidal capture ever did take place, it must have followed the formation of the earth with not more than such a lag in time. For this reason alone, any conjecture as to a late capture of the moon must be rejected as so improbable that it can be termed practically impossible. Further, the geological and geochronological record renders absolutely unacceptable theories which would put the date of lunar capture at less than 10^9 years ago (Alfvén, 1965), or would ascribe the "Cambrian-Precambrian non-conformity" in biological-geological sequences about

700 million years ago to the events of lunar capture (Olson, 1966) (instead of repeated world-wide ice ages as testified by boulder beds at this and earlier epochs). The medicine is too strong: Instead of boulder beds and interrupted organic evolution (with algae dating 2700 million years ago), a global lava sea several hundred kilometres deep would have engulfed all traces of previous history, and not simply produced a problematic "non-conformity". Under such circumstances, the critical appraisal of Olson's suggestion by Walter H. Munk (1968) sounds rather mild: "Twenty years ago a hypothesis relating this unconformity to a unique event in the Earth-Moon history might have received a sympathetic reception. Somehow the problem is less urgent now. In many places the geologic record is patched across the Precambrian-Cambrian interval, and the unconformity is not so very different from others in the geologic record. With regard to the explosive biological evolution we have succeeded only too well, by destroying all existing forms of life and insisting that life start anew. The biologists won't have it".

If the Alfvén-Olson idea of a recent (late Precambrian) catastrophic event of such a magnitude is not only refuted by geological evidence, but is also contrary to the concepts of probability of planetary encounters (the probability of a primitive moon delaying its fatal encounter with the earth for 5×10^{9} years is less than 10^{-1000}!), the mechanical variant of the capture theory proposed by Alfvén (1965, 1968) appears highly attractive, as it seems to reconcile the few critical data relating to crater ellipticities and the time of their formation (Öpik, 1961b) with the aesthetic merits of Gerstenkorn's mathematical model of tidal capture and evolution.

According to Alfven, if the primitive moon was non-homogeneous, with the outer layers being of lesser density than the average, while passing close to Roche's limit as Gerstenkorn's calculations would imply, it could have lost its lighter mantle while preserving the denser core which was still outside its own Roche's limit and able to keep together by gravitation. In synchronous rotation, the fragments of the tidally distorted elongated mantle released earthward would have been directed inwards in elliptical orbits, possibly even falling on the earth, while those from the opposite end, turned away from earth and possessing more angular momentum, would swing outwards in elongated elliptical orbits. On a two-body approximation, neglecting the gravitational action of the moon's mass, from the tips of a tidally deformed body, extended to double the moon's diameter and in synchronous rotation at a mean distance of 2.71 earth radii, the extreme inward fragments would enter elliptical orbits between 2.16 (apogee) and 0.73 (perigee) earth radii, thus colliding with the earth; and the extreme outward fragments would be thrown into elliptical orbits between 3.26 (perigee) and 22.0 (apogee) earth radii. 2.71 earth radii is Roche's limit at density 4.14 [equation (104)]; if half the original lunar mass was in a core of this density, a mantle of density 2.54 comprising the other half (and yielding 3.34 as for the mean density of the moon) could be thrown out by tidal action, leaving the core behind. A second approximation, on the basis of the restricted three body problem with earth and moon as the principal partners, would lead to more complicated orbits, the Jacobi integral however permitting more or less the same range of geocentric distances. Things are more complicated by the presence of considerable diffuse masses, and by the acceleration of the fragments in near-miss encounters with the accreting lunar core in a non-circular, precessing orbit, drifting outwards from tidal interaction. The inward fragments, partly absorbed by the earth, and the outward fragments will tend to coagulate into moonlets, colliding and breaking up again and ultimately collected by the moon. The outward cloud, originally swinging on an average orbit between, say 3 and 13 earth radii, $a_e = 8$, $e = 0.625$, will collect into moonlets and a coherent cloud of finer debris while more or less conserving the original angular momentum, moving in near circular orbits such that the mean distance becomes $a = a_e(1 - e^2) = 4.9$ earth radii; this is approximately the distance where the craters of the continentes appear to have been formed, judging from their systematic trend in ellipticities (Öpik, 1961b). The outer fragments must have been rapidly collected by the tidally advancing moon. As to the inner fragments, whatever of them was preserved from falling on the earth may have collected into a moonlet. This inner moonlet, too small to overtake tidally the main body of the moon, was perturbed and accelerated by the latter in apogee approaches until, in apogee, a collision (preceded by tidal breakup) with the earthward side of the moon took place; a salvo of large fragments led thus to the formation of the lunar maria.

Thus, except for the time scale, Alfvén's model of tidal capture and subsequent marginal close passage is able to account not only for the craters in the continentes and their systematic ellipticities, but also for the later formation of the lunar maria on the earthward hemisphere of the moon. Quantitatively, however, in this case one cannot put much reliance on precise calculations of tidal evolution near, and preceding the stage of the moon's closest approach because the assumptions, neither of the constancy of the lunar mass, nor of the limited number of interacting bodies, cannot be upheld even approximately.

The only difficulty with this most attractive model remains in the heat created by the impacting bodies during the last stage of crater formation on the continentes. The expected heating would be somewhere between that of Models 3 and 4 of Table IX, and probably nearer to the former; this is a bit too hot, and with too much melting, for the time when the highland craters were formed. Nevertheless, with all the other circumstances taken into account, Alfvèn's model of lunar capture appears to have a good degree of probability in its favor — about as much as Model No. 5, the most favored one of Table IX.

V. STRENGTH OF LUNAR CRUSTAL ROCKS

A. Crater Profiles

The depth to diameter ratio of lunar craters is known to decrease with crater size (Baldwin, 1949, 1963). This is obviously explained by gravitation influencing fallback. The average velocity of the ejecta is mainly conditioned by the strength of the material and the kinetic elasticity; for given velocity, the altitude and distance of flight is limited by gravitation, so that a smaller percentage of the crater volume can be ejected over the rim of a large crater than over a small one.

The theory outlined in Section II.F can be applied to the study of lunar crater profiles. In notations of this and the preceding sections, the apparent depth of a crater, x^q, as measured from the undisturbed ground level to the surface of the debris at or near the center of the crater (disregarding a central peak if present), can be assumed equal to

$$x_t = x_p(1 - F_B) \ . \qquad (129)$$

The throwout function $1 - F_B$ is represented in Fig. 2, the fallback fraction being given by equation (49). This is the fraction of crushed material falling back into the crater, but it may also be assumed to cover gravitational inhibition in raising a lip and in displacing the uncrushed rock of the crater bowl ($AALL_0$ in Fig. 1); this justifies the application of the fallback factor to x_p, the total depth.

Fallback mainly depends on parameter b [equation (48)] which approaches zero for small craters when fallback also tends to zero. In this case the gravitational friction component in lateral strength [equation (11)] may also become unimportant, and the crater profile, or the ratio of depth to diameter will be determined by (9) (except for erosion for very small craters). Of the parameters in this equation, the lateral strength $s + s_c$, or the product $s\xi$, is most uncertain. Nevertheless this, as well as velocity and density can be fairly well guessed for a given cosmogonic stage.

For the larger craters, when parameter b is increasing with the linear scale, gravitational friction in (11) becomes important and even dominant. Fallback then depends primarily on

$$\lambda^2 u_s^2 = \lambda^2 s/\rho \sim \lambda^2 f_s = \text{const.} \qquad (130)$$

or on the product of kinetic elasticity and friction, and on the marginal exit angle, β_o (Fig. 1). Setting $f_s = 0.78$, $\sin\beta_o = 0.8$, the depth to diameter curve for the large craters can be met by a proper choice of λ^2 which, thus, is another parameter that can be empirically determined almost independently of s_c (within the margin of uncertainty of the other, more certain parameters).

The measured crater profiles as used here are from Baldwin's (1949, 1963) work where the depth is reckoned from the crest of the rim. Average rim heights were therefore added to the calculated x' values; to render them comparable with the observed depths, the calculated values of $x'B_c$ as referred to ground level were multiplied by an empirical factor of 1.60 for Baldwin's Class 1 craters, and by 1.30 for those of Classes 2, 3, and 4; the ratios do not seem to depend on crater size.

Baldwin's crater classes are meant to represent relative age, Class 1 being the youngest, showing the least signs of later impacts or the least impact erosion. The classification is supposed to be uninfluenced by the depth to diameter ratio. The later or older classes are more shallow, which is partly the result of erosion but may also include some subjective bias. This is brought out by the distribution of crater classes as depending on size, taken from Baldwin's later work (1963) and represented in Table XII.

TABLE XII

Distribution of Crater Classes by Size in Baldwin's List

Class	1	2	3	4	5	All	Per cent Class 1
Diameter			Number				
> 40 mls	35	24	20	3	30	112	5[illegible]
20-40 mls	66	18	7	0	23	120	5[illegible]
10-20 mls	44	4	0	0	4	52	8[illegible]
< 10 mls	59	0	0	0	0	59	100

The smaller craters are registered predominantly as of Class 1, while among the largest craters this class is in a minority. It seems that the small craters, being less shallow for fallback reasons, tend to impress as being less eroded. Another explanation may be that; in an incomplete list, small craters are more often selected when they are sharp and neat, which makes for a preference in favor of Class 1 without classification itself being systematically at fault. In both cases only the largest craters would correctly represent the relative population of the classes. Hence we may conclude that the Class 1 craters, according to Table XII, are not all of post-mare age, being produced as the last 25-50 per cent of the total population of craters; they could well belong to a later stage of pre-mare bombardment when the lunar crust had somewhat cooled and hardened. Craters of Classes 2-4 are shallower (Baldwin, 1949, 1963) and can be
of the cohesive strength T, as well as [illegible] of the elasticity, [illegible] this [illegible]
explained by ~~lower values~~, to a hotter and softer crustal material at the earlier stages of the final bombardment.

It thus appears that the crater profile data are not a homogeneous selection. For throwout theory to be meaningfully applied, a closer study of the statistical material is required.

Table XIII represents the distribution of the craters in Baldwin's list (1963) according to their surface background. The selectivity is here very marked, small craters being chosen chiefly when of Class 1 and on the maria, apparently because they were easier to measure without interference from other craters. Of course, all post-mare craters except those of Class are expected to be practically unaffected by later impacts, hence the virtual

TABLE XIII

DISTRIBUTION OF BALDWIN'S MEASURED CRATERS ON MARIA AND CONTINENTS

Diameter, mls	> 40		20 - 40		10 - 20		< 10	
	Contin.	Maria	Contin.	Maria	Contin.	Maria	Contin.	Maria
			Ray Craters (Class 1)					
Number	2	5	3	3	5	2	0	3
Per cent post-mare	100	100	100	100	100	100	...	100
			Class 1 (excluding ray craters)					
Number	29	1	47	10	13	24	11	45
Per cent post-mare	3	100	22	100	100	100	100	100
			Classes 2, 3, 4 (with one ray crater)					
Number	47	0	25	1	1	3	0	0
Per cent post-mare	0	...	0	...	...	...	...	...
			Class 5					
Number	28	2	13	15	1	3	0	0

absence of Classes 2, 3 and 4 from the maria as revealed by the table; these classes undoubtedly represent pre-mare objects.

In Class 1, all craters on the maria are, of course, of post-mare origin, with ages ranging from 4.5 X 10^9 years to zero. With the exclusion of the predominantly "continental" limb areas, the maria represent about 50 per cent of the area of selection, so that the continentes should carry a number of post-mare craters equal to that on the maria. Assuming this, the percentages of post-mare craters on the continentes were estimated. It appears that, in Class 1, the largest craters ($>$ 40 mls) are predominantly of pre-mare age and, being less affected by later impacts, must correspond to the last stage of primitive cratering, say, at a distance of some 8 earth radii and 2000 years after the start of accretion (cf. Sections IV.E and F). Craters of Class 1 in the 20-40 mls group are also predominantly of pre-mare age, although some 22 per cent may be of post-mare origin, but craters less than 10 mls in diameter must all belong to the post-mare stage, including those on the continentes. This heterogeneity of Class 1 must be taken into account in the interpretation of crater profiles. From the correlations of diameter with depth as published by Baldwin (1949, 1963) it may appear that heterogeneity is insignificant, the curves running smooth over a diameter range of 10^{6} to 1, from the smallest terrestrial to the largest lunar craters, yet the impression is deceptive. Systematic differences amounting to a factor of 2 or 3 in the depth to diameter ratio become inconspicuous over the wide range when log absolute depth is correlated with log diameter, instead of the ratio, and an apparently smooth run of the curves for heterogeneous material (depending on diameter) can be achieved where actually there are discontinuities in the ratio.

As to Baldwin's (1963) Class 5, the lava filled or flooded craters, it actually contains two different kind of formations. Those on the continentes can be explained by local impact melting of the hot primitive crust when the crater was formed, while those in the maria appear to be flooded from outside by lava from the mare.

In Tables XIV and XV, in notations of, and from the equations of Section II, are collected some theoretically calculated depth (rim to bottom) to diameter ratios, corresponding to a priori assumed probable parameters of impact. A median angle of incidence, $\vartheta = 45^{\circ}$, as for isotropic bombardment, and a coefficient of friction $f_s = 0.78$ are assumed throughout. In Table XIV, $w_0 = 3$ km/sec as for accretion during the late pre-mare cratering phase (Hypothesis 5, Table IX), $\rho = 2.6$, $\delta = 1.5$ g/cm^3 as for a "sandball" planetesimal are further assumed. Also, with the assumed constants, and the lunar acceleration of gravity (162 cm/sec^2), from (11, (12) and (13) we have

$$s = s_c + 160\ x_1 \qquad (131)$$

in c.g.s. units. In Models A, B, D, E, F, and G, the compressive strength is assumed as for the hot and soft pre-mare lunar crust, $s_p = 2 \times 10^3$ dynes/cm^2 (cf. Section V.B); this, according to (6), yields

$$p = x_p/d = 1.093 \ ,$$

a value that is insensitive to the actual value of s_p. In Models A and B, a constant value of the lateral strength, about one-half of s_p, is assumed. In Model C a high crustal strength as for terrestrial rocks is assumed; this improbable assumption is definitely refuted by the observational data, as can be seen from Fig. 3 in which Baldwin's data for the pre-mare craters of classes 2, 3 and 4 are plotted. Of the two other models with constant s_c,

TABLE XIV

Calculated Crater Depth to Diameter Ratios (H/B_o)

for Lunar Gravity, Friction $f_s = 0.78$,

Average Angle of Incidence, $\gamma = 45^{\circ}$, and Pre-Mare Conditions.

$V_0 = 3$ km/sec, $\delta = 1.3$, $\rho = 2.6$ g/cm^3, $k = 2$.

x_p, km	0.25	0.5	1.5	5.0	15.0	25.0	50.0
Model A: $s_c = 1.04 \times 10^8$ dyne/cm^2 = const; $\lambda^2 = 0.35$; $s_p = 2 \times 10^8$; $p = 1.093$							
s, 10^8 dyne/cm^2	1.08	1.12	1.28	1.84	3.44	5.08	9.04
B_o, km	1.78	3.52	10.2	31.2	80.0	121	209
$H/B_o = 1.8x'/B_o$	0.210	0.177	0.113	0.0490	0.0317	0.0330	0.0349
Model B: B_o, s_c, s, p = same as in A; $\lambda^2 = 0.50$							
$H/B_o = 1.8x'/B_o$	0.222	0.196	0.144	0.0826	0.0586	0.0614	...
Model C: B_o same as in A; $s_c = 9 \times 10^8$; $\lambda^2 = 0.12$; $s_p = 2 \times 10^9$, $p = 1.014$							
s, 10^8 dyne/cm^2	...	...	9.3	9.8	11.4	13.0	17.0
B_o, km	...	...	6.75	22.2	64.2	105.5	194
$H/B_o = 1.8x'/B_o$	...	...	0.304	0.196	0.0759	0.0441	0.0251
Model D: s_c decreasing with depth; $s_p = 2 \times 10^8$, $p = 1.093$; $\lambda^2 = 0.25$							
s_c, 10^8 dyne/cm^2	...	...	3.0	2.0	1.5	1.2	1.0
s, 10^8 dyne/cm^2	...	...	3.2	2.8	3.9	5.2	9.0
B_o, km	...	...	8.14	28.1	77.5	120	209
$H/B_o = 1.8x'/B_o$	...	...	0.212	0.0703	0.0236	0.0181	0.0194
Model E: B_o, s_c, s, p = same as in D; $\lambda^2 = 0.50$							
$H/B_o = 1.8x'/B_o$	...	...	0.228	0.0837	0.0321	0.0264	0.0287

TABLE XIV (Contd.)

X_p, km	0.25	0.5	1.5	5.0	15.0	25.0	52.0
Model F: s_p, p as in D; s_c decreasing with depth but larger; $\lambda^2 = 0.23$							
s_c, 10^8 dyne/cm^2	...	...	5.0	3.3	2.5	2.0	1.7
s, 10^8 dyne/cm^2	...	...	5.2	4.1	4.9	6.0	9.7
B_o, km	...	...	7.22	25.5	73.1	116	206
$H/B_o = 1.6x'/B_o$	...	...	0.263	0.127	0.0443	0.0288	0.0273
Model G: s_p, p as in D; s_c decreasing with depth but still larger; $\lambda^2 = 0.28$							
s_c, 10^8 dyne/cm^2	...	...	7.5	5.0	3.8	3.0	2.5
s, 10^8 dyne/cm^2	...	...	7.7	5.8	6.2	7.0	10.5
B_o, km	...	...	6.54	23.4	69.0	111	204
$H/B_o = 1.6x'/B_o$	...	...	0.318	0.182	0.0735	0.0421	0.0313

TABLE XV

Calculated Crater Depth to Diameter Ratios (H/B_o)

for Lunar Gravity, Friction $f_s = 0.78$, Average Angle of Incidence

$\gamma = 45^o$, $\sin\gamma = 0.80$ and Post-Mare Conditions: $s_p = 2 \times 10^9$, $s_c = 9 \times 10^8$ dyne/cm^2

x_p, km	0.125	0.25	0.5	1.25	2.5	5.0	12.5	25.0
s, 10^8 dyne/cm^2	9.02	9.04	9.08	9.2	9.4	9.8	11.0	13.0
Model P: asteroidal bodies, $\delta = \rho = 2.6$, $w_o = 20$ km/sec, $k = 5.31$, $p = 1.65$, $\lambda^2 = 0.22$								
D	14.9	14.9	14.9	14.8	14.7	14.6	14.2	15.6
B_o, km	1.14	2.28	4.57	11.3	22.6	44.6	109	208
$H/B_o = 1.6x'/B_o$	0.170	0.169	0.161	0.145	0.120	0.0881	0.0581	0.0[illegible]
Model Q: cometary nuclei, $\delta = 2.0$, $\rho = 2.6$, $k = 4.44$, $w_o = 40$ km/sec, $p = 1.50$, $\lambda^2 = 0.23$								
D	26.6	26.6	26.5	26.4	26.3	26.0	25.3	...
B_o, km	2.21	4.45	8.83	22.0	43.8	86.7	211	...
$H/B_o = 1.6x'/B_o$	0.0889	0.0881	0.0828	0.0740	0.0604	0.0569	0.0126	...

B is completoly out on account of the assumed high elasticity, while A with $\lambda^2 = 0.35$ leads to a better fit which is still bad enough as can be seen from Fig. 3. While for large craters the curve can be adjusted by a suitable choice of λ^2, the smaller craters require an increase in s.

It is natural to assume that, on account of cooling, the outermost crust of the moon acquired somewhat greater strength. Tentatively, at an age of 2000 years from the beginning of accretion, when the presently surviving craters in the continentes were formed, the temperature distribution in the crust may have been about as follows [cf. equation (122)]:

depth, km (x_c)	0	0.4	0.80	1.2	2.0	3.2	∞
temperature, $^{\circ}$K	300	900	1250	1470	1630	1770	1800

Thus, at the depth of penetration of the smaller craters, noticeable cooling and hardening of the rocks may have taken place. In Models D and E this has been assumed, a triple value of $s_c = 3 \times 10^8$ (still only one-third that for cool terrestrial rocks) at $x_p = 1.6$ km or $x_c \sim 0.8$ km being proposed, with a corresponding softening of the material inwards. The representation of the Class 2-4 crater profiles (Fig. 3) is now good, the best fit being obtained at $\lambda^2 = 0.28$, and intermediate value between the two models.

Models F and G are similar to E and D but with more hardening of the crust, meant to represent a late stage of pre-mare cratering, perhaps 20,000 years after the start of accretion, when the "youngest" craters in the continentes - those of Class 1 - were formed. As has been pointed out above (cf. Table XIII), only the large Class 1 craters of Baldwin's list are of pre-mare age. In Fig. 4, the Class 1 crater profiles are plotted with background (mare or continens) indicated, and it can be seen that Model F represents reasonably well the observations for the pre-mare craters larger than 40 km, while Model G is "too strong".

The smaller craters of Class 1, as well as the larger craters in the maria and all ray craters are of post-mare origin. They must have been produced by high-velocity impacts of asteroidal and cometary bodies, such as calculated in Table XV, Models P and Q. At an average age of about 2×10^9 yea the lunar outer crust must have cooled and hardened completely, therefore a high strength, equal to that of terrestrial granite or basalt, has been assumed. The assumption has proved a success; in Fig. 4, the observed flat run of the depth-to-diameter ratio for post-mare objects (all ray craters, all craters in the maria, and all Class 1 craters smaller than 52 km on the c continentes) is well matched by the P and Q models, the average correlation falling between the two. From statistics of interplanetary stray bodies (Öpik, 1958a) it can be estimated that cometary impacts should account for about 40 per cent cratering events at the 5 km crater diameter level, for 60 per cent at the 10 km and 70-75 per cent at the 40-50 km level. Accordingly, the average correlation for a mixed impacting population of asteroidal and cometary bodies should lie between Models P and Q, nearer to P for small crater diameters, and to Q for the large ones, an expectation that is in surprisingly good accord with the observations as plotted in Fig. 4. Thus, despite the heterogeneity in age and background of the Class 1 crater selection, the data can be well represented as a combination of large pre-mare craters formed at low impact velocities (5 km/sec) and of post-mare asteroidal (20 km/sec) and cometary (40 km/sec) impacts. Together with the older pre-mare craters (Fig. 5), the successful representation of the crater profiles lends some strong independent support to our concepts of lunar origin (Section IV), as well as to the quantitative theory of cratering. Worth noticing is the narrow span of the kinetic elasticity, $\lambda^2 = 0.22 - 0.28$, corresponding to 11-14 per cent average kinetic (throwout) efficiency of the cratering shock, higher than for sand craters and diluvium but about equal to that of hard rock at low velocities of impact (cf. Sections II. C-F).

The dispersion of the depth to diameter ratios for a given crater diameter is considerable, showing variation within an extreme range of about 3 to 1 (cf. Figs. 3 and 4). Yet this can be accounted for entirely by the dispersion in the angle of incidence factor, $(\cos \gamma)^{1.5}$ (equation (9)). Very remarkably, there is little room left for an intrinsic variation of the other relevant parameters - velocity, density and strength of the material. This is especiall true of the pre-mare craters (Fig. 5 and Class 1 craters on continents larger than 40 km in Fig. 4), and for an understandable reason - their impact velocitis must have been close to the moon's velocity of escape, thus practically constant

Unlike the case of the experimental "Teapot" crater (Section II.F), for the lunar craters the density of the fallback material is assumed here to be the same as that of the original "bedrock" material. For the pre-mare craters this assumption naturally follows from the fact that the "bedrock" for new craters consists of the throwout and fallback material of their erased predecessors, so that the material must be identical in all respects including density. Besides, any significant difference in density would increase the fallback volume of large craters so much that, instead of depressions, their floor levels would appear as elevations above the original ground level which, as a rule, is not the case (with one notable exception, the large pre-mare crater Wargentinus, whose floor is 400 meters above ground level). For the large post-mare craters (Fig. 4), any increase in fallback volume could be countered by an increase in the elasticity coefficient, λ^2, yet in this case the large depth of erosion (x_p from 5 to 12 km) would ensure pressure compaction of the partially melted rubble. However, for the smaller post-mare craters, λ^2 cannot serve to balance a change in volume; instead, an increase in s_c would be required which does not appear to be plausible, the largest possible value (9×10^8 dyne/cm^2) as for hard rocks being already used. It seems that, partly by "soldering" through the molten spray, partly through subsidence helped by later impacts, the fallback must have nearly acquired the density of the original bedrocks.

Interpreted as the result of oblique impact, the pre-mare craters in the lunar highlands without regard to class are found to show a r.m.s. random ellipticity of 0.070 ($n = 55$) in central regions, and 0.093 ($n = 125$) in limb regions (Öpik, 1961b); the second figure is of lower weight despite being based on a greater number of craters. The values are corrected for observation error dispersion and are supposed to represent the true cosmic average of crater ellipticities; a weighted mean observed value of $\varepsilon = 0.030$ can be accepted, for a median diameter of about 27 km. With $p = 1.095$, $\gamma = 45^0$, equation (23) yields

$$\varepsilon = \text{[illegible]}519/D \; , \qquad (132)$$

where $D = pB_0/x_p$. This yields for Models A and B (Table XIV), at $B_0 = 51.2$ km $\varepsilon = 0.076$, and for Models D and E, at B_c = ~~2.31~~ 28.1 km, $\varepsilon = 0.034$. The predicted values are closer to the observed ellipticity than could be expected for these a priori calculations based solely on first physical principles. The value mainly depends on the relative crater diameter, D [equation (7)].

B. Orographic Relief and Strength of the Primitive Lunar Crust

The main orographic features of the moon, including the majority of its craters, must have been formed during and immediately after the accretion phase when the crust was hot and soft, and without significant changes afterwards. From the standpoint of supporting strength, with its smaller gravity the moon should be able to support six times greater differences in level than the earth. Actually, the absolute differences in level on the moon are considerabl smaller than on earth which points to a lower strength of its crust at the time of its formation, in agreement with the conclusions drawn from crater profiles (Section V.4). The mean difference between continents and ocean levels on earth is 4.3 km or, with the isostatic correction for the weight of sea water, the equivalent unbalanced difference amounts to 3.3 km; on the moon this would correspond to 19.8 km while the actual mean difference between the maria and the continentes is only 2.5 km or eight times less (Baldwin, 1963; Öpik, 1962a).

Of course, the differences in level occurring on a large scale are isostatically balanced, and the slopes are always smaller than the angle of repose, arctan f_s. Yet, when the unbalanced pressure (weight minus buoyancy) exceeds the plastic limit (compressive strength, s_p), friction is unable to prevent subsidence. Differences of level Δh over short stretches or continuo slopes thus set a lower limit to s_p which in the extreme cases approaches the value itself,

$$s_p \geq g\gamma\Delta h \qquad (153)$$

The stress is greatest at the "foot of the mountain", i.e. at the lowes uncompensated level from which Δh is reckoned. With depth the stress decrease on account of isostasy, beginning from a subsurface level where the heavier rock (sima on earth, compacted maria rock on the moon) begins, and reaches zero at the bottom of the lighter formation (sial on earth, battered rock on the moon, or a depth of about 5 Δh as depending on the ratio of the densities. The strength of the rock will vary with the depth, increasing on account of compaction but decreasing because of higher temperature, so that there is a certain ambiguity as to which depth (155) properly refers. It turns out that on the moon the insulating dust layer is rather thin and that solid rock of high thermal conductivity begins soon enough below the surface (at less than 20 meters, Section VI.B and VII.C); the differences in temperature are therefore not large, and the lower limit of s_p would therefore correspond to the near subsurface layers, of the order of Δh, where the stress is greatest. The strength would decrease downwards as the temperature rises, but this should not become significant before a depth of 10-20 km is reached.

In Table XIII typical estimates of the compressive strength of terrestrial and lunar rocks are collected. The most prominent slopes have been chosen for the moon from Baldwin's contour map (1963) and from the lunar limb profile as measured by C. B. Watts (1963). Of these latter data a twofold selection is used: Δh from the average limb profile over 10° position angle (300 km) and all librations (Öpik, 1964), in which the differences in level are partly smoothed out as it actually takes place with the highest summits and deepest troughs whose load is shared by nearby less extreme features; (b) Δh_e from extreme differences in level over continuous slopes tabulated over 2° position angle for zero libration and published by Baldwin (1963) with the contour map. For terrestial features, in consideration of isostatic compensation by water, 65 per cent of ocean depths is taken as the effective component of Δh reckoned from the sea bottom plus the effective elevation overy dry land smoothed so as to eliminate extreme mountain summits. In (135) $\rho = 2.6$ for moon and earth alike, and the full value of Δh, or 0.8 of Δh_e has been used, to allow for sharing of load.

The largest of the limiting values of s_p should approach the true average. Hence, for the earth, $s_p = 2 \times 10^9$ dyne/cm^2 seems to be indicated, a value very close to that for granite or basalt and a check on the reliability of the method. For the primitive moon, the compressive strength is found to be ten times smaller, $s_p = 2 \times 10^8$ dyne/cm^2.

C. Ray Craters and Strength of the Ejected Blocks

In Baldwin's (1963) list of 50 ray craters, 30 are on continentes and 20 on maria. This is also approximately the ratio of the respective areas occupied by continentes and maria on the earthward hemisphere of the moon (continentes, however, prevailing in the limb areas. There is no indication of greater density of these objects on the continentes, contrary to other types of craters. Clearly, no contribution to ray craters has come from the pre-mare stage to which 98 per cent of "ordinary" lunar craters, crowded 20 times more densely on the continentes than on the maria, belong. This is not so much a question of relative or absolute age, as that of the violence of the explosions caused by the impact of asteroids or cometary nuclei; these, at a velocity of some 15-60 km/sec, may lead to high-velocity ejecta travelling hundreds or thousands kilometers over the moon's surface, which the primeval impacts of planetesimals at 3 km/sec could not match. The larger secondary craters

TABLE XVI

Lower Limit of Compressive Strength (s_p, 10^8 dyne/cm^2) from Orographic Features,

Moon and Earth

Moon Limb

Position Angle	95°	103°	114°	125°	129°	143°	161°	169°	266°	276°	285°	325°
(a) Δh, km	...	3.0	2.4	...	2.6	2.2	2.7	...	3.4	...	...	3.1
(a) s_p, $>$	...	1.3	1.0	...	1.1	0.9	1.1	...	1.4	...	...	1.3
(b) Δh_e, km	2.6	2.3	3.9	3.0	2.6	4.1	4.3	3.2	6.9	4.1	3.0	...
(b) s_p, $\geq$	0.9	0.8	1.3	1.0	0.9	1.4	1.5	1.1	2.3	1.4	1.0	...

Moon Contour Map

Feature	NW of Eratosthenes (Appenines-Mare Imbrium)	N of Copernicus (Mare Imbrium)	SE of Archimedes (Mare Imbrium)	N of Mare Humorum	Sinus Iridum
Length of Slope, km	80	80	50	100	60
Δh_e, km	6.1	5.2	5.2	6.9	6.1
s_p, $\geq$	2.1	1.7	1.7	2.3	2.1

Earth

Feature	Andes 30°S and the Pacific	W Mexican Coast 17°N and the Pacific	Karakorum and the Indian Plain	Philippines Deep 10°N	Tuscarora Deep off Japan 43°N	Perguin Deep Kermadec Trough 30°S
Δh, km	8.8	7.7	5.2	7.5	5.7	5.3
s_p, $\geq$	23	20	14	20	15	14

(over 300m diameter) in the rays (Shoemaker, 1966) are of such a size that they should not be eroded by micrometeorite bombardment even during all the 4.5×10^9 years of exposure, while the smaller craters could last for several hundred million years (cf. Sections X.D, E). And, even when the craters are eroded, the ray substance should last and maintain its lighter coloration. It is most likely that the moon has not existed long enough for the first post-mare rays of ray craters to be erased and that the difference between ray craters and the rest lies in the original event, not in absolute age. The ages of the ray craters are expected to range uniformly over the span of 4.5×10^9 years, with an average of 2.25×10^9 yrs, the same as for the rest of post-mare craters. Besides, almost all large craters on the maria are ray craters; this supports the view that the ray craters are not exceptionally young; they are not formed during the recent one hundred million years or so -- their hypothetical forerunners whose rays are supposed to be obliterated by age are not there.

The secondary craters in the rays, known before but brought now to the fore by the Ranger pictures (Shoemaker, 1966), provide a means for estimating the strength of the post-mare lunar crustal materials. The ejected blocks which caused the secondary craters have withstood high accelerations which taxed their strength to a degree that can be approximately calculated on first principles from the cratering formulae.

Of course, under very particular circumstances all-sided compression may increase the strength of some blocks, instead of shattering them. These, however, must be exceptional cases; in general, the ejected blocks will be representative of the strength of the parent bedrock. Clumping of pulverized debris may also produce sizeable blocks, but of inferior strength, unable to withstand high accelerations; they will not reach to great distances from the crater.

Most of the throwout leaves a crater with relatively low velocities on a short trajectory. From the central regions the ejection velocities are higher, but most of the material is pulverized or broken up by the shock. In a high-velocity impact, leading to explosive development of gas, some blocks may be considerably accelerated and fired like missiles from a gun; the acceleration depends on favorable circumstances - position in the crater and timing of the first shock that breaks up the bedrock into large chunks. If the gas stream from the central funnel overtakes a block at the right time, it may send it out of the crater with a velocity that greatly exceeds the ordinary ejection velocity of the inelastic shock, v_o (Fig. 1). The relative mass of such high-speed ejecta may be small, yet sufficient to cause the ray phenomenon around large craters.

Without entering into details of the ejection process, the velocity v_o (lower limit) of the ejected block can be determined from the distance of flight; its size (d_1) is then related to the diameter (D_1) of the secondary crater through equation (7). If ξ is the acceleration during ejection, the crushing stress (lateral strength of the material inside the primary crater) $\frac{4}{\pi} s_1$ experienced by the projectile during ejection is then close to

$$s_1 = \rho \xi d_1 , \tag{154}$$

where ρ is its density.

The length of path during acceleration is of the order of the depth of the primary crater (diameter B_0), or about 0.1 B_0 whence a lower limit to acceleration can be set at

$$\xi = 5w_o^2/B_o \tag{135}$$

(using the equation for constant acceleration).

We assume also $\gamma = 45^{\circ}$ as a median and most probable angle of ejection ~~ejection~~ and impact alike; this leads to minimum velocity and minimum estimated strength (s). At this angle, the initial as well as final velocity of the projectile in its elliptical orbit is given by

$$w_o^2 = 2gR_p \sin\psi/(\sin\psi + \cos\psi) = gL/(\sin\psi + \cos\psi) \tag{136}$$

($2gR_p = 5.64 \times 10^{10}$ cm^2/sec^2 is the square of the velocity of escape), where R_p is the lunar radius, g the surface acceleration of gravity, 2ψ the selenocentric angular distance of flight and $L = 2R_p \sin\psi$ the linear distance of the flight measured along the chord. (For an arbitrary zenith angle γ, in equation (136) the factor 2 is to be substituted by cosec$^2\gamma$, and $\cos\psi\cos\xi\gamma$ is to be taken instead of $\cos\psi$).

The velocities are such that at impact formation of the secondary crater the stresses greatly exceed the strength of any rock, $w_o > w_m$ (10), wherefore (6) and (7) with k = 2 should be valid. The compressive strength which influences the result but slightly can be set equal to

$$s_p = 2.2\, s_c \quad \text{with } s_c = s = \sigma_s, \tag{137}$$

gravitational friction being relatively unimportant, while σ_s denotes the lateral strength for the secondary crater. The cratering equations for the secondary crater then yield

$$D_1 = B_1/d_1 = 1.51(w_o^2/\sigma_s)^{0.233}\,\xi^{\frac{1}{4}}, \tag{138}$$

while the density ρ of the bedrock cancels out.

For $\rho = 2.6$ the numerical coefficient becomes

$$1.51\,\rho^{\frac{1}{4}} = 1.91 .$$

Using this value for the density of the projectile, and setting

$$\sigma_s = \eta\, s_1 \quad , \tag{139}$$

simple relations are obtained for the crushing strength (s_1) and diameter (d_1) of the ejected block, as depending on the diameters of the secondary and parent craters and the velocity of ejection (136):

$$s_1 = 12.1\, w_o^{2}\, \eta^{0.5} (B_1/B_o)^{1.5} \tag{140}$$

and

$$d_1 = 0.94 B_1 (\eta B_1/B_o)^{0.5} \tag{141}$$

The secondary craters which are considered below are all on the maria; the depth of penetration is of the order of 100 meters and more. Recent Surveyor I photographs (Newell, 1966; Jaffe, 1966a) show the rim of an ancient crater south-west of the spacecraft, partly consisting of rounded boulders (Figs. 5 and 6) reminiscent of a stone wall. Almost level with the general terrain, this wall can be compared to a raised lip with top eroded. In Fig. 1, it can be compared to the lip L, bent upwards and raised from level LL_1 whose original position is 0.03-0.04 crater diameters below the undisturbed surface. The crater diameter is about 420 meters (estimated distance from spacecraft is 140 meters for the near side of the rim, 560 meters for the far side; cf. Fig. 6). Hence the original depth of the rocky strata from which the lip was raised is 15-17 meters. The layer of loose material on a mare must be less than this. It follows that the secondary craters which are here discussed must be the result of impact into a hard rocky substratum, not into granulated material; the strength must be of the order of that for the parent crater, so that the coefficient η (159) should not differ much from unity and even may exceed it, considering that s_1 is the actual stress which the block survived and which must be smaller than the ultimate strength of the parent crater interior, while σ_s is the ultimate strength of the upper crust at the point of impact.

A few typical cases of secondary craters to well known ray craters are considered below. Although the s_1-values so calculated are inferior limits, by choosing the largest objects at a given distance, or the largest distances for a given secondary crater size, these inferior limits should come close to the actual values.

(a) In Mare Cognitum, there is a conspicuous group of secondary craters along a ray from Bullialdus as shown by Ranger VII photographs A 103, 156, 176, (NASA, 1964) and pointed out by Shoemaker (1966). Near the south-east corner of A 176, there are three large craters in a line, two of which appear to be double on closer inspection, while the middle one is single. Allowing for overlapping and scale, from a study of NASA photograph A 176 the following dimensions of the five craters have been derived:

craters diameter, km:	northernmost double	middle single	southernmost double	Average
along ray	1.61 & 1.75	2.41	2.48 & 2.05	2.06 ± 0.08
at right angles to ray	1.61 & 1.55	2.05	1.75 & 1.90	1.83 ± 0.02

Ellipticity is thus $\varepsilon = (2.06 - 1.83)/2.06 = 0.112 \pm 0.040$ in the expected direction. It is, however, too uncertain for quantitative application according to equation (23). For the largest of the group, the middle single one, $B_1 = 2.23$ km is the average diameter. The distance from Bullialdus (south of the group) is $L = 256$ km, $2\psi = 0^\circ 48'$ (one selenocentric degree = 30.5 km) hence $w_o^2 = 3.53 \times 10^9$, $w_o = 0.60$ km/sec. With $B_o = 60$ km for Bullialdus, (140) and (141) are transformed into

$$s_1 = 6.0 \times 10^8\ \eta^{0.3} (\text{dyne/cm}^2) ,$$

$$d_1 = 0.78\ \eta^{0.3}\ (\text{km})$$

For η ranging from 0.5 to 2, $s_1 = 4.9$ to 7.4×10^8 dyne/cm^2, $\sigma_s = 2.5$ to 15×10^8, $d_1 = 0.65$ to 0.96 km as the diameter of the projectile. As a lower limit, and as referring to a block shattered by the blast, s_1 is found to be close to and compatible with a value of $s_c = 9 \times 10^8$, as for granite or basalt, valid for the post-mare lunar rocks (in a mare) at 5 – 6 km below the surface.

The volume of the ejected block is about 0.25 km^3, that of the Bullialdus crater [volume crushed, equation (15)] about 3000 km^3, so that there is no shortage of material for these exceptional ejecta.

On the same frame A 176 (NASA, 1964) (selenographic latitude 11°25 South, 21°44 East) of Ranger VII, there is a group of short parallel ridges going from northwest to southeast and not in the direction of Bullialdus. They are 10–15 km long, a few hundred meters high and are also well visible on the earth-based Lick Observatory photographs; they appear as bright at full moon as the continentes, in contrast to the dark mare background. They are similar in appearance to the isolated peaks in northern Mare Imbrium (Pico, Piton, and others) and are difficult to explain as ejecta from impacts. The central peak of Alphonsus (see below) belongs to the same kind. They have something to do with the melting of the mare and may be surviving relics of the pre-mare period. O'Keefe (1964) suggests a volcanic origin for the ridges as well as for a black marking which runs in the same direction. The marking is darkest at full moon (Lick Observatory and other photographs), reminiscent of the black spots in

Alphonsus and elsewhere and cannot be much of an elevation. Clearly, these features cannot be of direct impact origin. Secondary volcanic phenomena and lava effusion during solidification of the mare (4.5 billion years ago) can be advocated; yet there is little ground to assume "recent" volcanism (of a few hundred million years ago) as some authors would have it.

(b) Tycho's ray (latitude 10°.64 South, longitude 20°.72 East) on Ranger VII - A 196 (NASA, 1964) is studded with secondaries (Shoemaker, 1963). For the largest in the group just below the middle of the frame, $B_1 = 1.02$ km, $L = 1040$ km, $\psi = 17°52'$. With $D_o = 83$ km, $\eta = 1$, equations 140 and 141 yield $s_1 = 5.0 \times 10^8$ dyne/cm^2, $d_1 = 0.25$ km at $v_o^2 = 1.35 \times 10^{10}$, $v_o = 1.16$ km/sec. The blocks ejected from Tycho and originating from a continuous of post-mare age may be somewhat weaker than those from Bullialdus although, as a lower limit, the figure is not binding.

A crater just south of the conspicuous group but outside the ray (Frame A 195) has exactly the appearance of the members of the group; if considered a secondary of Tycho, with $B_1 = 1.56$ km, $s_1 = 7.5 \times 10^8$ dyne/cm^2 obtains, which makes the strength practically equal to that of the mare background of Bullialdus.

The material is not well suited for the study of crater profiles because of ambiguity in the interpretation of shadows. Also, the theory of fallback for isolated craters is not simply applicable because, in these crowded conditions craters of an extended area mutually contribute to each other, compensating thus for the ejecta; a considerable contribution may have come from dust and rubble of the ray jet which accompanied the secondary block in flight.

The secondary craters show marked ellipticity, the study of which however is complicated for reasons similar to those listed above. Thus, on Frame 199, the largest crater shows unusual elongation on reproductions (Shoemaker, 1966) but on the photographic original (NASA, 1964) it clearly consists of two overlapping craters, each measuring about 0.5 km in diameter. Also, it may be assumed that all the impact angles in a limited area of the ray are the same, systematically differing from the istropic average of 45° and thus considerably influencing Equation (23). Nevertheless, local differences can be noted even at inspection. Thus, the large ellipticities of a small group of secondaries in Frame 199 (NASA, 1964) are not repeated in other groups; either is the ground there harder [smaller D, larger g -- Equations (7) and 28)], or was peculiar shape and splitting of the projectiles responsible for the deviation.

On Frame 199, secondaries as small as 60 metres are still visible though eroded - perhaps filled to one-half their original depth. If a diameter of 300 meters is roughly the limit of erosion over 4.5 X 10^9 years (Öpik, 1965c, 1966c, d), the age of a half-eroded crater one-fifth this size would be one-tenth or 4.5 X 10^3 years. Ten times younger than the maria, this is still ten times greater than 50 million years proposed by Shoemaker (1963).

The interior of Tycho shows on Kuiper's Atlas (Kuiper et al., 1960) two craters above the limit of 2.0 km, one measuring 2.7 km on the inner eastern, the other of 3.6 km diameter on the inner western wall. For the area of 6000 km^2, Mare Imbrium carries 4.5 craters to this limit (Öpik, 1960). The age of Tycho could then be some (2 ± 1) X 10^9 years. Although uncertain, this supports the longer of the two estimates.

(c) Between Copernicus and Erathostenes, there are magnificent crater chains produced by a salvo from the Copernicus event. A secondary of D_1 = 6.0 km, at a distance of L = 150 km (reckoned from half-way between center and rim of

143

Copernicus), with $B_o = 88$ km, $\eta = 1$, $2\psi = 4^o57'$, $v_o^2 = 2.33 \times 10^9$, $v_o = 0.48$ km/sec, yields $s_1 = 8.2 \times 10^8$ dyne/cm^2, $d_1 = 2.5$ km.

(d) The anomalous frequency of craters in southwestern Mare Imbrium (Öpik, 1960) suggests that secondary craters up to $B_1 = 5.0$ km have been produced by ejecta from Copernicus to a distance of $L = 590$ km. Here $2\psi = 9^o44'$, $v_o^2 = 8.84 \times 10^9$, $v_o = 0.94$ km/sec, $B_o = 88$ km; with $\eta = 1$, $s_1 = 1.5 \times 10^9$ dyne/cm^2, $d_1 = 1.03$ km obtains. Possibly, the value of B_1 is taken here too high, but s_1 remains within the expected range.

From the evidence presented here and in the preceding section it appears that, from an unspecified depth (20-100 meters) down to some 10 km, the strength of post-mare lunar rocks is about equal to terrestrial igneous rocks.

In recent notes Kopal (1965, 1966b) expresses doubt in the impact origin of the "secondary" craters in Tycho's ray as revealed by Ranger VII photographs and interpreted by Shoemaker; he proposes to consider them "subsidence formations, possibly triggered of by moonsquakes", because the interpretation as secondary craters requires, according to his estimates, an unacceptably large total mass of the ejecta. From Shoemaker's (1963) crater counts in and outside the ray, and for one-fifth of the lunar surface to a distance of 1000 km around Tycho being covered with the secondaries (at an average equivalent thickness of 40 cm for the layer of ejecta according to Kopal), the total volume of the ejected boulders turns out to be 250 km^3 which is not all excessive for a total crater volume of 6000 km^3. Kopal arrives at a much larger figure by taking a larger area of coverage, and also by overestimating to a factor of 2 the crater area densities read from Shoemaker's (1963) very primitive logarithmic graph. Besides, his use of Nordyke's empirical crater diameter — kinetic energy correlation leads to a projectile mass of 3.4×10^{13} gram to make a crater 1.04 km in diameter, while our estimate (based on first principles, especially on momentum, not energy being the proper scaling factor) yields 2.1×10^{13} gram ($d_1 = 0.25$ km, $\xi = 2.6$) or 60 per cent of Kopal's empirical extrapolation. The disagreement is not significant, yet the smaller mass seems to be preferable. Further, the ray crater distribution is extremely patchy, and Ranger VII Frames A 195 - 199 (NASA, 1964) on which Shoemaker's statistics mainly depend contain an exceptionally dense cluster of secondaries which does not seem to be representative. The average coverage may be very much less. All in all, instead of Kopals $5 - 9 \times 10^3$ km^3, the actual secondary ray ejecta from Tycho would amount to a total volume of less than 75 km^3, some 1.2 per cent of the c crushed crater volume. Subsidence craters of a regular round or elliptical shape, densely populating the area with little mutual interference, and with a "meteoritic" diameter-frequency correlation, are very difficult to understand. From the combined evidence, hardly any doubt remains concerning the secondary impact origin of the craters on Tycho's ray.

D. The Lunar Surface as an Impact Counter

On earth, the atmosphere prevents the smaller meteoritic bodies from reaching the ground; they are not only decelerated, but also destroyed by ablation (evaporation, melting) and, in the denser atmospheric layers, through crushing and fragmentation. Irons can withstand the aerodynamical pressure to ground level up to a velocity of 55 - 60 km/sec, but stones, and especially the loosely bound comet nuclei (Öpik, 1966c) will be crushed at a considerable altitude and arrive as a diverging cluster of fragments. Nevertheless, when the total mass is large enough, and because the linear spread in passing the atmosphere is more or less constant and of the order of 200 meters (Öpik, 1961a), a cratering impact can take place; therefore on earth meteor craters below 1 km diameter down to a few meters can only be produced by iron meteorites, while larger craters can also be produced by stony asteroidal bodies or comet nuclei. Because irons are intrinsically rare, most of the large meteorite craters on earth must be due to the non-metallic bodies.

The moon being devoid of the protective shield of an atmosphere, will register as craters the impacts of all cosmic bodies irrespective of size. The range of craters larger than 1 km, originating from the present population of stray bodies, will be common for moon and earth, while smaller craters will be some 50 times more frequent on the moon as depending on the fraction of iron meteorites among the stray body population (about 2 per cent by mass). In addition, with insignificant erosion, the moon has preserved all its craters of significant size and post-mare age, while on earth most of them are erased. When the number of stray bodies of different size in terrestrial space incident on the moon, as derived from astronomical observations, meteorites incidence and meteor craters with allowance for statistical selection and erosion (Öpik, 1958a), is transformed into crater numbers with a scaling factor D = 20 [equation (7)], the number of craters in a lunar mare turns out to be in surprising agreement with the number predicted for a time interval equal to the age of the solar system, on the assumption of a constant flux of the stray bodies (Öpik, 1960) as shown in Table XVII. The crater to projectile diameter ratio of 20 is a fair average of the two models in Table XV, D = 15 for asteroidal and D = 26 for cometary nuclei [the Apollo group "asteroids" can also be only extinct cometary nuclei, (Öpik, 1965a, 1966b)], and depends on data and a priori theory unrelated to lunar crater counts, especially on the assumed high strength of the post-mare lunar crust. The agreement is good and within the limits of uncertainty of the calculation; it is another link in the remarkable sequence of concordant results based on cratering theory.

TABLE XVII

Cumulative Number of Cratering Impacts on Western Mare Imbrium (465,000 km^2) (Öpik, 1960)

Crater diameter, km, >	1.19	2.48	5.40	12.7	34.3	70.6
Observed number uncorrected	738	203	35(34)	10(7)	5(2)	1(0)
Observed number, corrected for secondaries	560:	180:	35(34)	10(9)	5(2)	1(0)
Calculated number (4.5 X 10^9 years)	1050	202	35	5.0	0.44	0.10

Archimedes, the largest crater in Mare Imbrium, is a flooded pre-mare object of Class 5 and diameter of 70.6 km; it should be excluded from the count (cf. bracketed ~~zero~~ numbers in the table). In the third line of the table, the numbers as tentatively corrected for Copernican and Eratosthenian secondaries (see Section IV.H) are supposed to represent primary craters only. The smaller observed number for the smallest craters could be due to incompleteness of the count, although it was considered complete by the author (Öpik, 1960). The constancy of the stray-body flux over so long an interval of time is readily explained by their transient character; their elimination life-time is short, of the order of 10^8 years, and they are steadily injected from two main sources which have suffered yet little depletion since the beginning - chiefly from

Oort's sphere of comets (Öpik, 1966a), and some few from the asteroidal belt (asteroids crossing the orbit of Mars).

Table XVIII contains a similar comparison for supposedly primary craters counted by Shoemaker and Hackman (1963) as adapted by Baldwin (1964b) over a much wider area of combined maria. The observed numbers are again smaller than the calculated ones for small craters, and definitely larger for the large craters (>10 km), confirming thus the trend shown by Table XVII based on a smaller sample. The very persistence of the deviations for the two differently selected samples points toward their reality, as well as to an external cause, and not an internal lunar factor governing the distribution.

The obvious conclusion is that all maria have been exposed to bombardment of interplanetary bodies for the same length of time, about 4,500 million years and that, when their surface solidified, no significant numbers of the original swarm of planetesimals orbiting the earth had survived.

Other comprehensive crater counts and discussions (Dodd, Salisbury and Smalley, 1963; Hartmann, 1965), especially the review by Hartmann (1966) which includes statistics of small craters from Ranger VII and VIII, support these conclusions.

Fielder (1963) attempted to estimate the absolute age of maria and continentes by assuming it to be proportional to the number of craters per unit area. In such a manner, assuming the continentes to be 4.5 billion years old, he ascribes to the maria an age of the order of 100 million years. This kind of reasoning is completely unfounded, even in the light of his "internal origin" hypothesis. However, relative ages can be inferred from the crater densities. The scarcity of crates on the maria rightly indicates that their surface solidified after the end of intense bombardment, but the time lag may be only a few thousand years. During the subsequent 4.5 billion years, about twenty times fewer craters per unit area were imprinted on their surface than in the preceding thousand-odd years on the continentes and on their own surface before it was flooded.

Crater counts by Baldwin (1964b) on the flooded floors of the Class 5 craters Ptolemaeus and Flammarion (in the central highlands) show intermediate crater densities between maria and continentes, about six times those in an average mare. Öpik even finds from Ranger IX photographs for Alphonsus and Ptolemaeus a density of about 20 times that in an average mare (Section V. K). Apparently, these floors solidified at a pre-mare stage when the remnants of the earthbound cloud of planetesimals were still there.

On the contrary, two major flooded craters around Mare Imbrium do not show excessive numbers of craterlets. On the same Mt.Wilson photograph of September 15, 1919, which was used ~~fro~~ for the Mare Imbrium counts (Öpik, 1960), there are 8 craters on the flooded floor of Archimedes (2560 km^2) and six on the floor of Plato (4340 km^2); down to the effective diameter limit of 1.1 km, this gives a crater density per 10^4 km^2 of 31±8 for Archimedes, and 14±4 for Plato, as compared to 13.5 for northern, and 25.6 for southern Mare Imbrium (Section IV. H) as affected by Copernican secondaries. Within the limits of the probable error of sampling (Archimedes being on the borderline between the two halves, the crater density in its strip being 20±1.5) these figures seem to indicate that the floors of Plato and Archimedes were more or less contemporary with, or following soon, the Mare Imbrium event, i.e. that no pre-mare impacts have left their traces on them.

The excessive number of craters in Ptolemaeus and Flammarion suggested to Baldwin (1964b) the possibility that some of them might be of internal origin, blowholes on these "lava extrusions". This suggestion is not only unnecessary, a sufficient increase in the number of impacts being obtained by pre-dating them a few hundred years into the pre-mare period; the "normal" crater numbers in ~~Plato~~ Plato and Archimedes weigh against the blowhole hypothesis--why should these be present in some, absent in other lava covered craters of comparable dimensions? As to lava "extrusions", apparently none did take place, the melting being caused <u>in situ</u> by impact heating of the already hot crustal material. Some limited volcanic events may have indeed taken place on the moon, on the background of collisional melting, but such formations seem to be few and small, like the famous black spots in Alphonsus which Urey (1966), on the evidence of Ranger IX photographs considers as caused by eruptions; they can hardly distort the cratering statistics.

Submerged "ghost craters", in which the outlines are feebly visible without any surface relief, may have a dual origin: either they are traces of normal craters caught and destroyed by the flood; or are they the result of impacts while the lava had not solidified. A list of 42 more conspicuous ghost craters in the maria is given by Fielder (1962). These objects are visible because of material with different reflectivity or coloration being admixed to the lava melt. The semi-destroyed flooded craters, chiefly on the borders of the maria, represent a transition from normal to ghost craters; typical examples are: Fracastorius (97 km) on the southern border of Mare Nectaris, LeMonnier (53 km) on the western border of Mare Serenitatis, Kies (45 km) near to ~~the~~ and Campanus (48 km) on the southern edge of Mare Nubium. And Sinus Iridum is perhaps the most striking example of this type of object.

To the same category belong the extended, sharply bounded color provinces in the maria, detected through multicolor photography (Whitaker, 1966), by superimposing an infrared positive (7800 Å) on an ultraviolet negative (3800 Å). As pointed out by Kuiper (1966), they are indications of lava flows of different composition; however, one cannot agree with his comment that "the lunar maria are not covered with even 1 mm of cosmic dust, which would have obliterated the color differences (loc.cit., p.21). There may be up to 20 cm cosmic dust material accumulated over the ages (cf. Section VII. B), but this is mixed with a much greater amount of granular material from the local bedrock which determines the coloration.

From Ranger photographs crater statistics have been extended down to meter size objects by Shoemaker (1966) and Hartmann (1966) (also Kuiper, 1966). For the post-mare craters, a very remarkable detail in the frequency curve of diameters is revealed; down from about 1.5 km diameter there is an upward surge in the crater frequencies (rate of logarithmic increase), which then is checked at about 300 m diameter where the rate of increase drops. The surge must be due to the appearance of secondary craters outnumbering the primaries, while the decline in the increment can be ascribed to erosion which limits the lifetime of the craters and thus their number roughly in proportion to the diameter itself (Öpik, 1965c, 1966c,d). The lifetime of a 300 meter crater can be set at 4.5 billion years, corresponding to an elevation (rim) of the order of 15 meters being carried away and an equivalent depression filled. This more or less agrees with theoretical estimates of erosion by micrometeorite impact (Sections VII.B, C; X. A, D, E).

On the Ranger IX photos, the density of craters on the flooded floor of Alphonsus is about the triple of that in adjacent Mare Nubium, but below 500 m diameter the numbers in Alphonsus and in the mare become approximately equal and more or less the same as in the Ranger VII and VIII mare samples (Öpik, 1966c, from a verbal communication by Shoemaker). The implication is again that the smaller pre-mare craters have become eroded, and only post-mare craters survive.

One of the requirements of the impact theory of lunar craters is randomness of their distribution. If randomness is defined as the unpredictability of place and time of an event, the distribution of lunar craters undoubtedly conforms to this definition.

Recently Fielder (1965), a prominent proponent of the volcanic theory, tried to prove that the craters are not distributed at random, yet he only demonstrated that the distribution is not of the elementary Poisson type---a conclusion which is obvious even from a casual inspection of the lunar map. The Poisson formula requires that all points (crater centers) are placed on the surface individually, independently, and without mutual interference. This by no means is fulfilled by the cratering phenomena; a large crater wipes out all former smaller craters within its ramparts, creating a void which would appear extremely improbable or even practically impossible in a random distribution of points. Overlapping may not be significant in the maria, but secondary throwout craters are there very numerous ; these have a tendency toward grouping (Copernican crater chains or salvos, Tycho rays), rendering futile the use of the Poisson formula.

Imagine that 2500 craterlet centers are thrown at random over an area divided into 100 squares without mutual interference, so that the average number per square is 25; now let a subsequent large crater erase all the craterlets in one square, and let a cluster of 25 secondary craters be added to another square, so that the total number remains unchanged. According to the elementary Poisson formula, the mathematical expectation or, practically, the probability of having one empty square is $100 \times \exp(-25) = 1.4 \times 10^{-9}$, and the probability of having 50 objects in another is $(100 \times 25^{50}/50!) \exp(25) = 3.6 \times 10^{-4}$. The Poisson probability of both these unusual squares equals then their product or 5×10^{-13}, a practical impossibility. Yet both abnormal squares are the result of random events which are not unusual at all.

Clearly, probabilities of crater distributions calculated from the Poisson formula are meaningless as pointed out by Öpik (1966e) and Marcus (1966a). Refined mathematical studies of the distribution of impact craters according to area density and diameter have been made by Marcus (1964, 1966a), by taking into account the formation of primary and secondary craters, overlap, destruction by obliteration and filling, with some of the relevant parameters based on observation or experiment. The spatial distribution of the lunar craters conforms to a purely random pattern, but the observed numbers of craters less than 1 km (from Ranger VII) are much greater (10 times at 100 m diameters, 20 times at 10 m) than those predicted from experiments with terrestrial explosion ~~xx~~ craters. Marcus concludes that "If the observed excess is real, then either some primary craters produce an unusually large number of secondaries, or else many of the smaller lunar craters are of internal origin". An internal origin of the small craters is the least likely thing to assume--those which originated soon after the melting stage have been obliterated now by erosion, and recent volcanic formations are no more provable than ghosts. On the other hand, terrestrial cratering

Continued on p. 156

experiments have been performed on weakly cohesive media (S_c= 6,5x10', desert alluvium) while the post-mare lunar crust is perhaps 15 times stronger and, according to (140), would produce 8 times larger secondary craters (B_1) for a given primary (B_0). Clearly, the results of terrestrial expriments cannot be directly adapted to the lunar craters without using proper scaling procedures in which all the parameters including the strength of the bedrock should be taken into consideration.

E. Alphonsus and its Peak

The Class 5 crater Alphonsus (Fig.7) is one of the most remarkable, yet still typical pre-mare formations. Despite the negative conclusion regarding the suggested recent "volcanic eruption" from its peak, the fact of fluorescent luminescence is important in itself, and there are many features in the crater which point to some kind of plutonic activity (Urey, 1965,1966), not recent but dating back to the pre-mare stage. The broad features of the crater, however, can be interpreted on the collisional theory of cratering, where also the original cause of melting and of the transient plutonic activity is to be sought.

The crater is bisected by a broad band in the N-S direction, a very low uneven ridge of lighter color; this is not an indigenous feature of the crater but a "scar", a splash from the Imbrian collision which came on top of the completely formed crater.

The simultaneous presence of a corner of Mare Nubium and Alphonsus on Ranger IX Frame A36 (NASA, 1965a) (Fig.7) lends itself readily to comparison. Table XIX contains results of crater counts by the author.

The predicted number of interplanetary impacts is calculated on the same basis (Öpik, 1958a,1960) as in the preceding section. Contrary to the observed deficiency of small craters as revealed in Tables XVII and XVIII, the number of craters in this part of Mare Nubium is 1,7 times the predicted number; the excess must be caused by secondaries, the region being within the reach of Tycho rays.

The interior of Alphonsus contains 6,4 times more craters than Mare Nubium; thus, the density of craters in Alphonsus may correspond to 15-20 times that in an average mare. The frequency of these small pre-mare craters (yet well above the erosion limit) thus exceeds the

Table XIX

Crater Counts on Alphonsus Floor and Mare Nubium, Effective Diameter Limit 0.91 km.

	Alphonsus, Strips E-W					
	Southernmost	South of Middle	North of Middle	Northern Edge	Alphonsus all	Post-Mare Primary Craters
Area, km^2	1230	1940	1420	1400	5990	...
Number	47	61	82	86	276	...
Number per $10^4 km^2$	382 ± 39	314 ± 28	577 ± 45	614 ± 47	460 ± 20	42
	Mare Nubium, Strips					
	Southern triangular	Middle	Northern bounded by reticle marks		Mare Nubium, all	
Area, km^2	1300	2470	2740		6510	...
Number	9	12	26		47	...
Number per $10^4 km^2$	69 ± 16	49 ± 10	94 ± 13		72 ± 7	42

mare crater density about in the same ratio as that for large craters in the highland surroundings. This indicates that the crater floor solidified rapidly [cf. equation (123)] and at an early stage, to become a recipient of the pre-mare bombardment. A superficial comparison with Ptolemaeus (also of Class 5) on Ranger IX Frame B17 (NASA, 1965a) indicated that its crater density, to diameter limit 1.1 km, is approximately the same as in Alphonsus. The floors of these two craters must have solidified about the same time, as for similar reasons has been suggested by Baldwin (1964b) for Ptolemaeus and Flammarion, although he gets a systematically smaller number of small craters.

The fluctuations of crater densities over different regions in Table XIX are also much grater than their sampling errors, apparently the result of unequal occurrence of secondaries.

It has been pointed out by O'Keefe (1966a) that the absence of craters on the illuminated slope of the peak of Alphonsus must have a very particular significance; he suggests a volcanic origin of the peak. Indeed, in a search by the author, on Ranger IX Frame A63, Fig.8 (NASA, 1965a), as well as on several other adjacent frames, no trace of craters could be found on the main slope; there are however two at the southern fringe of the slope, one just at the foot where the rise begins. Four or five small shadwos could be seen or suspected, but on the wrong side, indicating mounds, not cavities. This contrasts drastically with the plentitude of craterlets on Alphonsus floor, though the brighter band of the Imbrian splash again contains fewer. Counts in sample rectangles of 4.16x5.76= 24.0 km^2, equal to the illuminated area of the peak, are summarized in Table XX. In the

TABLE XX

Crater Counts to Limiting Diameter 0.270 km in Central Region (45x42km) of Alphonsus

	West (left) of Peak	Center	Imbrian Ridge	East of Peak
	W-E, On line with peak; per 24.0 km^2			
Number 28	38	1 (peak)	9	34
Number 21	52	46	18	40
	W-E, Just north of peak; per 24.0 km^2			
	W-E, near northern edge of frame; per 24.0 km^2			
Number 27	43	68	16	25
	Average density per 10^4 km^2			
Peak	400 $\pm$ 300*			
Imbrian Ridge	5950 $\pm$ 660			
Other Areas	16000 $\pm$ 550			
Interplanetary Post-Mare Impacts on Peak, Predicted (without erosion)	600*			

*Allowance is made for projected area and shadow of the peak.

bottom part of the table, average densities (with probable error of sampling indicated) are compared with the predicted number of interplanetary impacts during 4,5x10^9 years calculated as before. The "crater density" for the peak depends upon one single entry yet, if the systematic deviation observed-predicted keeps the same trend as in Tables XVII and XVIII, the agreement is "perfect", the observed value being two-thirds of the predicted. Besides, many crater diameters are now near 300 meters, the erosion limit, hence the older ones must have been strongly eroded and become unrecognizable, so that the observed number must be smaller also on this account.

It is clear that the peak must be susceptible to interplanetary high-velocity collisions, but that the other kind of impacts which account for the high crater density on the floor of Alphonsus did not impress the peak. These are secondary impacts of low velocity; the most probable explanation is that the peak material is harder than the throwout blocks, so that they are crushed at impact without leaving a crater mark on the peak.

The altitude of the sun over the photographed region of Fig.8 was $10^{\circ}.8$, and the slope of the peak turned towards the sun was rising another $10^{\circ}.8$ from the horizon (the steepest slope was $19^{\circ}.7$), so that the sunrays made an angle of $21^{\circ}.6$ with the slope. Shadows were shorter than on level ground which must have made more difficult the recognition of shallow craters. This, however, cannot explain the complete absence of craters, especially because on the sides of the peak sunrays were falling more obliquely; not more than 20-30 per cent of the craters could have been lost on this account. Indeed, counts in Mare Cognitum on Ranger VII photographs (NASA, 1964,1965b) where the sun's altitude was $22^{\circ}.1$ (A) and $22^{\circ}.0$ (P), respectively, showed an abundance of craters:

On Ranger VII, Frame A 193, in the upper left central quadrangle between the reticle marks covering 64.0 km^2, 46 craters down to an effective diameter limit of 0.24 km were counted. Reduced to a limit of 0.270 km as in Table XX (with the inverse square of the diameter as correction factor), this yields 5700 $\pm$ 590 craters per $10^4 km^2$. The area is free from Tycho's ray (48) [Shoemaker, 1966].

On Ranger VII, Frame P_3 128, in the upper half of the square free from clustering and probably not affected by Tycho's ray, 55 craters down to a limit of 0.260 km were counted in an area of 77.4 km^2. Reduced to the diameter limit of 0.270 km and $10^4 km^2$, this yields a density of 6500 $\pm$ 620.

The densities of small craters in the chosen regions of Mare Cognitum are comparable to, though smaller than, those in Alphonsus (Table XX); even allowing for less favorable illumination and the choice of less crowded regions (outside conspicuous clusters), the densities probably are still lower as it should be for post-mare craters if some pre-mare craters above the erosion limit have survived in Alphonsus. At the same time it is obvious that illumination is not responsible for the absence of craters on Alphonsus peak.

The absence or scarcity of craters on the peak is real. With an average of 38 craters found on an equal area on Alphonsus floor, and if 20 is taken by allowing for less favourable illumination, the Poisson probability of finding one or none in such an area is $4x10^{-8}$, too small to reckon with an accidental avoidance.

The assumption of a recent volcanic origin of the peak, some 10^8 years ago, may seem an easy way out. The undisturbed surface right to the foot of the peak (Fig.8), without traces of being disturbed by the eruption of an active volcano of this size, does not favor the suggestion. The shape is not that of a volcanic cone. Other peaks of similar character, like the group of angular blocks in Copernicus (shown on the much publicized picture taken on November 23, 1966, by Lunar Orbiter II, all confined to near-central regions of the respective craters, indicate close relationship to the entire buildup of the crater during impact. And, further, the assumption does not help much: the crater walls of Alphonsus are also conspicuously poor, almost devoid of craterlets, while a little plateau in between the Alphonsus wall resembling a dry lake bed, according to Urey (1965), is studded with craters (Fig.9). The crater wall cannot be explained away as being of recent origin. As rightly pointed out by Urey, the phenomenon could be explained by a harder material, even possibly nickel-iron, which is not affected by low-velocity impacts.

Another possibility suggested by Urey (1965) is that the majority of craterlets on the floor of Alphonsus are collapse features, not secondary impact craters at all. However, as shown by counts reported above, the densities of these small craters (not the large ones) in Alphonsus are not exceptional, but are closely the same as found in Mare Cognitum. Equality of the number of collapse features in such widely distant areas (and of different age and origin) is extremely improbable. Also, the craters at this size limit (0.2km) are still essentially round as a rule, a strange, nay incredible regularity. There may be some collapse features (none yet proved), but their statistical importance is undoubtedly negligible.

The crevasses or rills on the floor of Alphonsus (Figs. 7,8,9), as elsewhere, are apparently cracks caused by solidification and cooling. The width of the strongest rill in Fig.9 is 500 to 1000 meters and its average depth about 75 meters, with a slope of 11^o – not so very steep as it looks. An impression is partly formed that the crevasses are just chains of craters and that these are just collapse features, but this is hardly true. There are so many craters on the floor that any drawn line may attract the craters like "beads" on a string, with but small deviations – and the wiggles are actually there. Raindrops on a car window can also be seen running on almost straight lines, collecting previous drops that are distributed at random. A crater impacting near an existing crevasse will expand assymmetrically toward the void as the direction of least resistance and will thus be attracted by it. A pre-existing crater will tend to collapse and join the crevasse on its nearest side.

There remains the only plausible explanation that the Alphonsus peak, and to a slightly lesser degree its walls, consist of a hard material unaffected by the secondary impacts. The number of secondary craters on this hard rock must be reduced at least 10-20 times, if not to nil. According to Shoemaker (1966), the cumulative frequency of secondary craters, both in terrestrial experiments (sedan nuclear explosion) and on the moon (Langrenus), varies nearly as the inverse fourth power of diameter. If for given projectile size the diameters are reduced to one-half on hard rock, the crater numbers will be decreased 16 times, which would suffice to explain the deficiency on peak and wall, allowing also for unfavorable illumination.

Using the suffixes a and b for the hard resp. soft ground parameters, the following sample calculation illustrates the point.

The unevenness of the secondary crater distribution on the floor of Alphonsus points to nearby sources of the ejecta, either inside, or near outside the crater. A distance of 100 km, and a velocity of $W_0 = 400^m/s$ [equation (45)] suggests itself. The frontal inertial ("aerodynamic") component of pressure at encounter, with $\rho = 2.6$, Ka= 0.75, is then about 3×10^9 dyne/cm^2 and the total pressure higher by a value of $\mathrm{\rho}$, the weaker of the two (29). This is more than can be resisted by a stony material, so that equations (6) and

(7) would apply. With k=2 for both cases, $s_p = 2x10^9$, $s_c = 9x10^8$ as for granite for the hard substance (a), δ =2.6, ρ_a =2.6, ρ_b =1.3, s_p =1.3x10^8, s_c = 6x10^8 as desert alluvium for Alphonsus floor (upper 20-30 meters only), D_a/D_b = 0.447, $(D_a/D_b)^4$= 0.04 results, a ratio that is able to explain the virtual absence of craters on the peak, and their scarcity on the wall of Alphonsus, without recourse to exceptionally hard substances (iron).

So far we are mainly on a theoretical basis. If the explanation is correct, the peak should carry a great number of smaller craters, say 20 to a limit of 0.27x0.447= 0.12km. Unfortunately, there are no observations to confirm this, the last close view of the complete peak being obtained on Ranger IX Frame A65; at diameter limit 0.20km there are, indeed, seen 3 craters.

Better direct evidence is provided by the Alphonsus wall (Fig.9) which also exhibits a scarcity of craters, probably due to the same cause. On Ranger IX Frame B77, which contains a closer view of the wall, on an area of 112.7 km^2 the author counted 98 craters to effective diameter limit 0.141km; this gives a density per 10^{4}km^2 of 8700$\pm$620.

For comparison, down to 0.27km the density on the floor of Alphonsus is 16000 $\pm$ 550 (Table XX). Another count by the author on the same Frame A63 down to diameter limit 0.54km gave 1440 $\pm$ 120 per 10^4 km^2 (six equal marked quadrangles, excluding the two containing the peak, 88.3km^2 each, gave 17,18,11,11,9 and 10 craters each). The two counts correspond to a "population index" of 3.5 for the negative power law of cumulative crater numbers as depending on limiting diameter. Logarithmic interpolation then yields a diameter limit of 0.322km at a density of 8700. Assuming that at equal density, equal projectile populations were at work, the counts thus indicate that a projectile which produced a crater of D_b = 0.322km on Alphonsus floor, could only produce one of D_a = 0.141km on the wall. Hence D_a/D_b = 0.438 as derived from the crater statistics, in unexpectedly close agreement with the value predicted from plausible assumptions as to the mechanical properties of the surface materials. The empirical crater density ratio is then $(0.438)^{3.5}$= 0.056, essentially the same as the predicted ratio.

Combining this with crater profiles and other evidence for the mechanical properties of lunar rocks, it is evident that not only is there hard rock on the moon under a layer of more loose material (10-30 meters thick in the maria), but that crater walls and central peaks contain, or consist of, outcrops of these solid rocks, covered perhaps by a very thin insulating dust layer.

It remains to be seen how such an immense solid block could have arrived in the midst of Alphonsus (and other craters with peaks). From the shadow (Fig. 8), the summit, 970 meters, is asymmetrically placed over the south western sector of the base measuring 7.7km from north to south and 6.5km from east to west. The steepest slope is between southeast over south toward southwest, inclined 20° to the horizon, while the illuminated eastern slope is inclined 13°, and the northeastern only 10° (direction from summit to foot of the mountain) (East and West are reckoned astronomically). It could be compared to a more or less rectangular slab of butter on hot porridge. Undoubtedly, below the visible top there must be a broader extension underneath.

A tempting and most probable hypothesis is to consider the peak a direct remnant of the planetesimal which produced the crater. In the rear portion of the impacting body the pressure is smaller than at the shock front in proportion to the thickness of the layer, and a certain layer may survive when the pressure is less than the plastic limit, s_p. A loose aggregate (comet nucleus) may even be compressed into a dense mineral, part of which may be destroyed by shearing, yet a part may survive. By analogy with Equations (134) and (135), $X_o \sec\gamma$ substituting for 0.1 Bo, the average thickness h_p of a surviving hard kernel may be set equal to

$$h_p = 2 s_p X_o \sec\gamma / (W_o^2 \delta), \qquad (142)$$

in former notations or, for $W_o = 3 \times 10^5$ cm/sec as for the pre-mare collisions, $s_p = 2 \times 10^9$ dyne/cm^2, $\gamma = 45^\circ$, $\delta = 2.6$ g/cm^3,

$$h_p = 0.024\, X_o \qquad (142a)$$

Using Model D of Table XIV, at B_o = 120km (diameter of Alphonsus) X_p =25km, X_o = 20km, and hence h_p = 480 meters. This may be close to the average thickness of Alphonsus peak (one-third of a cone 970m high plus 160m underground).

It is thus possible to explain the peak as the hardened surviving kernel of the rear portion of the planetesimal, reflected back to the surface after penetration. Unlike the hot surface of the primitive moon easily melting at impact, the planetesimal was cold and its rear portion suffering little compressional heating was not melted.

The excess weight of a block of the above-mentioned dimensions, 320 meters average height above ground and 160m half-balanced by buoyancy amounts to 1.7×10^7 dyne/cm^2 which is much less than can be supported by a material of the assumed strength, $s_p = 1.3 \times 10^8$; the latter estimate, which successfully accounts for the scaling of cratering on the floor and walls of Alphonsus, refers to the mixed pre-mare and post-mare crater population, with prevalence of the post-mare stage (as follows from the comparison with Mare Cognitum) when the material had cooled and hardened. The Alphonsus event, however, belongs to the pre-mare stage when the material was hot and soft. A minimum bearing strength of 1.7×10^7 is thus required for this stage, too. Clearly, the material could not have been liquid lava, at least not to any considerable depth, otherwise the peak would have sunk in. Also, liquid lava would have solidified to hard rock, equal in strength to the peak and wall, while the cratering statistics indicate a much inferior strength for the floor. It follows that the material was not completely melted yet mobile enough to fill the floor to an approximately uniform level. A mechanism similar to ash flows as suggested by O'Keefe (1966a) appears to have been at work.

As shown in Section IV.3 a considerable fraction of the material must have become completely melted at impact. Where did it go? For Alphonsus we assume Model D of Table XII at X_p = 25km which yields the correct crater size of 120km; the parameters are the same as used in the mare impact model of Section IV.3 except that for the highly elastic liquid fraction $\lambda_x^2 = 0.5$ is to be assumed, instead of $\lambda^2 = 0.25$, $(\lambda_x^2)_{av} =$ 0.125 as for the crushed solid granul fraction with high internal friction. The diameter of the projectile ($\delta = 1.3$) is 25/1.093 = 22.9km, its penetration 25 x 0.8 = 20km but, because of flattening, the rear portion (presumably compressed from $\delta = 1.3$ to $\delta = 2.6$) will follow deep into the crater and must be reflected back to the surface to make the peak. The melted fraction is y_i = 0.375, ejected with a velocity $v = u\lambda$ = 0.74km/sec in a direction β (Fig.1) such that $\sin\beta = 0.8\, y_i$ = 0.300, [equation (27)]. The flight distance of the liquid spray is then 190km, starting from a melting fringe about 24km inside the present rim. All the liquid would have been sprayed around, far beyond the ramparts of a crater even of Alphonsus size. This is an intrinsic property of the mechanics of shock melting, depending only on the linear dimension of the crater, surface gravity, and state of pre-heating, and not on the velocity of impact or the strength of the material. A cold surface would require a stronger shock for melting and would spray the smaller liquid fraction to a greater distance. Real lava flows from meteorite impacts can thus be caused on the moon only on a scale of a mare. The Class 5 flooded craters cannot be regarded as lava covered, but rather as filled with the mobile "Porridge" of partially molten debris, remaining in the crater because of lower elasticity and shock velocity.

VI THE TOP LAYER

A. Dust and Rubble; Optical, Dielectric and Mechanical Characteristics

The uppermost reflecting and insulating layer on the moon's surface has been usually referred to as "dust". There have been objections to the term for various reasons, partly because proponents of the dust concept have sometimes ascribed to it extreme properties - great mobility, excessive depth - which did not appear realistic.

The small depth to diameter ratio [Equation (9)] of the craters on Ranger VII, VIII, IX, Luna IX and Surveyor I pictures definitely show that the surface is granular and finely divided, not pumice-like or continuous solid. A very convincing study in this respect by Gault et al. (1966) is based on cratering experiments in fragmental media at velocities of 0.6 and 6.5 km/sec and angles of incidence of 0° and 60°. The same follows from a consideration of the scope of hypervelocity cratering experiments (Walker, 1967). In O'Keefe's (1966_b) words, it is "a network of space with grains in it, rather than a network of rock with space in it." "Dust" is still the best term to describe it, notwithstanding ~~its~~ large rocky inclusions and its cohesive properties, the dust particles being cemented together through contact in vacuo, or by deposition of vaporized substances (from meteorite impact and solar wind sputtering). The dust possesses potential mobility, when, by impact shock, the particles are sent flying around in small or large cratering events.

The origin of the dust is to be seen in the battering of the surface by interplanetary particles, as well as by the secondary throwout debris of cratering events. Direct accretion of micrometeoritic material is but a minor source of the dust; most of it is the product of destruction of lunar rocks by impact [cf. equations (3), (4) and (14)]. For this reason the coloration of the dust must reflect the properties of the substratum from which most of the dust material is derived, whence the differences in shade not only between the maria and the continentes, but also between minor local formations such as ghost craters and color contrasts in the maria. Horizontal transport of dust on level ground is induced by micrometeorite impact; it is gravity dependent and, theoretically, limited to a few kilometers (Sections X A,B,C). The sharpness of some demarkation lines, such as the southern border of the eastern dark spot in Alphonsus (Fig.7; well visible on this and original Ranger IX Frames A 34-36 which show a broad dark band across the crater north of the peak, joining the eastern with a western dark spot), would limit effective migration to less than 0.5km. This also would deny electrostatic migration as first proposed by Gold (1955) any important role, as has been already pointed out on theoretical grounds by Singer and Walker (1962); their negative conslusion is even more valid if, instead of 30 volts, the photoelectric potential of the lunar surface is less than 10 volts (Öpik, 1962b), the electrostatic force on a particle varying as the square of the potential. Electrostatic "hopping" of the dust would provide a means of transport almost unlimited by distance and would obliterate all sharp coloration differences on the lunar surface (except the ridges of crater walls and other elevations), which certainly is contrary to the most obvious observational facts.

A clever experiment by Gold and Hapke (1966) led to a superficially close imitation of the main features of the lunar surface microstructure down to about the 1mm scale. By repeatedly throwing commercial cement powder (average grain about one micron) at a layer of similar powder "until the statistical mature of the surface is no longer changed by such further treatment", a close replica of the Luna IX or Surveyor I pictures of the small-scale lunar surface near a spacecraft was obtained, including apparent "boulders" of up to 8 cm diameter. Powdered dyes were added, to imitate the actual albedo and photometric properties of the lunar surface. The mineral composition of the powder is probably irrelevant, but a small particle size is essential to make it stick at impact. Little steep, almost vertical ridges were formed, in defiance of any angle of repose. "Pebbles" were also produced, but all these formations had little strength and collapsed when touched by hand.

The experiment differs from lunar conditions in that the material is taken from outside and thrown at the surface with a relatively low velocity. On the moon, the material is ejected from cratering impacts which destroy the previous structure in the crater area, and which also easily blow up the false "pebbles", "boulders", or miniature ridges of low cohesion. Otherwise there is considerable similarity, and it appears that fine dust would stick even to vertical surfaces (of true boulders), somewhat protecting them from further erosion until it is shaken off by new impacts.

The density of the dust is expected to increase with depth. Experiments by Hapke (1964) on the compressivity of fine powders suggest a density-depth relationship for dunite powder on the moon (particle size less than 10 microns), if gently placed and left undisturbed under its own weight, as in Table XXI. The data are slightly smoothed.

TABLE XXI

Density of Fresh Dunite Powder at Lunar Gravity

Depth, cm	0.16	1.0	5	10	100	1000	10^4	(∞)
Density, g/cm^3	0.40	0.43	0.50	0.55	0.71	1.0	1.3	(3.3)

On the moon, in the absence of an atmosphere, the cohesion between grains and resistance to compression may be greater and the density smaller. On the other hand, continuous battering by meteorites (micrometeorites) would lead to tighter packing and tend to increase the density of the dust. The figures of Table XXI are thus probably minimum values, especially near the surface. Dunite is believed to be characteristic of the silicates in the earth's mantle and more similar to undifferentiated cosmic material than granite or basalt. However, the mechanical properties of other kind of rock powder such as basalt (now believed to represent best the composition of the lunar surface) should be similar.

Radar reflectivity provides an observational means for estimating the density of the reflecting layer, as well as of slopes which extend over a linear scale greater than the wavelength (Evans and Pettengill, 1963; Hagfors, 1966), although not without a certain ambiguity. In the wavelength region from 3 cm to 8 m the lunar surface is essentially a specular reflector which indicates that the effective roughness is less than 1 cm. From the distribution of echo ranges it is found that nearly 90 per cent of the echo power comes from a central region about one-tenth of the lunar radius, explained by specular reflection from a gently undulating surface, with the reflecting elements only slightly inclined to the horizon. The remaining 10 per cent of the reflection is diffuse, continuing to the very limb, and can be ascribed to "boulders" or blocks of the order of 1 meter. This description, originally proposed as a hypothesis, is now confirmed by the Luna IX and Surveyor I (also III, V, VI, VII) photographs (Figs. 5,6).

For long wavelengths the dielectric constant ε_i equals the square of the refractive index and is determined through Fresnel's formula,

$$\sqrt{\varepsilon_i} = (1 + \sqrt{A_r}) / (1 - \sqrt{A_r}). \qquad (143)$$

where A_r is the reflectivity at normal incidence - which always is the case with radar. From the reflected power, A_r cannot be determined unambiguously; an assumption regarding the distribution of the reflecting elements has to be made.

The current model, confirmed by the close-up pictures, assumes reflecting elements which are small as compared to the lunar radius, with inclinations distributed at random. This leads to $\varepsilon_i = 2.6 - 3.0$ to compare with 2.6 for dry sand, 4.8 for quartz or sandstone, 5 to 6 for most sialic rocks, 17 for olivine basalt, 20 for meteoric material.

The interpretation in terms of bulk density (or porosity) is also somewhat ambiguous. A plausible formula by Twersky (1962) leads to

$$\rho / \rho_0 = (\varepsilon_i - 1)(\varepsilon_0 + 2) / (\varepsilon_i + 2)(\varepsilon_0 - 1), \qquad (144)$$

where ρ_0; ε_0 are density and dielectric constant of the compacted parent rock, ρ and ε_i those for its granular or porous derivative. For quartz sand the formula yields $\rho = 1.62$, close to the usual value. For the lunar surface, with $\varepsilon_i = 2.6$, the bulk density for quartz as parent would also be 1.6, and for typical silicate rock material, $\varepsilon_0 = 6$, $\rho_0 = 2.6$, ($\varepsilon_i = 2.6$,) the density results as $\rho = 1.44$ with 44 per cent porous unfilled volume. If olivine basalt is the parent, $\rho = 1.36$ with 59% porous volume would obtain. The depth to which this information pertains is of the order of a wavelength, thus from a few centimeters to 10 meters.

Another formula, by Krotikov and Troitsky (1962),

$$\rho / \rho_0 = 3(\varepsilon_i - 1)\varepsilon_0 / (2\varepsilon_0 + \varepsilon_i)(\varepsilon_0 - 1), \qquad (145)$$

yields for sand $\rho = 1.30$, a value that is too low, and for the lunar surface the same value, or even $\rho = 0.46$ if olivine basalt is the parent rock.

On this model, the surface is a random combination of relatively smooth elements, extending perhaps for 10-1000 meters and with an average inclination of 5-8° (Evans and Pettengill, 1963). According to Evans (1962), "the average gradient of points spaced 68cm appears to be 1 in 11.5 and of points spaced 3.6cm it is approximately 1 in 7.4"; the radio albedo is 7.4 per cent at meter wavelength. According to Hagfors (1966), on the scale of a meter the mean slope is 11-12° or 1 in 5, and at 3.6cm wavelength it is about 15°.

A different model of radar reflection, proposed by Senior and Siegel (1960), by Senior (1962), and favored by Russian workers, assumes reflections from large elements comparable to the lunar radius, with corresponding radii of curvature. It requires a larger reflection area and leads thus to a smaller reflectivity; $\varepsilon_i = 1.1$ and ρ of the order of 0.14 (144) are obtained. It is difficult to see how reflecting surfaces could retain a significant radius of curvature, or complete smoothness, on such a scale; close-up pictures of the moon deny a reality to this model which also leads to unacceptably low values of the density.

Other models are possible, too, and there is as yet no formal way of deciding between them on the evidence of radar alone. The detailed law of the distribution of the reflecting elements leaves some freedom of adjustment. With this reservation, the Evans-Pettengill model is to be regarded as the best approach to reality. Conventionally, the density of the upper layer at decimeter to meter depth will be assumed in further calculations as $\rho = 1.3$. This is also the probable density of comet nuclei and their dustballs after the evaporation of the ices (Öpik, 1963a, 1966a, c).

The average inclination of the reflecting elements increases with decreasing radar wavelength, which indicates increasing roughness with decreasing linear scale. This continues until in the visible region of the electromagnetic spectrum an extreme degree of roughness is attained, when there are but opaque reflecting grains of low albedo, much larger than the wavelength so that diffractional backscatter is virtually non-existent, nor are secondary reflections important. The grains are separated by cavities into which light and shadows deeply penetrate. This "fairy castle" structure explains the characteristic lunar phase effect. Near full moon or zero phase angle (angle between incident and reflected ray), shadows are not visible and reflection is observed from the deepest interstices, which leads to the characteristic upsurge of brightness. With increasing phase angle shadows become visible, while illuminated portions become screened and the brightness drops rapidly.

The most extended photographic measurements (on orthochromatic plates without filter) by Fedorets (1952) on 172 individual lunar points show without exception the dominance of the phase angle in the light curves; the angle of incidence, which in Lambert's photometric law is of exclusive cignigicance, is of secondary importance, so that maximum brightness is not reached when the sun is highest, but when the phase angle is near zero. The uniform brightness of the full moon is thus accounted for, despite the rapid decrease of illumination of a horizontal surface toward the limb (Öpik, 1962a). A comprehensive review of lunar photometry has been given by Minnaert (1961). Three-color photoelectric measurements on 25 lunar features over a close range of phase angle of $\pm$ 28° were made recently by Wildey and Pohn (1964), and meticulous studies of lunar polarization have been performed and discussed by Lyot and by Dollfus (1966).

The principal aim of photometric and polarimetric studies was the description of the surface structure and identification of the materials. Until recently the second task proved extremely disappointing when comparisons were made with terrestrial minerals. While the geometrical build-up of the lunar surface, as a "fairy-castle" structure of opaque grains with large-scale surface undulation superimposed on it, did account qualitatively for its photometric properties, the detailed variation with phase angle and other illumination parameters, the polarization, and especially the low albedo remained unexplained until it was shown that irradiation by a proton beam changes almost all mineral powders into substances of low albedo with lunar photometric characteristics almost independent of the chemical composition or lattice structure (Hapke, 1966a). The hope for chemical or mineralogical identification of lunar materials through photometric and polarimetric methods thus vanished. It became clear instead that what we observe is the result of "radiation damage" through continuous irradiation by solar wind and cosmic rays, as modified by erosion and mixing. Despite the equalizing effect of irradiation, differences due to the parent material remain. The ambiguity as to chemical composition has been now removed by scattering experiments on Surveyor V (Mare Tranquillitatis), VI (Sinus Medii), and VII (continens near Tycho) which all showed a basaltic composition (Turkevich et al., 1967, 1968; and NASA Reports)

Experimental and theoretical work, especially by Hapke (Hapke, 1966a, b; Hapke and Van Horn, 1963; Oetking, 1966; Halajian and Spagnolo, 1966; Gehrels et al., 1964; Coffeen, 1965; Egan and South, 1965) has led to satisfactory representation or imitation of lunar photometric and polarimetric properties on the basis of the "fairy castle" model. As a result of integration of a variety of elements, agreement of the final outcome is not necessarily a proof that all the assumed details are correct. Nevertheless, the broad outlines of the photometric behavior of the lunar surface are undoubtedly explained in such a manner. Dunite powder (grain $< 7 \times 10^{-4}$ cm), after 65 coulomb/cm^2 proton irradiation, equivalent to 10^5 years of solar wind as encountered by Mariner II, closely reproduces lunar photometric and polarimetric properties (Hapke, 1966a). Hapke's improved theoretical photometric function, with a surface covered to 90 per cent by little steep features (about or over 45° inclination) represents lunar brightness to the very limb. These features of a subcentimeter scale, "are probably primary and secondary meteorite craters and ejecta debris ..." (Hapke, 1966b).

Most remarkable is the blackening of materials under corpuscular bombardment, (Wehner, et al., 1963a; Rosenberg and Wehner, 196-

Hapke, 1965). I is accompanied by sputtering and deposition of active silicate compounds deficient in oxygen on the rear sides of the irradiated grains. The darkening increases with decreasing grain size; coarse powders darken the least, and rough rock surfaces more than smooth surfaces (Hapke, 1966a). There are differences due to composition, but it would be difficult to extricate them from those due to grain size.

The darkening of lunar materials is akin to that of interplanetary dust whose albedo is equal or less than that of soot and has also been explained by radiation damage (Öpik, 1956).

Sputtering by corpuscular radiation and deposition of the sputtered atoms, as well as sublimation of vaporized substances from meteorite impact offers a means of cementation of the dust-grains. The dust will loose its mobility and become a "weak, porous matrix", as Whipple has put it at an early date (1959). In vacuo, unimpeded by interposed air molecules, the grains may become slightly welded together by direct contact; when the contact cohesion exceeds the weight of the grain, the granular substance acquires the mechanical properties of a solid and will maintain slopes of any steepness. Clearly, the finer the grain, and the smaller the gravity, the more like a solid will the powder behave. This is the case of the experiment by Gold and Hapke (1966), and of the ~~the~~ lunar surface as seen by Luna IX and Surveyor I (Newell, 1966; Jaffe, 1966a).

According to Smoluchowski (1966), cohesion forces between neighboring grains of the order of 0.5 dyne or more will be present, sufficient to counterbalance on the moon the weight of a silicate grain 0.13cm in diameter. At an average grain size of 0.033cm (see below), cohesion between lunar dustgrains would exceed 60 times their weight. In ultrahigh vacuum, Ryan (1966) also found for silicates more or less constant adhesion forces of 0.3 to 1.5 dyne at loads below 5×10^4 dynes. For higher loads, the adhesion rapidly increased, reaching 100 dynes and more at a load of 10^6 dynes; "when this type of adhesion was observed, extensive surface damage was also noted". At lunar gravity and $\rho = 1.3$, the second type of cohesion would set in at a depth of 1000 meters for a grain size of 0.033cm; the depth is inversely proportional to the square of grain diameter. Thus, in the lunar upper layer only the first type of cohesion would be active. However, this refers to specially prepared clean samples. Cementation may lead to much stronger cohesive forces.

In view of this type of cohesion, it would be wrong to treat the small elevations or craters of the dust layer from the standpoint of the angle of repose. The dust possesses no spontaneous fluidity, and the inclinations of the radar reflecting elements are not conditioned by friction. From the mechanics of cratering in a weak medium [small s_c, equation (9)], shallow craters and low inclinations are expected as a rule. The dust is then induced to drift downhill, whatever the slope, by micrometeorite impacts (Öpik, 1962a), so that even the smallest slopes are ultimately levelled out (cf. Section X). As has been pointed out by Whipple (1959) and the author (Öpik, 1962a), there is no loose dust layer on the moon, which explains also the absence ofdust on Surveyor I external surfaces and the failure to record any great disturbance or raising of dust by a nitrogen jet 15cm from the surface (Jaffe, 1966a), or the lack of a covering of dust on the Luna IX camera lens (Lipsky, 1966). This, and the firm settling of the space probes on lunar soil has led even to suggestions that the ground was not dust (Hall, 1966). This viewpoint is shown to be erroneous by Hapke and Gold (1967) and is also refuted by Luna XIII (December 26, 1966) which drove a rod into the lunar soil, proving that "the mechanical properties of the moon's surface layer 20 to 30 centimeters deep are close to the properties ofmedium-density terrestrial soil" (Watts, R.K.,1967). The density of the lunar soil is estimated to be about 1.5 g/cm^3 (Jaffe, 1966a). In the following we still will call this the"dust layer", with proper reservations.

The color of the moon is reddish, its omnidirectional albedo in the optical range increasing from 0.05 in the violet to 0.073 in the visual (green-yellow) band of the spectrum. Infrared photoelectric measurements from Stratoscope II on Mare Tranquillitatis (Watson and Danielson, 1955) showed that the increase continues in the deep infrared, the reflectivity increasing about three times between 1 and 2.3μ. Ordinary rock powders cannot match these observations; yet an irradiation by a 2-kev proton beam equivalent to some 10^5 years of solar wind more or less produced the desirable effect (Wattson and Hapke, 1966), except that the infrared reflectivity of the powders remained still somewhat high as compared to the moon. The powders which responded to the treatment were from samples of basalt, tektite, and dunite. Contrary to these terrestrial samples, a powdered chondrite (Plainview meteorite) was not reddened by the proton beam, although its albedo decreased in all wavelengths. This may mean that the lunar mare material is more of the composition of the earth's crust and not meteoritic. Other recent ground-based results point in the same direction (Binder, etal., 1965) and decisive evidence has come from direct Surveyor V, VI and VII Tests (Turkevich, etal., 1967, 1968).

B. Thermal Properties

Measurements of the thermal emission help to disclose some properties of the layers just below the surface. Infrared thermal emission (around 10μ) and radio emission are used for this purpose, as it varies with the lunar day, or during an eclipse, studied locally as allowed by the resolving power of the instrument, or integrated over the whole disk. The effective depth for thermal emission, L_e increases with the wavelength, λ_e; by using different wavelengths, the thermal parameters can be studied at different depths, qualitatively at least, while absolute quantitative conclusions are less reliable in view of the many uncertainties involved in the construction of thermal models. Adapting a formula proposed by Troitsky (1962), the depth of emission from a layer of silicate rock or granulated material of bulk density ρ (g/cm^3) can be set roughly (to a factor of 2) equal to

$$L_e = 18 \lambda_e / \rho ; \qquad (146)$$

provided the grain is small as compared to wavelength.

For $\rho = 1.3$, this becomes

$$L_e = 14 \lambda_e , \qquad (146a)$$

to be used for the lunar surface. The depth is much greater than for radar reflection where it is of the order of $\frac{1}{2} \lambda_e$.

The rapid variation of lunar surface temperature during eclipse led Wesselink (1948) to a calculation of the heat conductivity of lunar soil; despite an additional component from radiative conductivity as depending on grain size, it turned out to be by an order of magnitude lower than for atmospheric air and to correspond to mineral dust in vacuo at a grain size of about 10^{-2} cm. Since then a wealth of observational material regarding thermal emission from the moon has accumulated. Despite elaborate models produced to account for the observations (Ingrao, etal., 1966; Linsky, 1966), the interpretation in terms of realistic physical parameters has advanced very little since Wesselink's work. One-layer and two-layer models with fixed parameters can be made to agree with one set of data, while they may fail in another. In the words of one of the authors, concluding a set of critically conducted adaptations of various models solely for the Tycho region, "In the light of our present inability to decide uniquely which of several plausible models applies ....., any detailed description of small-scale lunar surface structure, uncritically based upon any one kind of model yet devised, may be physically meaningless" (Ingrao, etal., 1966).

The "knee" in the thermal emission curve during eclipse, or the sudden change in the rate of cooling, has been interpreted through the presence of a layer of greater conductivity at a depth of a few centimeters, leading thus to the concept of a two-layer model. It seems now that solid blocks of different size strewn all over the surface, such as seen on the close-up pictures (Figs. 5,6) (Newell, 1966; Jaffe, 1966a), and as suggested by the diffuse component of radar reflection (Evans and Pettengill, 1963; Hagfors, 1966), are to a considerable degree responsible for the characteristic changes in the cooling rates after the cutoff or reappearance of insolation. According to Drake (1966), "there must be a second component, not in depth, but on the surface".

This surface component which principally must be responsible for the anomalies, through greater thermal inertia as well as through its non-horizontal profile, has not yet been treated theoretically, except for Gear and Bastin (1962; Bastin, 1965) who considered the effect of macroscopic roughness-steep cavities and elevations-on the thermal and radiative balance of the lunar surface, as distinct from the flat surface figuring in all the usual models.

The surface component, due to stony blocks, affects certain details, yet the general run of the thermal emission curve depends on the dust layer with small inclinations, satisfactorily approximated by a horizontal outer surface. Its thermal parameters are expected to be a function primarily of depth, to some extent also of temperature which again is mainly a function of depth. By applying the equations of the one-layer model to observations relating to different depths, the effective parameters so obtained (conductivity, grain size) may yield an approximate description of their variation with depth independent of the rigid prescriptions of a two-layer model, and perhaps more realistically. In any case, the errors of such an approximate model allowing for continuous variation of the parameters may be smaller than those of a "rigorous" procedure based on unproved assumptions. Besides, part of the variation of the conductivity with depth, due to mechanical compression and radiative transfer, can be estimated from first principles, so that only the grain size remains as the only depth-dependent parameter.

For thermal fluctuations of period τ_t(sec), a characteristic parameter

$$\gamma_t = (K_t \rho c_1)^{-\frac{1}{2}} \qquad (147)$$

can be determined, to a factor of the order of unity, almost free of hypotheses. Here K_t is the thermal conductivity (cal/cm.sec.deg), ρ the bulk density (g/cm^3) and c_1 the specific heat (cal/g).

$$\gamma_t = \theta_a \tau_t^{\frac{1}{2}}/Q_a \text{ x const} \qquad (148)$$

where θ_a is the amplitude of temperature of the radiating surface layer, Q_a the amplitude of heat content (cal per cm^2 column), obtained from the observed fluctuation of radiation (insolation minus radiation losses). For an inside (radio) layer at effective depth x, the amplitude θ_x is given by the observations, while the heat content Q_x is itself a function of K_t or γ_t.

The amplitude decreases exponentially with depth X,

$$\theta_x = \theta_a \exp(-X/L_t), \qquad (149)$$

where

$$L_t = \gamma_t K_t \tau_t^{\frac{1}{2}} \qquad (150)$$

is the effective depth of penetration of the thermal wave, to be identified with the depth to which the mean thermal parameters apply.

With c_1 = 0.2 cal/g as a close value for all kind of silicate rock, and γ_t determined observationally from (148), the ambiguity with respect to K_t rests solely with the adopted value of , [equation (147)]. Different values of γ_t, decreasing with wavelength and depth, have been obtained, indicating mainly an increase of the conductivity with depth as could be well expected. From lunar eclipses ($\tau_t \sim 1.8 \times 10^4$ sec), Wesselink obtained $\gamma_t \cong 1000$ cm^{2}deg sec$^{\frac{1}{2}}$/cal. In the radio range, smaller values have been found, as well as in the infrared for the lunar monthly cycle ($\tau_t = 2.5 \times 10^6$ sec). Russian authors have therefore doubled Wesselink's value. However, there is no real discrepancy, the different values being accounted for by increasing thermal conductivity with depth.

In a granular medium *in vacuo* and grain diameter d_g the heat flow [illegible] through the grain, the radiative flow between the grains, and the contact flow by conductivity between grains pressed against each other. The relative area of contact per cm^2 cross section at depth x will be assumed equal to

$$\sigma_\rho = g\rho x / s_\rho \tag{151}$$

in former notations. Setting the compressive strength $s_\rho = 2 \times 10^9$ dyne/cm^2, $g = 162$ cm/sec^2, $\rho = 1.3$g/cm^3, for the lunar dust consisting of hard silicate grains we obtain

$$\sigma_\rho = 10^{-7}\, x \tag{151a}$$

If ΔT_1 is the difference of temperature along the grain, ΔT_2 the contact difference, $\Delta T = \Delta T_1 + \Delta T_2$ being the total difference over depth d_g, the effective contact gradient can be assumed equal to $\Delta T_2 / (\sigma_\rho^{\frac{1}{2}} d_g)$. With this, the flow of heat through the grain being equal to the contact flow plus radiative transfer, as well as equal to the total flow, the double equation of heat flow can be written as

$$K_t \Delta T / d_g = K_0 \Delta T_1 / d_g = K_0 \Delta T_2 \sigma_\rho^{\frac{1}{2}} / d_g + 4K_s T^3 \Delta T_2$$

which, after elimination of the temperature differences can be reduced to

$$1/K_t = 1/K_0 + 1/(4K_s T^3 d_g + K_0 \sigma_\rho^{\frac{1}{2}}). \tag{152}$$

Here K_0 is the conductivity of compact rock, and K_s Stefan's constant. For our exploratory model, constant values of d_g, K_0 and T are to be used, which then can be considered as mean effective values, more or less valid at the particular depth L_t to which the observations refer.

With $T = 240°K$, $\kappa_0 = 0.005$ cal/cm.sec.deg. and equation (151a), this reduces to

$$1/\kappa_t = 200 + 10^5 / (7.5 d_g + 0.16\, x^{\frac{1}{3}}), \qquad (152a)$$

for d_g and x in cm.

With $\rho = 1.3$, $c_1 = 0.2$ in (147),

$$\kappa_t = 3.8\, \gamma_t^{-2} \qquad (153)$$

obtains. Setting into (152a) further $x = L_t$ as defined by (150), d_g can be calculated. Table XXII contains some typical results.

TABLE XXII

Effective Mean Thermal Characteristics of the Lunar Soil (Thermal Infrared, 10 μ)

Source	τ, sec	γ_t	κ_t	L_t, cm	d_g, cm
Eclipse (Wesselink, 1948)	1.8×10^4	1000	3.8×10^{-6}	0.5	0.035
Lunar Cycle	2.5×10^6	750	6.8×10^{-6}	8.0	0.031

The effective value of γ_t for the lunar cycle is based on the observations of Murray and Wildey (1964) and on the calculations by Ingrao etal. (1966) for "temperature-independent" models.

Now instead of two or more discrete layers, a continuous increase in the conductivity caused by compression, at a more or less constant effective grain size,

$$d_g \cong 0.033 \text{ cm}, \qquad (154)$$

is indicated. The effective grain size depends, of course, on the distribution of grain diameters; its constancy may indicate identical distribution at different depth, thus essentially a one-layer structure.

The low surface conductivity requires a large thermal gradiant, to deliver the internal flow of heat, E_i, according to

$$dT/dx = E_i / \kappa_t \qquad (155)$$

With (152a) and (154), this can be integrated. For very different initial conditions and different content of radioactive isotopes, Levin (1966a,b) cites calculations by Majeva (1964) which give for the present moon values of the thermal flux within a range of (2.3 4.6) x 10^{-7} cal/cm^2.sec. Taking 4.3×10^{-7}, which is the earth's value decreased in proportion to the radius, integration yields, ~~for~~ for the mean temperature T at depth x,

$$T - T_0 = 8.6 \times 10^{-5}\, x + 0.532\, x^{\frac{1}{2}} - 0.836\,(1.56 + x^{\frac{1}{2}}) + 0.37, \tag{156}$$

where T_0 is the mean temperature of the surface. Only the first two terms are significant.

For $x = 10^4$ cm as an upper limit of validity of the model, $T - T_0 = 49°$. This is insignificant; probably a solid rocky structure begins even at a smaller depth where the conductivity willbbe much higher. The pressure-induced increase in conductivity is rapid enough, so that the insulating capacity of the outermost dust layer has little effect on the thermal state of the moon's interior.

As compared to the pressure effect, the increase of the radiative conductivity with depth, dueto the increase of the mean temperature is insignificant in the granular layer. In the outer layers, however, where radiative conductivity plays an important role, a curious effect arises. The diurnal fluctuationsof temperature, affecting radiative conductivity, cause the daytime conductivity, when thetemperature is higher, to be higher, too: even in the absence of a net outward flux of heat from the moon's interior, the daytime intake of solar heat by the soil requires therefore a smaller inward negative thermal gradient than the positive nocturnal gradient needed to restore thermal balance at the surface. The net average thermal gradient will be positive, the temperature rising inward without producing a net leakage of heat. This effect has been investigated in detail by Linsky (1966); when radiative conductivity is taken into account, the thermal gradimt derived from radio data leads to a thermal flux of the order of 3.4×10^{-7} cal/(cm^{2}sec), in agreement with theoretical limitations (Levin, 1966a), while a conductivity independent of the fluctuating temperature yields ten times larger a flux, unacceptable for various reason

This explains also the excessive values of the lunar thermal flux, derived by Krotikov and Troitsky (1963) from the inward increase of temperature as shown by radio data.

As to temperature variation, for the subsolar point a value of 371° K (Pettit, 1961) and for theantisolar point, 104° K (Saari, 1964) can be assumed for the typical surface. On account of low thermal inertia, the extreme afternoon maximum and the pre-dawn minimum would differ little from these figures. These are black-body values; a small correction for emissivity could raise these values by 1-2 per cent. The mean equatorial near-surface temperature as determined from short-wave radio (3 mm), is near 206° K (Drake, 1966) though the scatter of individual determinations is large. In any case, the value should lie between 200 and 220° K.

If T_1 and T_2 arethe temperatures of the subsolar and anitsolar points, the mean arithmetical equator temperature is close to

$$T_m = \tfrac{1}{2}(T_1 + T_2) - 0.110\ (T_1 - T_2). \qquad (157)$$

This equation is empirically adjusted to the skew radio brightness temperature at λ=3mm (Drake, 1966). For the thermal infrared it yields T_m = 208°, which is close to, and less affected by observational error than, the radio value.

Table XXIII tentatively represents the variation of the mean subsurface temperature with depth. It is based on radio brightness temperatures as listed by Krotikov and Troitsky (1963), properly modified by Linsky (1966), with a systematic correction of -12° applied to make the zero point coincide with the surface value for the infrared.

TABLE XXIII

~~Mean Temperature and Depth, Lunar Equator~~

To table Top of next page

Table 26 Mean Temperature and Depth, Lunar Equator

Depth, cm	0	25	50	100	200	400	700
Temperature, °C	-65	-59	-54	-49	-43	-33	-23

The depth is calculated from the wavelength according to (146a).

C. Thermal Anomalies

The lunar night-time temperatures are too low for accurate observations in the 10-μ window. Using the 20-μ atmospheric window, LOW (1965) found a mean temperature of 90°K for the cold limb (dark near-polar or pre-dawn). Cold spots of 70°K and lower were found, tentatively explained as those of low conductivity (γ_t about 2300 cm^2 deg sec$^{\frac{1}{2}}$/cal), and a hot spot of 150°K was recorded near the south-eastern limb.

Hot spots, which are warmer than the normal surface during an eclipse but cooler in daytime, have been systematically observed and listed by Shorthill and Saari (1965, 1966). Among 330 such objects, 84.5 per cent are ray craters, craters with bright interior or bright rims at full moon, 8.7 per cent are bright areas of various qualifications, 0.6 per cent are craters not bright at full moon, the rest being unidentified. They occur over the entire lunar surface, but somewhat more densely over the maria, being expecially crowded in Mare Tranquillitatis. On a recent map (Saari and Shorthill, 1966) made from the observations of the lunar eclipse of December 19, 1964, 271 or 58.0 ± 1.7 per cent of the hot spots are on the maria, 196 or 42.0 ± 1.7 per cent on the continentes. Strong anomalies are even slightly more concentrated on the maria (125 out of a total of 201, or 62.2 ± 2.5 per cent). There may be some adverse selectivity for the limb areas where continentes predominate, so that the representative areas of maria and continentes may be about equal, or slightly in favor of continentes. The excess in the maria seems thus to be real, although the distributio is quite patchy, so that the random sampling error is not representat-ive of the actual statistical uncertainty. In any case, the anomalie are clearly post-mare features. The most prominent ones are Tycho and Copernicus.

During eclipse, the interior of Tycho (diameter 88km) retained a temperature around -70 to -60°C, with maxima of -51 and -48°C, while in the "normal" surroundings it dropped to -106 and -112°C. Just outside the crater's wall it was -82°C, at double radius around the crater -97°C, at 2.5 radii -101°C, at 3.5 radii -106°C. The resolving power of the apparatus was 10" of arc, 19km or 0.22 of the crater diameter, sufficient to resolve the gradual decline in the infrared radiation around the crater. At full moon, the crater is by a few degrees cooler than its surroundings (+77°C), but this may be partly due to its greater albedo. Otherwise the anomaly is undoubtedly accounted for by greater thermal inertia, i.e. smaller γ_t, or greater conductivity and density of the material.

In addition to the spots, extended areas, chiefly in the maria (Mare Humorum, Oceanus Procellarum between Aristarchus and Kepler, Northern Mare Imbrium, continens around Tycho, and others), are warmer by about 10°C during an eclipse (Shorthill and Saari, 1965a, 1965).

From their distribution, the anomalies around craters are undoubtedly due to crater ejecta, similar to the rays but more concentrated in the vicinity of the crater. The median distance to which massive ejecta are flying can be calculated from equations (45), (27), (16), (4) and (19) with $s_c = 9 \times 10^8$, $\rho = 2.6$, $\lambda_x^2 = \frac{1}{2}\lambda^2 = 0.14$ (Table XV, Model Q), $y = 0.5$, $\sin\beta_o = 0.8$, this yields $V_x = 1.39 \times 10^4$ cm/sec, $L = 8.8$ km. The radius of the circle over which most of the ejecta are sprayed may be taken twice this value or 17 km, almost equal to the resolution of the radiometer used by Shorthill and Saari. This radius is independent of crater diameter. The effective diameter of the anomaly is then B_o + 34 km, where B_o is the crater diameter. The area cannot be less then the 34-odd km across and always well resolvable by the radiometer. Therefore it is expected that the measured thermal excess will not depend on the size of the crater even when its diameter is smaller than the resolving power, except for the thickness of the overlay when it drops below a certain limit.

This is exactly what Shorthill and Saari (1965b) had found but they gave it a different interpretation. By assuming that the thermal excess is restricted to the crater itself, for craters below the resolution limit they reduced the excess to the crater area and obtained a strange increase for the smaller craters. Their "corrected signal differences" have no physical meaning; even when the meteoric theory is discarded (which no longer is possible with the present state of knowledge), a volcanic eruption on the moon would also spread the ejecta to distances independent of crater size.

The uncorrected observed anomalies (Shorthill and Saari, 1965b) yield for all craters within the diameter range from 4 to 90 km consistently the same value of the thermal parameter $\gamma_t = 600$ from the eclipse observations. In terms of our pressure-adjusted thermal model, from (153), (150), (152a) with $\tau_t = 1.8 \times 10^4$ sec, $K_t = 1.0 \times 10^{-5}$, $L_t = 0.81$ cm, and $d_g = 0.115$ cm are obtained. The thermal anomaly of the hot spot is readily explained by a coarser grain near the surface, just of the order of ordinary terrestrial sand. The upper layer is continually ground and overturned by meteorite impact and supplemented by the smokelike products of sublimation; it is expected that, without fresh overlay, it will become more and more fine-grained with age. Also, small meteorites and especially the numerous secondary ejecta which do not penetrate the dust and rubble layer, but which are responsible for most of the overlay outside the reach of the large post-mare cratering events, will eject and spread around material of a smaller grain size than large meteorites which penetrate the top layer (craters over 0.5 km in diameter) and crush the fresh bedrock underneath. The difference in the thermal properties of the environs of large primary post-mare craters, as compared to the surface at large, can thus be understood without postulating for them improbably short ages. All ages from 45×10^9 years to zero would do.

In addition, there may be blocks of solid rock on the surface which, even when in a small proportion, will contribute to the anomaly; in such a case the calculated effective grain size is an upper limit.

On the other hand, an exposed solid rocky surface of this size, as it figures in some interpretations, is physically inconceivable except when the ages of all these objects are assumed unbelievably short, some 10^6-10^7 years. Nor would small corrugations on a cm scale (Gear and Bastin, 1962; Bastin, 1965) help in the interpretation- these would be levelled out by erosion and substituted by the naturally undulating and small-scale roughness identical with the rest of the surface, so that no anomaly could arise on this account alone.

The young ray craters, like Tycho and Copernicus, in addition to their quality as nocturnal hot spots, have proved to be strong back-scatterers of radar (Gold, 1966). As first noted by Pettengill and Henry (1962), the intensity of radar backscatter from Tycho is some 10-20 times that from the surroundings (at λ_e= 70cm). Partly this is due to greater roughness. The diffuse, non-specular general component of backscatter from the moon (Evans and Pettengill, 1963; Hagfors, 1966) is most plausibly explained by reflections from compact rocky "boulders", similar to those shown on Luna IX and Surveyor I pictures (Figs. 5,6), with dimensions larger than λ_e/π. Similar blocks in greater numbers must be present on the surface and buried among the ejecta of the ray craters. A correction for general roughness; i.e. the more frequent occurrence of large inclinations ~~scattering~~ of the scattering elements than corresponging to normal surface undulation has been attempted by Thompson and Dyce (1966). In this way they separated the component due to the increase in reflectivity (A_r) from that caused by roughness. In such a manner, for craters larger than the resolution limit; corrected values of the dielectric constant are suggested as follows: Aristillus, 4.5; Tycho, 5.2; Copernicus, 6 5. Of the 25 craters which showed radar refelction enhancement, 23 would suggest dielectric constants within this range, or less, among them 7 ray craters, 11 non-rayed craters of Class 1, and 3 non-rayed Class 5 craters (Atlas, Posidonius, and Vitruvius, with lesser enhancement, all within or near the borders of Mare Serenitatis and Mare Tranquillitatis). Two objects, Diophantus and Plinius, both of Class 1 non-rayed, yield extraordinary values of the dielectric constant, 15 and 35, respectively; heavy meteoritic material may be suspected in these cases.

The rest appear to have backscatter characteristics of bare rock. However, it is not necessary to postulate a solid rock surface, neither exposed, or buried under a thin layer of loose material. Rocks of more than λ_e/π = 23 cm in diameter, buried in the upper 5-10 meters of the soil, would act in a similar manner if their projected cross section covers the area; for this, they need not occupy more than 10 per cent of volume of the "boulder bed". Surveyor I pictures suggest this possibility which, in a much weaker degree, exists even in this mare landscape of Oceanus Procellarum (Figs. 5,6).

7. E R O S I O N

A. Surface Modification Processes

In the following sections, a quantitative physical theory of the evolution of the lunar surface under the influence of external cosmic factors is developed. The basis for it is the theory of cratering and encounters, as well as observational data referring to features on the lunar surface and the material contents of interplanetary space. As already could be seen from the preceding sections, independent lines of evidence converge in checking and confirming the predictions. Although not precise, these predictions are supposed to be close approximations, to ± 20-30 per cent in some cases, within a factor of 2 or 3 in others when the quantitative basis is uncertain, as it is with the density of interplanetary matter. It turns out that the present state of the lunar surface can be completely understood in terms of external factors acting alone for all the 4,5 billion years of post-mare existence, any signs of endogenic-volcanic or lava-activity belonging to the initial short pre-mare and mare stage.

Conclusions in the opposite sense are either based on improbable assumptions, on disregard for physical realities, or on qualitative judgment by terrestrial analogy not applicable to the moon.

As an example of the latter, the very interesting article by O'Keefe etal. (1967), "Lunar Ring Dikes from Lunar Orbiter I" may be cited. The argument hinges on the contention that "the slopes are less than the angle of repose of dry rock; hence an explanation in terms of mass wastage is hard to support". Now, in lunar processes of erosion, the angle of repose is irrelevant. It could be decisive when the eroded chips of rock were left lying *in situ*, to roll downhill when the slope is steep enough. The only process on the moon where this could be operative is the destruction of rock by the extreme variation of temperature yet, in the absence of water, it can work only to a very minor extent; otherwise the observed presence of stony blocks and extrusions would be utterly incomprehensible. Actually, however, meteoritic impact (independent of velocity) will disperse the rock fragments over a radius of about 17 km (cf. Section VI C); Flamsteed's rocky ring is about 3 km wide [(O'Keefe et al., 1967), Fig. 1], and the debris will disperse into the engulfing plane without any relation to the slopes of the ring. Granular material settling on the ring will be partly swept out by the impacts in a similar manner, and partly it will drift downhill under the instigation of micrometeorite bombardment at a calculable rate (Section X.B) proportional to the tangent of the slope angle, however small the angle is, independent of friction and without any relation to the angle of repose. Besides, the notion of angle of repose is inapplicable to the fine lunar dust when the cohesion between the grains exceeds their weight (grain diameter less than 0.13 cm). Also, on the photograph of Flamsteed's ring (O'Keefe et al., 1967) little craterlets, witnesses of continuing erosion, are seen though in much smaller numbers than on the surrounding plain; the analogy with the peak and wall of Alphonsus is complete (cf. Section V.E). The ring may be an ancient ring dike of near-mare age although interpretation as the remnant of a raised impact crater lip is much more plausible (cf. Figs. 5,6 and Fig.1); however, the argument about the angle of repose is not only irrelevant, but misleading.

The mechanical processes at work on the lunar surface have been realistically described by Whipple (1959) and Öpik (1962a). These are sputtering by corpuscular radiation, accretion from micrometeoric material, destruction and transport by primary and secondary impacts.

Most of the destroyed mass, much greater than the mass of the impacting bodies, returns to the lunar surface, though not necessarily in the immediate vicinity of the impact. Except for the fallback fraction, it settles on the ground outside the crater covering previous small features with an "overlay". The overlay is subsequently disturbed by micrometeorite and small meteorite impacts, forced to leave elevations and collect into depressions. An equilibrium state between new small craters and their levelling out by erosion establishes itself, the crater profiles becoming flatter with age. This lasts until a large crater erases the traces of previous formations.

Using an ingenious method, Jaffe (1965, 1966a,b) attempted to interpret the profiles of small craters by overlay only. By sprinkling sifted sand on sharp artificial craters, imprinted in sand, the washout of laboratory crater profiles as depending on the added sand layer was compared with the profiles of small craters (5 to 10^4 meters) on Ranger <u>VII</u>, <u>VIII</u>, and <u>IX</u> photographs, and the thickness of overlay was estimated in proportion to crater diameter when the laboratory and lunar crater profiles were similar. In such a manner it was found that "at least 5 meters of granular material, and probably considerably more, have been deposited on Mare Tranquillitatis, Alphonsus, and nearby highland areas, subsequent to the formation of most of the craters 55 meters in diameter or larger", and similar results have been obtained for Mare Cognitum (Jaffe, loc.cit.). It is interesting to note that, despite objections to the validity of the method, Jaffe's figure comes close to the estimate of 14 meters made below for post-mare overlay, calculated a priori from astronomical data and cratering theory. Walker (1966) raised some objections to the method, and others are pointed out here. The profiles of lunar craters change more from erosion (which may carry away an elevation or fill a depression of 20-30 meters in 4.5×10^9 years), and little if at all from overlay. The washout of experimental craters depends on friction and rolling of sandgrains (size about 0.03 cm) which in air are much more mobile than in the lunar vacuum, and for which the angle of repose is decisive when there are no percussions or collisions. The lunar loose material is forced downhill by meteorite impacts as well as by the secondary spray of debris which accounts for the overlay and which at the same time disturbs the grains and sends them downhill. Apparently, the same role was played by the laboratory sandgrains falling on the artificial craters and disturbing by their impacts their surface even when the slope was less than the angle of repose. The agreement between the empirical and the theoretical estimates of overlay is thus not quite as fortuitous as it seems, a certain amount of injected overlay causing a corresponding slumping of the crater profile. It seems that a given overlay of terrestrial sand at terrestrial gravity sprinkled from a small altitude has the same effect as an equal amount of dust and rubble on the moon thrown with much higher velocity on the lunar compacted dust plus direct erosion by a smaller mass of interplanetary meteoric material. As to the apparent increase of the estimated overlay depth with crater diameter suggested by Jaffe's experiments, it can be ascribed to increase in age, craters below 300 meters having existed but for a fraction of the total span of 4.5 billion years and having thus received a smaller sprinkling. At a diameter of 300 meters, Jaffe's figures as plotted by Walker (1966) point to an overlay of 7 meters, at 5m, diameter the overlay is about 0.07m, while in proportion to diameter or age it is expected to be 0.12m; the order-of-magnitude agreement is satisfactory.

B. Sputtering by Solar Wind; Loss and Gain from Micrometeorites

Solar wind bombardment causes the sputtering of atoms from the silicate lattice. From a semi-empirical theory of sputtering, and with a pure proton solar wind flux of 2×10^8 ions/cm^2, sec (Mariner II data) Öpik's (1962b) estimates lead to a sputtering rate of 8×10^{-9} g/cm^2. year. From thorough experimental investigations of sputtering of various materials, Wehner et al. (1963b) arrive at a much better founded sputtering rate for a stony rough surface of 0.4Å or about 1.5×10^{-8}g/cm^2. year, for 2×10^8 protons and 3×10^7 helium ions per cm^2 and sec with energies above the sputtering threshold in the normal solar wind, with allowance for solar storms; this figure will be further adopted. For a pure proton flux Wehner's figure would be 4×10^{-9}g/cm^2. year, or one-half the author's estimate.

About two-thirds of the sputtered atoms are ejected with velocities greater than the velocity of escape from the moon. The annual loss to space from sputtering thus can be set at 1.0×10^{-8}g/cm^2; at a constant solar wind, this would amount to a loss in 4.5×10^9 years of 45g/cm^2, equivalent to a dust layer ($\rho = 1.3$) of 35cm or to 17cm of solid rock. About an equal amount is sputtered inward and contributes to cementation of the dust; the continued stirring and turnover by micrometeorite impact (10^4 years mixing time for the top 1cm layer, Öpik, 1962a) ensures mixing of the irradiated layer with the deeper lunar soil.

Meteorite influx may lead to gain or loss of mass, according to velocity (cf. Section IVA), and to crushing and redistribution of the debris which are ejected from the craters and spread as "overlay" over the surroundings or falling back unto the crater floor. At cosmic velocities of impact, the mass of overlay may be 2-3 orders of magnitude greater than that of the impacting bodies. While secondary ejecta may add to the overlay and its redistribution, the net balance of mass over the entire lunar surface depends of course only on the impacting extraneous mass and its velocity.

From the consideration of energy transfer and vaporization in the central portion ("central funnel") of a meteor crater (Öpik, 1961a, Table 23), the author estimated that below a velocity of 10.7 km/sec, all the impacting mass will remain on the moon at its present gravity; at 20 km/sec, a stony meteorite will cause a loss to space 17 times its own mass, and at 40 km/sec a 44-fold loss occurs.

The first case is that of the micrometeors of the zodiacal cloud (particle radius ≤ 0.035 cm) which thus, at a space density of 2×10^{-21} g/cm^3 and relative velocity $U = 0.187 = 5.6$ km/sec (Öpik, 1956) lead to a gain of 0.01g in one million years (Öpik, 1962a) or 45g in 4.5×10^9 years per cm^2 of the lunar surface. The gain turns out to be equal to the loss from sputtering but, with factors of uncertainty of the order of 2-3 in the assumed rates, the balance is uncertain even as to sign.

Higher velocities are those of meteors and meteorites which thus cause a net loss of mass. They consist of different populations, with different distributions of particle sizes. The ordinary "dustball" meteors, flaking off from comet nuclei and with masses in the range of 10^{-3} to about 10 gram, (evaluated from theoretical luminous efficiency empirically confirmed (Öpik, 1963c)) rapidly decrease in numbers with increasing size so that little mass is contained in the largest categories. The main mass (about 86 per cent) of these "visual" meteors is contained in an "E-component" with asteroidal orbits (Öpik, 1956), and the total influx is estimated at $d\mu_0/dt = 80 \times 10^{-11} g/cm^2$. year, leading to a loss about 20 times this amount or to 7 gram per cm^2 in 4.5×10^9 years.

A more important component of the mass influx represent the "asteroids" of the Apollo group whose frequency exponent, a -2.7 power of the radius, appears to join them into one continuous group from meteorites of 25 to 400cm radius up to bodies in the kilometer range.

From combined observational data (Öpik, 1958a) the mass accretion from this group in grams per cm^2 and year and within the range of radii from R_1 to R_2 (cm) is estimated at

$$d\mu_1/dt = 1.11 \times 10^{-11} (R_2^{0.3} - R_1^{0.3}), \qquad (158)$$

at a density of 3.5 g/cm^3.

Comet nuclei, according to the same source contribute (at density 2.0 g/cm^3)

$$d\mu_2/dt = 1.55 \times 10^{-14} (R_2^{0.8} - R_1^{0.8}), \qquad (159)$$

and Mars asteroids deflected by perturbations, at density 3.5g/cm^3, give

$$d\mu_3/dt = 1.27 \times 10^{-18}(R_2^{1.4} - R_1^{1.4}). \qquad (160)$$

These accretions correspond to differential number fluxes at the lunar surface per cm^2 and year and interval dR according to

$$dN/dt = CR^{-n}dR, \qquad (161)$$

with $C_1 = 2.26 \times 10^{-13}$, $n_1 = 3.7$; $C_2 = 1.48 \times 10^{-15}$, $n_2 = 3.2$; $C_3 = 1.22 \times 10^{-19}$, $n_3 = 2.6$. All the fluxes and accretions are insignificant at small radii (as compared to the visual meteors), so that $R_1 = 0$ can be assumed. For an upper limit of crater diameter of about 200 km, $R_2 = 5 \times 10^5$cm, equations (158), (159), and (160) yield comparable values,

$$d\mu_1/dt = 5.6 \times 10^{-10},\ d\mu_2/dt = 5.6 \times 10^{-10},\ d\mu_3/dt = 1.2 \times 10^{-10},$$

and with the 'visual" dustball meteors contributions 8×10^{-11}, the total mass influx becomes 1.32×10^{-9} g/cm^2. year). With a 30-fold loss ratio as the mean for impact velocities of 20 and 40 km/sec, the loss to space from these components would amount to 178 g/cm^2 in 4.5×10^9 years. This appears to be the dominant component; within the uncertainty of our estimates this represents also the net mass loss to space from ~~micrometeorites and sputtering by solar wind mutually~~ the lunar surface, accretion from micrometeorites and sputtering by solar wind mutually cancelling out.

Most of the loss is accounted for by large cratering events and, thus, affects crater interiors without directly influencing those portions of the surface between the craters. The loss from the average surface, undisturbed by the localized large cratering events, must be calculated to a crater diameter of 300 meters or $R_2 = 7.5 \times 10^2$cm which is the limit of erosion or levelling out of the craters during the total age of the moon. This yields now

$d\mu_1/dt = 8 \times 10^{-11}$, $d\mu_2/dt = 3 \times 10^{-12}$, $d\mu_3/dt = 1.4 \times 10^{-14}$, plus $d\mu_0/dt = 8 \times 10^{-11}$ from the visual dustballs.

With a loss factor of 17 for μ_1 and μ_3, and one of 44 for μ_2 and μ_0, a total loss from the surface undisturbed by large surviving craters ($\beta_0 > 300$m) becomes 5.0×10^{-9} g/cm^2 per year or 23 g/cm^2 in 4.5×10^9 years. This is practically the effective loss from meteorite impact, for an outwardly "level" surface outside the boundaries of large craters if sputtering by solar wind is assumed to be balanced by the gain from micrometeorites. Whatever uncertainty is involved in this figure, it shows the order of magnitude of the very small changes in the mass load of the lunar surface as caused by external factors. These are very much smaller than those due to redistribution of mass through cratering.

The most important component in the external mass exchange is the influx from micrometeorites, 45 g/cm^2. Although an at least equivalent amount of mass, 45 g/cm^2 from solar wind and 23 g/cm^2 from meteorite impact, is sputtered back to space, this does not mean that the micrometeoric material is immediately lost again. Before being subjected to sputtering, it becomes mixed with 10-30 times its mass of overlay debris, ejected from the bedrock by meteorite impacts (see next subsection), and the material sputtered to space would contain only some 3-10 per cent of micrometeoric material. With the figures of external mass exchange as estimated above, over 4.5×10^9 years there is a gain of 45 g/cm^2 from micrometeors, and a loss of 45 + 23 = 68 g/cm^2, of which only 2-7 g/cm^2 would belong to micrometeorites. In such a case the present lunar surface should contain some 40 g/cm^2 ($\pm$) of micrometeoric origin, admixed to, and diluted in, the overlay debris or the "dust" layer.

C. Overlay Depth

Much more important than intrinsic gain or loss is the material crushed and thrown about by cratering impacts; this may exceed several hundred times the infalling mass. From the crater bowl excavate by the impact it is ejected to distances of tens or more kilometers from the crater, where it settles as "overlay", a mixture of dust, rubble, and boulders which is subject to further modification by meteor and radiation bombardment, to form what we have called the lunar soil or "dust" layer. The average distances of ejection depend essentially on the strength of the material [equations (4), (16), (19), (27), (45)] and are thus greatest for impact into bedrock, while insignificant for most of the stirred-up mass of dust. In large craters, when the distance of ejection is of the order of the crater radius, most of the debris falls back into the crater bowl where overlay may attain a thickness of several kilometers. For the post-mare cratering impacts as represented by Table XV, the thickness of overlay (as due to the single impact) in central portions of the crater is

$$\Delta Z = B_o (P/D - 0.625\ H/B_c)$$

Table XXIV shows the thickness of overlay in post-mare craters.

TABLE XXIV

Thickness of Central Overlay, ΔZ, From Fallback in Post-Mare Craters

B_o (diameter), km	2.2	4.5	22	44	210
ΔZ, asteroidal impact, meters	8	34	780	2500	23000
ΔZ, cometary impact, meters	1.8	6	230	840	10800

Undoubtedly, pressure compaction takes place when the thickness of the layer is great; except its topmost layer, it cannot be regarded as just loose rubble or dust.

Outside the crater rim, massive ejecta may be reaching over a fringe of about 8-17 km (cf. Section II.C); at 9 km beyond the rim, the thickness of ejecta can be roughly estimated to be one-eigth of ΔZ which leads to thick overlay in the vicinity of large craters, and a neglibible one near small craters. ~~There are but few.~~ The distribution of overlay must be extremely spotty, following the pattern of the distribution of craters larger than 10 km in diameter, and with a more or less uniform "background" of area not disturbed by the vicinity of large craters (the areas being removed by more than 15-30 km from the nearest rim of a crater 20-100 km in diameter).

These considerations apply chiefly to the maria where a pre-existing rocky (lava) base has been subjected to destruction by impacts. In the continentes the crust appears to be completely formed by accretion of overlay during the pre-mare stage, any earlier maria surfaces of the accreting moon being buried under the final shower of overlay.

The formation of overlay has been in principle described by Whipple (1959) and Öpik (1960, 1962a). There are two kinds of processes at work; (1) all impacting bodies and radiations contribute to modification (grinding, cementation), mixing and displacement of the existing overlay or "dust" layer; (2) only those meteorites large enough to penetrate the layer contribute to erosion of the bedrock and are instrumental in adding new material to, and increasing the thickness of, the layer. Hence the growth of the layer with time becomes slower as its thickness and the inferior size limit of the active meteorite population increases.

In addition to primary impacts, secondary and higher order contribute to overlay. At first we will consider only post-mare primary impacts on an initially hard surface, supposed to be solidified lava, of a strength about that of terrestrial igneous rocks (cf. Section V.C).

Let X (cm) be the thickness of overlay, p [equation (6)] the relative penetration in a layer of infinite thickness at $\gamma = z = 45^\circ$ (as an average), R the radius of the projectile. Although the velocity of the projectile decreases at penetration, its flattening at hypervelocity events increases the cross section area, so that loss of momentum can be assumed roughly proportional to depth of penetration. Hence the fraction of momentum retained after penetration of the dust layer is

$$\eta = 1 - X/(2pR). \tag{162}$$

The condition $\eta \geq 0$ yields a minimum radius for penetration that reaches the bedrock,

$$R_o = X/2p \tag{163}$$

Only projectiles with $R > R_o$ are capable of eroding the bedrock. An infalling mass $\Delta\mu$ at radius R produces a mass of overlay

$$\Delta M = \Delta\mu \cdot (M_c/\mu) \cdot \eta \tag{164}$$

where M_c/μ is given by equations (24), (3), (7).

Micrometeorites and visual meteors are too small to penetrate the dust layer and do not contribute significantly to overlay (except at the very beginning, when incident on a bare rocky surface). For the remaining three components, $\Delta\mu$ is to be substituted by $\frac{d}{dR}(d\mu/dt) \cdot dR$ with $R = R_2$, R_1 = const.

as given in (158), (159), (160), and equation (164) integrated from $R_1 \geqslant R_0$ [equation (163)] to an upper limit R_2. For the main background, unaffected by the vicinity of large craters, we assume an upper limit of crater diameter B_0 = 2.48 km and $R_{2} = B_0/2D$ (cf. Table XV) for which the mean spacing in Mare Imbrium is $(4.65 \times 10^5/207)^{\frac{1}{2}}$= 47 km, about the double of the extreme flight distance of massive ejecta from hard bedrock. Ejecta from craters up to this limit will have by now produced a more or less uniform overlay X_0, with little spottiness. The ejecta from larger craters from B_0 = 2.48 km to B_0 = 44 km, or from corresponding larger projectiles (from R_{2} to R_M = 44/D km) will cause locally much deeper overlay which, spread uniformly over the entire area, would amount to an average layer X_1; however, for these larger projectiles, loss of momentum in equation (162) is to be calculated with $X = X_0$, not X_0+X_1, because of the spottiness and low probability of coincidence of the major impacts. Actually, for these latter, R is so large that η = 1 can be assumed for the present and past state of the lunar surface. The upper limit B_0 = 44 km for major craters is that for which throwout is about 50 per cent of the total detritus. For still larger craters, most of the overlay remains in the crater, forming an average layer 1/5-1/3 of ΔZ as given in Table XXIV; it must be treated as purely local enhancement, and there is no point in calculating its contribution to the average depth of overlay elsewhere.

For the three components of meteorite influx, the following numerical constants have been assumed:

for Apollo group [equation (158)] and Mars asteroids (160), δ= 3.5 $\bar{W}_0$= 20 km/sec, p= 2.88 (at ρ = 1.3, A_ρ= 2 x 10^8 as for the dust layer), $R_0 = X_0/5.76$, R_m = 8.3 x 10^3cm, R_M = 1.5 x 10^5cm, M_c/μ = 232; for comet nuclei (159), δ= 2.0, W_0 = 40 km/sec, p=2.28, R_0=X_0/4.56, R_M= 4.66 x 10^6cm, R_m = 8.35 x 10^4cm, M_c/μ = 637. After integration with these data of equation (164), separately from R_0 to R_m and from R_m to R_M, with $dX = dM/\rho = \Delta M/1.3$ as for the overlay rubble of assumed density 1.3, and omitting small irrelevant terms, the a priori calculated rate of growth of background overlay from primary meteorite impact (craters smaller than 2.5 km) in a lunar mare (solidified lava as the bedrock), in cm/year (at density 1.3g/cm^3), as listed separately for the three components. becomes

$dX_o/dt =$

$$\left.\begin{aligned} &= 2.97 \times 10^{-8} - 1.67 \times 10^{-9} X_o^{0.3} && \text{(Apollo group)} \\ &+ 6.55 \times 10^{-9} - 8.96 \times 10^{-12} X_o^{0.8} && \text{(Comet nuclei)} \\ &+ 7.0 \times 10^{-11} && \text{(Mars asteroids)}, \end{aligned}\right\} \quad (165)$$

and the annual rate of smoothed-out growth from major impacts (craters from 2.5 to 44 km diameter) equals

$dX_1/dt =$

$$\left.\begin{aligned} &= 4.10 \times 10^{-8} && \text{(Apollo group)} \\ &+ 6.57 \times 10^{-8} && \text{(Comet nuclei)} \\ &+ 3.94 \times 10^{-9} && \text{(Mars asteroids)}. \end{aligned}\right\} \quad (166)$$

Integration of (165) (in which the negative terms are not very significant, reducing the outcome by only 10 per cent) yields, for $t = 4.5 \times 10^9$ years, a background overlay of $X_o = 147$ cm from primary impacts alone; to this is to be added a spotty overlay from the larger craters (2.5 - 44km) of average thickness $X_1 = 468$cm (184cm from Apollo group, 266cm from comet nuclei, 18cm from Mars asteroids). The total average overlay from primary impacts, calculated a priori from cratering theory and astronomical data, is $X_o + X_1 = 615$cm or 800 g/cm^2 (at density 1.3); because of the spottiness, the figure has not a very definite meaning.

Secondary impacts probably contribute very little to craters over 2.5km in diameter, and the value of X_1 should not need any correction in this respect. As to X_o, the contribution from secondary impacts by large ejecta from the larger craters must be considerable.

There exists a direct empirical method of evaluating the thickness of overlay, based on the volume actually excavated by observed craters in a mare. While the crater diameters are directly measured, for the depth to diameter ratio, $p/D = x_p/B_o$, the average theoretical values (diameter range 2.5-44km) of 0.1105 (Apollo group) and 0.0569 (comet nuclei) will be assumed, according to Table XV, weighted in a ratio of 1 to 3, so as to give a volume ratio proportional to the calculated values of overlay X_1, 184/266 = 1/1.45; in other words, it is assumed that, within the chosen diameter range, there are three cometary craters to one of the Apollo group. This gives an average ratio $x_p/B_o = 0.0703$. Further, doubling the volume as for surface ejecta of density 1.3 originating from bedrock of density 2.6 (however for thick overlay or fallback, the doubling is not justified, as the material is compressed under its own weight), equation (15) yields the volume of ejecta as

$$V_e = 0.0344\ B_o^3 . \qquad (167)$$

The thickness of overlay averaged over area S is then

$$X_A = \sum V_e / S . \qquad (168)$$

Öpik's (1960) counts in Western Mare Imbrium yield thus "observed" values of overlay as represented in Table XXV.

All craters of the area except Archimedes are included; Archimedes as a pre-mare crater (B_o = 70.6km) is omitted. The cumulative number of craters in the third column is from largest (∞) down to the given limit, while the cumulative thickness of overlay in the fifth column is counted in the opposite direction from 2.48 km up. In the last column, the average separation of the craters at given cumulative number, N, calculated from $(S/N)^{\frac{1}{2}}$, is given. This characterizes the spottiness of overlay; little will spread beyond a radius of $\frac{1}{2}B_o$ + 20km from the center of the crater or roughly, beyond an average separation of B_o + 40km. Thus the large contributions to X_A beyond B_o > 21.4km are localized to a fraction less than (61.4/241) = 0.065 of the area and are not characteristic of the background but largely depend on single major impacts. As the figures stand, for the diameter limits 2.5-44km, the averaged observed overlay is X_A = 1489cm, to be compared with the value of X_A = 468cm as calculated above theoretically for primary impacts only. The difference may be partly due to some secondary craters larger than 2.5km in the Copernicus and Eratosthenes rays, but mainly it is the manifestation of the excess in the true number of large craters above that calculated from the present population of interplanetary stray bodies, as persistently revealed also in crater statistics (Table XVII). Although due to a few individuals, the excess is always there, and essentially in the same proportion, such as in more extended counts on an 8 times larger area (Table XVIII); these counts as presented by Baldwin (1964 b) agree so closely with those in Western Mare Imbrium that no revision of Table XIV is necessary.

TABLE XXV

Overlay (X_A) from Large Craters (>2.5 km) in Western Mare Imbrium, averaged over S = 465,000 km^2

B_0 Crater Diameter, km	Number n interval	Number N cumulative	ΔX_A cm	X_A cumulative, cm	Average separation km
2.48		207		0	47
	97		14.1		
2.92		110		14	65
	36		8.3		
3.35		74		22	79
	21		8.0		
4.10		53		30	94
	19		15.1		
5.40		34		46	117
	9		14.6		
6.70		25		60	136
	7		20.4		
7.99		18		80	161
	3		15.4		
9.72		15		96	176
	6		62.2		
12.7		9		158	227
	0		0		
16.6		9		158	227
	1		50		
21.4		8		209	241
	4		432		
27.0		4		647	340
	2		423		
34.3		2		1064	480
	1		425		
43.0		1		1489	680
	1		888		
55.5		0		2377	-
	0		0		
∞	–	–	–	2377	..

TABLE XXVI

Observed and Calculated Overlay (X_1) from Large Craters (>2.5 km) in Western Mare Imbrium, averaged over S = 465,000 km^2

	X_1 Calculated (cm)				X_1 Observed (cm)
Crater Diameter, km	Apollo group	Comet nuclei	Mars asteroids	All	
2.48–5.40	37	27	1.0	65	46
2.48–21.4	124	140	6.8	271	209
2.48–43.0	184	266	18	468	1489
21.4–43.0	60	126	11	197	1280

In Table XXVI, averaged overlay from primary impacts, calculated from interplanetary data for different crater size limits is compared with the observed values on the moon derived from crater volume. It can be seen that the figures are in reasonable agreement except for craters larger than 21 km where there is a significant [illegible] craters being observed instead of 1.2 predicted for this range.

The discrepancy has little bearing on the general overlay background between the craters, determined by the contributions from smaller craters for which reasonable accord is expected as shown by the data of Table XXVI.

The data of Tables XXV and XXVI show the average thickness of overlay if the ejecta were spread uniformly over the entire area. Actually no such uniformity can take place; most of the ejected mass comes from the sparsely distributed large craters whose separations greatly exceed the ejection range. The distribution of overlay must therefore be extremely spotty, following the distribution of large craters in whose vicinity the thickness of the layer must by orders of magnitude exceed that of the average background.

A schematic representation of the distribution of overlay can be obtained by assuming an effective radius L_m of spread of the ejecta around the crater center and by distributing uniformly the ejected mass over an area of πL_m^2. With the assumed elastic parameters of lunar rock as in Section II.F, the flight distance at y = 0.5 (half mass of crater) is 8.8 + 0.35 D_o (km) from crater center, and at y = 0.25 (quarter-mass or half-distance from center of crater) ~~it is~~

it is 18.5 + 0.25 B_o(km). An average can be assumed,

$$L_m = 15 + 0.3 B_o \text{ (km)}. \qquad (169)$$

With this and the data of Table XXV, the frequency distribution of overlay thickness in a mare has been calculated as shown in Table XXVII. The values are based on the actual crater statistics in Mare Imbrium but for an average basic overlay of B (as explained below) being added, due to craters less than 2.48km in diameter. Figure 10 represents this very uneven distribution graphically. The thickness values are

TABLE XXVII

Distribution of Overlay Thickness in Lunar Maria as based on Volume and Range of Ejecta

Thickness, meters	13	14.5	18.5	23	29	39	60	180	330	550	880	1470
Percentage Area	61.7	22.6	7.1	1.7	1.4	0.6	1.4	0.3	1.3	0.8	0.5	0.6

averages over intervals of the crater statistics for Mare Imbrium (which is representative of all lunar maria, cf. Tables XVII and XVIII).

Were primary impacts only to be considered, the basic overlay would have been expected to be equal to X_o= 147cm as calculated above for craters below 2.5km. However, ejecta from secondary craters are making a very much larger contribution in the small diameter range, increasing the thickness of the overlay and, by its protective action, decreasing the role of the very small primary impacts.

We shall use as typical the actual counts of small craters in Mare Cognitum, as derived from Ranger VII photographs by Shoemaker (1966); from his curve on Fig. 2-42, loc.cit., cumulative crater numbers at various diameters were taken (dots on full line). The curve, after a marked twist upwards below B_o = 1.2km, interpreted as due to secondaries bends sharply down below $B_o = B_1$ = 285 meters. This can be plausibly attributed to erosion, B_1 being the diameter eroded in 4.5×10^9 years and the lifetime, as well as the number of smaller craters presently surviving being proportional to B_o/B_1. The counted numbers for $B_o < B_1$ must thus be multiplied by the erosion factor

$$E_i = B_1 / B_o, \qquad (170)$$

to allow for eroded craters which are no longer there but whose ejecta may have contributed to the overlay.

The cumulative number of primary impacts per $10^6 km^2$ and 10^9 years is assumed according to (161), after integration and with the proper constants, with R in cm:

$$\log N_a = 11.921 - 2.7 \log R_a \qquad (171)$$

for Apollo group or meteorites,

$$\log N_c = 9.828 - 2.2 \log R_c \qquad (172)$$

for the comet nuclei, while the contribution from Mars asteroids is negligible within the range considered. As in Table XV, $2R_a = B_o/14.9$ and $2R_c = B_o/26.6$ as for interplanetary stray bodies impacting on hard rock.

The adopted crater statistics are collected in Table XXVIII.

~~Cumulative Crater Number per $2.22 \times 10^5 km^2$.~~ N observed, Mare Cognitum according to Shoemaker (1966)*; N_a, N_c, primaries on hard ground, calculated; B_o, lower limit of crater diameter.

* Shoemaker gives his crater densities "per $10^6 km^2$ and 10^9 years ", introducing the hypothetical element of an age of 4.5×10^9 years and a uniform incidence into his straightforward counts. If the total age is more or less correct, the effective age is shorter on account of erosion, at least for the smaller craters (cf. Table XXIX). His ~~figures are actually counted numbers per $10^6/4.5 km^2$.~~

From the equations of Section II, the geometric parameters of cratering in two characteristic media - the hard bedrock, and the rubble of overlay, are determined as follows.

It will be found that, in the range below 2.5km, secondary craters are the main contributor to overlay; also, in the smallest class of craters, the Apollo-meteorite group prevails among primaries, while in the larger classes the comet-nuclei group is more prominent (cf. Table XXVIII). A simplification is therefore admissible, in assuming an equal proportion of the two groups among primaries. This gives an average of $x_p/B_o = 0.0837$ and, instead of (167), a volume of ejecta from unprotected hard rock (cf. Equation (15))

$$V_e'^{*} = 0.0204\ B_o^3 \qquad (173a)$$

for the primaries. On the other hand, overlying rubble will prevent, partially or totally, the projectile striking the underlying bedrock; this condition is most critical for the smallest projectiles among which the Apollo group prevails. For this group, with $w_o = 20 km/sec$, $\gamma = 45^o$, $\delta/\rho = 2$ and $\lambda_c = 6 \times 10^7$, $\lambda_p = 2 \times 10^8$ about, as for

T A B L E XXVIII

Cumulative Crater Numbers per 2.22×10^5 km^2 : N observed, Mare Cognitum according to Shoemaker (1966)*; N_a, N_c, primaries on hard ground, calculated; B_o, lower limit of crater diameter

log B_o (meters)	1.247	1.636	1.947	2.270	2.512	2.716	2.935	3.071	3.282	3.536
logN obs.	7.332	6.590	6.000	5.414	4.758	4.071	3.402	2.873	2.437	1.798
log R_a, cm	1.775	2.162	2.473	2.796	3.038	3.242	3.461	3.597	3.808	4.162
log R_c, cm	1.521	1.910	2.221	2.544	2.786	2.990	3.209	3.345	3.556	3.910
log(N_a+N_c)	7.220	6.212	5.483	4.609	4.010	3.512	2.984	2.659	2.164	1.338
N_a /N_c	4.48	2.86	2.01	1.39	1.05	0.83	0.64	0.55	0.43	0.29

* Shoemaker gives his crater densities "per 10^6 km^2 and 10^9 years", introducing the hypothetical element of an age of 4.5×10^9 years and a uniform incidence into his straight-forward counts. If the total age is more or less correct, the effective age is shorter on account of erosion, at least f for the smaller craters (cf. Table XXIX). His figures are actually counted numbers per $10^6/4.5$ km^2.

TABLE XXIX

Calculation of Maria Overlay (X) (at density 1.3 g/cm^3) from Ejecta of Craters smaller than 2.5 km

(Superior numbers indicate decimal power factors, thus $3.62^5 = 3.62 \times 10^5$)

B_o, av., meters	2190	1500	1010	759	590	462	366	283	214
n_o observed (per 2.22×10^5 km^2)	107	472	1770	2920	6400	1.41^4	3.14^4	6.5^4	1.37^5
E_f	1	1	1	1	1	1	1	1.04	1.33
n_c corrected (per 10^6 km^2, 10^3 yrs.	107	472	1770	2920	6400	1.41^4	3.14^4	6.8^4	1.82^5
Part (A) Upper limit of overlay: all impacts on unprotected hard rock									
n_p primary, calculated	69	310	508	806	1480	2520	4470	1.02^4	2.02^4
$n_s = n_c - n_p$, secondary	38	162	1262	2114	4920	1.16^4	2.69^4	5.8^4	1.62^5
ΔX_p, (4.5×10^9 yrs.) cm	13	19	10	6	6	5	4	4	4
ΔX_s, (4.5×10^9 yrs.) cm	38	51	125	89	97	110	127	128	153
$X = \sum \Delta X$	51	121	256	351	454	569	700	832	989
Rubble penetr. I_p primaries (m)	169	116	78	59	46	36	28	22	16.6
Rubble penetr. II_s secondaries (m)	790	540	370	270	210	170	133	102	78
Part (B) Assumed: Present Overlay thickness = 12 meters and uniform accretion with time									
Aver. age t_f, in units of 4.5×10^9	0.5	0.5	0.5	0.5	0.5	0.5	0.5	0.48	0.38
Aver. overlay X_a in meters	6.0	6.0	6.0	6.0	6.0	6.0	6.0	6.2	7.4
n_p primary calcul.	70	319	540	907	1750	3280	6250	1.85^4	4.76^4
$n_s = n_c - n_p$, secondary	37	153	1230	2010	4650	1.08^4	2.49^4	4.95^4	1.34^5
η_p (efficiency primaries)	1.00	1.00	0.99	0.99	0.98	0.97	0.95	0.93	0.87
η_s (efficiency secondaries)	1.00	1.00	1.00	1.00	1.00	1.00	1.00	1.00	0.99
New Overlay									
ΔX_p, cm (primaries)	13	20	10	7	7	6	6	7	8
ΔX_s, cm (secondaries)	37	48	122	85	92	102	117	109	125
$X = \sum \Delta X \longrightarrow$, cm	50	118	250	342	441	549	672	788	921
Total Present Rate of Ejecta, cm per 4.5×10^9 yrs. (from overlay + bedrock)									
$d/dt\ \Delta X_p$, cm	13	20	10	7	7	6	6	8	9
$d/dt\ \Delta X_s$, cm	37	48	122	85	92	102	117	109	127
$d/dt\ X$, cm	50	118	250	342	441	549	672	789	927

262

TABLE XXIX (cont'd.)

Calculation of Maria Overlay (X) (at density 1.3g/cm³) from Ejecta of Craters smaller than 2.5 km

(Superior numbers indicate decimal power factors; thus $3.62^5 = 3.62 \times 10^5$)

B_o, av. meters	164	129	100	79	62	49	37	28	20
n_o observed (per $2.22 \times 10^5 km^2$)	1.47^5	2.32^5	3.62^5	5.7^5	9.0^5	1.41^6	2.98^6	5.4^6	9.4^6
E_f	1.73	2.22	2.85	3.63	4.60	6.56	7.64	10.3	13.9
n_c corrected (per $10^6 km^2$, 10^9 yrs.	2.54^5	5.15^5	1.03^6	2.07^6	4.14^6	9.26^6	2.28^7	5.56^7	1.31^8
Part (A) Upper limit of overlay: all impacts on unprotected hard rock									
n_p primary, calculated	3.88^4	7.7^4	1.48^5	2.28^5	3.99^5	7.0^5	1.91^6	4.15^6	9.0^6
$n_s = n_c - n_p$, secondary	2.15^5	4.38^5	8.82^5	1.84^6	3.74^6	8.56^6	2.07^7	5.14^7	1.22^8
ΔX_p, (4.5×10^9 yrs.) cm	.3	3	4	2	2	.2	2	2	1
ΔX_s, (4.5×10^9 yrs.) cm	91	91	89	87	86	97	101	109	94
$X = \sum \Delta X$	1083	1177	1266	1355	1443	1542	1665	1756	1851
Rubble penetr. h_p primaries (m)	12.7	10.0	7.8	6.1	4.8	3.8	2.9	2.2	1.5
Rubble penetr. h_s secondaries (m)	60	47	35	29	22	18	13.4	10.1	7.3
Part (B) Assumed: Present overlay thickness= 12 meters and uniform accretion with time									
Aver. age t_f, in units of 4.5×10^9	0.29	0.23	0.20	0.14	0.11	0.08	0.07	0.05	0.04
Aver. overlay X_a in meters	8.5	9.2	9.6	10.3	10.7	11.0	11.2	11.4	11.5
n_p primary calcul.	1.49^5	3.77^5	8.14^5	1.25^6	2.19^6	3.85^6	1.05^7	2.28^7	5.0^7
$n_s = n_c - n_p$, secondary	1.05^5	1.38^5	2.16^5	8.2^5	1.95^6	5.41^6	1.23^7	3.28^7	8.1^7
η_p (efficiency primaries)	0.78	0.62	0.48	0.38	0.30	0.24	0.18	0.14	0.09
η_s (efficiency secondaries)	0.99	0.98	0.97	0.96	0.93	0.89	0.80	0.63	0.46
New Overlay									
ΔX_p, cm (primaries)	9	9	7	4	3	2	2	1	1
ΔX_s, cm (secondaries)	44	29	20	37	42	55	48	44	29
$X = \sum \Delta X \longrightarrow$, cm	974	1012	1039	1080	1125	1182	1232	1277	1307
Total Present Rate of Ejecta, cm per 4.5×10^9 yrs. (from overlay + bedrock)									
$d/dt\ \Delta X_p$, cm	12	15	15	11	10	8	10	9	7
$d/dt\ \Delta X_s$, cm	45	30	21	39	45	61	60	70	62
$d/dt\ X$, cm	984	1029	1065	1115	1170	1239	1309	1388	1457

desert alluvium, ρ=2.17, D= 28.0, D/ρ = 12.9, the penetration into an unlimited layer of rubble in a primary impact becomes

$$x'_p = B_o / 12.9. \qquad (174a)$$

For the secondaries, only those of high velocity as in the rays of ray craters being important (the penetrating low velocity ejecta are unable to crush the bedrock; they as well as the non-penetrating ones are only able to produce craters in the overlay; cf. Table XXXV D below) we assume W_o = 0.75 km/sec, γ = 45°, δ = 2.6. At impact of secondaries upon bedrock,

$$x''_p / B_o = 0.439, \qquad (175)$$

and from (15) the volume of ejecta from unprotected hard rock becomes

$$V_e'' = 0.1070\ B_o^3. \qquad (173b)$$

The relative penetration of secondaries into rubble is then

$$x''_p = 0.352\ B_o. \qquad (174b)$$

With 1.3 as the density of overlay or one-half that of the bedrock, and n_i the number of impacts per 10^9 years upon an area of S = 10^6 km^2 = 10^{12} m^2, the contribution to overlay thickness in 4.5 billion years from a given group of craters (B_o) equals

$$\Delta X = 2V_e \cdot 4.5 n_i / S \qquad (176)$$

For the primary craters this becomes

$$\Delta X_p = 1.84 \times 10^{-11}\ n_p B_o^3, \qquad (177a)$$

and for the secondaries

$$\Delta X_s = 9.63 \times 10^{-11}\ n_s B_o^3 \qquad (177b)$$

in cm per 4.5×10^9 years when B_o is given in meters; both equations are provisionally disregarding the protective layer of the overlay itself and represent thus upper limits.

In the four upper lines of Table XXIX the basic cumulative crater numbers of Table XXVIII are broken up into discrete data, interpolated for more or less comparable (not quite constant) logarithmic intervals of B_o; the median values of crater diameter are given in the first line, the observed differential numbers in the second, the erosion factor E_f in the third, and the rates of impacts per 10^6 km^2 and 10^9 years as corrected for erosion in the fourth line.

In the following Part (A) of Table XXIX the data are interpreted conventionally by disregarding the braking action of the overlay. While the total cratering rate n_c in the 4th line may be considered independent of this action of overlay, being based on purely empirical data, the number n_p of primary impacts (6th line) does depend on our conventional assumption, as this determines the ratio of projectile to crater diameter, thus the size and the number of projectiles. ~~will~~ With the rubble layer, smaller projectiles will produce craters of a given size and, thus, there will be more primary impacts and, after substracting their number, the difference yields fewer secondaries. As these latter chiefly contribute to the overlay (lines 8 and 9 of the table), the overlay in Section A represents an over-estimate. Even as the figures stand, new overlay cannot be produced when its thickness exceeds the imaginary "depth of penetration", into rubble (lines 11 and 12 of the table) or the crater depth in rubble of infinite thickness at crater diameter B_o. The penetrations are given by

$$H_p = B_o/12.9 \tag{178a}$$

for the primaries, and

$$H_s = 0.352\ B_o \tag{178b}$$

for the secondaries. These quantities are independent of the radius of the projectile and depend on crater diameter only. In Part A this takes place at $B_o < 49$ meters, whence a rough upper limit for overlay thickness of about 16 meters follows. This compares favorably with the estimate of 13-17 meters at a particular spot in Oceanus Procellarum, made in Section V.C from Surveyor I pictures of an eroded boulder wall of an ancient crater (Figs. 5,6).

Part (B) of Table ~~XXIX~~ represents a more sophisticated calculation for an assumed overlay thickness of 12m at present. The thickness is assumed to grow uniformly with time, average values instead of differential equations being used henceforth. In Part (B), the first line gives the average age, in units of 4.5 billion years, of the presently surviving craters, calculated from

$$t_{\varsigma} = 1/2 L_{\varsigma} \tag{179}$$

and the second line contains the average overlay thickness at the time of impact,

$$X_a = 12(1-t_{\varsigma}) \tag{180}$$

in meters.

When overlay thickness exceeds "rubble penetration",

$$X \geqslant H_{p}'s \quad , \tag{181}$$

the bedrock is untouched and no increase of overlay takes place. For the primaries in this case $D = 28.0$, $2R_p = B_o/28.0$. For unprotected bedrock or $X = 0$ the figures are $D = 14.9$, $2R_p = B_o/14.9$, which also is the case of Part (A) of the Table. For a given crater diameter, the radius, and thus the predicted number of impacting projectiles is different according to the kind of target. With the logarithmic intervals for B_o or R in Table XXIX, the frequency index is the same as for cumulative numbers, n-1 according to integration of (131). For Apollo group the index is thus 2.7, and the ratio of primary incidence in the two cases is

$$(28.0/14.9)^{2.7} = 5.50 \ .$$

Thus, when (181) is valid, or for $B_o \leqslant 120$m in Part (B) of the table, the primary incidence will be 5.5 times that given in Part (A). The incident mass, however, contains an additional factor of F^3, and thus decreases with the 0.3 power, in a ratio of

$$(14.9/28.0)^{0.3} = 0.83.$$

When (181) is not fulfilled, two-layer cratering takes place. Instead of a complicated analysis, we simply use an interpolation formula between the two extremes for $B_o \geqslant 120$ meters in Part (B):

$$n_p = n_A \left[1 + 4.5\ (120/B_o)^2\right] \tag{182}$$

whereas for $B_c \leqslant 120$m, $n_p = 5.5n_A$ is to be assumed. Here n_A is the value of n_p in Part (A). The calculated values of average incidence rates are given in the 3rd and 4th lines of Part (B). These are incidence rates of projectiles of the same average size that have produced the observed craters, although in the past the craters in each class - and not the projectiles - may have been smaller because of less overlay and more hard bedrock involved.

Equations (177a) and (177B) require certain additional efficiency factors, η, to allow for the average fraction of bedrock crushed as depending on overlay thickness, and on the time t_p during which penetration to bedrock level was possible. Two cases present themselves.

For a given overlay thickness X and potential penetration H_p, the condition must be fulfilled that at $X/H_p \geqslant 1$, $\eta = 6$ and at $X/H_p = 0$, $\eta = 1$.

206

We assume thus the individual efficiency in the second case as

$$\eta = 1 - (X/H_p)^2, \tag{183}$$

and the average over the entire time of existence of the mare (4.5×10^9 yrs.), for which $X_a = 6$ meters,

$$\eta_1 = 1 - (6/H_p)^2 \tag{183a}$$

In the first case, when the layer is thicker than average penetration, penetration stops after a relative time interval

$$t_p = H_p/12 \tag{184}$$

(H_p being given in meters) during which the average $X_a = \frac{1}{2}H_p$. Substituting this into (183) and multiplying by t_p, the efficiency of ~~Part (B)~~ the average, as compared to ~~Part (A)~~ the initial, becomes

$$\eta_2 = H_p/16. \tag{183b}$$

(For secondaries, use H_s for H_p).

These efficiencies and the corresponding differential overlay accretions, are given in the 5th to 8th lines of Part (B) of Table XXIX.

The 9th line of Part (B) of the table contains the cumulative accretion of new overlay, in centimeters at density 1.3 for the total time span of 4.5×10^9 years until present. Extrapolation toward smaller crater diameters ($B_o < 20$ meters) will not yield much, on account of the rapid decrease of H_p, t_p, and η. A total extrapolated overlay thickness for Part (B) must be close to X = 14 meters, while the starting assumption was X = 12 meters. The solution is practically self-consistent. X = 13 meters can be assumed as an average thickness of overlay (density 1.3) in the maria on regions removed from the vicinity of large craters, consistent with the observed volume and number of craters and not critically depending on theory and interpretation. This agrees remarkably well with the estimate from the Surveyor I picture (Fig.6) (cf. Section V.C) and is not in contradiction with more crude estimates by Jaffe (1965,1966,1967) which point to an overlay thickness of 5-10 meters. Besides the accretion of new overlay from an environmental standpoint of interest may be the total influx rate of overlay material, new from the bedrock and old stirred up from the existing layer of overlay. i.e. the accretion rates when setting $\eta_p = \eta_s = 1$. The rates are given in the 10th, 11th and 12th lines of Table XXIX (B). Extrapolation to smaller crater sizes (45m) would yield about 2000 cm per 4.5×10^9 yrs, but the addition consists of "soft spray", which is not relevant from most standpoints.

The preceding results refer to the maria surface, originally molten and solidified into hard rock and subsequently battered by the interplanetary population of stray bodies, assumed to be the same as presently observed.

For the lunar continentes the conditions were different. We do not know what was underneath, but the exposed top layer is battered to a great depth by a saturation coverage of craters. The great protective depth of overlay leaves only the larger craters to contribute to it.

Let us assume that the base of the continentes consisted of a rock surface, possibly partly melted and solidified but still hot and soft. The impact parameters which suit best the relevant crater range from 16 to 64 km are those of Models D and E of Table XIV (Fig. 3). We may thus set $x_\rho/B_o = p/D = 5.0/28.1 = 0.178$, w_o = 3km/sec, $\lambda^2 = 0.25$, $s = 2.8 \times 10^8$ dyne/cm^2. From (15) the volume excavated is

$$V_e = 0.0435\, B_o^{\,3} \qquad (184)$$

The flight range of the ejecta, proportional to the product $s\lambda^2$ at ρ = const. (cf. Section [illegible]), is now only about 0.26 that for post-mare craters. On the other hand, the craters of relevant size on continentes are about 25 times more numerous than on maria (Baldwin, 1964b), or their spacing is about 5 times closer: the overlapping of ejecta of neighbouring craters is thus similar on the continentes and maria.

In Table XXX, Baldwin's (1964b) crater counts on the continentes as contained in his Table XV are used to estimate the thickness of ultimate overlay, i.e. the layer of ejecta of density $\rho = 1.3$, produced from a rock layer of $\delta = 2.6$ by the counted visible craters of the highlands. The rubble layer thickness so obtained is a lower limit, the original surface was rubble itself and not hard bedrock. However, from the model of origin of this surface as depicted in Section IV.G, it is probable that the bedrock ~~preceding~~ the final bombardment was partly melted and essentially compacted, as also is supported by the evidence of crater profiles (Table XIV and Fig. 3). The estimated overlay thickness distribution as arrived at in Table XXX is therefore likely to be a close approximation.

~~The layer thickness marked with an asterisk is so great that~~

TABLE XX

Crater Statistics (Baldwin, 1964b) and Overlay Distribution on the Lunar Continents.

Crater diameter, km (average of group) D_c	Number per 10^5 km^2 n_c	Crater Area single S_c km^2	Crater Area fractional coverage	Crater ejecta fringe single S_f, km^2	Crater ejecta fringe fractional coverage τ	Cumul. coverage $\Sigma\tau$	Distribution Percentage area	Distribution Overlay, meters X	Averaged ΔX meters
412	0.106	135000	0.143	240000	0.148	0.148	13.8	43000*	5990
206	0.458	33200	0.152	36500	0.167	0.315	13.2	20800*	2750
103	1.99	8300	0.165	10000	0.199	0.514	13.2	9480*	1250
51.5	8.67	2070	0.179	2970	0.258	0.772	11.0	4000*	440
25.8	37.7	520	0.196	1060	0.400	1.172	17.9	1410	252
12.9	164	130	0.213	411	0.674	1.846	15.0	455	68
6.4	712	32	0.223	211	1.500	3.346	12.4	108	13
3.2	3100	8	0.247	137	4.240	7.586	3.45	20.8	1
1.6	...	2.0	...	105	...		0.05	≤ 3.4	0
All	...	...	...	...	...	...	100.0	...	10764

* The layer thickness marked with an asterisk is so great that compaction under own weight must have taken place as well as partial deep-layer melting. These layers may have slumped to two-thirds or less of the indicated thickness and to a density of 2.0 or more.

compaction ~~under own weight must have taken place as well as partial deep layer melting. These layers may have slumped to two-thirds or less of the indicated thickness, and to a density of 2.0 or more.~~

In the table; the 3rd column gives the crater area $S_o = 0.75\pi B_o^2$; the 4th column, the fractional crater coverage $n_i S_o/10^5$; the 5th column, the area within a 5 km fringe over the crater rim, $S_f = 0.75\pi (B_o+10)^2$, or the effective area covered by the ejecta, including the crater interior; the 6th column, $\tau = n_i S_f/10^5$, the fractional coverage by crater ejecta, and the 7th - the cumulative coverage, $\Sigma\tau$ (this may exceed unity which means overlapping); the actual coverage or fractional area is then $1 - \exp(\Sigma\tau) = \theta_c$. Considering that a deeper overlay takes exclusive precedence over a shallower one, the distribution of overlay in order of thickness is that of the distribution of the fringe areas in the order of decreasing crater size. The percentage area in the 8th column is thus the differential of $\theta_c \times 100$, and in each group the average thickness of overlay as given in the 9th column is that over the fringe area of a crater, $X_{(m)} = 2V_c/S_f = 87.0\ B_o^3(\text{km})/S_f(\text{km}^2)$ (m.km) according to (184), the factor of 2 allowing for the smaller density of the ejecta. Fig. 11 represents this distribution of overlay thickness in the continentes. The 10th or last column of Table XXX contains the differential overlay, ΔX, as averaged over the entire area. The total cumulative thickness exceeds 10km, but this levelled-out average conveys an inaccurate impression of the actual non-uniform distribution featured in the 9th column and Fig. 11.

D. Overlay Particle Size Distribution

From Surveyor and Ranger pictures, as well as from an understanding of the process of fragmentation in cratering impact, it follows that the overlay rubble contains all particle sizes from microscopic dimensions up to meter size boulders. Let us attempt to predict the particle size distribution from the physics of cratering as outlined in Section II.

It is a well known fact that the strength of materials increases with decreasing linear dimensions. The effect is caused mainly by imperfect cohesional coupling between the molecules of the lattice, only a small fraction of them being in full contact with each other. One of its consequences is the layered morphology of meteor crater debris; in the inner portions of the crater bowl, the greater shock pressure produces fine-grained rock-flour, while on the outskirts the rock is fractured into sizable boulders.

Let y be the fractional crater mass as in Section II and Fig. 1. The shock pressure is proportional to y^{-2} and this can be set equal to the destruction strength s_y,

$$s_y = s_c y^{-\nu/2} \tag{185}$$

which results in fragments of average size R, such that

$$s_R \cong s_y \; .$$

We assume a power law for the strength dependence on size,

$$s_R = CR^{-\nu} \tag{186}$$

The exponent ν can be roughly estimated as follows. For granite, at dimensions of the order of 20cm as in building industry, $s_c = 1.2 \times 10^9$ dyne/cm^2. Its typical molecule, SiO_2, has a lattice energy of 2.8 ev or 4.5×10^{-12} erg and occupies a volume of 3.7×10^{-23} cm^3 corresponding to a mean distance between lattice molecules of 3.4×10^{-8}cm. For a bond of two molecules the energy equals one-third of the lattice energy or 1.5×10^{-12} erg, and the force of cohesion, with an inverse fifth-power law of interaction, equals

$$1.5 \times 10^{-12}/(0.2 \times 3.4 \times 10^{-8}) = 2.2 \times 10^{-4} \text{ dynes.}$$

Distributed over an effective contact area of $(3.4 \times 10^{-8})^2$ cm^2, this corresponds to a cohesive (tensile) strength $s = 1.9 \times 10^{11}$ dyne/cm^2, at effective dimension R(stands here for diameter) of $3.4 \times 10^{-8} \times 2^{\frac{1}{3}} = 4.3 \times 10^{-8}$ cm. Applying equation (186) to the two extreme values of s, we find $\nu = 0.254$ as an average exponent over a relative range of 5×10^8 to 1 in the linear scale.

For a check, consider the Arizona crater with boulders up to 20 meters, supposedly from the periphery (y=1) and rock flour of $R \sim 10^{-3}$cm at an effective value of $y=y_f$. With the value of ν as suggested above the ratio s_y/s_c becomes then $(2000/10^{-3})^{0.25} = 38$ whence, according to equation (185), $y = 0.16$ is found to be the fractional mass at which rock flour of the specified grain size is expected to be produced, a not unreasonable result.

Substituting $s_R = s_y$ from (186) into (185), we have

$$R = y^{1/\nu} \times \text{const.} \tag{187}$$

$$y = R^{\nu/2} , \; dy \sim R^{\frac{1}{2}\nu - 1} \, dR, \tag{187a}$$

$dy \sim R^{\frac{1}{2}\nu-1} \cdot dR$.

/21/

The number of particles in the mass element dy is proportional to dy/R^3 or, with (187a), the frequency of fragments among crater debris ranging in size from R to $R + dR$ becomes

$$F(R)\,dR \sim R^{\frac{1}{3}\gamma-4}\,dR = R^{-n}\,dR, \tag{188}$$

where

$$n = 4 - \tfrac{1}{3}\gamma \tag{189}$$

is the "frequency index" in the power law of particle diameters as in equation (161). With $\gamma = 0.254$, we find $n = 3.87$ for the predicted frequency law of cratering fragments as counted in a volume. For comparison, B.G. Smith (1967) finds for the surface distribution of fragments with $R = 2$–20 cm on the Russian Luna 9 pictures $n-1 = 2.9 \pm 0.2$ or $n = 3.9$. A similar value of $n = 3.77$ is found by Hapke (1968) from the Surveyor pictures. It may be relevant to note that for volcanic ejecta in Hawaii which produced impact craters in the surroundings, Hartmann (1967) finds an empirical value of $n = 3.64 \pm 0.1$, close but not quite equal to the exponent for lunar overlay.

The agreement between the predicted and observed frequency functions of lunar surface debris is remarkable and quite unexpectedly supports the cratering theory as presented in Section II. Of course, erosion by micrometeorites and repeated turnover of the overlay by new impacts will tend to increase the number of small fragments at the expense of the larger ones, increasing thus also the value of n above that predicted. Apparently, none of these effects has been very efficient; the first, probably, because the surface fragments ~~are~~ are buried and protected from erosion sooner than they are eroded; the second because the mass fraction of old overlay in cratering ejecta is small as compared to the contribution from new crushed bedrock.

The dependence of strength on size would apparently invite some revision of the cratering formulae of Section II. The size of the largest blocks, as formed at the crater rim, is about 1/40 to 1/60 of the crater diameter for the Arizona crater, and 4/450 ~ 1/110 for the largest block seen on the far side of the stone-wall lunar crater of Surveyor I (Fig.6). The Surveyor I bedrock seems to have been shattered before the formation of this crater, and the blocks may be too small. It appears plausible to assume that geometric similarity holds, and that the characteristic value of the marginal crushing strength (s_c) determining the volume and diameter of the crater corresponds to a particle diameter equal to $1/60B_o$, so that for typical granitic or basaltic bedrock, the effective lateral strength, according to (186) with $v = \frac{1}{4}$, becomes

$$s_c = 4.0 \times 10^8 \, B_o^{-\frac{1}{4}} \tag{190}$$

dyne/cm^2, with B_o in km. According to equation (7), when $s = s_c$ without a gravity frictional component the crater diameter then varies as the 1.06 power of projectile diameter, instead of strict proportionality

The effect on penetration, amounting to the −1/120th power of linear dimension according to (6), is negligible. Thus, leaving the penetration parameter p unchanged, the cratering parameters in the first half of Table XV are somewhat changed through the application of (190) and are now as given in Table XVa. The new figures for crater diameter B_o, in the fourth line of the table, are now markedly larger than the former values (5th line), but the ratio of the two does not increase monotonously with crater size, the decrease in the cohesional lateral strength, s_c, being balanced by the increasing friction component. For this reason the effect remains small; the decrease of strength with increasing dimensions, although favoring greater numbers of incidence of larger craters, is utterly inadequate to account for the observed excess in the numbers of big craters (Tables XVII, XVIII).

VIII. Mechanical Properties of Lunar Top Soil

Surveyor spacecraft pictures and experiments as televised to earth have shown that the lunar soil is granular, with a very broad distribution of grain size from meter size boulders to submillimeter particles (Newell, 1966,1967; Jaffe et al. 1966,a,b, NASA, 1967; Christensen et al 1967; Hapke, 1968). Hard pebbles are present, as well as clumps of coagulated finer material. Impacts of the Surveyor footpads (Figs. 12, 13) as monitored by strain gage force record data and supplemented by static penetration tests (Surveyor III), yielded experimental data similar to those described in Section II.E from which the strength parameters of lunar soil could be derived. The parameters can be defined in different ways, depending on the mechanical model used. Although the data are scarce, they are sufficient to show considerable qualitative and quantitative similarity with terrestrial natural

TABLE XVa

Cratering Parameters for Post-Mare conditions with Size-Dependent Lateral Strength (s, s_c in 10^8 dyne/cm^2) (cf. Table XV).

566

x_f, km	0.125	0.25	0.5	1.25	2.5	5.0	12.5	25.0
s_c	3.9	3.3	2.7	2.2	1.8	1.5	1.2	1.0
s	3.92	3.34	2.78	2.4	2.2	2.3	3.2	5.0
B_o, km	1.40	2.93	6.15	16.2	32.4	64.2	148	264
B_o, Table XV	1.14	2.28	4.57	11.3	22.6	44.6[illegible]	109	208
Ratio	1.23	1.28	1.35	1.43	1.43	1.44	1.36	1.27

TABLE XXXII

Surveyor I, Footpad 2: reconstruction of motion during penetration

(a) Strain gage data

t, seconds	0.0000	0.0166	0.0705	0.1140
F_d, dynes	0	1.74×10^8	2.12×10^8	2.55×10^8
s_ρ, dyne/cm^2	0	5.37×10^5	6.52×10^5	7.87×10^5
x, cm	0	4.72	5.24	5.80
Average velocity, $\bar{w}$, cm/sec		284	9.6	12.9

(b) Interpolated velocities: $w_o = 364$ cm/sec*, $w_1 = 256$ cm/sec; $dw_1/dt = 6850$ cm/sec^2

($\rho = 1.3$ g/cm^3, $K_a = 0.75$)

t, 10^{-3} sec	0.5	1.5	2.5	3.5	4.5	5.5	6.5	7.5	8.5	9.5
w, cm/sec	256	256	268	284	299	319	338	348	352	351
t, 10^{-3} sec	10.5	11.5	12.5	13.5	14.5	15.5	16.0– 70.5		70.5– 114.0	
w, cm/sec	345	331	304	275	190	108	10		13	

*The NASA team (Jaffe et al. 1966b, p.69) gives 3.6 ± m/sec.

beach gravel, especially in that the cohesive strength rapidly increase with depth. Equations (37) and (37a) appeared to be appropriate also for the frontal and lateral resistance of lunar soil. Some compressibility of the lunar soil was observed, though insignificatn enough to justify the aplication of the penetration and cratering equations of Section II. Table XXXI contains the results.

In Part (a) of the table, static tests with Surveyor III ("Tidbinbilla") [on an inner crater slope of about 14°; crater about 230 meters in diameter, in Oceanus Procellarum, $\varphi = 2^{\circ}.9$ south, $\lambda = 23^{\circ}.3$ east (astronomical) or west (astronautical)] are listed and interpreted with equation (37) and three assumed values of a^2; test No. 6 is decisive and would require $a^2 = 2.4 \pm 0.8 cm^2$, while other tests are indifferent in this respect. It was decided to assume $a^2 = 2 cm^2$, the same as for terrestrial sand (Section II.E). There is not much uncertainty in S_p as depending on the particular value of a^2, and for the value chosen the logarithmic mean is

$$S_p = 3.21 \times 10^4 \text{ dyne/cm}^4 \ (+23 \text{ to } -19\%),$$

to be compared with a value of 5.55×10^4 for similar experiements with terrestrial sand [Table III (a)].

Test No. 4, made on a trench bottom, yielded $9.15/3.21 = 2.85$ times a higher value at a depth of 6 cm after removal of the overlying material; this compares favorably with Experiment (2a) in Table III (a) where an 8.4-fold increase in the bearing strength parameter was obtained at an excavated depth of 15 cm.

The dynamic tests are based on the impact of Surveyor footpads. The footpad has a circular top 30.5 cm in diameter (Fig. 12) and a total height of 12.8 cm; the circular bottom is narrower, 20.3 cm in diameter and widens upwards over a conical section of 45° angle, 5.1 cm thick. The footpad is not rigidly connected with the very much more massive main body, but it is linked to it by a system of shock absorbers with strain gages. At the first contact, the footpad acts almost as an independent projectile, but as soon as it decelerates, the shock absorber yields and increases its pressure on the footpad which no longer moves freely by its own inertia. The equations of motion of Sections II.D, E which refer to a rigid projectile do not apply therefore in this case. On the other hand, the strain gage data provide a

TABLE XXXI

Mechanical Strength and Cratering in Top Lunar Soil.

(a) Static Bearing Strength Experiments with Surveyor III (Scoop NASA, 1967, p. 97).

			$a^2 = 2 cm^2$ assumed		$a^2 =$ [illegible] cm^2 assumed		$a^2 = 3 cm^2$ assumed	
Test No.	s_p $10^5 dyne/cm^2$	x_o cm	S_p $10^4 dyne/cm^4$	$s_p (10^5 dyne/cm^2)$ (calculated, with $S_p = 3.21 \times 10^4$	S_p $10^4 dyn/cm^4$	$s_p (10^5 dyne/cm^2)$ calcul. with $S_p = 3.70 \times 10^4$)	S_p $10^4 dyne/cm^4$	$s_p (10^5 dyne/cm^2)$ (cal. with $S_p = 2.81 \times 10^4$)
1	3.92	2.5	4.75	2.65	5.4	2.68	4.24	2.50
2	2.16	2.5	2.62	2.65	2.9	2.68	2.34	2.50
3	1.76	1.9	3.13	1.80	3.8	1.71	2.66	1.36
5	2.16	2.2	3.15	2.20	3.70	2.16	2.76	2.20
7	2.16	2.9	2.07	3.34	2.3	3.48	1.89	3.21
8	2.32	1.9	4.13	1.80	5.0	1.71	3.51	1.36
6	0.72	(0.0)*	...	0.64	...	0.37	...	0.34
*compressed clod								
Logarithmic mean			3.21	...	3.7	...	2.81	...
Probable deviation ratio			1.23	1.23	1.2	1.28	1.22	1.23

Bearing test No. 4, made on an excavated trench bottom 5-7.5cm below the surface, yielded $s_p = 2.16 \times 10^5 dyne/cm^2$ at $x_o = 0.6$cm or $S_p = 9.15 \times 10^4$ $dyne/cm^4$ (with $a^2 = 2$)

(b) Dynamic (Impact) Experiments

$\sigma = 324 cm^2$ ($m = 16 gr/cm^2 \pm$, $R = 10.15$ cm, $\rho_R = 1.3 gr/cm^3$ assumed, $w_1/w_o = 0.704 \pm$), $F = 0.118$ and $a^2 = 2 cm^2$ assumed.

Test	s/s_a	x_o, cm	w_o cm/sec	B_o, cm	s_p max. $10^5 dyne/cm^2$	S_p $dyne/cm^4$	S_c $dyne/cm^4$	S_p / S_c
Surveyor I, Footpad No.2	5.14	5.8	364	42	7.87	22100	1190	18.6
Surveyor I, Footpad No.3	3.39	5.1	364	37	6.35	22700	1830	12.4
Surveyor III, Footpad No.1, 2nd touchdown	21.1	2.5	(53)	32.6	2.01	24400	930	26.2
Surveyor III Footpad No. 2, 3rd touchdown	25.2	2.5	(60)	26.5	3.30	40000	2380	15.8
							...	...
Surveyor III Footpad No.3, 3rd touchdown	...	5.0	..	...	5.18	19200		
Logarithmic mean	...	...	..	...	...	24300	1490	17.6
Probable deviation ratio	...	...	..	...	...	1.19	1.39	1.25

more direct means of evaluating the mechanical parameters of the soil and the amount of radial momentum transmitted during penetration.

Theory of impact cratering requires that the target material parts laterally with a velocity determined by the proceeding history of penetration, higher than the instantaneous penetration velocity. A cone of 45° as in the footpad will not therefore, in its forward motion, be able to overtake and contact the material parting sideways. It has been here assumed therefore (contrary to some hints by the NASA team) that, during impact, contact was maintained only with the bottom area of 324 cm² of the footpad.

The shock absorber records give the time variation of the force F_a along the absorber axism making an angle α with the direction of impact from about 61° at no load to 70° at full load. The decelerating force is then $F_\alpha = F_a \cos\alpha$. From graphical and tabular data describing the impact events (<u>loc.cit.</u>) a plausible approximation, $\cos\alpha = 0.487 - 0.147\,F_a/C$ with $C = 7,5 \times 10^8$ dynes, was introduced. The maximum load which is reached at greatest penetration, x_o, yields then

$$s_p(\max) = F_\alpha(\max)/\sigma \quad \text{with} \quad \sigma = 324 \text{ cm}^2$$

and, from (37) with $a^2 = 2$ cm²,

$$S_p = s_p(\max)/(x_o^2 + 2) \qquad (37b)$$

is obtained directly.

With this parameter, the values of s_p as derived from the strain gage when entered into (37) yield a few discrete values of x and the average speed of penetration between them for successive intervals of time. The initial speed at impact, v_o, and the shock entry speed, w_1, as well as the initial deceleration dw_1/dt at entry (uninfluenced yet by the shock absorber) being estimated, a history of the forward motion of footpad bottom surface can be reconstructed (graphically), to fit the average velocities and the boundary condition. In such a manner, for Footpad 2 of Surveyor I, a reconstruction has been obtained as described in Table XXXII.

The time variation of velocity as shown in Table XXXII (b) is more or less empirical. It can be interpreted in the following way: during the first 0.002 sec the deceleration is balanced through increasing coupling, by way of the shock absorber, with the main mass of the spacecraft; between t = 0.002 and 0.009 sec the coupling accelerates

the footpad to virtually the velocity of the spacecraft; (after that,
(between [illegible] the velocity of the spacecraft)
the footpad is brought almost to rest within the next 0.007 seconds by increasing resistance and acts now as an effective brake on the main body during $t = 0.016$ to 0.114 sec, while its own penetration is slow and the kinetic energy of the spacecraft is dissipated in the three shock-absorber legs.

The radial momentum released in the lunar soil by the impact consists of two components — the shock momentum imparted to the target at first contact, and the hydrodynamic pressure integral

$$J = \left[(w_0 - w_1)\ \tfrac{1}{2}R\,\rho\sigma + K_a\rho\sigma\int_0^t w^2dt\right] / 2\,K_a \qquad (19a)$$

to be used with (42). The lateral strength parameter is then derived ultimately from equation (44), using the terrestrial beach average of $F = 0.118$ as the only available guess.

The data for Footpad No. 2 of Surveyor I [which landed on a practically horizontal surface in Oceanus Procellarum, at $\varphi = 2^\circ.5$ south, $\lambda = 43^\circ.3$ east (astron.)] are the best of those quoted in Table XXII (b). The penetration, 5.8 cm, was derived from the shadow of the top surface ($2R = 30.5$ cm) at low solar altitude; the surface was tilted, 9 cm above undisturbed ground level at one end, 5 cm at the other, or a mean of 7 cm above ground level. Substracting 12.8 cm as the thickness of the footpad, we obtain $-x_0 = 7 - 12.8 = -5.8$ cm for the bottom surface, with 4.5 cm at one end and 7.1 cm at the other end of the bottom ($2R = 20.3$ cm). The difficulty of estimateś by mere inspection of the photographs is illustrated by the fact that in preliminary reporte (Newell, 1966; Jaffe, et al. 1966a) the depth of penetration, x_0, was estimated to be only 2.5 cm. The crater rim-to-rim diameter, B_0, was more easy to estimate, although the darker material ejected beyond the rim may have produced the impression of a somewhat broader crater than the actual size (cf. Fig. 14 which shows more contrast than Fig. 12). Besides, because of the motion of the legs as controlled by the shock absorber, the footpad came to rest about 5 cm inwards (toward the spacecraft) from the original center of the crater, and assumed thus an asymmetric position (Fig. 12).

f.

In the other four cases of Table XXXI (b) the parameters were more difficult to estimate. The publications (Jaffe et al., 1966b; Christensen et al., 1967; Newell, 1967; NASA, 1967) as well as NASA photographic prints were consulted and compared. The penetrations are probably good to ± 0.5 cm, the crater diameters to ± 2 cm, while the velocities and velocity histories were considered in parallel or in homology with the data of Table XXXII as of better quality. The very low velocities for Surveyor III are not in accord with some statements in the NASA reports, but follow directly from the strain gage time records (less reliable than those of Surveyor I) and are supported by the concordant values of S_c so obtained.

The dark ejecta surrounding the impact craters (Fig. 12) seem to indicate that radiation damage blackening is not a one-way process and that the very surface, exposed to immediate radiation, becomes slightly bleached or, rather, that the material when buried and protected from direct radiation becomes spontaneously darker with time. However, as suggested by Hapke (1968), the difference in albedo may be due to different graininess and porosity, and not to physico-chemical changes in the grains. Footpad No. 2 of Surveyor III was ejected from its original crater at third touchdown and came to rest at a distance of about 30 cm from it. The bottom of the original crater (Fig. 13) (used in Table XXXII) is laid open and appears to have a higher albedo than the undisturbed surface or the ejecta--a result of compression. This seems to support the geometrical interpretation of the differences in albedo.

The dark halo of ejecta from Surveyor I (Fig. 14) shows an average outer margin at 34 cm, in some sectors reaching to 47 cm from the crater center (reckoning with the asymmetry of the footpad), and a ray is going to a distance of at least 61 cm. The extreme not-to-unusual flight distance of the ejecta from the edge of the footpad can be set equal to $L = 47 - 10 = 37$ cm. With $s_c = 1190$, $x_o = 5.3$, $s_c = 4.25 \times 10^4$ dyne/cm^2. To this a small contribution from friction, $130x_o$ [equations (11) and (12)] or 750 dyne/cm^2, is to be added, making $s = 4.33 \times 10^4$. With $\rho = 1.3$ g/cm^3, u_s equals 182 cm/sec according to equation (4). Following the line of reasoning of Section II. K, and with $w_o = 364$ cm/sec, from equation (16) we find $y_o = u_s / w_o = 0.5$. Further, with $\sin\beta_o = 0.8$, $y = 0.6$ as nearest to y_o, $u = 303$ cm/sec, $\beta = \chi$, $\sin\chi = 0.48$, $\cos\chi = 0.38$ [from (27)] ; $g = 162$ cm/sec^2, equation (45) yields the ejection velocity to $L = 37$ cm as $v = 84$ cm/sec whence $\lambda \cong 84/303 = 0.28$, $\lambda^2 = 0.08$ only. For the conspicuous ray, $L = 51$ cm, $y = 0.5$, $u = 364$ cm/sec, $\sin\chi = 0.4$, $\cos\chi = 0.92$, $v = 106$ cm/sec and $\lambda = 106/364 = 0.29$, $\lambda^2 = 0.08$ or the same value. The lunar dust seems to possess higher internal friction and lower kinetic efficiency as compared to terrestrial gravel.

The two Surveyor experiments yielded very similar mechanical parameters despite the difference in terrain, Surveyor I having landed practically on level ground, Surveyor III on the inner slope of a crater wall inclined about 14° to the horizon (NASA, 1967, Part II, p.20). Although both are on a mare surface of Oceanus Procellarum, near the lunar equator but separated by

20^{o} in longitude or by 600 km, the mechanical properties are probably representative of the upper layer of lunar soil in general and to a depth of 50--100 cm to which extrapolation of equations (37), (37a) and (37b) is permissible. The parameters are chiefly determined by the fine-grained matrix, of the order of 0.001--0.006 cm as shown by the retention of the imprints of the footpad pattern of a network of about 1 cm mesh with ridges 0.006 cm high on Surveyor III Footpad No. 2 crater of the third touchdown (however not visible in the reproduction of Fig. 13). Lumps of coagulated grains were present, from 0.1 to 5 cm, about 1 cm average size; they apparently consist of loosely bound smaller grains and are easily crushed. These lumps, as well as admixed occasional hard pebbles or rock splinters, by virtue of the cooperative action of the constituent grains at inner contacts, are probably responsible for increasing the thermal conductivity and yielding a larger effective "thermal" grain size of the order of 0.03 cm (Table XXII).

Table XXXIII contains a summary of the mechanical characteristics of lunar soil (from Table XXXI) as compared with those of terrestrial natural gravel (from Table III). The notations are those of Sections II. E, F. In the fifth and eights columns are given the surface bearing strength, s_{po} and the surface lateral strength or "cohesion", s_o, both corresponding to zero penetration, $x = 0$ or $x_o = 0$. With $s_{op} = 6 \times 10^4$ dyne/cm^2, an astronaut with heavy equipment totalling 150 kg but weighing only 2.4×10^7 dynes on the moon will be supported

TABLE XXXIII

Average Mechanical Properties of Lunar Soil and Natural Terrestrial Gravel to be used in particular with equations (37), (37a) and $a^2 = 2$ cm

	f_s Coeff. of Fric.	S_p Average 10^4 d/cm^4	S_p Probable Range 10^4 d/cm^4	s_{po} Surface Strength 10^4 d/cm^2	S_c Average 10^4 d/cm^4	S_c Probable Range 10^4 d/cm^4	s_c Surface Strength 10^4 d/cm^2	λ^2 Kinetic Efficiency
	Bearing (Compressive) Strength				Lateral (Crushing) Strength			
		Dynamic				Dynamic		
Lunar Soil	...	2.5±0.2	2.1–3.0	5.0	0.14±0.02	0.10–0.20	0.23	0.08
Terr. Gravel	...	4.9±0.6	3.0–8.0	9.7	0.44±0.05	0.28–0.68	0.87	0.16
		Static				Static		
Lunar Soil	(1)	3.2±0.3	2.6–3.9	6.4	...	...	...	...
Terr. Gravel	0.63	5.6±0.6	3.8–8.1	11.1	0.22±0.03	0.16–0.30	0.44	...

without sinking a centimeter into the lunar surface by 400 cm^2 contact surface--just about what may be provided by his two feet.

The minimum lateral strength of lunar soil, or its surface value of $s_0 = 2800$ dyne/cm^2 can be compared with the minimum adhesion of grains in vacuo, about 0.5 dynes (Smoluchowski, 1966; Ryan, 1966; cf. Section VI. A); with an average of three contacts or 1.5 dynes per grain; it would require 1870 grains in contact per cm^2, or an average spacing (diameter) of about 0.023 cm to account for the cohesion of the matrix. This does not differ so very much from 0.033 cm as the average "thermal" diameter (Table XXII). It may be noted that meteoric dustballs, or the grainy skeletons of cometary material which remain after ices have evaporated, have a crushing strength s_0 of about 10^4 dyne/cm^2, at average grain diameter from 0.01 to 0.1 cm (Öpik, 1958c); their strength is about that of lunar soil at $x_0 = 2$ cm, thus at an average depth of about 1 cm, although the density is less. The two kind of material seem to have much in common.

Extrapolation of equation (37a) with $S_c = 1400$ dyne/cm^4 would yield the strength of terrestrial alluvium $s_c = 4 \times 10^6$ dyne/cm^2 (a probable upper limit for granular material) at a depth of penetration of $x_0 = 170$ cm. The overlay is much thicker than this (Section XVII. C), and a constant value of cohesive strength of this order can be assumed to hold for most of the thickness of the overlay. The corresponding upper limit for the compressive strength is $s_p = 7 \times 10^8$ dyne/cm^2.

IX. The Ballistic Environment

A. Electrostatic versus Ballistic Transport

It has been pointed out in Section VII. A that electrostatic transport of lunar dust, so ingeniously proposed by Gold (1955), does not work on the lunar surface--de facto because it would have obliterated sharp transitions of contrast which are actually observed, and de jure because its effect in the actual environment of the moon cannot be significant (Singer and Walker, 1962). The ratio of electrostatic repulsion to gravity of a small particle on a planetary surface equals

$$F_e/F_g = 2.66 \times 10^{-6} I^2/(gR^2 L_d \delta) \quad , \qquad (192$$

where I is the common electrostatic potential of the surface and the particle in volts, g the acceleration of gravity, R the spherical radius and δ the density of the particle; L_d is the electrostatic plasma screening length (similar to Debye length) for a planetary surface charge. For the moon, $g = 162$ cm/sec^2, $\delta = 2$ g/cm^3 for individual irregular particles, $I = +6$ volt and $L_d = 100$ cm (Öpik, 1962b); whence

$$F_e/F_g = 8.20 \times 10^{-11} I^2/R^2 = 2.95 \times 10^{-9} R^{-2} \qquad (192a)$$

The effect would be noticeable for $R < 10^{-4}$ cm, $F_e/F_g > 0.3$ and of decisive importance for $R < 5.8 \times 10^{-5}$ cm, $F_e/F_g > 1$, or at submicron sizes. When disturbed by meteor impact, these small particles may float in sunlight within the screening length or range, about 100 cm from the surface, their charge sustained by the photoelectric effect until entering a shadow when they become neutralized and fall back. The virtual absence of any trace of detail blurring (which should be caused by particles of so high a mobility) indicates that these small particles cannot play any significant role on the lunar surface. The thermal conductivity and the cohesion of lunar soil also indicate that the relevant average particle size of lunar dust is at least 100 times greater than that at which eletrostatic transport efficiently begins.

Therefore only the ballistical transport of dust on the lunar surface, caused by meteorite impact, is of relevance.

B. Impact Fluxes and Cratering in Overlay

As distinct from accretion and loss, two main sources are causing the mobility of the dust: direct meteorite impact into the dust layer, and the impact of debris from secondary ejecta broken off the bedrock and accumulating as overlay. Although the latter source signifies also a kind of transport, from ~~from~~ the standpoint of the local material balance of a "normal" plain undisturbed by large-scale cratering its effect amounts to virtual accretion, while the "abnormal" area of a new crater from which the material is taken begins a new history and is atypical. Of course, the factors of dust transport begin at once to work on the surface of the newly formed crater, but some of the starting conditions, such as the thickness of overlay, are different.

The quantitative importance of the different sources in stirring the dust can be provisionally measured by the radial momentum imparted to overlay by non-penetrating projectiles, $J = k\mu w_0$, where μ is the impinging mass rate per unit of time --say, 4.5×10^9 years-- and area (cm^2). For micrometeors of the zodiacal dust, $w_0 = 6.0$ km/sec (including acceleration by the moon), $k = 2$, $\mu = 47$ gram (Table XXXV. A and Section VII. B), whence $J_M = 564$ in the units chosen. For the "visual" meteors, chiefly belonging to the "E-component" and which are all non-penetrating, $\mu = 0.56$ g, $w_0 = 13$ km/sec (Öpik, 1965a), $k = 3.1$, $J_0 = 20$. For the Apollo-meteorite group, $R_2 = 200$ cm (non-penetrating, the larger members lead to basic cratering and produce new overlay from the bedrock), from equation (158) $\mu = 0.25$, $w_0 = 20$ km/sec (Öpik, 1965a), $k = 3.3$, $J_1 = 16$. For comet nuclei, equation (159), $R_2 = 300$ cm, $\mu = 0.0067$, $w_0 = 40$ km/sec, $k = 4.4$, $J_2 = 1.2$. For Mars asteroids, $R_2 = 200$ cm, $\mu = 9.5 \times 10^{-6}$, $w_0 = 9$ km/sec (Öpik, 1965a), $k = 2.3$, $J_3 = 2 \times 10^{-4}$ or utterly negligible. As to secondary ejecta, only the hard spray component is here of importance, which originates from the bedrock and thus is representative of the new overlay; its rate at present may be close to 12 meters, $\mu = 1500$ g/cm^2 in 4.5×10^9 years as given by the thickness of overlay (Table XXIX (E); with $s = 6 \times 10^3$ dyne/cm^2, $\rho = 2.6$, $\lambda^2 = 0.22$ for the parent bedrock, at $y = 0.5$ as the median mass and $x/x_0 = 0.5$, equations (4), (16), (24) and (25) suggest an average ejection or secondary impact velocity of $w_0 = 0.10$ km/sec, $k = 0.63$ and

and an additional factor $u/v_a = V/V_a = 1.1$ for "static work" (cf. Table XXXV. D) the relative radial momentum becomes $J_e = 0.63 \times 1.1 \times 1560 \times 0.10 = 108$. Hence the relative stirring power of the different components obtains as given in Table XXXIV.

Because the velocities and flight distances of massive ejecta depend solely on the mechanical properties of the target, the figures of the table must approximately represent the relative mixing efficiency of the seperate sources with respect to the fine granular component of overlay. There is, however, a qualitative difference depending on the statistical character of the different populations. Components J_M and J_0 are concentrated in small particle sizes and sweep the surface without much penetration and with shallow cratering, while J_1 prevails in large projectile sizes which are penetrating and cratering through the entire thickness of overlay. J_e, despite prevalence of large sizes, possesses a low velocity and does not penetrate deep enough to stir the entire layer. Thus, despite the lesser mechanical sweeping power, J_1 and J_e are mainly responsible for cratering in the surface layer, and J_e in addition provides sizable boulders; the role of J_M and J_0 then consists in levelling out the craters and craterlets, and in ablating (grinding) the boulders, or in "polishing" — smoothing out the surface roughness continually produced by the two other components and themselves. The actual state of the surface is then determined by an equilibrium between the two opposing processes. The role of components J_2 and J_3

with respect to the overlay layer is negligible and need not be further considered in this context.

In Table XXXV, theoretically predicetd flux and empirically supported flux and cratering data in overlay are given for the four relevant sources of particulate flux, and for a typical level mare surface. The surface sample is supposed to be remote from large craters; it should correspond to a "normal" overlay thickness of 13 meters which, according to Table XXVII, may be representative of about 62 per cent of the total mare surface (and, with some indulgence, even of 61.7 + 22.6 + 7.1 = 91 per cent). For Parts A, B, and C of Table XXXV, the flux rates and velocities are based on astronomical data in the author's interpretation (loc. cit.; Sections VII. B, C, V. D, E, et alias) which he believes gives a well balanced account of the observations and which he is reluctant to exchange for data from other sources; the cratering parameters, equations and notations are those of Sections II. B, C, F, while n is the frequency index of radii according to equation (161); the cohesive strength data for the overlay are those of Section VIII. R is the equivalent "spherical" radius of the impacting meteoroid, B_o the rim to rim crater diameter, x_o the penetration, x' the apparent crater depth below the undisturbed surface (assumed to have been flat) as corrected for fallback.

Part D of Table XXXV contains the flux and cratering data for the ejecta which are contributing to the overlay. The total mass influx is assumed to correspond to a present accretion

228

f_{10}

TABLE XXXIV

Relative Sweeping or Stirring Momentum, Per Cent

	J_M	J_o	J_1	J_2	J_3	J_e	
Source	Micro-	Dustball	Meteorites	Comet	Mars	Secondary	Total
Stirring	meteorites	Meteors	Apollo Group	Nuclei	Asteroids	Ejecta	
Power, %	79.5	2.8	2.3	0.2	0.0	15.2	100.0

TABLE XXXVI

Expectated Number of Punctures on the Moon from Meteorite Hazard

Magnesium sheet thickness, mm	0.4	1.2	1.4	4.2	14	42
Steel sheet thickness, mm	0.14	0.42	0.5	1.5	5	15
Number of punctures per 100 m^2 and 10 years	2000	200	1.5	0.015	1.5×10^{-4}	1.5×10^{-6}

TABLE XXXV

Incident Fluxes and Cratering Parameters in Overlay at Present ($\rho = 1.3$)

"Normal" Overlay Surface, Remote from Large Craters

A. Micrometeors of Zodical Cloud

(J_M) (the projectile is explosively destroyed)

$w_o = 6.0$ km/sec; $\delta = 3.5$ g/cm^3; upper limit radius $R_o = 0.035$ cm; $n = 2.7$; cumulative number flux, $R < 0.035$ cm, $dN/dt = 1.27 \times 10^{-5}\left[(R_o/R)^{1.7} - 1\right]$ per cm^2 horizontal surface and year; cumulative mass flux, $d\mu/dt = 1.05 \times 10^{-8}\left[1 - (R/R_o)^{1.3}\right]$ gram per cm^2 and year. Cratering parameters: penetration negligible, $\bar{s}_p = 5.0 \times 10^4$, $\bar{s}_c = 2.32 \times 10^3$ dyne/cm^2; $k = 2.0$, $\eta = 45^o$, $p = 3.52$, $D = 169$, $D/p = 48.0$, $B_o = 333\ldots$, $x_p = 7.04$ R, $x_o = 5.92$ R < 0.2 cm, $x' = x_o(1 - F_B)$; cumulative crater coverage $\left(\frac{cm^2}{cm^2 \cdot year}\right)$, $\sigma_B = 0.00231\left[1 - \left(\frac{R}{R_o}\right)^{0.425}\right]$ ~~per year~~.

R, cm	0.035	0.0205	0.0121	0.0060	0.0010
Cumul. mass fraction	0	0.50	0.75	0.90	0.99
Cumul. number	0	1.88^{-5}	6.54^{-5}	2.45^{-4}	5.22^{-3}
cumul. crater coverage, σ_B	0	4.72^{-4}	8.39^{-4}	1.23^{-3}	1.81^{-3}
B_o, cm	11.8	6.7	4.1	2.1	0.3
x_o, cm	0.207	0.121	0.072	0.035	0.006
x', cm	0.125	0.092	0.063	0.033	0.006
B_o/x' (profile ratio)	95	73	55	63	60
Fraction of granular target, G_g	0.44	0.41	0.38	0.35	0.28

TABLE XXXV, Continued

B. Visual Dustballs (J_s)

(the projectile is explosively destroyed)

$w_0 = 18$ km/sec; $\delta = 0.65$ g/cm^3; lower limit radius $R_o = 0.061$ cm; $n = 5.2$; cumulative number flux, $R > 0.061$ cm, $dN/dt = 2.93 \times 10^{-13} R^{-4.2}$ per cm^2 and year; cumulative mass flux, $R > R_o$, $d\mu/dt = 3.02 \times 10^{-11} (R_o/R)^{1.2}$ gram per cm^2 and year. Cratering parameters: penetration of majority small; $\bar{s}_c = 2820(1 + 1.47R^2)$ dyne/cm^2; $k = 2.1$; $\gamma = 45°$; $p = 1.82(1 + 1.47R^2)^{-1/30}$; $D = 228(1 + 1.47R^2)^{-0.233} = B_o/2R$; $x_o = 2.91(1 + 1.47R^2)^{-1/30} \cdot R$; $x' = x_o(1 - F_B)$; cumulative crater area coverage $\sigma_B = 0.785 \int B_1 B_2 (G_g \Delta N)$.

R, cm	0.061	0.109	0.194	0.416	0.743	1.32	2.84	5.08	9.08
Cumul. mass fraction	1.00	0.50	0.25	0.10	0.05	0.025	0.010	0.005	0.0025
Cumul. number	3.72^{-8}	3.28^{-9}	2.86^{-10}	1.18^{-11}	1.04^{-12}	9.12^{-14}	3.75^{-15}	3.30^{-16}	2.89^{-17}
$\bar{s}_c$	2830	2870	2970	3520	5100	10030	36100	135000	344000
B_o, cm	27.8	49.5	87.3	180	294	449	716	935	1350
x_o, cm	0.177	0.317	0.565	1.20	2.12	3.67	7.60	13.0	22.4
x', cm	0.044	0.022	0.01	0	0	0	0	0	0
B_o/x'	630	2500	9000	∞	∞	∞	∞	∞	∞
Fraction of granular target, G_g	0.49	0.52	0.57	0.63	0.67	0.72	0.79	0.85	0.92
Cumul. crater coverage σ_B	2.21^{-5}	6.64^{-6}	2.02^{-6}	3.17^{-7}	7.28^{-8}	1.55^{-8}	1.51^{-9}	2.67^{-10}	4.50^{-11}

TABLE XXXV. Continued

C. Meteorites--Apollo Group (J_1)

(the projectile is explosively destroyed)

$w_o = 20$ km/sec; $\delta = 3.5$ g/cm^3; radius non-penetrating upper limit, $R_o = 200$ cm (when penetrating, not limited); $n = 3.7$; cumulative number flux, $R > 0$, $dN/dt = 8.4 \times 10^{-14} R^{-2.7}$ per cm^2 and year; cumulative mass $d\mu/dt = 5.5 \times 10^{-11}(R/R_o)^{0.3}$ gram per cm^2 and year. Cratering parameters: $\bar{s}_p = 2.48 \times 10^4 (2 + \frac{1}{3} x_o^2)$ dyne/cm^2 when $x_o < 173$ cm and $\bar{s}_p = 7.4 \times 10^8 (1 - 1\frac{1}{3}/x_o)$ when $x_o > 173$ cm; $\bar{s}_c = \bar{s}_p / 17.6$; $B_o = 2DR$, $x_p = 2pR$, $x_o = 1.6pR$, $x' = x_o(1 - F_B)$; $k = 3.3$, $\gamma = 45^o$,

R, cm	200	100	50	20	10	5	2	1	0.5	0.2
Cumul. mass fraction $R < R_o$	1.000	0.813	0.659	0.501	0.408	0.330	0.251	0.205	0.165	0.12
Cumul. number $R < \infty$	5.15^{-20}	3.34^{-19}	2.18^{-18}	2.57^{-17}	1.68^{-16}	1.09^{-15}	1.29^{-14}	8.40^{-14}	5.44^{-13}	6.49^{-1}
$\bar{s}_c$	3.64^7	3.12^7	2.04^7	4.20^6	1.16^6	3.23^5	5.95^4	$1.8[illegible]^4$	6830	339[illegible]
B_o, cm	13800	7140	3940	2270	1530	1030	612	404	254	117
Cumul. crater coverage σ_B, year^{-1}	0	2.18	6.20^{-11}	2.28^{-10}	5.98^{-10}	1.54^{-9}	5.36^{-9}	$1.2[illegible]^{-8}$	2.81^{-8}	7.39^{-8}
x_o, cm	880	443	224	94.4	49.6	26.0	11.0	5.7[illegible]	2.96	1.24
x', cm	830	432	219	87.7	4[illegible].5	17.0	1.9	0.2	0.0	0.0
Cumul. crater number	5.15^{-20}	3.34^{-19}	2.18^{-18}	2.57^{-17}	1.62^{-16}	8.94^{-16}	8.62^{-15}	4.53^{-14}	2.38^{-13}	2.20^{-1}
B_o/x'	16.6	16.5	18.0	25.9	36.9	60.7	322	2000	∞	∞
G_g	1.00	1.00	1.00	1.00	0.91	0.74	0.57	0.4[illegible]	0.38	0.23

TABLE XXXV. Continued

D. Ejecta from Penetrating Cratering Events

(J_e.; the projectile is not destroyed; $\delta = 2.6$)

Part (a) refers to primary impacts. Contibuting impacts (Apollo -Meteorite type) with R from 400 to 1600 cm (larger impacts are outside reach of "normal" surface sample); typical "feeding" impact $R = 800$ cm, $B_o = 30R = 24000$ cm, yielding largest ejecta blocks $r_{max} = \frac{1}{4}R = r_o = B_o/120 = 200$ cm, $n = 3.875$. Cumulative number influx of ejecta, $r < r_o$, $dN/dt = 1.73 \times 10^{-16} \left[(r_o/r)^{2.875} - 1\right]$ per cm^2 and year; cumulative mass influx of ejecta, $d\mu/dt = 3.47 \times 10^{-7} y$ in gram per cm^2 and year, with $y = (r/r_o)^{0.125}$ Maximum velocity of ejection, $w_{max}^2 = u_s^2 \lambda^2/y^2$, and average $w_o^2 = \frac{1}{2} w_{max}^2$; for parent crater, $\bar{s}_c = 5.7 \times 10^8$ dyne/cm^2, $\rho = 2.6$, $u_s^2 = 2.19 \times 10^8$, $\chi^2 = 0.22$; $\sin\gamma = 0.8\, y$; maximum distance of ~~xx~~ flight from parent crater, $L_{max} = (w_{max}^2/g) \cdot 2 \sin\gamma\cos\gamma$.

Impact into overlay, $w_1/w_o = 0.842$, $s_p = 2.48 \times 10^4 (2 + x^2)$, $\bar{s}_p$ and $\bar{s}_3$ as in Part C of this table, $P = 0.562/r$ (cm^{-1}), $Q = 8.05 r^3 \cos^2\gamma$ $(cm/sec)^2$, $x_o = (\xi_o \cos\gamma)/P$, $x_p = x_o + \frac{1}{2} r\cos\gamma$, $\sigma = \pi r^2$ (cm^2), $\mu = 10.9 r^3$ (gram), $m = 3.47 r$ (g/cm^2), $a^2 p^2 = 0.62/(r\cos\gamma)^2$ $x_o B_o^2 = V_p$(pressure component) $+ V_d$ (dynamic component) $= V$ (total volume), $V_p = 5.72\, \delta\, x_o \sec\gamma$, $V_d = 10.13 k \mu w_o (\bar{s}_p)^{-\frac{1}{2}}$, $x' = x_o(1 - F_B)$, all to be used with the equations of Section II. E. The blocks under oblique incidence are ricocheting and usually settle on the undisturbed surface not far from the ~~earth~~ crater.

Part (b) contains crater statistics for the sum total or ricocheting chains: Cumulative number of craters to indicated limit (B_o), $dN_r/dt = \sum 1.57 \cdot (G_g \Delta N) \cdot (1.5 - 0.5 G_g)$ per cm2 and year (primaries + ricocheting chain), where ΔN is the differential number of primary impacts.

TABLE XXXV, Continued

D. Continued

r, cm	200	100	50	20	10	5	2	1	0.5	0.2
(a) Primary Impacts										
Cumul. mass fraction, y	1.000	0.916	0.841	0.750	0.687	0.631	0.562	0.515	0.475	0.422
Cumul. number, $r < r_o$	0	1.10^{-15}	9.14^{-15}	1.29^{-13}	9.50^{-13}	6.96^{-12}	9.49^{-11}	7.13^{-10}	5.24^{-9}	7.30^{-8}
$\cos\gamma$	0.600	0.681	0.740	0.800	0.835	0.863	0.893	0.911	0.926	0.941
w_o cm/sec	4905	5350	5830	6550	7250	7770	8740	9530	10390	11620
L_{max}, km	2.83	3.55	4.20	5.10	5.98	6.50	7.59	8.41	9.30	10.6
x_o, cm	69.1	58.5	47.9	34.4	25.6	18.2	10.90	7.02	4.36	2.19
k	0.189	0.219	0.256	0.302	0.398	0.472	0.567	0.613	0.646	0.656
V_d/V	0.612	0.611	0.619	0.653	0.712	0.762	0.831	0.873	0.907	0.929
B_o, cm	1460	655	339	143	80.0	44.6	21.0	12.1	7.00	3.26
x', cm	62.7	53.6	43.7	30.6	22.3	15.0	7.89	4.52	2.68	1.11
B_o/x'	23.3	12.2	7.76	4.62	3.59	2.97	2.66	2.68	2.61	2.92
G_g ~~primary~~ Gran. impact	1.00	1.00	0.92	0.81	0.75	0.69	0.62	0.56	0.52	0.46
cumul. number ($cm^{-2} yr^{-1}$)	0	1.10^{-15}	8.82^{-15}	1.13^{-13}	7.54^{-13}	5.03^{-12}	6.27^{-11}	4.28^{-10}	2.88^{-9}	3.66^{-8}
r, cm	0.1	0.05	0.02	0.01	0.005	0.002	0.001	0.0005	0.	
(b) Primary Ricocheting Impacts (numbers reduced to same crater diameter limit, B_o, as in the 10th line above)										
Cumul. Crater number per cm^2 & year	0	1.23^{-15}	1.09^{-14}	1.48^{-13}	1.02^{-12}	7.10^{-12}	9.04^{-11}	6.32^{-10}	4.34^{-9}	5.65^{-8}
Cumul. Crater coverage, yr^{-1}	0	1.18^{-9}	3.33^{-9}	1.00^{-8}	2.00^{-8}	4.17^{-8}	1.20^{-7}	2.68^{-7}	5.72^{-7}	1.76^{-6}
Average x_o cm	61.2	51.7	42.3	30.4	22.6	16.1	9.6	6.2	3.9	1.9
Average x' cm	53.3	44.7	36.4	25.5	18.6	12.5	6.57	3.77	2.24	0.92
Average B_o/x'	27.9	14.6	9.3	5.6	4.3	2.6	3.2	3.2	3.1	3.5

TABLE XCV Continued

(a) Primary Impacts, Continued

r^*, cm	0.1	0.05	0.02	0.01	0.005	0.002	0.001	0.0005	0.0002	0.0001	5×10^{-5}	2×10^{-5}
Cumul. mass fraction, y	0.386	0.355	0.316	0.290	0.266	0.257	0.217	0.200	0.173	0.163	0.150	0.133
Cumul. number $r < r_0$	5.35^{-7}	3.92^{-6}	5.45^{-5}	4.02^{-4}	2.94^{-3}	4.11^{-2}	0.304	3.21	30.6	223	1660	23100
$\cos \zeta$	0.951	0.959	0.965	0.973	0.977	0.982	0.985	0.987	0.990	0.992	0.993	0.994
w_0 cm/sec	12700	13800	15500	16900	18500	20700	22600	24600	27600	30200	32700	33900
L_{max}, km	11.7	12.8	14.6	16.0	17.5	19.8	21.7	23.6	26.4	28.9	31.6	35.8
ϵ_g	0.42	0.39	0.35	0.32	0.29	0.26	0.24	0.22	0.19	0.13	0.16	0.15

* Here r is used for the radius of a secondary fragment, while R would denote the radius of an impacting interplanetary body.

rate of 12 meters or 1560 g/cm^2 in 4.5 x 10^9 years, which gives 3.47 x 10^{-7} gram of debris per cm^2 and year. The rate is slightly less than the average arrived at in Section VII.3 and would correspond to present time and a greater protective layer than the average in the past. The figure is essentially an empirical value, as it is based on the actual volume ejected from observed craters (Table XXIX). With another empirical datum, linking the largest projectile size to the diameter of the crater (Section VII. D), the effective radius of the largest fragment will be assumed to be

$$r_{max} = B_o / 120$$

where B_o is the diameter of the crater in the bedrock from which the fragments were ejected. With a maximum fligth distance of the largest fragments about 3 km (6th line of Table XXXV. D) for a source area of 27 km^2, and 400 million years as their life of survival on the lunar surface (cf. Section X. A), one cratering event per 27 km^2 and 400 m.y. would correspond to 9 x 10^4 events per 10^6 km^2 and 10^9 years; in Table XXIX, this corresponds to B_o = 240 meters, r_{max} = 200 cm as an effective upper limit of debris sizes. Of course, several hundred such blocks could be ejected in one cratering event and, in the case of a large crater, the blocks could be larger such as in a strewn field in Mare Tranquillitatis (Fig. 15) where, on a Lunar Orbiter II photograph, blocks up to 9 meters diameter are discernible. The Surveyor fields, however, seem to agree with the expected average conditions, with blocks only up to meter size visible

(Fig. 5,6). Setting $r_{max} = 200$ cm, $n = 3.875$ [equation (161) and Section VII. D], and the total mass flux being given, the cumulative number and mass infall rates as given in Part D of Table XXXV have been calculated with the aid of well known integral formulae (Öpik, 1956).

The velocities and angles of ejection from the parent crater, independent of the parent velocity when $y > y_2$ and solely depending on crushing strength and density of parent target rock, were calculated according to the formulae of Sections II. B, C, F, with $\lambda^2 = 0.22$ (Table XV) and $s = 5.7 \times 10^8$ dyne/cm^2 at $B_0 = 2.4 \times 10^4$ cm as the assumed typical parent crater diameter according to equation (190). With $\rho = 2.6$ g/cm^3, this gives $v_s{}^2 = 2.19 \times 10^8$ (cm/sec)^2 and a maximum velocity of ejection

$$w_{max}{}^2 = (\lambda u_s / y)^2 \quad , \; w_{max} = 6950/y \text{ (cm/sec)}$$

where y is the cumulative relative mass as given in the third line of the table, identical with fractional crater volume of Section II. B. The average velocity of ejection is assumed equal to $w_0 = w_{max}/\sqrt{2}$, although $\frac{2}{3}\, w_{max}$ could also be used: the arbitrary span of the model is much greater, anyway. The upper part of Table D(a) (lines 2 to 5) contains these source data of overlay--flux, angle, velocity and range L of the fragments.

The ejecta are landing at same velocity and angle as those of ejection. This is the low-velocity problem of impact into granular target, solved with the aid of the equations of Sections II. E, F. The lower part of the table contains the calculated cratering data, especially B_0, the crater diameter, x_0: the penetration, and x', the apparent crater depth as corrected for fallback.

We note that, in our schematically regular model, the ejecta radii are assumed to be a unique function of y, which defines the position and shock pressure inside the crater during ejection. This is assumed to be matched in a unique manner by the increasing cohesive strength as the particle size decreases, an assumption which led to a successful prediction of overlay particle size distribution (Section VII. D). In nature there will be, of course, considerable statistical fluctuation around the average relationships. Also, those high-velocity ejection phenomena connected with ray craters are here not taken into account. Our model is meant to represent the bulk of the ejection processes, while the exclusive ray-forming processes are not quantitatively prominent enough to modify essentially our conclusions (cf. concluding paragraph of Section V.C).

Table XXXV purports to describe quantitatively the cratering events at impact into the <u>granular</u> target of overlay. Yet when the projectile happens to hit a fragment considerably larger than itself, the projectile will react solely with this fragment; the impact will then be virtually as onto hard rock, and not of the granular type. The last line in each of the sections of the table contains a probability factor, G_g, derived as subsequently described and indicating the fraction of impacts which are of the granular type, while the remainder, a fraction of

$1 - G_g$, are limited to impacts into single large grains or blocks and are thus of the hard-target type as dealt with in Section II. B.

For a hypervelocity projectile (Groups J_M , J_0 and J_1 of the table), a small grain though larger than the projectile itself may be demolished completely and the radial momentum transmitted to other grains. The ultimate result will not differ essentially from a truly granular cratering where the grains are all smaller than the projectile. The blocking effect of large grains will be felt only when the shock wave from the collision does not transcend, partially at least, the boundaries of the target grain, in other words, when the virtual crater diameter, B_R , produced by the impact into the hard substance of the target grain by a projectile of radius R, will be of the order of the target grain diameter, 2 r (capital R stands for projectile radius, r for target grain radius). On a model of a circular target-grain cross section , the blocking effect, measured by the product of target grain area, πr^2, and the blocking efficiency was roughly evaluated as follows (blocking efficiency measured by the azimuthal angle of shielding by the grain).

(1) For $r \gg B_R$, blocking effect πr^2.

(2) For $r = B_R$ and Δ = distance between grain center and impact center, the rough estimate by zones of Δ yields:

Δ =	0	0.5r	r	1.5r
blocking angle	..	..	150	..

f_{20}

Δ =	0		0.5r		r		1.5r
blocking angle	...		....		130°		...
blocking efficiency	= 1		1		5/12		0
aver. bl. efficiency		1		17/24		5/24	
area/πr^2		0.25		0.75		1.25	
blocking effect/πr^2		0.25		51/96		25/96 total	$(25/24)\pi r^2 \pm$.

(3) For $r = \frac{1}{2}R_R$, total blocking effect $= (5/12)\pi r^2 \pm$.

(4) For $r = \frac{1}{4}R_R$, the surface of the grain (not necessarily its root) is destroyed completely at contact and the blocking effect is zero.

It is concluded therefore that, for hypervelocity (destructive) impacts, the blocking effect of large target grains can be represented satisfactorily by the grain area, πr^2, when $r > r_b = \frac{1}{2}R_R$, and taken equal to zero when $r < r_b$; r_b can be called the granular blocking limit. From the equations of Section II. B, with $\rho = 2.6$ g/cm^3, $s_p = 2 \times 10^9$, $s_c = 9 \times 10^8$ dyne/cm^2 for the hard target material, we find for the micrometeorities (J_M), p = 4.01, D = 7.82, R_R = 15.3 R and conveniently r_b = 8R. For the visual dustballs (J_o), p = 0.934, D = 10.7, R_R = 21.4 R and the blocking limit r_b = 11 R. For the Apollo-meteorite group (J_1), D = 14.9 (Table XV), R_R = 29.8R and r_b = 15R. All these limits are quite high, due to the destructive efficiency of the high-velocity impact.

Different is the case with the secondary ejecta(J_e); at their low velocities, they are reflected without destruction from a larger target grain. Considering only head-on collisions, a fragment of velocity w_o and mass μ_R will impart to a grain of mass μ_r a forward velocity of

$$w_r = \mu_R w_o (1+\lambda)/(\mu_r + \mu_R)$$

and will itself acquire a reflected velocity of

$$w_R = w_o\ (\mu_R - \lambda \mu_r)/(\mu_r + \mu_R) \qquad (193)$$

which is negative when the projectile is bouncing back. In the limiting case of $\mu_R / \mu_r \to 0$, $w_R = -\lambda w_o$, where $\lambda \sim 0.5$ ($\sqrt{0.23}$ according to experiments mentioned in Section II. F) is the linear kinetic elasticity, comparatively high for this case of a single collision of rocky particles. The target grain which was hit proceeds further as an independent projectile, but its penetration $x_o = x_r$ into the granular substratum will be smaller than the normal penetration of the projectile, $x_o = x_R$. With the equations of Section II. E, the degradation of the target, measured by the ratio of the penetrations was found to be as follows:

$r/R =$	1	2
$\mu_r/\mu_R =$	1	8
$x_r/x_R(\lambda=0)=$	0.625	0.294
$x_r/x_R(\lambda=0.5)=$	0.825	0.382

It appears that a blocking limit of $r_b = 2R$ can be assumed. On account of the slow variation of the cumulative mass of the overlay ejecta with radius (Table XXXV. D(3) 4th 2nd line), the exact limit is irrelevant. The blocking effect is thus equal to the relative cumulative cross section. $\sigma_B = \sum \pi r^2$, of the overlay particles with $r > r_b$. The surface frequency exponent of particle sizes is obviously $n - 1$, where n is the volume frequency exponent in equation (161) (each particle lying on the surface occupies a volume $dV \sim \frac{4}{3}r$ per cm^2, whence an additional r-factor). The cumulative cross section area is then (to a constant factor) $\int r^{-n+1} \cdot r^2 dr = \left| r_2^{4-n} - r_1^{4-n} \right|$, and this is exactly the same as the expression for cumulative volume or mass reckoned per volume. Hence the blocking effect, $1 - G_g$, equals the cumulative mass of the fragments for $r > r_b$, and G_g , the fraction of granular target impacts, equals thus the cumulative mass to $r \leq r_b$ as tabulated in the ~~second~~ 1st line of Table XXXV, Part I (a).

As a consequences of the broad frequency distribution of overlay particle sizes, quite a considerable proportion $(1 - G_g)$ of the impacts are non-granular in character, the proportion increasing with decreasing size. The mean values (weighted by mass) of the granular impact fractions can be assumed to be: micrometeorites (J_M), $\overline{G}_g \approx 0.40$; visual dustballs (J_o), $\overline{G}_g = 0.53$; Apollo meteorites (J_1) non-penetrating), $\overline{G}_g = 0.78$; secondary ejecta (J_e), $\overline{G}_g \approx 0.55$. Thus, the granular target model alone cannot serve even as a first approximation. Of course, "blocked" impacts into large grains or blocks will not ~~be~~ produce craters observable in overlay but only small craterlets or pockmarks on the rocky targets. All the craters in overlay recognizable as such on Surveyor pictures must therefore be produced in the granular impact process; the factor G_g gives their number

244

relative to the total, and can be called the "overlay cratering fraction".

C. The Astronautical Hazard

The astronaut on the lunar surface is exposed to the bombardment by flying secondary debris from cratering impacts elsewhere on the moon, though mostly from his immediate vicinity, in addition to direct bombardment by interplanetary particles. The total mass of the secondary fragments exceeds 30 times the incoming meteoritic mass; although its momentum, on account of the low velocity, is only one-sixth of the meteoritic one (Table XXXIV), the hazard from this source may appear serious. Thus, from the cumulative numbers of Table XXXV, the number of hits per 100 m^2 and 10 years would be:

k or r $\geq$ x cm	0.02	0.2	2
J_M (micrometeorites)	180	...	...
J_0 (dustballs)	...	0.0029	1.5×10^{-3}
J_1 (Apollo meteorites)	0.032	0.00006	1.3×10^{-7}
J_e (secondary ejecta)	550	0.73	9.5×10^{-4}

Among the small particles, the micrometeorite impacts of course prevail over the ejecta, on account of their much higher velocity, despite their mass being only one-third of the mass of the ejecta. Among the larger particles the ejecta appear to dominate.

However, unlike the direct meteoritic components which appear as a flux of statistically independent individuals, the ejecta are coming in in bursts from large and rare cratering events in the vicinity. They are spaced by long intervals of time during which no ejecta are falling. The total frequency of the parent cratering events (primary meteorites and secondary ray-crater ejecta), given by the cumulative sum in the 4th line of the Table XXIX , is 2.3×10^8 per 10^6 km^2 and 10^9 years. The maximum flight distance of fragments with $r > 0.2$ is 10.6 km, so that spray of this size can reach a given point from a surrounding area of only about 350 km^2, which corresponds to an expectation of one event in 14000 years. 90 per cent of the spray comes from $B_0 > 49$ m [Table XXIX (B), 9th line] , with an expectation of one event in 6×10^5 years. For comparison, the expectation to be killed in a car accident in the U.S.A. is one in 5000 years, and to be injured one in 200 years. Clearly, with all the other sources of accidents on earth--earthquakes, hurricanes, fires and warring hostilities--the moon is a much safer place to stay on; in any case, the hazard from flying secondary debris of component J_e can be disregarded altogether, not only because of their low velocities but also because of their wide spacing in time.

There remains the hazard from direct individual interplanetary meteorite hits, which may be more dangerous on account of the greater velocities involved. The shielding by the lunar body reduces the hazard precisely to one-half that in interplanetary space. Table XXXVI contains the relevent expectations based on data from another publication (Öpik, 1961a).

On account of the micrometeorites, the hazard in the case of weak protection is quite considerable; an astronaut with 1-mm magnesium sheet metal armour runs the risk of being badly hit during 5 years of exposure. With 4 mm protection, the risk drops to one hit in 70,000 years. Thus, from this standpoint also, the moon may be easily made a much safer place to stay on than our earth.

D. Observability/Shallow of Craters and Ricocheting

From the B_o/x' ratios in Table XXXV it appears that the craters produced by secondary fragments (J_e, Part D) are deep and must be well observable when not degraded by erosion. On the contrary, the craters produced by the meteoritic components are shallow and practically non-observable even when fresh. From a study of Surveyor I pictures and crater counts on them by the NASA team at the sun's altitudes of 20° and 8° (Jaffe et al., 1966b, pp. 18--25) it appears that those with profile ratio of $B_o/x' < 20$ were certainly detectable (unless covered by shadows inside larger craters); the detection of those with a profile ratio from 20 to 50 is dubious, and those with $B_o/x' > 50$ are certainly missed (on Fig. 3, the largest ratio is 120 for craters observed on the moon at large; however, it seems that a ratio of 80 is an upper limit for recognition by repeated observations on the moon, and at the Surveyor conditions 50 appears to be a generous upper limit). Taking 50 as limit, we can say that the craters produced by micrometeorites and dustballs (Parts

A and B of Table XXXV) are unobservable even when fresh, although the volume disturbed can be large and may be the chief contributor to the migration of dust; these components do not contribute to the roughness of the surface but cause only a smoothing or polishing and sweeping effect. In the Apollo Group (Part C of the table), craters in overlay larger than 15 meters in diameter ($R > 10\frac{1}{2}$cm) have observable profiles when fresh, but still are relatively shallow. On the contrary, secondary ejecta (Part D of the table) produce in overlay deep well observable craters, the profile ratio decreasing with size. Therefore practically all craters less than 15 meters in diameter observable on the lunar surface must be produced by the secondary ejecta.

A beautiful example of such a feature is rimmed Crater No.5 of the Surveyor I pictures (Jaffe et al., 1966a,b ; Newell 1966). It is placed about 11 meters to the south-east (astronautical) from the spacecraft, and can be seen left of the middle on Fig.5, and on Figs. 16 and 17 at different illumination, with the sun at a low angle on the latter. Its diameter is 3.3 meters and the depth is stated to be $\frac{2}{3}$ m. From a study of the pictures I find a smaller depth, $x' = 34$ cm as the depth below the undisturbed surface, which gives $B_o/x' = 9.7$. The nearest description is for $r = 50$ cm as the secondary fragment radius in Part D of Table XXXV which gives $B_o = 339$ cm, $x' = 44$ cm, $B_o/x' = 7.8$. The observed crater is somewhat shallower, possibly due to some erosion or a different angle of impact and velocity (if the figures are taken literally).

The boulder which produced it, however, is missing from the interior of this--and similar other craters. It must have ricochetted out, possibly even breaking up into a few large pieces, and the somewhat eroded boulder visible in the right corner of the picture (measuring 59 x 26 x 15 cm above ground), or another in the south-west (astronautical) (50 x 25 x 15 cm above ground), or both, could be (improbably, however, as they are too near the crater) portions of the original projectile. The remarkable feature of small and large, often angular boulders lying on top of the lunar soil (cf. Surveyor photographs) without definite traces of cratering around them, can be explained by multiple ricocheting of the impacting fragments, something similar to what happened to surveyor III ("Tidbinbilla"), (NASA, 1967) although in this case the vernier rockets were mainly responsible. If λ^2 is the kinetic efficiency of ricocheting (in the sense of Section II. F), in repeated jumps the velocity would decrease in a ratio of λ, each time making smaller craters, so that in the last jump no visible crater is produced, the fragment finally coming to rest at a depth of not more than a few centimeters as did the surveyor footpads. With $\lambda^2 = 0.09$, $\lambda = 0.3$, initial velocity $w_0 = 60$ m/sec as in the table, the ricochetirg velocities and distances will be ($\gamma = 45^o$):

ricochet	0 (impact)	1	2	3	4
w, m/sec	60	18	5.4	1.62	0.49
L, jumpins distance λw meters		200	18	1.62	0.15

The Surveyor experiments permit of an estimate of the ricocheting elastic efficiency, $\lambda = \lambda_r$. Oscillations of the spacecraft on hard ground had a frequency of 8.0 sec^{-1}, while on the lunar surface the frequency was 6.5 sec^{-1} (NASA, 1967, II, p.146). For harmonic oscillations this means that, at equal peak load, the amplitude A_o on hard ground was increased in the ratio of $(A_o + A_s)/A_o = 1.51$ on the moon, yielding $A_s = 0.51\ A_o$—the lunar surface responding with nearly one-half the amplitude of the spacecraft (which was about 0.2 cm). From computer-simulated strain gage data of landing on a hard surface (Jaffe et al., 1966b, p. 73), a very low value for the shock absorber, $\lambda_o \sim 0.114$, results, while on the lunar surface the velocity decay ratio for Footpad 2 of Surveyor I was 0.20 (the velocities being given by gt, where $g = 162$ cm/sec^2 on the moon, and t is the time of free flight between two touchdowns). Hence $(\lambda_o{}^2 A_o + \lambda_s{}^2 A_s)/(A_o + A_s) = (0.20)^2$ and, with the ratio of A_s to A_o given, $\lambda_o{}^2 + 0.51\ \lambda_s{}^2 = 0.06$ and $\lambda_s{}^2 = 0.092$, accidentally almost exactly the value (0.03) estimated in Section VIII for the kinetic efficiency of lunar soil in a cratering process. The value of $\lambda^2 = \lambda_s{}^2 = 0.09$, $\lambda = 0.3$ seems to be well justified for all impact processes in the lunar soil, to be compared with a value of about 0.5 for hard rock.

As a consequence of ricocheting, a rock fragment impinging onto the lunar surface with a moderately low velocity will produce several craters in successive leaps, the velocity de-the

creasing with a damping ratio of λ. The upper limit of initial velocity for survival of the fragment at impact is given by equation (10); with $\rho = 1.3$, $s_p = 2 \times 10^9$, it is of the order of 0.5 km/sec. Hence cratering from component J_e is not completely exhausted by the data for primary impacts as contained in Table XXXV (D) (a). Table XXXVII describes some crater chains produced by ricocheting, schematically calculated by assuming a constant angle γ throughout the ricocheting sequence. After a ricochet from a granular surface (probability G_g), the velocity is assumed to decrease by a factor of $\lambda = 0.2$ with a crater imprint to be left behind; a ricochet from a hard target (large grain, $r_b \gg 2r$) does not make a crater but the damping factor is larger, $\lambda = 0.5$ being assumed. The notations are those of Table XXXV and Sections II. E, F.

The 9th column gives B_o^2 , the relative cratering area; the 10th gives $x_o B_o^2$ or the total volume excavated, in units of 0.363 cm^3; the 11th gives $x' B_o^2$, the volume ejected beyond the crater rim, in same units; the 12th column contains kw_c , or the average radial momentum imparted to 1 gram of the "volume affected" [equations (2) and (36)]. The chain is terminated either when $L < \frac{1}{2} B_o$, or when the altitude of the rebound is less than x_o , so that the projectile falls back into its last crater. The last line in each section of the table shows the "amplification ratio" or a factor by which each of the items is increased in the sum total of the chain , as compared to a first and direct impact into granular target. Except for the

TABLE XXXVII

Sample Calculated Ricocheting Crater Chains, Component J_e

(1) $r = 0.5$ cm; $G_g = 0.52$. Intermittent Granular and Hard Target

($G_g = 0.5$) Calculated

Granular Start

No. of Impact	w_0 cm/sec	x_0 cm	B_0 cm	k	x' cm	B_0/x'	L cm	Area (0.785cm^2)	Cratering Volume (0.363cm^3) total	ejected	momentum (cm/sec per gram
S_1 Gran.	10380	4.36	7.00	0.646	2.63	2.61		49.0	214	130	6710
							4.2)^4				
S2 Hard	3110	...	...	...	...	...		...	...	...	...
							1.05^4				
S_3 Gran.	1555	2.24	4.28	0.431	1.13	3.79		18.3	41	21	750
							944				
S_4 Hard	466	...	...	...	...	...		...	...	...	...
							236				
S_5 Gran.	233	0.46	2.73	0.201	0.36	7.7		7.5	3	3	50
							21.3				
S_6 Hard	70	...	...	...	...	...		...	...	...	...
							5.3				
S_7 Gran.	35	0.014	1.13	0.108	0.014	33		1.3	0	0	0
							0.5				
S_8 Stop	...	...	...	...	...	...		0	0	0	0
Chain total							5.35^7 ~~x 10~~^{6}	76.1	258	154	7510
Amplification ratio							1.27	1.55	1.17	1.16	1.12

250

TABLE XXXVII, Continued

(2) $r = 0.5$ cm; $G_g = 0.52$. Intermittent Granular and Hard Target ($G_g = 0.5$) Calculated

Hard Start

No. of Impact	w_o cm/sec	x_o cm	B_o cm	k	x' cm	B_o/x'	L cm	Area (0.785cm²)	Cratering Volume (0.363cm³) total	Cratering Volume ejected	Radial momentum cm/sec per gram
S_1 Hard	10380	...	...	...	...	...		...	...	...	...
							1.16^5				
S_2 Gran.	5190	3.55	5.92	0.629	1.87	3.16		35.0	124	65	3260
							1.05^4				
S_3 Hard	1555	...	...	...	...	...		...	...	...	...
							2620				
S_4 Gran.	778	1.53	3.60	0.376	0.82	4.39		13.0	20	11	290
							236				
S_5 Hard	233	...	...	...	...	...		...	...	...	...
							59				
S_6 Gran.	117	0.145	2.14	0.135	0.127	16.7		4.6	1	1	20
							5.3				
S_7 Hard	35	...	...	...	...	...		...	...	...	...
							1.3				
S_8 Gran.	17.5	0.004	(0.77)	0.106	0.004	192		(0.6)	0	0	0
							0.1				
S_9 Stop	...	...	...	...	...	...		0	0	0	0
			Chain total				1.29^5	53.2	145	77	3570
			Amplification ratio				3.07	1.09	0.68	0.59	0.53

TABLE XXXVII, Continued

(3) $r = 0.5$ cm; $G_g = 0.52$. All Granular Target ($G_g = 1$) Calculated

No. of Impact	w_0 cm/sec	x_0 cm	B_0 cm	k	x' cm	B_0/x'	L cm	Cratering Area (0.785cm^2)	Cratering Volume (0.363cm^3) total	Cratering Volume (0.363cm^3) ejected	Radial momentum (cm/sec per gram)
1	10380	4.36	7.00	0.646	2.68	2.61		49.0	214	130	6710
							4.20^{4}				
2	3110	2.98	5.12	0.567	1.54	3.32		26.2	78	40	1760
							3780				
3	933	1.71	3.76	0.403	0.90	4.18		14.1	24	13	370
							340				
4	280	0.58	2.90	0.232	0.41	7.0		8.4	5	3	70
							30.6				
5	84	0.075	1.86	0.127	0.063	17.4		3.5	0	0	10
							2.7				
6	25	0.0070	(0.93)	0.107	0.0068	137		(0.9)	0	00	0
							0.2				
7 Stop								000	0	0	0
			Chain total				4.61^{4}	102.1	321	186	8920
			Amplification ratio				1.10	2.08	1.50	1.43	1.33

(4) $r = 50$cm; $G_g = 0.92$. All Granular Target ($G_g = 1$) Calculated

No. of Impact	w_0 cm/sec	x_0 cm	B_0 cm	k	x' cm	B_0/x'	L cm	Cratering Area (0.785cm^2)	Cratering Volume (0.363cm^3) total	Cratering Volume (0.363cm^3) ejected	Radial momentum (cm/sec per gram)
1	5830	47.9	339	0.256	43.7	7.8		1.15^{5}	5.50^{6}	5.03^{6}	1490
							1.88^{4}				
2	1749	23.3	293	0.192	18.6	15.7		0.86^{5}	2.01^{6}	1.60^{6}	340
							1690				
3	525	11.3	242	0.153	5.7	42		0.59^{5}	0.67^{6}	0.34^{6}	80
							152				
4	158	5.0	191	0.129	0.54	354		0.36^{5}	0.18^{6}	0.02^{6}	20
							14				
5 Stop (47)	...	...	...	...	...			0	0	0	0
			Chain total				2.07^{4}	2.96^{5}	8.36^{6}	6.99^{6}	1930
			Amplification ratio				1.10	2.57	1.52	1.39	1.30

TABLE XXXVII, continued

(5) $r = 200$ cm; $G_g = 1.00$. All Granular Target ($G_g = 1$) Calculated

No. of Impact	w_0 cm/sec	x_0 cm	B_0 cm	k	x' cm	B_0/x'	L cm	Cratering: Area (0.785cm²)	Volume (0.363cm³) total	Volume (0.363cm³) ejected	Radial momentum (cm/sec per gram)
1	4905	115.2	1460	0.139	62.7	23		2.13^6	2.46^8	1.34^8	930
							1.29^4				
2	1472	56.3	1050	0.149	26.0	40		1.10^6	0.62^8	0.29^8	220
							1160				
3	442	15.0	844	0.124	4.7	179		0.71^6	0.11^8	0.03^8	50
							105				
4 Stop(133)	...	...	...	...				0	0	0	0
			Chain total				1.41^4	3.94^6	3.19^8	1.66^8	1200
			Amplification ratio				1.09	1.85	1.30	1.24	1.29

TABLE XXXVIII

Comparison of Ricocheting Amplification Ratios

$r = 0.5$ cm	Crater Area	Volume excavated	Volume ejected	Radial momentum	All, average
Average [(1)+(2)]/2(G_g = 0.50)	1.32	0.925	0.875	0.825	...
Case (3)(all soft)(G_g=1.00)A_0	2.08	1.50	1.43	1.33	...
Correction factor to(3)	0.635	0.616	0.612	0.620	0.621

total cratering area, these factors are all within the order of unity.

While G_g is the probability of impact into granular target, a ricocheting chain may have all combinations of hard and granular impacts according to the binomial law of probability. To calculate all these combinations would mean stretching our numerical analysis too far; the calculations are very approximate anyway, although certainly better than a mere qualitative appraisal.

For $r = 0.5$ cm, $G_g = 0.52$, three typical cases have been considered: (1), an alternating chain of hard and "soft" impacts, starting with a soft one; (2) a similar chain, starting with a hard impact; (3) a "soft" chain throughout. The true statistical mean for $G_g = 0.50$ should not differ essentially from the average of the first two cases, and a comparison with the third case could show then the error of neglecting the hard impacts altogether, at the given value of $G_g = 0.50$. The comparison is made in Table XXXVIII. The last line gives the ratio of the first two lines, or the correction factor in a transition from $G_g = 1$ to $G_g = 0.5$. Within the uncertainties of the model, the factor is the same for all four parameters, its average value of 0.621 showing the result of the difference in the elastic constant ($\lambda = 0.3$ and 0.5, respectively) between the two cases. For equal λ, the true average should equal $G_g = 0.5$ exactly, but because elasticity in hard impacts is higher, the chain loss is partly compensated; as compared to the "all soft" chain

($G_g = 1$), the correction factor of the amplification ratio can be assumed to be $G_g + \frac{1}{2}G_g(1 - G_g) = 1.5G_g - 0.5G_g^2$, which gives $1.5G_g$ at $G_g \to 0$, 0.625 at $G_g = \frac{1}{2}$, and 1 at $G_g = 1$ which very closely describes the true factor at a "soft" amplification ratio of 1.5 and is a good approximation for other ratios.

The amplification ratios, A_o, calculated at $G_g = 1$ do not differ very much in the sample cases (3), (4) and (5) of Table XXXVII, so that averages can be taken: $A_o = A_a = 2.17$ for cratering area, $A_o = A_v = 1.44$ for total volume excavated and $A_o = A_e = 1.35$ for volume ejected. The chain amplification ratio for rock fragments or hard grains impacting with moderate velocity ($\lesssim 500$ m/sec) and ricocheting on lunar overlay is then

$$A_q = G_g A_o (1.5 - 0.5\, G_g), \qquad (194)$$

with the proper value of A_o corresponding to the particular parameter q (area, volume, etc) to be used. The sum total for the ricicheting chain is obtained by applying the factor A_q to the area, volume, etc. of a direct "soft" first impact. This kind of amplification of cratering by ricocheting can be take place only when the projectile is not destroyed, i.e. in the case of component J_e. Another kind of amplification, caused by the granular ejecta themselves, is common to all types of impact. Because of smallness of the grain, small k and G_g values and low velocities of ejection, cratering proper in overlay by the secondary ejecta from the overlay itself can be discounted, but as a factor of mobility of the "dust" this has to be considered. Only transmission of radial momentum is of importance here.

Of the ejecta, only those with $w > u_s$ (all notations are those of Section II) are to be considered as a factor of causing further mobility in the target. This limits the active mass to a fraction of $\lambda x'/x_p$ of the total mass affected; on the other hand, the velocity of ejection increases toward the inner portions of the crater [equations (16)---(26)] which partly balances the limitation of mass. For hypervelocity impact, the ratio of radial momentum transmitted by the ejecta into the surroundings to radial momentum of the primary cratering event is found to be

$$J/J_I = 4\lambda k\left[\ln(\lambda k_0 w_0/25u_s) + (25u_s/\lambda k_0 w_0)^3 - \frac{1}{3}\right] \cdot x'(1.5G_g - 0.5G_g^2)/9x_p,$$

where k_0 and w_0 are radial momentum factor and velocity for the primary event, and k is the radial momentum coefficient in the secondary shower. For micrometeorite impact, $w_0 = 6.0 \times 10^5$ cm/sec, $u_s = 200$ cm/sec, $k_0 = 2$; with $\lambda = 0.3$, $k = 0.2$ (cf. Table XXXVII, $r = 0.5$ cm, at $w' = 200$ cm/sec), and from Table XXXV (A), $G_g = 0.4$, $x'/x_p = 0.75$, the factor in square brackets (accounting for increased velocity of ejection from the interior) becomes 4.0 and $J/J_I = 0.04$---an utterly insignificant increase. For non-destructive impact (J_e), the gain in total momentum from ejecta is still smaller, and can be neglected completely. Thus, only ricocheting is of significance in amplifying the action of primary impacts on overlay, while the contribution from secondary ojecta is too small to be taken into account.

XA The amplification factor in (194) consists of two distinct factors : G_g , the straightforward probability of "soft" cratering, which thus rules the number of successful cratering events in each ricocheting step, the same as for the primary impacts; and the product A_o $(1.5 - 0.5G_g)$ which measures the total quantitative gain in the parameter (sum of area, volume, etc, of craters) for one primary impact. We may assume the crater parameter (area, volume) to decrease in geometrical progression with each ricochet (which is an idealization of a more complex process) (cf. Table XXXVII); if Δ is the common ratio of the progression (assumed infinite), evidently

$$\Delta = \left[A_o\ (1.5 - 0.5G_g\ ) - 1\right] / \left[A_o(1.5 - 0.5\ G_g\right] . \qquad (195)$$

At $G_g = 1$ as for the "test case" of completely granular target,

$$\Delta_o = (A_o - 1)/A_o \text{ or } A_o = 1/(1 - \Delta_o\ ) . \qquad (196)$$

For crater area (B_o^2), $A_o = 2.17, \Delta_o = 0.539$ whence for crater diameter (B_o), $\Delta_o = (0.539)^{\frac{1}{2}} = 0.734$ and $A_o = 3.76$. For total crater volume $(B_o^2 x_o)$, $A_o = 1.44, \Delta_o = 0.306$; this is the product of the common ratios for B_o^2 and x_o, whence the ratio for crater depth or penetration (x_o) becomes $\Delta_o = 0.306/0.539 = 0.566$ with $A_o = 2.30$. Similary, for the apparent depth (x'), $\Delta_o = 0.480$, $A_o = 1.92$. This of course is an oversimplification, as can be seen from Table XXXVII, and is meant only to convey an overall idea of the ricocheting process which is too complicated to be represented by a uniformly decreasing geometrical progression. Nevertheless, for the sake of simplicity, some of the ricocheting chain parameters can be expressed through such a progression of a constant common ratio, with an error of a few per cent only.

The cratering area of a ricocheting chain, according to equation (194), is amplified by a factor of 2.17 as compared to the parent crater when $G_g = 1$. However, the ricocheting craters are smaller, and when the sum total (cumulative number, area, volume) to a fixed limit of crater diameter is taken, the ricocheting members arise from larger and less numerous crater sizes, so that the relative contribution at the fixed limit is less than 2.17. The actual contribution depends on the frequency function of the primary diameters. Similarly, the contribution to crater numbers is also a decreasing progression. With an emprical value of $n = 3.27$ as representing the cumulative primary crater numbers B_o^{-n} between $B_o = 339$ and 7.0 cm ($r = 50$ & 0.5 cm, last line of Part (a), Table XXXV. D), and with the progression ratios as quoted above, simplified expressions for the ricocheting chain parameters were adopted as follows. For the cumulative crater number, primary + ricochets, to same limit B_o,

$$dN_t/dt = 1.57 \sum (1.5 - 0.5\, G_g)(G_g \Delta N) \qquad (197)$$

was assumed, where ΔN is the differential frequency of primary impacts, or $(G_g \Delta N)$ the differential ~~frqm~~ frequency of "soft" (granular) primary impacts [last line of (a), Table XXXV. D].

The cumulative crater coverage to limit B_o (area per cm² & year, or fractional area per year) is then

258

$$\sigma_B = 0.785 \sum B_1 B_2 \Delta N_{\psi} \qquad (198)$$

where ΔN_{ψ} is the differential frequency of crater numbers (primary+ricochets) for the interval from B_1 to B_2 as can be obtained from (197) or from the 1st line in Part (b), Table XXXV. D.

Through admixture of degraded shallower ricochets, crater depth is decreased. The depth-to-diameter ratio in a chain forms a progression with a common ratio of 0.566/0.734 = 0.772 for x_0/B_0, and one of 0.480/0.734 = 0.653 for x'/B_0. With $0.734^{+\alpha} = 0.365$ as the "degradation ratio" of crater numbers (ratio of ricochet crater numbers to primary crater numbers at B_0 = const.) for a ricocheting diameter decrement of 0.734, the average penetration, x_0, at constant crater diameter, requires a correction factor of

$$(1 - 0.365)(1 - 0.365 \times 0.772) = 0.884,$$

and the apparent depth, x', must be similarly multiplied by a factor of 0.834. It turns out that, despite multiple ricocheting, neither the crater numbers nor their total areas and volumes are changed very much as compared to the primary impacts when statistics are made to constant crater diameter limits. The degraded chain members join the ~~groups~~ more numerous groups of smaller craters where their numbers are relatively small and little affect the average.

In Part (b) of Table XXXV. D the ricocheting chain data, primary and secondary members counted to the same limit of B_0, are given.

E. <u>Overlapping and Survival of Craters</u>

Table XXXV contains the predicted rates of crater formation from the main sources. The actual crater numbers depend on the balance of formation and removal.

Two main processes of removal of craters by extraneous agents can be discerned: through superposition or overlapping of a later larger crater; and through erosion by smaller cratering impacts. Erosion works gradually, exponentially with time, and cannot erase a crater completely although it may become too shallow for recognition; this will be discussed in a subsequent section. Overlapping changes the terrain completely and no trace of a small crater can be expected to remain when it happened to fall within the bounds of a later, sufficiently large crater. Quantitative estimates of overlapping can be made on the basis of Table XXXV.

Only a very schematic approach to the problem can be justified. The demarkation line between "small" and "large" craters cannot be sharp. Yet without allowing for intermediate transitional cases, we choose a conventional sharp margin of crater size for deletion by overlapping which, from some rough estimates, should lead to more or less the same statistical result as mathematical adaptation with gradual transition.

Let B_c, x' be the diameter and apparent depth of the earlier crater, B_a and $x_0 = x_a$ the diameter and depth of penetration of the later crater. Several conditions of removal can be set up to be applied in different cases.

The overall condition of removal or erasure is set by a effective minimum ratio of diameters which we find must be close to

$$B_a \geqslant 2\,B_o \quad ; \tag{199}$$

also, the center of B_o must fall within the boundary of B_a. This condition is sufficient only when the larger crater digs to sufficient depth, namely when

$$x_a > \tfrac{1}{2}\,x' \tag{200}$$

In such a case the rate of removals, ν_B , is evidently equal to the cumulative coverage by craters larger than 2 B_o,

$$\nu_B = \sigma_{2B} \tag{201}$$

When (200) is not fulfilled, or when the larger crater is much shallower than the small one, partial filling to a depth of $2x_a$ after one overlap is assumed, and the rate of removals becomes

$$\nu_B = 2x_a\,\sigma_{2B}/\,x' \tag{202}$$

A variant consists in selecting $B_a \geqslant cB_o$, with $c \geqslant 2$ and such that (200) is fulfilled and setting

$$\nu_{B_o} = \sigma_{cB} \tag{203}$$

Of the alternatives presented by (202) and (203) that is to be chosen which yields the larger rate of removal.

Table XXXV contains only those components of impacting flux which do not penetrate the overlay at present. A fourth component, represented in Table XXIX in so far as it does not overlap with those of Table XXXV, must be added although it is important only in the larger crater classes. The "primaries" of this component are essentially an extension of the Apollo

-Meteorite group of Table XXXV and shall be entered only beginning with $B_{o\ av} > 129$ meters ($B_c > 114$ m). The "secondaries" in Table XXIX are primaries from the standpoint of Table XXXV; they are probably energetic ejecta from ray craters with respect to which component D (J_e) of Table XXXV is secondary. An upper limit to crater size is also set at $B_{o\ av} < 233$ m ($B_o < 325$ m), in conformity with our assumption that our region is "normal" and beyond the reach of large craters. In such a manner the area coverage by the additional " component J_c" of the large craters, calculated from Table XXIX, is given in Table XXXIX.

In Table XL a summary of crater formation and removal by overlapping is given. Only craters with a profile ratio of $B_o / x' < 50$ at the moment of formation are included. This restricts the small-crater statistics chiefly to components J_e, and part of J_1 (Table XXXV, D & C), in the larger sizes supplemented by component J_c (Tables XXXIX and XXIX). Micrometeorites and dustball meteors (Table XXXV, A & B) produce flat unrecognizable craters which are not included in the counts, although their ability of deleting smaller craters by overlapping must be reckoned with.

The top of the table gives the necessary explanations. F_i (F_o) in the 5th, 4th or 10th columns of each subsection is the theoretically calculated differential rate of cratering (on the basis of observed interplanetary populations and, for J_c, from the rate of growth of overlay, itself based in turn on

264

observed excavated crater volume), with allowance for the factor G_g or the proportion of granular impacts; its cumulative rates are given in the 1st line of Table XXXV, D (b).

Without yet allowing for erosion, the time variation of crater area density n_i, subject to creation rate F_i and deletion rate ν, is determined from the differential equation

$$dn_i/dt = F_i - \nu n_i .$$

When integrated from $t = 0$, $n_i = 0$ to $t = t_o$, $n_i = n_i$, this yields

$$n_i = (F_i/\nu)(1 - e^{-\nu t_o}) \quad (204)$$

For $\nu t_o \rightarrow \infty$, the equilibrium density F_i/ν is reached. When νt_o is small, $n \rightarrow F_i t_o$. In the 6th or 5th column of each Part of Table XL the calculated crater density n_o corresponding to $t_o = 4.5 \times 10^9$ years of uneroded existence is given.

When constructing Table XXIX on the basis of Shoemaker's counts, erosion was assumed to delete a crater after an erosion lifetime of

$$t' = 1.58 \times 10^5 B_o \quad (205)$$

years when B_o is given in centimeters. The equation is based on a discontinuity in the observed gradient dN/dB_o explained as an erosional removal of craters with $B_o = 286$ meters in a time interval of 4.5×10^9 years. The provisional erosion time scale as given by (205) is shown in the 8th or 7th columns of Table XL.

When $t' > \tau_o$, erosion is too slow and craters are removed mainly by overlapping; this is the case of the small-crater end of the table, when ~~in which case~~ the theoretical craters density will be close to n_o. When $t' < \tau_o$, erosion prevails

TABLE XL

Balance of Crater Creation by Impact and Deletion by Overlapping and Erosion to Profile Ratio $B_o/x' > 50$ (Table XXXV for impact parameters, Tables LI and LII for erosion). Normal Mare Region (outside the ejecta from craters larger than 590 m). F_i ($cm^{-2}yr^{-1}$), differential influx; ν, deletion expectation per year (from all five sources); B_o/x', crater profile ratio at impact; $\tau_o = 1/\nu$, years; n_o is the differential number of craters per 100 m^2 which would survive if uneroded for 4.5×10^9 years; $t' = 1.58 \times 10^5 B_o$ (yrs) is a rough first-approximation erosion lifetime as used in Table XXIX, and t_e the lifetime according to the final solution (Tables LI, LII). The differential crater densities per 100 m^2, predicted from $n_i = 10^6 F_i \left[1 - \exp(-t\nu)\right]/\nu$ are n_o, n', n_e, corresponding to 4.5×10^9, t', and t_e, respectively. N (N_o, N', N_e) are the predicted cumulative crater densities per 100 m^2. B_o = crater diameter, x' = crater depth.

(a) Component J_e : secondary ejecta from nearby penetrating cratering events (i.e. which are penetrating the overlay); primary and ricochets combined

B_o(cm)	B_o/x'	ν	τ_o	F_i	n_o	N_o	t'	n'	N'	t_e	n_e	N_e
1460	27.9	1.92^{-10}	5.2^{9}			0			0			0
				1.23^{-15}	2.4		1.55^{8}	0.19		3.54^{7}	0.044	
655	14.6	1.02^{-9}	9.3^{8}			2.4			0.19			0.04
				9.70^{-15}	4.9		7.45^{7}	0.67		2.22^{7}	0.22	
339	9.3	3.76^{-9}	2.66^{8}			7.3			0.86			0.26
				1.37^{-13}	16.6		3.43^{7}	4.42		1.05^{7}	1.38	
143	5.6	1.81^{-8}	5.5^{7}			23.9			5.1			1.64
				8.77^{-13}	28		1.89^{7}	12.5		4.62^{6}	3.8	
80.0	4.3	5.52^{-8}	1.81^{7}			53			17.6			5.4
				6.08^{-12}	62		9.45^{6}	38		2.23^{6}	12.4	

TABLE XL (continued)

(a) Component J_e: continued

[redacted](cm)	B_o/x'	ν	τ_0	F_i	n_o	N_o	t'	n'	N'	t_e	n_e	N_e
44.6	3.6	1.74^{-7}	5.75^{6}			114			56			17.8
				8.33^{-11}	230		4.85^{6}	190		9.07^{5}	64	
21.0	3.2	7.56^{-7}	[illegible]$.32^{6}$			344			246			82
				5.42^{-10}	480		2.52^{6}	450		3.94^{5}	172	
12.1	3.2	1.71^{-6}	5.4^{5}			820			700			254
				3.71^{-9}	690		1.45^{6}	690		2.03^{5}	460	
7.00	3.1	1.7^{-5}	5.9^{4}			1510			1390			710
				5.22^{-8}	1200		7.55^{5}	1200		8.70[illegible]	1130	
3.26	3.5	1.11^{-4}	[illegible]$.0^{3}$			2700			2590			1890

(b) Component J_1 : Meteorites--Apollo

[redacted](cm)	B_o/x'	ν	τ_0	F_i	n_o	N_o	t'	n'	N'	t_e	n_e	N_e
13800	16.6	2.7^{-12}	3.7^{11}			0			0			0
				2.82^{-19}	1.27^{-3}		1.57^{9}	4.4^{-4}		9.37^{8}	2.6^{-4}	
7140	16.5	[illegible]$^{-11}$	6.2^{10}			1.27^{-3}			[illegible]$.4^{-4}$			2.6^{-4}
				1.85^{-18}	7.9^{-3}		8.38^{8}	1.55^{-3}		4.11^{8}	7.6^{-4}	
3940	18.0	4.47^{-11}	2.24^{10}			9.2^{-3}			1.99^{-3}			1.02^{-3}
				2.35^{-17}	0.092		4.73^{8}	1.11^{-2}		1.52^{8}	3.6^{-3}	
2270	25.9	9.1^{-11}	1.10^{10}			0.101			1.31^{-2}			4.6^{-3}
				1.26^{-16}	0.44		2.95^{8}	0.040		4.43^{7}	6.0^{-3}	
1530	36.9	1.77^{-10}	5.6^{9}			0.54			0.053			1.06^{-2}
				7.58^{-16}	2.0		1.98^{8}	0.148		1.8^{7}	0.014	
1030	60.7	3.89^{-10}	2.57^{9}			2.54			0.201			0.025

K51

TABLE XL (continued)

(c) Component S : major secondary ejecta from ray craters, corresponds either to n_s in the 4th line of Table XXIX. B, (F_o, n_o and 1st approximation, n') or in the 4th line from bottom of Table LII(F, 2nd approximation, n_e); identical with Component J_e after exclusion of overlapping Component J_1. $B_o/x' \sim 4$ to 6 initially.

B_o(cm)	ν	τ_o	F_o	n_o	N_o	t'	n'	N'	F_i	t'_e	n_e	N_e
14500	1.23^{-12}	7.3^{11}			0			0				0
			1.38^{-20}	6.2^{-5}		2.03^{9}	3.2^{-5}		1.23^{-20}	4.5^{9}	5.5^{-5}	
11350	4.01^{-12}	2.6^{11}			6.2^{-5}			3.2^{-5}				5.5^{-5}
			2.16^{-20}	9.7^{-5}		1.58^{9}	3.4^{-5}		2.04^{-20}	4.21^{9}	8.6^{-5}	
8350	1.24^{-11}	8.1^{10}			1.6^{-4}			6.6^{-5}				1.21^{-4}
			3.2^{-20}	3.7^{-4}		1.24^{9}	1.03^{-4}		5.02^{-20}	3.32^{9}	1.67^{-4}	
6970	1.79^{-11}	5.7^{10}			5.3^{-4}			1.69^{-4}				3.08^{-4}
			1.95^{-19}	8.5^{-4}		9.73^{8}	1.88^{-4}		2.96^{-19}	9.83^{8}	2.92^{-4}	
5500	5.03^{-11}	3.3^{10}			1.38^{-3}			3.57^{-4}				6.0^{-4}
			5.41^{-19}	2.2^{-3}		6.85^{8}	3.7^{-4}		6.97^{-19}	7.09^{8}	4.9^{-4}	
4530	4.18^{-11}	2.4^{10}			3.6^{-3}			7.3^{-4}				1.09^{-3}
			1.23^{-18}	4.3^{-3}		5.88^{8}	7.2^{-4}		2.36^{-18}	4.62^{8}	1.09^{-4}	
3210	5.66^{-11}	1.77^{10}			8.4^{-3}			1.46^{-3}				2.18^{-3}
			3.23^{-18}	1.28^{-2}		4.36^{8}	1.46^{-3}		8.22^{-18}	2.52^{8}	2.12^{-3}	
2330	3.57^{-11}	1.17^{10}			2.12^{-2}			2.91^{-3}				4.3^{-3}
			8.1^{-18}	0.026		3.24^{8}	2.6^{-3}		3.70^{-17}	1.03^{8}	4.00^{-3}	
1770	2.31^{-10}	4.3^{9}			0.047			4.5^{-3}				8.3^{-3}

and the calculated crater densities smaller than n_o. Setting $t_o = t'$ in (204), the probable values n_e of differential crater density as due to the combined removal by overlapping and hypothetical (empirically-established) erosion have been calculated (9th or 7th lines in Table XV). The last column in each subdivision of Table XL contains the predicted cumulative frequency N_e of craters per 100 m^2. The three components of the table are not overlapping and their sum, obtained as shown in the 5th column of Table XLI, is then the predicted 1st approximation total cumulative crater density as derived from the influx rate of the projectiles, cratering theory, available knowledge of the mechanical properties of the lunar soil and bedrock, elimination through overlapping by larger craters (well defined) and erosion by smaller projectiles (provisional rate of erosion, empirically suggested by a discontinuity in the gradient of the crater frequency function). This can be compared with observed crater densities from three different sources as derived from the lunar probes (10th, 11th, and 12th columns) : Ranger VII and VIII, (Shoemaker, 1966), Ranger VIII (Trask, 1966), and Surveyor I (Jaffe *et al.*, 1966 b).

A comparison of the 1st approximation (N, 5th column of Table XLI) and observed (10th--12th columns) crater densities seems to show convincingly that prediction even with the provisional assessment of erosion is in satisfactory accord with observation and that, in the same manner as with the dis-

TABLE XLI

Comparison of Predicted (N', N_o) and Observed (N)

Cumulative Area Densities of Small Craters (B_o, crater diameter, cm) having a Profile Ratio $B_o/x' < 50$*

B_o (cm)	N' Predicted, 1st Approxim. Component: S	J_i	J_e	all	N_o Predicted, 2nd Approxim. Component: S	J_i	J_e	all	N Observed (Shoemaker) (1966)	(Trask) (1966)	(Jaffe et al.) (1966b)
7140	1.6^{-4}	4.4^{-4}	...	6.0^{-4}	2.9^{-4}	2.6^{-4}	...	3.5^{-4}	5.7^{-4}	10.6^{-4}	...
3940	3.1^{-4}	19.9^{-4}	...	2.9^{-3}	1.50^{-3}	1.02^{-3}	...	2.5^{-3}	3.1^{-3}	3.5^{-3}	...
2270	3.3^{-3}	13.1^{-3}	...	1.64^{-2}	5.1^{-3}	4.6^{-3}		9.7^{-3}	6.0^{-3}	10.4^{-3}	...
1530	5.0^{-3}	5.3^{-2}	...	5.8^{-2}	8.0^{-3}	1.06^{-2}		1.86^{-2}	1.28^{-2}	2.30^{-2}	...
1030	5.0^{-3}	0.201	0.090	0.296	8.0^{-3}	0.025	0.020	0.053	0.027	0.060	...
655	5.0^{-3}	0.201	0.190	0.396	8.0^{-3}	0.025	0.014	0.077	0.067	0.126	...
339	5.0^{-3}	0.201	0.86	1.07	8.0^{-3}	0.025	0.22	0.25	0.22	0.47	2.0
143	5.0^{-3}	0.201	5.1	5.3	8.0^{-3}	0.025	1.64	1.67	1.13	2.64	9.5
80.0	5.0^{-3}	0.201	17.6	17.8	8.0^{-3}	0.025	5.4	5.4	...	...	27.0
44.6	5.0^{-3}	0.201	56	56	8.0^{-3}	0.025	17.8	17.8	...	...	77
21.0	5.0^{-3}	0.201	246	246	8.0^{-3}	0.025	82	82	...	...	300
12.1	5.0^{-3}	0.201	700	700	8.0^{-3}	0.025	254	254	...	...	810
7.00	5.0^{-3}	0.201	1390	1390	8.0^{-3}	0.025	710	710	...	...	2170
3.26	5.0^{-3}	0.201	1590	2590	8.0^{-3}	0.025	1890	1890	...	...	8590**

* Thus sufficiently deep to be observed

** The counted value at $B_o = 3.26$ cm was 3850 (Jaffe *et al.*, 1966b); but somewhat arbitrarily allowance was there made for the incompleteness in the counts of these small craters and the number was increased accordingly.

tribution of large craters in the maria, the small-scale relief of the lunar surface can be well accounted for theoretically in terms of the physical factors as listed above. The divergencies between the different sources of crater counts are even greater than those between prediction and observation. Only within the 10 to 6 meter diameter range there seems to be a major discrepancy , the predicted numbers being some 5 times too high, but even this deviation is contradicted by the Surveyor data at 3 meters which show twice as many craters as those predicted, and 5 times the number derived from the Ranger photographs. The weak point of the prediction is the provisional and oversimplified treatment of erosion. In Section X. D, E a more sofisticated treatment of erosion is applied with the calculated results given in the middle part (columns 6--9) of Table XLI. There is certainly better agreement now in the most discrepant crater range (3--20 meters). However, the main features of the statistical balance of cratering on the moon are not much altered by this more detailed theoretical study of erosion: the observational data (partly reflecting real differences on the lunar surface) are not concordant enough to permit a check on the more subtle details of the theory.

F. Mixing of Overlay

Each cratering event displaces a volume of $0.363x_oB_o^2$ [equation (1) with x_o now standing for x_p] which is partly ejected, partly falling back. This material becomes thoroughly mixed, to an average mixing depth h_o over the crater area $\frac{1}{4}\pi B_o^2$, given by

$$h = h_o = 0.462\ x_o \qquad (206)$$

For a static overlay layer at depth h_o the mixing efficiency per unit of time (year) equals $\sigma_B(x_o)$, the fractional area of the surface covered in unit time by craters reaching to and beyond central penetration depth x_o; this can be derived from the data of Tables XXXV and XXXIX though the latter does not add much. Over a time interval of t years the mixing factor Q_m, or the effective number of times of complete exchange of material of this specific layer situated at depth h_o with the overlying soil, is then

$$Q_m(h_o) = \sigma_B(x_o) \cdot t \ , \qquad (207)$$

and the mixing time t_m, corresponding to $Q_m = 1$ or complete single mixing is

$$t_m = 1/\sigma_B \qquad (208)$$

However, the simple mixing process is complicated by the accretion of overlay which not only adds new material to the surface but provides an ever increasing protective layer. The average accretion of overlay on our "normal" region was estimated to equal at present 12 meters per 4.5×10^9 years or 2.67×10^{-7} cm per year; any marked layer at depth h_o can be assumed to sink under the surface at this rate, so that its age in years is

$$t = t_o = h_o / 2.67 \times 10^{-7} = 3.75 \times 10^6 h_o \ . \qquad (209)$$

When $t_o > t_m$, mixing is efficient; when $t_o < t_m$, the layer sinks faster than its time scale of mixing, and becomes only partly mixed with the overlying strata, or not at all.

A question of identity arises for mixed strata. Physical identity is maintained only over short intervals of time during which the rate of sinking is thus physically meaningful. The rate remains the same although the material content may change with efficient mixing.

The differential equivalent of equation (207) is

$$dQ/dt = \sigma$$

and with the linear dependence of age on depth (209) the mixing factor can be integrated in terms of increments of either t or h_o , $Q_m = \int \sigma dt$ or

$$\Delta Q_m = \sigma_B(h_o) . \Delta t = 3.7 \times 10^6 \sigma_B . \Delta h_o . \qquad (210)$$

The integral from $t = 0$ to $t = t_o$ yields the total mixing factor for the past history of the layer when its depth was less than h_o . The integral from $t = t_o$ to $t \to \infty$ defines the mixing factor for the future, Q_f ; when this is small, mixing can be assumed to cease and the layer becomes stagnant, The probability of eventual subsequent mixing is

$$\epsilon_m = 1 - \exp (- Q_f) ; \qquad (211)$$

for small values it is close to Q_f, for large values it approaches unity.

Table XLII contains the calculated mixing probabilities as depending on the depth h_o below the surface . The crater coverage, σ_B , is the sum for all four components of Table XXXV, logarithmically interpolated when needed for the chosen values of x_o.

The dividing line of $t_m/t_0 = 1$ is at a depth of $h_0 = 11$ cm, while the one-half probability depth ($p_m = 0.5$) is near $h_0 = 8$ cm. At $h_0 < 4$ cm the layers become well mixed, with mixing times running from a few million years to 160,000 years at a depth of from 2 to 0.5 cm. Below $h_0 > 25$ cm the chance of ultimate mixing becomes very slight and the layers become stagnant, preserving the stratification once formed when they were near the surface. The stratification is washed out over a layer thickness of 8 cm (linear dispersion ± 4 cm); chronologically it reflects the average conditions (e.g. with respect to cosmic-ray interactions) over a time interval of 30 million years. Fluctuations of a shorter period must be smoothed out and cannot be detected, unlike the high resolution in time of terrestrial sediments. With (Continued p. 275)

TABLE XLII

Cumulative Mixing Factor (Q_f) and Eventual Mixing Probability (q_m) of Overlay at Present Depth h_o (cm)

σ_B = relative crater creation area per year; x_o = crater penetration depth; t_o = accretion age, years; t_m = time scale of mixing, years

x_o (cm)	224	94.4	69.1	58.5	47.9	34.4	25.6	18.2	10.9
h_o	104	43.6	32.0	27.0	22.2	15.9	11.8	8.40	5.04
σ_B	6.26^{-11}	2.28^{-10}	3.64^{-10}	1.65^{-9}	3.96^{-9}	1.10^{-8}	2.16^{-8}	4.44^{-8}	1.26^{-7}
t_m	1.60^{10}	4.39^{9}	2.75^{9}	6.06^{8}	2.53^{8}	9.09^{7}	4.63^{7}	2.25^{7}	7.94^{6}
t_o	3.90^{8}	1.63^{8}	1.20^{8}	1.01^{8}	8.32^{7}	5.96^{7}	4.32^{7}	3.15^{7}	1.89^{7}
Q_f	0.052	0.079	0.091	0.107	0.112	0.128	0.152	0.55	1.49
q_m	0.051	0.076	0.087	0.101	0.106	0.120	0.141	0.42	0.77
x_o (cm)	~~7.02~~	7.02	4.36	2.19	1.03	0.54	0.27	0.135	0.0675
h_o		3.25	2.02	1.01	0.50	0.250	0.125	0.0625	0.0312
σ_B		2.69^{-7}	5.98^{-7}	1.87^{-6}	6.26^{-6}	2.05^{-5}	6.64^{-5}	6.06[illegible]	1.45^{-3}
t_m		3.72^{6}	1.67^{6}	5.35^{5}	1.60^{5}	48800	15100	1650	690
t_o		1.22^{7}	7.58^{6}	3.78^{6}	1.88^{6}	9.4^{5}	4.7^{5}	2.35^{5}	1.17^{5}
Q_f		2.72	4.54	8.5	Large $\longrightarrow$				
q_m		0.93	0.99	1.00	1	1	1	1	1

TABLE XXXIX

Cumulative Area Coverage (σ_{cB} per year) by Karge Craters

Component J_c (supplementary to Table XXXV) which contains component J_1 only down to $B_o > 139$ meters, the rest of it being represented by Table XXXV. C

B_o, meters	325	246	186	145	113.5	88.5
σ_{cB}, primaries	0	1.16^{-12}	2.87^{-12}	6.01^{-12}	1.09^{-11}	1.09^{-11}
σ_{cB}, secondaries ($x_o = 0.35B_o$)	0	3.11^{-12}	7.92^{-12}	1.01^{-11}	1.19^{-11}	1.36^{-11}
σ_{cB}, total	0	4.27^{-12}	1.08^{-11}	1.61^{-11}	2.28^{-11}	2.45^{-11}

B_o, meters	69.7	55.0	43.3	32.1	23.8	17.7	<17.7
σ_{cB}, primaries	1.09^{-11}	1.09^{-11}	1.09^{-11}	1.09^{-11}	1.09^{-11}	1.09^{-11}	1.09^{-11}
σ_{cB}, secondaries ($x_o = 0.35B_o$)	1.76^{-11}	2.34^{-11}	3.36^{-11}	4.68^{-11}	6.70^{-11}	9.25^{-11}	9.25^{-11}
σ_{cB}, total	2.85^{-11}	3.43^{-11}	4.45^{-11}	5.77^{-11}	7.79^{-11}	1.03^{-10}	1.03^{-10}

such a low resolution, the Quaternary and Pliocene would have been lost in the preceding Miocene, even the large subdivisions of the Tertiary and the Cretaceous- Paleocene transition would have been washed out.

X. Erosion Lifetimes of Surface Features

A. Transport and Sputtering; Lifetime of Boulders

In Section IX. E deletion of small craters (or other features of roughness) by later superimposed larger ones was evaluated on a firm statistical basis, while erosion by continuous influx of small projectiles producing craters smaller on a linear scale than a given roughness feature was treated, as a first approximation, summarily by invoking an empirically adjusted unspecified smoothing process whose linear scale is proportional to age. In this section we will consider theoretically the actual processes of this gradual erosion or "polishing", the final results, however, having been included in the middle part of Table XLI. Two main processes are at work: sputtering of large grains, boulders, and crater rims, and transport of the granular matrix.

Outstanding large grains or blocks, sufficiently larger than the impacting projectile, which do not behave as part of the granular matrix but retain their individuality (cf. Section IX. B), and unprotected crater rims, are sputtered by hard impacts. They are not much affected by the infalling accreting overlay (J_e) on account of its low velocity (some grinding and collisional damage occurs; however, the mass affected is insignificant); only hypervelocity bombardment by the meteoritic components is here relevant and, because of the large mass influx rate (cf. Table XXXIV), bombardment by micrometeorites (J_m) is the main agent and may be considered alone.

Transport, as distinct from plain mixing of the granular medium on a horizontal surface and discussed in the preceding section, works on slopes of craters or other elements of roughness. At a cratering impact, more grains are farther ejected downhill than uphill, which leads to a net downhill displacement or flow of the granular material. Also, out of a hole fewer grains will be ejected by cratering events into the surrounding terrain, then injected into the hole from the surroundings; this leads to a gradual filling of the hole (crater).

In transport, besides the micrometeorites (J_m), overlay influx (J_e) may be of some importance (cf. Table XXXIV), somewhat enhanced by the higher velocities of ejection (u_g) due to greater strength (s_c) at greater penetration (x_o) than in the case of micrometeorites. In addition to momentum as determining the mass ejected, the transport efficiency can be assumed proportional to the flight distance, L [equation (45)]. On this basis, the transport efficiency is to be measured by the product $M = kG_g w_o (d\mu/dt)L$, which thus differs from the plain momentum used in Table XXXIV. The comparison between J_m and J_e can be made at the median (50 per cent) cumulative mass (Table XXXV). For J_m, this is at $h=0.0205$ cm, $w_o=6 \times 10^5$ cm/sec, $k=2$, $G_g=0.41$, $D_o=6.7$ cm, $\bar{s}_c=2820$ dyne/cm^2, $d\mu/dt=1.05 \times 10^{-8}$ g/cm^2. year. For J_e, the typical parameters are $r=1.0$ cm, $w_o=9.53 \times 10^3$ cm/sec, $k=0.513$, $G_g=0.56$, $D_c=12.1$ cm, ~~and~~ $\bar{s}_c=2.61 \times 10^4$ dyne/cm^2, $d\mu/dt=3.47 \times 10^{-7}$ g/cm^2.year. The comparison then consists of two steps. An inner portion ($y_m' = 0.328$) of the J_m crater which has the same shock velocity (u) as the entire ($y_e = 1$) harder J_e crater, yields (L calculated for $\lambda = 0.3$, $y=\frac{1}{2}y_m$ or $\frac{1}{2}y_e$) $L_e/L_m=10.5/4.7=2.24$, $k_m/k_e=3.26$, $w_m/w_e=63$, $G_e/G_m=1.37$, $\mu_e/\mu_m=32.1$, and $E_e/E_m'=0.476$. The total transport efficiency of the J_m crater (for $y_m=1$) is $E_m=2.57\ E_m'$, whence $E_e/E_m=0.476/2.57=0.185$. The ratio turns out to be nearly the same as that arrived at in Table XXXIV from a more rough estimate. To allow also for the other small components and going back to Table XXXIV, the transport efficiency of the J_m-component may thus be taken with an additional increase of 25 per cent of its value. The predominance of micrometeoritic erosion thus greatly simplifies the calculation of transport, which anyway cannot be estimated better than to a close order of magnitude.

The experiments by Gold and Hapke (1966) as mentioned above could suggest that, simultaneous with dispersal of the granular substance through impacts, a build-up of surface roughness ("fairy castles") would take place as due to adhesion. This ~~must~~ can be only partly true for lunar overlay. The stickiness of the cement powder in the experiments was due to the very small grain size, of the order of 10^{-4} cm. It can be shown that, for a greatly simplified model of two colliding equal spherical semi-elastic grains, the maximum relative velocity of encounter which can be balanced by the tensile elastic force as limited by cohesion, or the "velocity of inelastic capture", equals

$$v_a=(6/Y\delta)^{\frac{1}{2}}A_d/(\pi\lambda r^2) \quad , \qquad (212)$$

where Y=Young's modulus, δ=density, A_d=force of cohesion between two grains, λ= linear elastic efficiency, r= radius. For silicate grains in vacuo, $Y=5\times10^{11}$ dyne/cm^2, δ=2.5 gr/cm^3, A_d=1.0 dyne (Smoluchowski, 1966; Ryan, 1966), λ=0.5 as for hard rock in a single collision, we have

$$v_a=1.27\times10^{-6}r^{-2} \quad (\text{cm/sec}) \qquad (212a)$$

For $r=10^{-4}$ cm as in Gold - Hapke's experiments, v_a=127 cm/sec and the particles can be efficiently captured at moderate velocities of impact, while at $r=10^{-2}$ cm, v_a=0.0127 cm/sec, they hardly could stick, especially when perturbed by other oncoming particles. Yet, according to Table XXIV, D (y), the mass of the small particles from 2×10^{-5} to 2×10^{-4} cm could only amount to 4.5 per cent of the total mass of the overlay, while those larger than 10^{-2} cm account for 71 per cent. There are not enough "sticky" particles in the overlay, and the build-up of "fairy castle" structures must be greatly inhibited, as compared to the formation of regular impact-crater depressions, while the former are much more easily destroyed by "hard" impact than the latter.

We will first consider the levelling action of meteoritic bombardment on the granular elements of surface roughness, A_s, the consequence of meteoritic (and other) impact, different parts of the overlay surface are exchanging material (the influx from component J_c, or secondary ejecta from nearby craters descends equally on all surface elements, leading to a continuous growth and simultaneous redistribution or filling, in Section X. C considered). For an element of surface placed at the same level as its surroundings (differences of level that matter are of the order of L, the flight distance of the ejecta), ejection and influx are obviously balanced. A surface element placed in a depression will receive more or less the same influx as if it were placed on level ground, but, on account of gravity, there will be some fallback at ejection, so that influx over the rim of the depression will exceed ejection and the depression will begin filling. On the contrary, an elevation will eject over its rim the same amount as when placed on level ground, while receiving less from the surroundings; its height will decrease. We will try to obtain a quantitative estimate for the time rate or "smoothing lifetime" for the elements of roughness as depending on their linear scale.

Only a crude approach is attempted. Strict evaluation of the integrals as conditioned by the adopted model is not justified, the model of cratering ejecta being itself but approximate, involving arbitrary quantitative relations [such as equation (27) for the ejection angle, β , and the use of a mean coefficient of elastic efficiency, λ]. As one of the simplifications, average quantities of ejection or influx over entire areas are here used, instead of the integrals. The mathematical error, perhaps some 10-20 per cent, is probably much smaller than the uncertainty in the basic assumptions.

The granular surface is assumed to be horizontal on the average, except for the randomly distributed elements of roughness (chiefly craters). Meteorite impacts on inclined surfaces will lead to systematic flow downhill, a process to be considered seperately.

For granular overlay, with the cratering parameters as adopted in Table XXXV. A and equation (4), the marginal shock velocity is

$$u_s = 2170^{\frac{1}{2}} = 46.6 \text{ cm/sec} ,$$

and the equivalent volume of granular ejecta, proportional to $G_g = 0.41$ (the fraction of granular encounters), and increased by 25 per cent to allow for other components of meteorite influx, and to the product kw_o/u_s according to equation (14), becomes

$$\chi=0.669\times 1.05\times 10^{-8}\times 0.41\times 1.25\times 2\times 6\times 10^{5}/(46.6\times 1.3) \tag{213}$$
$$\chi=7.13\times 10^{-5}\ \text{(cm/year)}$$

(cm^3/cm^2 . year). In a successful granular impact, the ratio of mass ejected or disturbed (including fallback) to the micrometeorite projectile mass is then

$$M_c/\mu=1.72\times 10^4 \tag{214}$$

The profile ratio, B_o/x_o, is of the order of 60 for micrometeorite impact into the granular surface (Table XXXV. A). The crater is extremely flat and the rim angle, β_o, nearer 90° (cf. Fig.1); instead of 0.8, in equation (27) we set $\sin\beta_o=1$. Within the same mathematical framework as used for the determination of fallback in Section II. F, the average velocity of ejection in the direction β and at crater mass fraction y is

$$\bar{v}=\tfrac{2}{3}u_s\lambda/y=31.1\,\lambda/y\quad \text{(cm/sec)}\quad , \tag{215}$$

the factor $\frac{2}{3}$ allowing for the assumed damping of ejection velocity with depth x [Fig. 1 and equation (24)]. The layer radiated from a horizontal level element of surface beyond a circle of radius L (45) around it and thus lost to the surroundings beyond L is then

$$\Psi_L=\chi\left[(1+\xi^2)^{\frac{1}{2}}-\xi\right]\ \text{(cm/year)}\ , \tag{216}$$

where

$$\xi=\alpha' L$$

and

$$\alpha'=\tfrac{1}{2}g/v_o^{\,2}\,\lambda^2=0.084/\lambda^2\ . \tag{217}$$

$v_0 = 31.1$ is the velocity corresponding to $y=1$, $\lambda=1$, as of equation (215). The same amount Ψ_L is, of course, gained by the element of surface through influx from beyond radius L, as follows from the condition of equilibrium, and can be proved directly by integration. In the framework of the prescribed conditions, (216) is mathematically exact.

Imagine now the entire level circular portion of the surface of radius L radiating over its boundary. The case is more complicated than the fallback problem, because in a single cratering event the ejecta were supposed to fan out radially though at different angles, and the distance from crater rim was unique for each radiating spot, while in the presently considered process each spot emits ejecta in all directions along which the ~~directions~~ distances to the borderline are different. Instead of numerical integrations, we estimate the average radiation from the entire surface, sent over the borderline L, to correspond to a point at 0.75 L from the center of the area, and to equal the mean of two expressions (216), one for $L' = L/4$ and the other for $L'' = 7L/4$ (antipodal distance). Thus, for the entire level circular area of radius L, the average emission as well as influx over, or from over its border, becomes

$$\Psi_L = \tfrac{1}{2}\lambda \left[(1 + \xi^2/16)^{\frac{1}{2}} + (1 + 49\xi^2/16)^{\frac{1}{2}} - 2\right] \text{ (cm/year)}. \quad (218)$$

For $\xi > 3$, the bracketed expression can be closely approxi-

K_c

mated by $2\left[8/(7\xi) - 4/\xi^3\right]$.

Consider now a cylindrical depression of radius L, flat at the bottom and of depth H. From equation (45) for the flight distance, as compared with the vertical range of the flight trajectory, at $\beta = 45^\circ$ a particle ejected from the center will just pass over the rim when $H = \frac{1}{2}L$. We make the schematic assumption that when $H \gg \frac{1}{2}L$, ejection is virtually blocked and (218) represents the net average accretion at the bottom. Further, when $H < \frac{1}{2}L$, we assume a linear decrease of the accretion balance from its maximum value (218) to zero at $H=0$. This defines thus the time scale of filling of the depression,

$$\tau_f = \tfrac{1}{2}L/\bar{\varphi}_L \,, \tag{219}$$

so that, when $H_1 < \frac{1}{2}L$ is the initial depth, the depth after time t will be

$$H_t = H_1 \exp(-t/\tau_f) \tag{220}$$

For $H > \frac{1}{2}L$, the accretion is constant,

$$dH/dt = -\bar{\varphi}_L \tag{221}$$

Equations (218)--(221) apply also to a cylindrical elevated circular plateau of radius L with a granular surface, which at a positive height $H \; \frac{1}{2}L$ does receive but a negligible influx from the lower placed surroundings and loses the net amount given by (218). Table XLIII contains the parameters and lifetimes of depressions (craters) or elevations (granular mounds).

TABLE XLIII

Lifetimes (τ_f) of Craters or Granular Mounds of $H < \frac{1}{2}L$ with Respect to Stirring of Overlay by Small Projectiles

(Crater or mound diameter $B_o = 2L$)

$\lambda^2 = 0.09$; $\delta' = 0.933$; $B_o = 2.14\,\varphi$; $\tau_f = \frac{1}{4} B_o / \bar{\Psi}_L$

φ	1	2	3	4	5	10
$\bar{\Psi}_L / \lambda$	0.523	0.379	0.315	0.242	0.202	0.110
$\bar{\Psi}_L$, 10^{-5} cm/year	3.73	2.70	2.25	1.73	1.44	0.785
B_o, cm	2.14	4.28	6.42	8.56	10.7	21.4
$d\log \tau_f / d\log B_o$	1.47	1.54	1.71	1.77	1.87	1.94
τ_f, years	14300	39600	71300	12400	186000	682000
φ	20	50	100	200	500	1000*
$\bar{\Psi}_L / \lambda$	0.057	.0228	.0114	.0057	.00228	.00114
$\bar{\Psi}_L$, 10^{-5} cm/year	0.407	0.163	0.081	.0407	.0163	.0081
B_o, cm	42.8	107	214	428	1070	2140
$d\log \tau_f / d\log B_o$	2.00	2.00	2.00	2.00	2.00	
τ_f, years	2.62^6	1.64^7	6.60^7	2.62^8	1.64^9	6.60^9

* For larger value, $\tau_f \sim B_o^2$

These lifetimes are shorter than the hypothetical t' values [Table XL(a)] for the small craters for $B_0 < 100$ cm, and somewhat shorter than the overlapping lifetimes τ_0 for the crater diameter range from about 8 to 2000 cm and, thus, must appreciably affect the crater statistics (Tables XL and XLI, 1st versus 2nd approximation). Also, the condition $\bar{H} < qB_0$ may practically apply to all craters and mounds, so that Table XLIII may be considered as of general applicability with respect to this particular process of erosion.

That part of meteorite flux which is not instrumental in granular cratering (i.e. a fraction $1 - G_g$ of the total) produces hard sputtering of single grains or exposed boulders. The soft component, J_e, is inefficient in this respect and only micrometeorites may be considered. With $s_c = 9 \times 10^8$, $\rho = 2.6$, $k = 2$, $w_0 = 6 \times 10^5$, $u_s = 1.86 \times 10^4$ cm/sec, equation (214) yields for the sputtering mass ratio a value 400 times less than that of (214) and negligible as a factor of mass transport. Also, with $\lambda^2 = 0.25$, $y = 0.5$, the high-speed ejecta (and of very fine grain) are spread over a radius of over 20 km and are not available for small-scale local smoothing. If equation (190) is accepted, for the small craters of about 0.2 cm produced by the micrometeorites in rock, the effective strength of the material must be greatly increased, to about $s_c = 1.04 \times 10^{10}$ dyne/cm^2; this sets

$u_s = 6.3 \times 10^4$ cm/sec, and (14) then yields only

$$M_c / \mu = 12.7 \tag{222}$$

The layer carried away from an exposed horizontal grain or rock surface (density 2.6) by micrometeorite sputtering is then $\frac{1}{2}\, \chi_s$, when χ_s denotes the equivalent layer of overlay (density 1.3) created,

$$\chi_s = 1.05 \times 10^{-8} \times 12.7/1.3$$

or

$$\chi_s = 1.03 \times 10^{-7} \ (\text{cm/year}) \tag{223}$$

This will be the ablation when $\bar{H} > \frac{1}{4} B_0$ for the block. A rocky surface on level with the surroundings will be covered by overlay ejecta and thus protected from direct sputtering. For an intermediate height, the thickness of the protective layer will be such that micrometeorite bombardment will sweep away it as it comes in. As the influx is decreased in an assumed ratio of $\kappa = 4\bar{H}/B_0$ [basis of equations (219) and (220)], the micrometeorites will spend a fraction $1 - \kappa$ of their momentum in sweeping away the thin protective sheet (actually it is an exponental function of κ, cf. next following subsection); ~~for~~ the sputtering efficiency for the underlying rock will thus be κ. In addition, overlay is showering on the block, burying its base at a rate of $1200/4.5 \times 10^9 = 2.67 \times 10^{-7}$ cm/year. The outstanding height of such a block with flat top decreases thus at a rate of

$$dH/dt = -2.67 \times 10^{-7} - 2.06 \times 10^{-7} H/B_0,$$

whence

$$H=(H_1+1.29B_0)\exp(-2.06\times10^{-7}t/B_0)-1.29B_0 \qquad (224)$$

The block is completely buried when H=0 or

$$\exp(-2.06\times10^{-7}t/B_0)=1/(1+0.775\,H_1/B_0) \qquad (224a)$$

when the initial average height $H_1\leq\frac{1}{4}B_0$; the linear scale is in cm, the time in years.

As an example, set typically B_0=50 cm, H_1=25 cm$>\frac{1}{4}B_0$ in the beginning (cf. Figs. 5, 16, 17). The surface is at first unprotected, being sputtered at $\frac{1}{2}\lambda_s=0.515\times10^{-7}$ cm/year (223) and buried at 2.67×10^{-7} cm/year, or a combined rate of 3.18×10^{-7} cm/year. After an initial period of $12.5/3.18\times10^{-7}=3.9\times10^{7}$ years the outstanding height is reduced to 12.5 cm after which (224) applies, with H_1=12.5, B_0=50 cm. The total lifetime of the block until complete burial becomes

$$3.9\times10^{7}+4.3\times10^{7}=82\text{ million years},$$

when its thickness will be reduced to

$$2.67\times10^{-7}\times8.2\times10^{7}=21.8\text{ cm},$$

having lost only 3.2 cm through sputtering. This typical case shows that blocks of this and other sizes are not ground to powder by meteorite impact before being buried in overlay; after a lifetime of 10–100 million years (according to size), they become incorporated in overlay, being no longer disturbed except in a rare large cratering event. Such hidden collections of blocks may then be the cause of thermal anomalies, even when they are not visible, being covered entirely by overlay precipitation (cf. Section VI. C).

B. Downhill Migration of Dust

In Fig. 18, a micrometeorite strikes a granular surface SS, inclined under an angle α to the horizon HH. The meteorite MO impacts in an arbitrary unspecified direction and causes a spray of ejecta from the point of impact, O (which stands for an infinitesimal craterlet), symmetrical with respect to the normal ON , whatever the direction of OM. Two opposite, symmetrically with respect to ON directed jets (angle β) OA and OB are asymmetrical with respect to the vertical OZ, resulting in a greater downhill flight distance, L_B , than uphill, L_A . The result is a net downhill displacement

$$OO_1 = \Delta L(\beta, \alpha) = \tfrac{1}{2}(L_B + L_A),$$

L_A being taken algebraically, negative when to the left of O. The displacement projected on the horizontal plane is evidently

$$O'O_1' = \Delta S = \Delta L \cos\alpha$$

and this is the measure of migration of a mass fraction, dy, ejected under an angle β such that

$$\sin\beta = y$$

[equation (27) with $\sin\beta_0 = 1$ as in the preceding section]. From elementary kinematical considerations we then find

$$\Delta S = (2v^2/g)(1 - y^2)\tan\alpha \ , \tag{225}$$

where v is the average ejection velocity (215). Substituting this, integration over y yields the average displacement of the ejecta. There, however, are some complications which refer to the validity of equations (215) or (16), limited by the condition $y > y_3$ [equation (17)] ; for ejecta of micrometeorite impact, the limit (with $\Lambda = 0.3$) corresponds to flight distances of the order of 5 km, far above the crater dimensions we are concerned with. Such fast ejecta will go equally up and down hill of smaller craters without a systematic drift, their effect being covered by the theory of the preceding section while for downhill drift they are of no avail. Clearly, ejecta from the inner portions of the craterlet are irrelevant in the context. Only slow ejecta from the outer portions of the craterlet, whose flight distances are not large as compared to crater diameter, will contribute to filling the crater by downhill drift. In Fig. 18a, a crater of diameter B_0 is schematically represented by a cone HO_1H, of constant slope α. Ejecta (OO_1) from a middle point O (the micrometeor craterlet) on the slope will travel downwards allright when $\Delta S \leq O'O_1' = \frac{1}{4}B_0$ but will mount the opposite ledge ($\rightarrow OO_2$) and even climb up or leave the crater when $\Delta S > O'O_2' = \frac{3}{4}B_0$. Instead of proper integration whose accuracy is not justified by the uncertainty in the basic data, we use averages as in many other cases of this

289

treatise and set the lower limit of integration for equation (225) at a horizontal flight distance one quarter of the crater diameter,

$$v^2/g = 1/(4\alpha' y^2) \leq \frac{1}{4}B_0$$

whence the lower limit of integration becomes

$$y_1 = (\alpha' B_0)^{-\frac{1}{2}} \qquad (226)$$

There is a lower limit to the validity of the treatment, $B_0 > 1/\alpha'$ (corresponding to the upper limit $y = 1$ not to be exceeded), ~~α' being given~~ by equation (217). Hence the average downhill displacement inside a crater of diameter B_0 and average slope α, such that $\tan\alpha = 2x'/B_0$, with an additional mean factor of $(2/\pi)$ to allow for slant (non-meridional) directions, becomes

$$(2/\pi)\int_{y_1}^{1} \Delta S \cdot dy \ ,$$

or

$$\overline{\Delta S} = \left[2x'/(\pi\alpha' B_0)\right]\left[(\alpha' B_0)^{\frac{1}{2}} + (\alpha' B_0)^{-\frac{1}{2}} - 2\right] , \qquad (227)$$

with α' (cm^{-1}) defined by (217). $\alpha' B_0$ is thus a dimensionless quantity. The flow through 1 cm of crater circumference (πB, not necessarily πB_0, where $B = OO_2$ is an inner diameter, Fig. 18a) is then evidently

$$F_d = \chi \cdot \overline{\Delta S} \cdot \left[1 - \exp(-\mathcal{H})\right] , \qquad (228)$$

where χ is the volume of granular material ejected per cm^2 and sec (213) and $\mathcal{H}$ the "kinetic depth" of overlay at the spot so that the expression in brackets denotes the fraction of projectile momentum spent in the (not infinite) granular layer, the rest being applied to the bedrock with much less sputtering efficiency (223) but of long range (10 km) and thus indifferent for the downhill migration problem.

Assuming the availability of sufficient supply, thus maintaining a thick layer of overlay, $\chi \longrightarrow \infty$, the time scale for filling a conical depression of volume $V = (\pi x' B_o^2)/12$ by drift becomes

$$\tau_F = V/(\pi B_o F_i)$$

or

$$\tau_F = \pi \alpha' B_o^2 / \left\{ 24 \chi \left[(\alpha' B_o)^{\frac{1}{2}} + (\alpha' B_o)^{-\frac{1}{2}} - 2 \right] \right\}. \quad (229)$$

With α' and χ as in the preceding section this becomes

$$\tau_F \doteq 1710 B_o^2 (0.966 B_o^{\frac{1}{2}} + 1.035 B_o^{-\frac{1}{2}} - 2)^{-1} \quad (229a)$$

in years when B_o is in cm. The formula is valid for $B_o > 2$ cm, and the filling is supposed to proceed exponentially with time .

For craters completely imbedded in overlay, there is no shortage of supply to feed the flow downhill, rim and craterbed consisting equally of the dust and rubble of great depth. From Table XXIX the size limit for this condition ($H_p < 13$ meters) to be fulfilled is $B_o < 160$ meters for primaries and $B_o < 36$ m for the "ray" secondaries. In this case the flow sucks away the rim, the crater diameter increases , encroaching on the surrounding terrain, while the interior is filling. Shallow craters without elevated rims (as seen on the Surveyor and Ranger pictures) are thus produced. Equations (229) or (229a) give unconditionally the flow lifetime, τ_F, for these overlay craters.

When supply is insufficient, and when, as for larger craters, there is bedrock underlying the crater profile, the flux defined by (222) adjusts itself to supply through a finite value of the overlay kinetic thickness $\mathcal{H}$; a thin layer of overlay attains then equilibrium with supply and downhill flow, especially in the outer portions of the crater where bare unprotected rock will be exposed and subject to erosion by sputtering, at a rate of

$$dx/dt = \tfrac{1}{2}\mathcal{X}_s \cdot \exp(-\lambda) \qquad (230)$$

(cm/year) where $\mathcal{X}_s$ is given by (223).

Supply to the outer regions of these larger craters can be assumed to consist of three main components:

(1) low velocity granular ejecta from the surroundings, however mostly non-sticking [cf. equation (212a)], ricocheting inwards, and not apt to provide much of supply near the crater rim; the rate of crater filling is measured by $1/\tau_c$ (Table XLIII) but only one-half of this should apply to the rim region.

(2) High velocity sputtered material, of deposition rate $\mathcal{X}_s$ (223) corresponding to a time scale (on the conical profile model) $\tau_s = \frac{1}{3}x'/\mathcal{X}_s$ (no correction factor of $1 - \alpha_g$ shall be applied because the sputtering applies equally to granular and non-granular impacts); the fine-grained material (partly atomized) sticks to the spot without ricocheting and thus equally feeds the rim and the central regions.

(3) Low-velocity mostly coarse ejecta (J_e) of the accumulating overlay, with a time scale $\tau_e = \frac{1}{3}x'/J_e$ and $J_e = 2.67 \times 10^{-7}$ cm/year as in the preceding section; these are even more mobile than the finer ejecta from the surrounding, and one-third of the rate can be assumed, somewhat arbitrarily, for the rim region. The condition of sufficient supply, and thus of the validity of (229) is then evidently

$$1/\tau_n = 1/2\,\tau_f + 1/\tau_s + 1/3\,\tau_e > 1/\tau_F \quad , \tag{231}$$

in which case the overlay thickness increases everywhere while the crater profile is gradually levelled out. When this is not fulfilled, partly or entirely unprotected rock is exposed beginning from the rim inwards, and drift is adjusted to supply through the proper value of γ in equation (223):

$$1 - \exp(-\gamma) = \cancel{\tau_m}\,\tau_F/\tau_m \; . \tag{232}$$

The grinding of the incompletely protected rim proceeds then at a rate of

$$dH/dt = -\tfrac{1}{2}J_s\; e^{-\gamma} = -5.2 \times 10^{-8}\, e^{-\gamma}\,(\text{cm/year}). \tag{233}$$

The maximum rim erosion from this effect in 4.5×10^9 years amounts thus to 234 cm, i.e. about $2\frac{1}{2}$ meters.

Craters less then 300 m, which are eroded in less than 4.5×10^9 years, would at present appear now in various stages of erosion, according to age. With an initial depth to diameter ratio of x'/B_0 about 0.12 (cf. Fig. 4), in an average half-eroded crater $x' = 0.06\,B_0$ can be assumed. With this the supply parameter according to equation (231) becomes

$$1/\tau_m = 1/(2\tau_F) + 9.6 \times 10^{-6} / B_o \qquad (231a)$$

The calculated drift lifetimes, τ_F (229a) with the corresponding supply lifetimes, τ_m, are given in Table XLIV.

From the table we can see that condition (231), or $\tau_m < \tau_F$, is not fulfilled within the range of B_o from about 6 cm to 28 meters, where it is irrelevant because these small craters are completely built into overlay. Therefore, within the validity of our assumptions (in which respect undoubtedly considerable uncertainty exists), the values of τ_F (229a), or the drift rates F_d [equation (228) with $x = \infty$] seem to be valid unconditionally.

This refers to the average flat crater rims. Steep (moderately steep) rims of larger craters with bedrock exposed will retain their unprotected rocky surfaces, while the inpouring ejecta are rolling or ricocheting toward the interior. Alphonsus is an example (Figs. 7, 8, 9), although on a much larger scale and representing a more primitive stage. Another example is the boulder rim or stone wall of the Surveyor I crater on the horizon (Figs. 5 and 6).

C. Filling by Ricocheting Overlay Injection

The last, and most important factor of erosion for the lunar surface features (craters) to be considered is the filling of depressions by incoming overlay. The ricocheting grains of overlay, as they are losing kinetic energy in successive semi-elastic impacts, will have a preferential

TABLE XLIV

Drift Relaxation-time, τ_m, of Craters

[Valid either when $\tau_F > \tau_m$, or when crater diameter $B_o < 32$ meters (produced by "ray secondaries") or $B_o < 160$ m (produced by interplanetary primaries)]

The conditions of validity are always fulfilled

B_o, cm	2.14	21.4	214	2140	4280	2.14^4	4.28^{4}*
τ_F, years	64900	2.92^5	6.41^6	1.84^8	5.13^8	5.62^9	1.59^{10}
$d\log\tau_F / d\log B_o$		0.65	1.34	1.46	1.47	1.49	1.50
τ_m, years	25300	8.48^5	1.91^7	2.19^8	4.42^8	2.25^9	4.46^9

* For larger values, $\tau_F \sim B_o^{1.5}$ and $\tau_m \sim B_o$.

tendency to collect in "holes" from which they are unable to escape. Therefore the holes will receive more accretion than their surroundings and will be gradually filled at the latter's expense. This differential levelling action of accretion is superimposed on a continuously rising general level of overlay . With this, as well as with the two other types of erosion discussed earlier (Sections X. A, B), the levelling of the depression takes place preferentially at the expense of its nearest surroundings; they are, so-to -speak, sucked in by the crater vortex and a secondary, wider but shallower, depression is formed around the original crater; thus, the depression never disappears completely except when erased by a subsequent larger impact; it only is made increasingly shallower until becoming unobservable.

The theory of these processes, though more or less straightforward when the initial conditions (coefficient of elasticity, λ, etc) are defined, leads to complicated statistical integrations, amounting to an unjustified overdiscussion. In the following, a simplified artificial mechanical model is introduced, amply sufficient to estimate the trapping efficiency of a depression without pretending to describe the actual statistical complexity of trapping.

It also must be pointed out that the prefential trapping in depressions applies only to the non-sticking, ricocheting part of accretion. Micrometeorite material (J_m) retained by the moon is not only quantitatively insignificant as compared with the overlay ejecta (J_e'), but it is fine-grained or even partly atomized and must stick at the spot where it settles, equally over a hole or an elevation; it covers the terrain with a uniform layer without a levelling action on its roughness profile. Similarly, the fine-grained component of overlay, say below $r = 5 \times 10^{-5}$ cm which, according to (212a), would stick at an impact velocity as high as 5 m/sec, must be excluded as non-active; according to Table XXXV. D, this component accounts for 15 per cent of the incoming mass. On the other hand, large projectiles are not filling but destroying a depression through overlap. For a given crater size B_o , one may set an upper limit of a "filling" projectile size as that producing a crater twice the given size, i.e. one of diameter $2B_o$ (the limit is rough, made to coincide with the lower limit assumed for overlapping; the conventional vagueness of it is of little practical consequence because of the slow variation of the cumulative mass of J_e with projectile radius). Thus, for $B_o = 21$ cm, Table XXXV. D indicates $r = 4.8$ cm at $2B_o = 42$ cm, and a cumulative mass fraction $y = 0.628$; subtracting 0.15 as for the sticking fine-grained fraction, the actively filling fraction of overlay for this size of crater becomes $y_f = 0.628 - 0.150 = 0.478$ (of the total stated to be 3.47×10^{-7} gram per cm^2 and year).

Instead of the statistical complexity of particle size and velocity distributions (Table XXXV. D), we choose a typical average size which best represents the entire particle spectrum. For a given crater diameter, the median particle size is that corresponding to half-mass or $\frac{1}{2}y_f$ as defined above. In Table XLV some sample impact parameters for this median size are listed.

It will be found that, as compared with the other two erosion processes, filling is important only for the larger craters. With this in view, we assume the typical projectile parameters as $r_o = r_m = 0.5$ cm, $\cos\gamma_o = 0.926$, $\sin\gamma_o = 0.373$, $\gamma_o = 22^{\circ}.3$, $w_o = 1.033 \times 10^4$ cm/sec; ~~and with~~ $G_g = 0.52$ or, conventionally, 0.5 at this size (Table XXXV. D), which means alternating "soft" and "hard" ricochets with $\lambda = 0.3$ and 0.5, respectively as represented in Table XXXVII (1) & (2). As an additional schematization, we assume at impact the specular law of reflection for the angles, while the velocities are reduced by a factor of λ after each impact.

Let G_g denote the "gain factor" or the ratio of accretion trapped in a depression, to that accreted by a level surface of equal area. Obviously this is a function of the depth and profile of the depression. Provisionally a single depression situated on an infinite level area is considered, competition from other depressions being thus disregarded.

Let in Fig. 19 S_1 be the point of first impact of the projectile upon level surface SS, and S_2, S_3, S_4, S_5 the ricocheting impacts which finally come to rest at S_0, all the points being conventionally assumed to line up on a straight line (zig-zag paths will not essentially alter the gain factor; rectilinear path and specular reflection angle are convenient simplifications which should have little effect on the numerical results). A level circular area, C_1 or C_2, of diameter B in which the ricocheting path is assumed to pass through the middle, will contain the point S_o; thus accrete the particle when the center of the area is displaced over a range of distance $C_1C_2=B$ along the path SS, its "catch length" being thus B. A circular depression of equal diameter may trap the particle when impacting at S_3, (bottom part of figure, A_2; particle impinges at S_3, is reflected inwards and trapped at S_{oo}). though unable to trap it at S_2 when the distance $S_2S_3 > B$; its catch length is then obviously $A_1A_2 = B + \Delta L_o$ where $\Delta L_o = S_3S_o$ is the total tailpiece of the ricocheting path which can be trapped. We have thus obviously, from simple probability considerations,

$$G_f = A_1A_2/C_1C_2 = 1 + \Delta L/B \quad , \tag{234}$$

where $\Delta L = \Delta L_o$ in the particular case considered.

If ΔL_2, ΔL_1, ... are the trapping lengths for impacts S_2, S_1 (which may not be zero in the general case), each of the preceding impacts adds to the probability. In such a case

$$\Delta L = \Delta L_o + \Delta L_2 + \Delta L_1 + \ldots = \sum \Delta L \ . \tag{235}$$

An overall thumb rule, already applied in Section X. A, would set the extra trapping length equal to four times the average depth which, for the conical cross section, equals one-half the maximum depth, x'. Hence

$$\Delta L \doteq \tfrac{1}{2}x' \times 4 = 2x' \quad ,$$

or

$$G_f = 1 + 2x'/B \tag{236}$$

For an actually worked out numerical case (mental experiment, see below) of $x'/B = 0.25$, $G_f = 1.529$ has been found while (236) yields 1.5, a surprisingly good confirmation of the thumb rule.

For a non-central path S_1S_0 through a conical depression the reflections cannot be kept in the same plane but, disregarding this finesse (in line with other simplifications), the ratio of depth to chord in a cross section remains equal to x'/B and (236), as well as its more sophisticated original (234), should remain valid for the entire depression area, and not only for its central section.

Of course, these expressions presume a depth to diameter ratio considerably smaller than unity, as is always the case with actual impact craters. In the case of a very deep or infinite hole, every particle entering it is trapped. The gain factor then is evidently

$$G_{\infty} = 1 + (S_3S_0)/B + N \quad , \tag{237}$$

where N is the number of touchdowns preceding S_3 (when $S_2S_0 > B$). (Here S_3 stands for the more general S_n, the n-th touchdown.)

With an average for the two types of ricocheting as represented

TABLE XLV

Median Particle Radius (r_m), Impact Velocity (w_0) and Impact Angle ($\cos\gamma$) of Overlay Accretion, Filling Crater of Diameter B_0

B_0, cm	r_m, cm	$B_0/2r_m$	w_0, cm/sec	$\cos\gamma$
$\geq$655	2.4	>135	$\leq$8400	0.890
80	0.37	216	11000	0.930
21	0.1	210	12700	0.951
3.26	0.017	191	16000	0.962

TABLE XLVI

Trapping Gain Factor for Infinitely Deep Circular Hole of Average Chord B, or Diameter $B_o = \frac{4}{\pi} B$

B, cm	2	10	50	200	1000	5000	10^4	$2x10^4$	$4x10^4$	$8x10^4$	$1.6x10^5$
G_∞	7.50	6.68	5.83	5.23	4.28	3.41	3.21	2.63	2.06	1.92	1.57

TABLE XLVII

Cumulative Deficit or Negative Gain Factor, ω_e, (normalized to unity) around a Depression with $x'/B = \frac{1}{2}$. $\xi = \Delta L/B$ is the relative distance from the edge, so that the corresponding distance from the center of the depression is $B(\frac{1}{2} + \xi)$

ξ	0	0.121	0.168	0.241	0.292	0.330	0.47	0.54	0.61
ω_e	0	0.257	0.346	0.474	0.558	0.608	0.762	0.834	0.891
ξ	0.70	0.91	1.01	1.74	2.08	2.75	4.66	5.35	11.1
ω_e	0.932	0.954	0.959	0.979	0.985	0.992	0.997	0.999	1.000

by cases (1) and (2) of Table XXXVII, the gain factor is then as shown in Table XLVI. Unlike depressions of finite depth, the gain factor is different for a chord and a diameter. The case, however, is only of academic interest as the moon is concerned, although it probably helps in understanding the significance of the notion of gain factor.

Fig. 20 explains in detail the conditions set up in the sample calculation of the gain factor for a triangular (conical) trap (cross section ACB) of a depth one-quarter its diameter, $OC/AB = x'/D = \frac{1}{4}$. AB represents the ground level. The portion of the graph above this line pictures the transition from trapping to escape velocity (escape from the hole), for lunar acceleration of gravity (162 cm/sec^2), in the form of $\log(v_e^2/B)$ where v_e is the first rebound velocity after any impact at first entry just sufficient to make the rim of the depression (thus, in Fig. 19, v_2 is the velocity after touchdown S_2)), and $B = AB$ is the diameter of the trap.

The succession of "soft" and "hard" impacts was assumed exactly as in Table XXXVII, variant (1) ("soft" start) and variant (2) ("hard" start) being considered separately and an average of the two results then taken. The elementary kinematical problem consists in the condition for a projectile shot up from a point S_1 (Fig. 19, leg S_1S_2 as an example) under zenith angle z_1 with initial velocity v_1 to reach point M at distance $L = S_1E$ and altitude $h = ME$. The equation of the parabolic trajectory

$$h = L\cot Z_1 - gL^2/(2v_1^2 \sin^2 Z_1) \quad , \qquad (233)$$

to be represented also as a condition for velocity,

$$v_1^2 = gL \Big/ \left\{ \sin 2Z_1 \left[1 - (h\tan Z_1)/L \right] \right\} , \qquad (233a)$$

when applied to the single or double reflected trajectories (CA, MA, NP : PB, NQ : QB, Fig. 20) inside the depression, solves the problem of the velocity of escape from the trap. In the single/repeated (double) collisions the degradation of velocity was assumed to proceed with strictly alternating elasticity factors $\lambda_1 = 0.3$ and $\lambda_2 = 0.5$ in continuation of the sequence of Table XXXVII. If the point M (Fig. 19) was on the rim (B or A; Fig. 20) of the depression and the velocity v_1 was a minimum as compared to other combinations, this was then the escape velocity (v_e) required for a single impact. In Fig. 20, impacts on the back slope, CB, are indeed reflected in such a manner that most efficient escape is achieved by the first reflection : FM reflected into MA with velocity F'(F"); DC reflected into CA with velocity D'(D"); ~~etc~~ etc. (the curvature of the incoming trajectories is neglected). The escape velocity for these impacts is represented by the curve D'F'B' (Fig. 20, upper graph), based on three calculated points:

for entry at D, at velocity (D'), $v_e^2/B = 131.0$; for entry at F, velocity (F'), $v_e^2/B = 152.6$; for entry at B, velocity (B'), $v_e^2/B = 123.4$. The curve D'F'B' shows the logarithms of these quantities.

For impacts on the front slope (somewhere all along AC, Fig. 20), the first reflection (parallel to CK) runs at zenith angle $Z_K = Z_1 = 75^\circ.4$ and either meets the opposite slope (CB), or, even when not meeting, requires a double touch-down for escape at minimum velocity. If cb (Fig. 19, first leg ag is the opposite slope CB (of Fig. 20), the impacting zenith angle Z_2 is determined from

$$\cot Z_2 = dh/dL = \cot Z_1 - gL/(v_1^2 \sin^2 Z_1) \quad , \tag{239}$$

the impact velocity from

$$(v')^2 = v_1^2 - 2gh \quad ; \tag{240}$$

and the reflected zenith angle (Fig. 19) from

$$Z_3 = 180^\circ - 2\alpha - Z_2 \tag{241}$$

where α is the inclination of the slope cb or CB ($28^\circ.6$ in the present case).

The left-hand side of the velocity diagram in Fig. 20 (above AD) represents the escape velocities $\{\log(v_e^2/B)\}$ for impacts on the front slope AC. Two different cases occur, corresponding to two possible values of the elasticity factor at second impact, $\lambda\div$.

Thus, a projectile entering at H along HN (Fig.20) will leave the depression at B with minimum velocity H" by double trajectory HP:PB when $\lambda\div = 0.3$ at point P of second impact, and with minimum velocity H' along NQ:QB when $\lambda\div = 0.5$ at point Q. This bifurcation of escape velocity at impact on the front slope AC is represented in the upper graph of Fig. 20 by curve A"H"D"' for $\lambda\div = 0.3$ and by curve A'H'D" for

$\lambda = 0.5$.

For a given touchdown S_n (S_1; S_2; S_3 ..., Fig.19) the catch length is then equal to the abscissa interval in the upper portion of Fig. 20 over which the actual rebound velocity, v_n, falls below v_e. Thus, for $v_e^2/B = 100$, $\log v_e^2/B = 2.00$, this condition is fulfilled over the entire length AB, or the catch length $\Delta L = B$. For $v_e^2/B = 200$, $\log v_e^2/B = 2.3$, the condition is fulfilled only over the left-hand portion, AD, or for impacts on slope AC while those impacting on slope CB all do escape; $\Delta L = 0.408B$ obtains in this case.

Calculations of the gain factor at $x'/B = \frac{1}{4}$ along these principles for the same chosen set of diameters as in Table XLVI yielded G_f from 1.40 to 1.67, non-systematically fluctuating over the entire range of B from 2 to 8 x 10^4 cm, i.e. the range for which $B < S_1S_2$ (Fig.19) (the first ricochet length, Table XXXVII), and an expected systematic decrease only for larger depression diameters. The fluctuations were due to a "resonance" or "interference" effect between the diameter and the set of ricochet intervals. Otherwise the absolute value of B was irrelevant, and the individual values of G_f found for each B were considered as fair random samples of the gain factor. An average of

$$G_f = 1.529 \pm 0.039$$

was obtained. Of this the unit part is accounted for by the length B itself, a fraction of 0.387 is the average of the tailpiece $\Delta L_0/B$ (S_3S_0 in Fig.19) and a fraction of 0.142

is contributed by higher order touchdown (chiefly S_2, Fig. 19). By analogy with the thumb-rule equation (236), we may set (when $x'/B < 0.5$)

$$G_f = 1 + 2.116x'/B \quad , \qquad (242)$$

the coefficient being based on the outcome of our "numerical experiment". This gain factor is not dependent on absolute dimension when $B < 800$ meters and, thus, practically applies to craters of all sizes which can be eroded in 4.5×10^9 years or less and which are the object of our interest.

Gain in accretion inside a crater must be compensated by a loss in its neighborhood. The trapped tailpiece of the ricochet, $\Delta L = S_3S_o$ (Fig. 19), would have passed on level ground to a distance ΔB ranging from 0 to ΔL beyond the rim of the crater and is thus subtracted from a ring around the crater, bounded by the radii $\frac{1}{2}B$ and $\frac{1}{2}B + \Delta L$, the distribution function being uniform over this range (of the linear displacement of the source S_1, Fig. 19). In a first approximation, $\Delta L \sim G_f - 1$ and, therefore, when G_f decreases, the range ΔL decreases also and the withdrawal is effected chiefly by narrowing the ring of withdrawal, while little changing its depth.

From the same numerical experiment of filling a depth with $x'/B = \frac{1}{4}$ overlay (for a progression of the diameters as in Table (LVI), the distribution of the deficits (withdrawals) in the surroundings was obtained as represented in Table XLVII (each particle trapped in the depression corresponding to one missing from its prospective landing point outside the depression). $\xi = \Delta L/B$ denoting the relative radial extension of the catch area, each individual (unity) event contributing ΔG_f to the gain factor inside the depression (B) is conventionally to be spread uniformly over ΔL and contributes over this length to a uniform deficit $\Delta G_f / \xi$. The cumulative sum of these deficits, ω_e normalized to unity, is given in the table for each ξ-value without smoothing, i.e. as it directly turned out in the calculation for single chosen B-values

The deficit integrated over the interval of $\xi = 0$ to $\xi = \infty$ (radius $0.5 + \xi$ to ∞ in B-units) must equal the gain $G_f - 1$ over an area of $\frac{1}{4}\pi$ (in B^2 units). From this condition, accretion χ/χ_0 (in units of average accretion, χ_0) around the depression (crater) is given by

$$\chi/\chi_0 = 1 - \frac{\pi}{4}(G_f - 1).(d\omega_e/d\xi)/\pi(1 + 2\xi),$$

or

$$\chi/\chi_0 = 1 - \tfrac{1}{4}(G_f - 1)(d\omega_e/d\xi)/(1 + 2\xi) . \qquad (243)$$

Here $1 + 2\xi$ is the relative radius, or the relative diameter of the zone. The gradient $d\omega_e/d\xi$ was determined graphically from the smoothed data of Table XLVII, and the resulting relative accretion function (slightly smoothed) is given in Table XLVIII, for the original case of $x'/B = \frac{1}{4}$ and for a number of other depression (crater) profiles based on equations (242), (243) and a homology relation following from them when $\xi \sim G_f - 1$,

$$(\chi_o - \chi_b)/(\chi_o - \chi_a) = (1 + 2\,\xi_a)/(1 + 2\,\xi_b), \quad (244)$$

where

$$\xi_b / \xi_a = (x'/B)_b / (x'/B)_a \quad (244a)$$

Figure 21 represents the distribution of accretion rates inside and around a crater, according to the table.

The data of Table XLVIII can be used to calculate the evolutionary changes in the crater profile as it is filling, x' decreasing while a conical cross section is assumed to be maintained. If $dH = \chi_o dt$ is the increment of total accretion, the local increment is $dh = \chi dt$ and that at the crater edge (initially level outwards, without raised rim) $dh_o = 0.69dH = 0.69\chi_o dt$ (a). Filling of the crater depth by an amount $-dx'$ relative to the edge (simultaneously raised by dh_o) requires the addition of an average accreted layer over the crater area equal to $\frac{1}{3}dx' + dh_o$, whence

$$\chi_o G_f dt = \frac{1}{3}dx' + dh_o$$

or, eliminating the time, dt, as well as χ_o from expression (a), we obtain

$$0.69dH/dx' = dh_o/dx' = 0.23/(G_f - 0.69) \quad (245)$$

Also, for any point at distance ξ from the crater edge, with its proper accretion rate χ, the relative increment of accretion becomes

$$d(h - h_o)/dx' = \frac{1}{3}(\chi/\chi_o - 0.69)/(G_f - 0.69) \quad . \quad (245a)$$

Starting with $x'/B = 0.25$ or the first case of Table XLVIII, the evolution of the crater profile as calculated by approxi-

TABLE XLVIII

Relative Accretion, χ/χ_0, Outside a Crater at Distance $\Delta L = \xi B_0$ from the Rim; Inside, the Average Value is G_f; x'/B is the depth to diameter ratio of the circular depression

$\xi =$	0.0	0.05	0.10	0.15	0.20	0.3	0.4	0.5	0.6	0.7	0.8	1.0
						$x'/B = 0.25$; $G_f = 1.529$						
χ/χ_0	0.690	.730	.769	.805	.835	.882	.912	.938	.962	.983	.995	.998
						$x'/B = 0.20$; $G_f = 1.423$						
χ/χ_0	0.690	.735	.779	.818	.850	.896	.931	.964	.989	.996	.998	
						$x'/B = 0.15$; $G_f = 1.317$						
χ/χ_0	0.690	.744	.794	.838	.871	.922	.969	.987	.998			
						$x'/B = 0.10$; $G_f = 1.212$						
χ/χ_0	0.690	.758	.825	.872	.911	.934	.997					
						$x'/B = 0.05$; $G_f = 1.106$						
χ/χ_0	0.690	.809	.897	.981	.997							

mate numerical integration of (245a) and (245) is represented in Table XLIX.

The consecutive stages of evolution by filling are represented in Fig.22, according to the data of Table XLIX. The gradual degradation of the crater at the expense of its nearest surroundings leads to the formation of a depression around the crater border, gently sloping toward it without sharp outlines, reminding of some "washed-out" crater structures on Ranger photographs (shallow depressions and "dimple" craters, Fig. 23). At stage V, the crater and its surroundings have melted into one such shallow structure of increased diameter and indefinite outline. This is as far as the integration of (245a) is self-consistent and can be trusted. As to Stage VI, it is the result of a linear extension of (245a) and is but of qualitative or symbolic significance.

Although derived for the process of filling by incoming overlay, the sequence of evolution of a crater profile as shown in Fig. 22 would also apply to the two other processes of degradation (filling by spray, and downhill migration) because they, too, are working at the expense of the nearest surroundings of a crater; only the appropriate time scales of the processes will be different. The presence initially of a raised "soft" rim, consisting of the same overlay rubble, will not alter essentially the time scales of degradation, although geometrically there will be some difference while

TABLE XLIX

Evolution of Crater Profile by Filling

$\overline{B} = (2/\pi)B_o$

Stage	x_1'/B	h_H/B	0.1	0.2	0.3	0.4	0.5	0.6	0.7	0.8	1.0	h_c/B
			$10^5(h - h_o)/B$									
I	0.25	0	0	0	0	0	0	0	0	0	0	0
II	0.20	0.0212	178	322	422	492	552	606	635	650	657	0.0146
III	0.15	0.0457	414	739	959	1129	1254	1351	1390	1410	1417	0.0315
IV	0.10	0.0747	762	1322	1722	1979	2136	2237	2289	2309	2316	0.0515
V	0.05	0.1103	1370	2162	2662	3035	3232	3340	3392	3412	3413	0.0761
VI	0.00	0.1562	2537	3576	4085	4458	4656	4768	4815	4835	4842	0.1078

the rim is eroded simultaneously with the filling of the crater.

As to a hard rocky rim, such as presently could be expected for craters larger than 150 m, a two-staged process of their degradation will be considered separately.

By the nature of the filling process, the absolute rate of filling is roughly proportional to the relative depth x'/B, implying the rate of degradation to be an approximately exponential function of H, the total accretion (3rd column of Table XLIX). Multiplying these values by a factor of $2/\pi \approx 0.637$ as for an average chord of a circular crater, to obtain the accretion in units of B_o,

$$x'/B_o = (x_1'/B_o)\ \exp(-\tilde{H}/H_e)\ , \qquad (246)$$

where x_1' as before denotes the initial depth, the average linear measure of degradation, H_e, corresponding to the different intervals of the table, is found as follows:

Interval, x'/B	0.25--0.05	0.20--0.05	0.15--0.05	0.10--0.05
$\bar{H}_e/B_o$	0.0437	0.0410	0.0375	0.0323

The variation of this parameter partly reflects the approximative character of Equation (245a) in which changes in the surroundings are not taken into account, and only partly seems to be due to a real acceleration of the process at shallower profiles. This detail is only of academic interest, and we can assume safely an overall value of $H_e/B_o \approx 0.0375$.

The exponential relaxation time for filling is then

$$\tau_e = H_e/\chi_o$$

or, with the non-sticking influx of overlay being given by

$$\chi_0 = 2.66 \times 10^{-7}(y_2 - 0.15) \ (g/cm^2 . \ year), \qquad (247)$$

where y_2 is the cumulative mass fraction in the 2nd line of Table XXXV. D for double crater size,

$$\tau_e = 1.41 \times 10^5 B_0 / (y_2 - 0.15) \qquad (248)$$

in years for B_0 in cm. These values are calculated and used jointly with the two other processes of erosion in the next following section.

D. Erosion Lifetime of Soft-Rimmed Craters

As distinct from τ_f, τ_F, τ_e, or the exponential time scales of erosion and filling, the erosion lifetime as used in (204) and which is to be set against elimination by overlapping of larger craters, is the time interval during which the crater profile becomes so shallow as to become practically unrecognizable in the crater counts. For this we had already set a conventional limit of degradation, $x'/B_0 = 0.02$. Hence the erosion lifetime of a crater starting with a profile ratio of x'/B_0 can be set equal to

$$t_e = \tau_E \ln\left[(x'/B_0)/0.02\right] . \qquad (249)$$

where

$$1/\tau_E = 1/\tau_e + 1/\tau_F + 1/\tau_f \qquad (249a)$$

and τ_E is the total crater degradation time scale.

In Section VII. C, when discussing the accretion of overlay, a bend in the frequency of lunar craters at $B_1 = 285$ m suggested a lifetime of 4.5×10^9 years at this size and a

TABLE L

Filling Time Scale (τ_e), Total Degradation Time Scale (τ_E), and Degradation Lifetime (t_e) for Craters in Overlay Without Hard Rim

(a) Component J_e with Ricochets

B_o, cm	3.26	7.00	12.1	21.0	44.6	80.0	143	339	655	1460
x_1'/B_o, aver.	0.286	0.323	0.313	0.313	0.278	0.232	0.179	0.108	0.068	0.036
y_2 - 0.15	0.32	0.38	0.42	0.48	0.55	00.61	0.67	0.77	0.84	0.85
τ_e, years	1.44^{6}	2.60^{6}	4.06^{6}	6.17^{6}	1.14^{7}	1.85^{7}	3.01^{7}	6.21^{7}	1.10^{8}	2.42^{8}
τ_F, years	8.70^{4}	1.41^{5}	2.01^{5}	2.92^{5}	7.77^{5}	1.70^{6}	3.73^{6}	1.26^{7}	3.29^{7}	1.05^{8}
τ_f, years	2.66^{4}	8.25^{4}	2.34^{5}	6.57^{5}	2.84^{6}	9.17^{6}	2.92^{7}	1.66^{8}	6.20^{8}	3.08^{9}
τ_E, years	2.01^{4}	5.10^{4}	1.05^{5}	1.96^{5}	5.78^{5}	1.33^{6}	2.99^{6}	9.86^{6}	2.43^{7}	7.15^{7}
t_e, years	5.35^{4}	1.42^{5}	2.89^{5}	5.39^{5}	1.53^{6}	3.26^{6}	6.55^{6}	1.67^{7}	2.95^{7}	4.22^{7}

(b) Component J_1 (Meteorites—Apollo); y_2 - 0.15 = 0.85

B_o, cm	1530	2270	3940	7140	13800
x_1'/B_o	0.027	0.039	0.056	0.060	0.060
τ_e, years	2.54^{8}	3.77^{8}	6.54^{8}	1.19^{9}	2.29^{9}
τ_F, years	1.13^{8}	1.97^{8}	4.54^{8}	1.10^{9}	2.92^{9}
τ_f, years	3.33^{9}	7.43^{9}	2.23^{10}	7.36^{10}	2.75^{11}
τ_E, years	7.53^{7}	1.28^{8}	2.62^{8}	5.67^{8}	1.28^{9}
t_e, years	2.29^{7}	8.59^{7}	2.70^{8}	6.24^{8}	1.41^{9}
t', years	2.12^{8}	3.59^{8}	6.23^{8}	1.13^{9}	2.13^{9}

linear dependence of the lifetime on crater diameter for smaller craters,

$$t' = 1.58 \times 10^5 B_o \qquad (25C)$$

in years when B_o is in cm. The formula was meant to apply only to larger craters, $285 > B_o > 20$ meters. This provisional lifetime (without allowance being yet made for removal by overlapping) is quoted in the last line of Table L. At the largest size (138 m), where the linear effect of filling ($\mathcal{T}_e$) prevails, the two figures are close enough for this sort of data, while for smaller sizes the a priori calculated values of t_e become rapidly shorter than the rough linear approximation, t', on account of the non-linear effects of flow ($\mathcal{T}_F$) and spray ($\mathcal{T}_f$). The t_e values carry, of course, a greater weight than t', a rough approximation.

E. Erosion Lifetime of Hard-Rimmed Craters

A raised rocky rim can at present only be an attribute of moderately large craters, measuring hundreds of meters or more. Smaller craters will be completely built in overlay, with the projectiles not reaching down to the bedrock (as those of Table XXV). A rocky wall will isolate the crater from its surroundings as spray and flow are concerned, while the mechanism of filling by ricocheting overlay will be less impeded. We assume that, while the wall lasts, the crater bowl is filled by all the incoming overlay (2.66×10^{-7} cm/year) without excluding any part of it (the "sticking" fraction is taken care of by the flow and spray mechanism inside the crater's walls); plus straightforward micrometeorite accretion (8×10^{-9} cm/year) which makes an average accretion of

$$\chi_i = 2.74 \times 10^{-7} \text{ cm/year},$$

while outside the crater, in view of the outward slope (Fig. 1), the accretion will increase outwards, being negligible on the wall top. This would lead to a levelling out of the outward terrain and burying of the rocky wall, accelerated by direct sputtering as considered in Section X.A. With some protective layer being present, we assume one-half of the maximum sputtering rate of 5.2×10^{-8} cm/year. This gives the rate at which the wall is buried into a level terrain as

$$\chi_e = \chi_i + 2.6 \times 10^{-8} = 3.00 \times 10^{-7} \text{ (cm/year)} \qquad (251)$$

A rocky rim of height h_r above the terrain will thus be buried in a time interval of

$$t_I = h_r / \chi_e \qquad (252)$$

which represents the duration of the first stage of erosion.

According to equation (1), with $x' + h_r$ standing for x_r, the average depth of a typical crater reckoned from the wall top is $0.463(x' + h_r)$. During the first stage, this decreases by $\chi_i t_I$, whence the depth at the end of the first stage becomes

$$x_1' = (x' + h_r - \chi_i t_I)/0.463 \qquad (253)$$

The second, rim-less stage begins at this point and is to be treated according to the rules of Section X.D. The relaxation times, τ, are assumed to depend solely on crater diameter as before, while the erosion lifetime in the second stage, t_e, is calculated for a degradation of the profile from x_1'/B_0 to 0.02 [equation (249)]. The results are collected in Table LI. The total lifetime equals then the sum of the two time intervals,

$$t_t = t_e + t_I \tag{254}$$

The provisionally estimated linear lifetime, t' [equation (250)], differ by chance very little from the values of t_e or t_I of Case B of the table. Contrary to what was found for the small rimless craters, the erosion lifetimes of the craters with a hard rim are found here to be longer than the t'-values: by 20--30 per cent in Case A (primaries) and by a factor of about 2.5 in Case B (ray secondaries). The turning point in the frequency of craters would then be expected to take place at B_0= 234 meters when the primary craters (Case A) begin to be completely eroded in 4.5 x 10^9 years, and a second turning point is predicted at about B_0= 112 meters when the deeper profiles of the secondaries (Case B of the table) are erased during this interval of time. Of course, the transition in the frequency function of crater areal densities is expected to take place gradually, on account of the spread in the physical and geometrical parameters of cratering. The empirically suggested start of complete erosion at B_1= 285 meters is thus not in contradiction but in satisfactory agreement with the prediction which, besides, cannot pretend to suggest anything more than a close order of magnitude.

TABLE LI

Erosion and Filling Degradation Lifetimes (t_t) of Craters with a Hard Rim

B_o, cm	4.62×10^4	3.66×10^4	2.83×10^4	2.14×10^4	1.64×10^4	1.29×10^4	1.00×10^4

Erosion relaxation times independent of profile

$\tau_e = 1.66 \times 10^5\ B_o$ for filling by overlay; $\tau_F = 1790\ B_o^{1.5}$ for downhill transport; $\tau_F = 1440\ B_o^2$ for spray over the rim (too long to be considered); all in years; $\tau_E = (1/\tau_e + 1/\tau_F)^{-1}$ the total relaxation time.

τ_e	7.67^9	6.07^9	4.70^9	3.56^9	2.72^9	2.14^9	1.66^9
τ_F	1.78^{10}	1.26^{10}	8.53^9	5.61^9	3.76^9	2.62^9	3.62^8
τ_E	5.40^9	4.10^9	3.03^9	2.18^9	1.58^9	1.18^9	1.08^9

A. Typical Primary Craters (Asteroidal)

$x' = 0.100\ B_o$; $h_r = 0.020\ B_o$; $t_I = 6.67 \times 10^4 B_o$; $x_1' = 0.031\ B_o$; $t_e = 1.40\tau_E$

t_e	7.56^9	5.74^9	4.24^9	3.05^9	2.21^9	1.69^9	1.51^9
t_I	3.08^9	2.44^9	1.89^9	1.43^9	1.09^9	0.86^9	0.68^9
t_t	10.64^9	8.18^9	6.13^9	4.48^9	3.30^9	2.55^9	2.19^9

B. Typical Secondary Craters (Ray Crater Ejecta)

$x' = 0.25 B_o$; $h_r = 0.05\ B_o$; $t_I = 1.67 \times 10^5 B_o$; $x_1' = 0.201 B_o$; $t_e = 2.35\tau_E$

t_e	12.7^9	9.63^9	7.12^9	5.13^9	3.72^9	2.78^9	2.54^9
t_I	7.7^9	6.11^9	4.73^9	3.58^9	2.73^9	2.15^9	1.67^9
t_t	20.4^9	15.74^9	11.85^9	8.71^9	6.45^9	4.93^9	4.21^9

Interesting is the case of $t_{\Sigma} > 4.5 \times 10^9$ years which defines the survival of an original stone-walled rim/ since the "beginning". In Case A (asteroidal), the lower limit of unconditional survival of a hard rim is $B_o > 700$ meters, while in Case B(secondaries) the deeper profile would allow the rocky rim to survive when $B_o > 270$ meters.

A striking example, almost a test case, is presented by the stone-walled crater on the horizon of Surveyor I pictures (Fig. 6). The boulder wall is apparently the crest of a buried rocky rim of a crater which has come near the end of the first stage of erosion. Although there is much freedom in the interpretation, some limitations can be discerned. With $B_o = 450$ meters, its age must be less than t_{Σ} which is 7.5×10^9 years when a secondary (Case B) and 3.0×10^9 years when a primary crater (Case A). If a secondary, its actual age cannot exceed 4.6×10^9 years, during which time its outward rim height, chiefly buried and partly eroded, must have decreased by $\chi_e \times 4.5 \times 10^9$ cm (251) or 13.5 meters. An original height of $h_r = 0.05B_o = 22.5$ m would leave thus 9.0 meters of a stony rim towering above the surrounding plain, and more if the age is shorter; the actual height of the stone wall at its conspicuous part is 1.7 m, and the all-round average is less, perhaps 1.0 m. Case B is difficult to reconcile with the data and appears to be improbable.

It remains to assume that the crater is a primary one, of an age less than about three billion years. There is, of course, an uncertainty in the initial profile ratio, but assuming the typical Case A of Table LI, the initial rim height may have been $h_r = 0.02B_o$ or 9.0 meters of which, however, the top may have consisted of overlay. The finer ingredients of overlay are rapidly removed by micrometeorite impacts, leaving the coarser fraction, about 60 per cent of its mass (Table XXXV A, $1 - G_d = 0.60$ average), to be sputtered as hard rock. The effective height of the rocky rim is thus to be decreased by 0.4 of the overlay layer. If t is the age of the crater as a fraction of 4.5×10^9 years, the overlay thickness at time of impact can be set at 14(1 - t) meters, the effective initial altitude of the hard crater wall at 9.0 - 0.4 x 14(1 - t) meters, which is to be buried and eroded at a rate of $3.00 \times 10^{-7} \times 4.5 \times 10^9$ cm or 13.5 meters per chosen unit of time [the initial rate of overlay formation, 14 m before the cratering event is purposedly taken larger than its later or present rate, $2.66 \times 10^{-7} \times 4.5 \times 10^9$ cm or 12 meters per unit time (aeon)] If the wall height has been decreased by burial and erosion to an average altitude of 1.0 m, this leads to an equation for the determination of age :

$$9.0 - 5.6(1 - t) - 1.0 = 13.5\ t$$

which yields.

$$t = 0.30 = (1.35 \pm 0.5) \times 10^9 \text{ years},$$

roughly 1.4 billion years for the age of the stone-walled crater of Surveyor I.

F. Overlay Accretion : Second Approximation

In Table XXIX the overlay volume was calculated from observed crater volume statistics with provisional allowance being made for the disappearance of smaller craters through erosion, and for two limiting cases of a protective layer : A, for zero overlay thickness; and B, for 12 meters as its present thickness. The linear equation (250) for the lifetime was used. Now we are in possession of erosion lifetimes, calculated a priori by more sophisticated methods which can be applied to a revision of the expected accumulated volume of overlay. Only those craters whose lifetime is shorter than 4.5×10^9 years are affected by the lifetime condition. Part B of Table XXIX has been recalculated accordingly, with the new lifetime data as of Tables L and LI, separately for primaries and secondaries. Overlapping is a minor effect for these large craters, affecting their numbers but by a fraction of a percent and is here disregarded. The crater areal densities are then simply proportional to the lifetime, t_e. Table LII contains the results of the revision.

The result does not differ essentially from the first one and firmly indicates an overlay layer of about 14 meters at present. The total sum in the last line of the table, 1535 cm replacing the former result of 1307 cm, is increased chiefly at the expense of small secondaries which were actively affecting the bedrock only a very short time after the formation of the maria. This detail is highly conjectural, and we may leave the subject at that, being satisfied that the new refined treatment of crater lifetimes has little affected our original estimate of overlay thickness.

TABLE LII

Recalculation of Overlay Accretion, Case B of Table XXIX, by assuming the Present Overlay Thickness to be 12 meters and a uniform rate of accretion (data which are not quoted are identical with those of Table XXIX) (the crater numbers are for an area of 2.22×10^5 km^2)

B_o, meters	$\gtrsim$214	164	129	100	79	62	49	37	28	20
n_p(true number, 4.5×10^9 yrs, calculated, primaries)	...	1.49^5	3.77^5	8.14^5	1.25^6	2.19^6	3.85^6	1.05^7	2.28^7	5.00^7
t_e(primaries, all "soft") years	...	1.68^9	1.32^9	9.46^8	7.11^8	5.11^8	3.67^8	2.39^8	1.35^8	5.61^7
E_f(primaries deletion ratio)	...	2.63	3.41	4.77	6.33	8.81	12.3	18.8	33.4	80.8
n_p/E_f(predicted observable number of primaries)	...	5.6^4	1.09^5	1.71^5	1.98^5	2.48^5	3.13^5	5.59^5	6.83^5	6.19^5
n_o(total observed)	...	1.47^5	2.32^5	3.62^5	5.70^5	9.00^5	1.41^6	2.33^6	5.40^6	9.40^6
$n_o - n_p/E_f$(concluded observable number of secondaries)	...	9.1^4	1.23^5	1.91^5	3.72^5	6.52^5	1.10^6	2.41^6	4.72^6	8.83^6
t_e secondaries ($B_o \geq 79$m, hard-rimmed; $B_o \lesssim 62$, soft-rimmed, 1.93 times the value for primaries)	...	$>4.5^9$	$>4.5^9$	4.21^9	3.32^9	9.83^8	7.09^8	4.62^8	2.58^8	1.08^8
E_f, secondaries	...	1	1	1.07	1.35	4.55	6.34	9.75	17.4	41.6
n_s(true number of secondaries)	...	9.1^4	1.22^5	2.04^5	4.02^5	2.96^6	6.97^6	2.36^7	8.22^7	3.70^8
Σ ΔX_p(unchanged), cm Accretion	...	9	9	7	4	3	2	2	1	1
ΔX_s, cm	...	38	26	19	23	64	71	92	110	133
$X = \Sigma \Delta X$, cm	921	968	1003	1029	1056	1123	1196	1290	1401	1535

Figure Captions

Fig. 1. Vertical semi-cross-section, to scale, of an impact crater (the prototype is the nuclear explosion "Teapot" crater in Nevada; Shoemaker, 1963). The linear scale unit is B_o, the rim-to-rim diameter of the crater.

Fig. 2. Throwout integral $1 - F_B$ (ordinates, logarithmic scale) as function of log $\underline{t}$ for four discrete values of $\underline{a}$ (0.20, 0.39, 0.70, 0.91). Fig. 2a, same as a function of log ($\underline{ab}$), when $\underline{a} > 0.91$. The parameters: $\underline{a} = 8\chi/\delta \sin\beta_o/B_o$; $\underline{b} = g\,B_o/(4\chi^2 s \sin\beta_o)$; $\sin\beta_o = 0.8$.

Fig. 3. Crater profiles for Baldwin's later classes (pre-mare age). All on continentes. Logarithmic scale. Abscissae, crater diameter (B_o, km); ordinates, depth to diameter ratio, $(x' + H)/B_o$. Measured points: centered circles, Class 2; crosses, Classes 3 and 4; dots, Class 5. The four calculated curves are those of Table XIV, with the parameters indicated in the Figure.

Fig. 4. Crater profiles for Baldwin's Class 1 (post-mare age). Coordinates as in Fig. 3. Measured points: ~~centered circles~~ dots; on maria; crosses, on continentes; ~~double~~ centered circles, ray craters. The two lower calculated curves (P and Q) are those of Table XV, and the two upper ones (G and F) are from Table XIV. The assumed parameters are indicated with the curves.

Fig. 5. Surveyor I photograph 66-H-834, June 2, 1966. At center left, a crater of 3 meters diameter, probably of secondary origin, its rocky projectile having ricocheted out. In the foreground, a rock about 70 cm,

a secondary ejectum having come to rest on the surface after ricocheting. On the horizon, a stone-walled crater 450 meters in diameter, with the stone wall seen best preserved in the upper right corner; probably interplanetary primary 1500 ± 500 million years old. - Courtesy of NASA and Jet Propulsion Laboratory

Fig. 6. Surveyor I photograph 66-H-807, June 15, 1966. Stone-wall detail of the crater (same as in Fig. 5) on the horizon (450m); average blocks in its wall measure 70 cm. Courtesy of NASA.

Fig. 7. Crater Alphonsus (left) and Mare Nubium (right). Ranger IX 2 min 50 sec before impact on March 24, 1965, from altitude of 258 miles. Dimensions of frame 121 x 109 miles. Courtesy of the NASA Goddard Space Flight Center, Greenbelt, Maryland.

Fig. 8. Peak of Alphonsus (middle top). Ranger IX 39 seconds before impact, from altitude of 53 miles. Dimensions of frame 28 x 26 miles. - Courtesy of NASA Goddard Space Flight Center, Greenbelt, Maryland.

Fig. 9. The East (astronautical) or West (astronomical) (left) wall of Alphonsus. Ranger IX 1 min 17 sec before impact, from altitude of 115 miles. Courtesy of NASA Goddard Space Flight Center, Greenbelt, Maryland.

Fig. 10. Distribution of overlay thickness in lunar maria. Abscissae, percentage area. Ordinates, thickness in meters. For full line, scale to the left; for dashed line, scale to the right.

Fig. 11. Distribution of overlay thickness in lunar highlands (continentes). Cf. Fig. 10.

Fig. 12. Surveyor I, Footpad 2 on lunar surface. Diameter of footpad top, 30.5 cm. Courtesy of NASA.

Fig. 13. Surveyor III, Footpad 2, third touchdown, with surface sampler and a depression made by it (bottom left). - Courtesy of NASA.

Fig. 14. Surveyor I, Footpad 2, enhanced contrast. - Courtesy of NASA.

Fig. 15. Orbiter II photograph (November 19, 1966) of an area 360 x 450 meters in Mare Tranquillitatis, showing strewn fields of blocks ranging up to 9 meters in diameter. - Courtesy of NASA.

Fig. 16. Surveyor I photograph 66-H-589, June 2, 1966. Crater No. 5 (3m diameter) and rock, the same as in Fig. 5. - Courtesy of NASA.

Fig. 17. Surveyor I photograph 66-H-814, June 15, 1966. Crater No. 5 and block (see Figs. 5 and 16) at low sun illumination. - Courtesy of NASA.

Fig. 18. Downhill migration of dust. A micrometeorite MO strikes a slant surface SS. OA, OB are trajectories of particles ejected symmetrically with respect to the normal ON which makes an angle α with the vertical OZ. Fig. 18a. Cross section of conical crater H O_1H, with impact craterlet at O. Trajectories shorter than O O_1 lead to unrestricted downhill drift, those longer than O O_2 end uphill or outside the crater.

Fig. 19. Trapping of incoming ricocheting overlay particles by a depression with a circular horizontal contour.

Fig. 20. Trapping mechanism through semi-elastic riccocheting in a depression of triangular (conical) vertical cross section. The impacting projectiles enter along HN, DC, FM, at an angle $z = \Upsilon = 22^{o}.2$ from the vertical.

Fig. 21. Relative accretion rates of overlay, X / X_o (ordinates), inside and outside a rimless crater. ξ (abscissa) is the distance reckoned outwards from the crater edge, in units of crater diameter. Profile ratios: centered circles, $x_1'/B = 0.25$; dots, $x_1'/B = 0.20$; crosses, $x_1'/B = 0.15$; centered squares, $x_1'/B = 0.10$; centered triangles, $x_1'/B = 0.05$.

Fig. 22. Evolution of rimless crater profile and its surroundings by trapping and filling. Initial profile ratio $x_1'/B = 0.25$. Qualitatively valid also for erosion.

326

Fig. 23. Ranger IX photograph, March 24, 1965, showing shallow eroded craters in Alphonsus. Frame 1.6 x 1.4 miles. Smallest craters are 9 meters in diameter. Courtesy of NASA.

XI. Summary

(1) Impact cratering and erosion are the prevailing factors which have been shaping the lunar surface for the past four billion years.

(2) Impact melting has produced the lava flows of the maria, at an early stage, 4.5 billion years ago. The maria were also the seat of primeval volcanism as testified by some less conspicuous surface details such as the domes and dykes.

(3) No traces of contemporary orogeny or volcanism on the moon are indicated. The Alphonsus event of 1958 was not a gaseous eruption but a case of fluorescence of the solid crater peak.

(4) Cratering formulae are proposed as derived from first principles, with little empirical adaptation. The main arguments are momentum of the projectile and strength of the target, not energy as has been often used in limited interpolations of experimental results. The range of application of the formulae is almost unlimited, for velocities from tens of centimeters to tens of kilometers per second. Without using empirical coefficients of proportionality, the formulae represent the cratering dimensions – penetration and volume – better than within ±20 per cent. Special formulae are derived and empirically tested for low-velocity impact of rigid projectiles into granular targets, with direct application to the lunar surface layer. The cratering formulae, including throwout and fall-back equations, are used to derive the cohesive strength of lunar rocks, in its bearing on the origin and history of the lunar surface.

(5) Formulae for the encounter probabilities, lifetimes and statistical accelerations of particles in planetary encounters are given, with emphasis on small relative velocities as for near-circular nearly co-planar orbits. The

328

damping effect of an orbiting ring of particles upon its individual members, and its bearing on accretion of larger bodies is considered.

(6) The problems of the origin of the moon are analysed with the help of the theories of cratering and planetary encounters. The mathematical theory of tidal evolution can describe the past history of the earth-moon system with some confidence only as far back as to a "zero hour" corresponding to the moon's distance near Roche's limit, somewhat less than 3 earth radii, whence the moon started receding. From geologic evidence, the date of this phase could not have been later than 3.5 billion years ago, the age of the oldest dated terrestrial rocks; most probably, it coincided with the age of the earth, 4.5 billion years, because all the initial events connected with the origin of the moon must have evolved on a short time scale of 10^5 - 10^7 years. Tidal friction at the time of closest approach, working on a time scale of 10^3 years or less (too short for significant cooling by radiation), must have melted the outer mantle of the earth, erasing all previous geologic records.

(7) The history of the earth-moon system prior to this zero hour is open to conjecture, because neither the identity of the interacting bodies of which most have disappeared, nor their masses and initial orbits can be ascertained. If, however, the theories are to conform with the meagre observational evidence, requiring (a) that the craters on the continentes were formed on the receding moon by projectiles orbiting the earth at about 5 earth radii (as testified by their ellipticities, and by the lack of an excess of crater numbers on the preceding hemisphere of the moon), and (b) that the surface of the moon at that time, though solid but soft, was hot but only insignificantly or moderately melted by the impacts, - two models appear more probable than the others: (I) Model 5 of Table IX, implying an origin from debris orbiting inside Roché's limit, either

analogous to the rings of Saturn, or thrown off through instability of the rotating earth; with sufficient mass load in the rings, cohesive clumping of the debris enables them slowly to work their way out tidally, beyond Roche's limit, to collect first into some six-odd intermediate moonlets, and ultimately into one lunar body at about 5 earth radii; (II) Alfven's adaptation of Gerstenkorn's model of tidal capture, in which the incoming moon, originally captured into a retrograde orbit and put into synchronous rotation, passes slightly outside Roche's limit at closest approach where it sheds off its outer and lighter mantle, retaining a denser core. This, while receding, again collects most of the lost material. The formation of the maria on the earthward side of the moon, through a belated impact of a moonlet (broken up tidally before impact on the moon), previously formed from the material ejected inwards, is also plausibly accounted for by Alfvèn's model. As to the time of the event, it never could have happened as recently as 700 - 1000 million years ago, for reasons stated under point (6).

(8) The formation of a mare is explained by impact melting of a hot crust in a cratering collision, on a linear scale sufficiently large for the melt to fall back into the crater; on a smaller scale, the liquid is sprayed over the crater walls in all directions and cannot form one coherent fluid body of lava.

(9) Crater profiles, orographic differences in level, and the secondary craters produced by the ejecta of ray craters can be consistently interpreted on assuming (a) that the post-mare craters were produced in a relatively cool rocky target of the strength of granite or basalt, by interplanetary projectiles (asteroidal bodies and comet nuclei) at velocities of 20 - 40 km/sec, and (b) that the pre-mare craters were produced by slow projectiles, about 3 km/sec, impacting on a hot and relatively soft surface, about one-tenth of the strength of granite, and c) that th

orographic differences of level on the moon were formed during the same period of primeval bombardment when the crust was hot and soft.

(10) The statistics of craters (larger than 1 - 2 km) in lunar maria are consistent with astronomical observation, cratering theory and theory of planetary encounters when target rock is assumed to be of the strength of granite or basalt. There is no basis whatever for interpreting the origin of the overwhelming majority of the craters as not being caused by impacts.

(11) Details in the frequency function of the diameters of smaller craters suggest a minimum survival limit of about 300 meters diameter against erosion during 4.5×10^9 years. This roughly agrees with theoretical calculations of the rate of erosion on the moon.

(12) Statistics of small craters in Alphonsus are consistent with their impact origin from a mixed population of pre-mare projectiles, among which slow secondary ejecta prevailed; the scarcity of craterlets on the peak and wall of Alphonsus is explained by the hardness of these targets (bare rock or rock under a thin protective cover), while the floor of Alphonsus carrying 15-20 times more craterlets per unit area is consistent with a loose target about the strength of terrestrial desert alluvium. The collapse or caving-in hypothesis of the craterlets is unacceptable, both because of their prevailing circular shape, and because of the relative uniformity of their distribution, the crater density down to the same diameter being similar in distant regions of the maria as well as in Alphonsus. The floor of Alphonsus, formed probably without coherent melting, may have spread out into a level surface in a kind of "ash flow". Its peak (as well as the peaks of many other craters) can be interpreted as a surviving remnant (compacted at impact) of the rear portion of the projectile that produced the crater.

(13) The top layer of lunar soil consists of a heterogeneous mixture of particles of a broad distribution of sizes. Effective values of different physical quantities may depend on particles of different size. Thus the thermal conductivity of the upper 10 cm, consisting of three components - the bulk conductivity through a grain, the radiative conductivity between grains, and the contact conductivity (depending on contact area, increasing with pressure and depth) - can be accounted for by a constant effective grain diameter of 0.033 cm, while the strong radar reflectivity and thermal inertia of the hot spots requires the presence of a prominent component of sizeable boulders, imbedded in the rubble as well as strewn over its surface. The normal radar reflectivity, pointing to a bulk dielectric constant of 2.6 - 3.0, is compatible with an average density of 1.3, or 50% porosity for a basaltic composition. Cohesion of grains in vacuo is sufficient to balance the lunar gravity of grains smaller than about 0.13 cm; these are responsible for the "fairy-castle" structure of the top layer determining the optical properties of the moon, especially the dominance of phase angle and the strong backscatter at zero phase, in the visible portion of the spectrum. On a scale of centimeters and meters, the top soil is polished by micrometeorites into a gently undulating surface with specular reflectivity.

(14) The dependence of radioactive conductivity on temperature leads to a day-night asymmetry and a positive thermal gradient in the top soil even at zero flux. If this is taken into account, radio observations of the thermal gradient in the lunar soil lead to a net flux from the moon's interior of 3.4×10^{-7} cal/(cm^{2}sec) as compared to 4.3×10^{-7} which is the earth's value decreased in proportion to the lunar radius (thus corresponding to equal content of radioactive sources if thermal equilibrium is assumed).

(15) The average temperature on the lunar equator is $-65^{\circ}C$ on the surface, $-49^{\circ}C$ at one meter and $-23^{\circ}C$ at 7 meters depth. The pressure-dependent increase of conductivity with depth prevents the top layer from playing any significant insulating role, so that the thermal state of the moon's crust is not much affected by it: at equal depth, the crust is only about $50^{\circ}C$ warmer than it would have been without the insulating top layer.

(16) Impact erosion leads to levelling out of lunar surface features without relevance to an "angle of repose".

(17) The amount of lunar surface material sputtered to space by solar wind, about 45 g/cm^2 in 4.5 billion years, is nearly equal to the gain from the slow micrometeorites of zodiacal dust. The meteoritic material is admixed to an average accumulated overlay layer of about 13 meters or 1700 g/cm^2 (over the maria and outside the range of ejecta of large craters). The other, fast meteoric components lead to a loss of about 23 g/cm^2 of lunar material.

(18) In building-up of overlay from the underlying rock, three penetrating components of meteorite flux are relevant: the Apollo-meteorite component (pseudo-asteroidal); the comet nuclei; and the asteroids deflected from Mars crossings. Frequency formulae for the three fluxes as depending on particle radii are given and the corresponding crater densities (numbers per unit area) calculated. The observed excess in the densities of small craters is consistently interpreted as due to a fourth component, namely to secondary ejecta from violent cratering events (ray craters). With little dependence on this interpretation, the overlay thickness and its statistical distribution over maria and continentes is calculated from the volume excavated by the actually observed craters, the numbers of those smaller than 300 m being corrected for survival from erosion.

(19) From cratering theory and an empirical dependence of the strength of brittle materials on particle size ($-\frac{1}{4}$ power of diameter), the exponent of the differential frequency (per unit of volume or mass) of particle radii in cratering ejecta is found to be $n = 3.875$, in good agreement with particle counts in lunar overlay from spacecraft landings.

(20) The mechanical properties of lunar soil are similar to those of terrestrial sand. The bearing strength at equal depth, and the kinetic efficiency at impact are nearly one-half of those of typical terrestrial beach gravel. The bearing strength (frontal resistance) is about 5×10^4 dyne/cm^2 at the surface, 6×10^5 at 5 cm and 2.5×10^6 at 10 cm penetration. The cohesive lateral resistance (crushing strength) is about 1/18th of the bearing strength at equal depth.

(21) Electrostatic transport is theoretically limited to particles of submicron size. The absence of blurring of detail (less than 0.5 km for demarkation lines in Alphonsus) indicates that such particles and "electrostatic hopping" do not play a significant role on the lunar surface.

(22) The ballistic fluxes impinging on the lunar surface consist of five interplanetary components (J_M, the micrometeorites; J_O, the dustball meteors; J_1, the Apollo-meteorite group; J_2, comet nuclei; J_3, Mars asteroids deflected to earth crossing) and of secondary ejecta of primary cratering events (component J_e). The quantitative characteristics of the interplanetary components are deduced from observation as corrected for selectivity, while J_e is assessed from the excavated cratering volume as corrected for interplanetary impacts and erosion.

(23) Cratering parameters for the ballistic fluxes are calculated for overlay. For component J_e, quantitatively assessed ricocheting is viewed as amplifying

crater generation in overlay. Only a fraction G_g (0.4 - 1.0 as depending on particle size) of the impacts are of the granular target type while the rest are into larger grains or boulders and are of the hard target type.

(24) Components J_M and J_o produce too shallow craters in overlay to be observed; the action of these components is limited to erosion, 82 per cent of which can be accounted for by them. Component J_e accounts for 97% of the ballistic mass, but only for 15% of the impact momentum and erosive capacity. Components J_2 and J_3 (comet nuclei and the Mars asteroids) are negligible for small cratering in the sub-kilometer to meter range where J_e and the meteorite groups, J_1, are solely of importance, but they - chiefly J_2 - gain in importance and dominate in large cratering events (above 5 km).

(25) With a conventional limit of observability of 0.02 for the crater depth to diameter ratio, the a priori calculated crater generation rates, as set against deletion through overlapping and degradation through filling and erosion, lead to theoretical crater areal densities in the diameter range from 3 cm to 150 m and beyond which are in satisfactory agreement with observation from space probes.

(26) Mixing of overlay proceeds slower than its accumulation. The mixing thickness is about 8 cm, corresponding to a difference or "blurring" in age of the strata of about 30 million years; this represents the "stratigraphic resolving power" of overlay. There is practically no interchange of material between layers separated by more than 25 cm or 100 million years.

(27) The ballistic astronautical hazard on the lunar surface is negligible, being by orders of magnitude smaller than the hazards we are willing to accept in everyday life on earth.

(28) Crater and boulder degradation rates from filling by overlay, and from several types of erosion (spray from micrometeorite impact, downhill migration of dust,

sputtering of crater rims and boulders and their burial by overlay) have been quantitatively assessed theoretically from first principles and from the observed properties of interplanetary populations. The results are in satisfactory accord with the observed areal densities of small craters on the moon.

(29) Ablation of exposed rock on the lunar surface is estimated to be about 5×10^{-8} cm/year, while the average rate of burial into overlay (however, a widely fluctuating quantity, according to cratering events in the vicinity) is about 2.7×10^{-7} cm/year, so that it is buried before becoming eroded. Rocks lying on the surface are secondary ejecta which have come to rest after several ricochets. Craters in overlay left behind the ricocheting impacts are relatively deep (Fig. 6, the 3-meter crater), contrary to those made by primary interplanetary impacts which are too shallow to be observable.

(30) As the result of filling and erosion, which takes from the surroundings the filling material, the crater profile becomes shallower while the effective diameter increases.

(31) Some examples of theoretical degradation lifetimes of craters, or the time of reduction to a profile ratio of $x'/B_o = 0.02$:

Crater diameter, B_o(cm)	3.3	45	650	1.5×10^3
Origin and description	Secondary, soft rim	Secondary, soft rim	Secondary, soft rim	Interplanetary, primary, soft rim
Lifetime, years	5.4×10^4	1.5×10^6	3.0×10^7	2.3×10^7
Crater diameter, B_o(cm)	4×10^3	1.4×10^4	1.15×10^4	2.1×10^4
Origin and description	Interplanetary primary, soft rim	Interplanetary primary, soft rim	Secondary hard rim	Interplanetary primary, hard rim
Lifetime, years	2.7×10^8	1.4×10^9	4.5×10^9	4.5×10^9

REFERENCES

Alfvèn, H. (1963). Icarus, 1, 357-363.

Alfvèn, H. (1965). Science, 148, 476-477.

Alfvèn, H. (1968). Personal discussion.

Allan, D. W., and Jacobs, J. A. (1956). Geochimica et Cosmochimica Acta, 9, 256-272.

Baldwin, R. B. (1949). "The Face of the Moon". Univ. of Chicago Press, Chicago, 239 pp.

Baldwin, R. B. (1963). "The Measure of the Moon". Univ. of Chicago Press, Chicago, 488pp.

Baldwin, R. B. (1964a). Ann. Rev. Astron. Astrophys., 2, 73-94.

Baldwin, R. B. (1964b). Astron. J., 69, 377-392.

Bastin, J. A. (1965). Nature, 207, 1381-1382.

Binder, A. B., Cruikshank, D. P., and Hartmann, W. K. (1965). Icarus, 4, 415-420.

Christensen, E. M., et al. (1967). J. Geophys. Research, 72, 801-8 3.

Cloud, P. E. (1968). Science, 160, 729-736.

Coffeen, D. L. (1965). Astron. J., 70, 403-413.

Comerford, M. F. (1966). Smithsonian Astrophysical Observatory Preprints in Meteoritics: "Comparative Erosion Rates of Stone and Iron Meteorites under Small Particle Bombardment". 36 pp.

Darwin, Sir George (1879). Philos. Transactions Roy. Soc., 170, 447-530.

Dodd, R. T., Salisbury, J. W., and Smalley, V. G. (1963). Icarus, 2, 466-480.

Dollfus, A. (1966). In "The Nature of the Lunar Surface", 155-172. Johns Hopkins, Baltimore, 320 pp.

Drake, F. (1966). In "The Nature of the Lunar Surface", 277-284. Johns Hopkins, Baltimore, 320 pp.

Egan, W. G., and Smith, L. L. (1965). Grumman Memorandum RM-304, 65 pp.

Evans, J. V. (1962). Tech. Report No. 256, Lincoln Lab., M.I.T., Bedford, Mass.; Conference on Lunar Exploration, Paper VIII, 48 pp; Va. Polytechnic Institute.

Evans, J. V., and Pettengill, G. H. (1963). In "The Moon, Meteorites and Comets", 129-161. Middlehurst, B. M., and Kuiper, G. P., Eds., Univ. of Chicago Press, Chicago, 810 pp.

Fedorets, V. A. (1952). Public. Astron. Observatory Kharkov, 2, 49-172.

Fielder, G. (1962). J. British Astron. Association, 72, 223.

Fielder, G. (1963). Nature, 198, 1256-1260.

Fielder, G. (1965). Monthly Notices Roy. Astron. Soc., 129, 351-361.

Fielder, G. (1966). Monthly Notices Roy. Astron. Soc., 132, 413-422.

Gault, D. E., Quaide, W. L., Oberbeck, V. R., and Moore, H. J. (1966). Science, 153, 985-988.

Gear, A. E., and Bastin, J. A. (1962). Nature, 196, 1305.

Gehrels, T., Coffeen, T., and Owings, D. (1964). Astron. J., 69, 826-852.

Gerstenkorn, H. (1955). Z. Astrophys., 36, 245-274.

Gold, T. (1955). Monthly Notices Roy. Astron. Soc., 115, 585-604

Gold, T. (1962). In "The Moon", 433-439. Kopal, Z., and Mikhailov, Z. K., Eds., Academic Press, New York, 571 pp.

Gold, T. (1966). In "The Nature of the Lunar Surface", 107-121. Johns Hopkins, Baltimore, 320 pp.

Gold, T., and Hapke, B. W. (1966). Science, 153, 290-293

Hagfors, T. (1966). In "The Nature of the Lunar Surface", 229-230. Johns Hopkins, Baltimore, 320 pp.

Hapke, B. W., and Van Horn, H. (1963). J. Geophys. Research, 68, 4545-4586

Hapke, B.W. (1964). J. Geophys. Research, 69, 1147-1151.

Hapke, B.W. (1965). Annals New York Ac. Sc., 123, 711-721.

Hapke, B. W. (1966a). In "The Nature of the Lunar Surface", 141-154. Johns Hopkins, Baltimore, 320 pp.

Hapke, B. W. (1966b). Astron. J., 71, 333-339.

Hapke, B. W. (1968). Planetary Space Sci., 16, 101-110

Halajian, J. D., and Spagnolo, F. A. (1966). Grumman Memorandum, RM-308, 89pp., Bethpage, N.Y.

Hapke, B., and Gold, T. (1967). Sky & Telescope, 33, 84

Hartmann, W. K. (1965). Icarus, 4, 157-165 and 207-213.

Hartmann, W. K. (1966). "Nininger Meteorite Award Paper", 24 pp., Arizona State University.

Hartmann, W. K. (1967). Icarus, 7, 66-75.

~~Jaffe, L. D. (1965). J. Geophys. Research, 70, 6129-6138~~;

Jaffe, L. D. (1967). J. Geophys. Research, 72, 1727-1731,

Jaffe, L. D. and NASA Team (1966a), Science 152, 1737-1750

Jaffe, L. D. and NASA Team (1966b). "Surveyor I Mission Report", Part II, JPL Pasadena, Tech. Report No. 32-1023, 100 pp.

Jeffreys, Sir Harold (1947a). Monthly Notices Roy. Astron. Soc., 107, 260-262.

Jeffreys, Sir Harold (1947b). Monthly Notices Roy. Astron. Soc., 107, 263-267.

Kopal, Z. (1965). Boeing Sci. Research Lab. Mathem. Note No. 430, 39 pp.

Kopal, Z. (1966a). In "The Nature of the Lunar Surface", 173-183. Hess, W. N., Menzel, D. H., and O'Keefe, J. A., Eds. Johns Hopkins, Baltimore, 320 pp.

Kopal, Z. (1966b). Icarus, 5, 201-213.

Krotikov, V. D., and Troitsky, V. S. (1962). Astron. Zh., 39, 1089-1093.

Krotikov, V. D., and Troitsky, V. S. (1963). Uspekhi Fizicheskikh Nauk, 81, 589-639

Kozyrev, N. A. (1959a). Priroda, March 1959, 84-87.

Kozyrev, N. A. (1959b). Sky Telescope, 18, 561.

Kozyrev, N. A. (1962). In "The Moon", 265-266. Kopal, Z., and Mikhailov, Z. K., Eds., Academic Press, New York, 571 pp.

Kuiper, G. P. (1954). Proc. Natl. Acad. Sci. U.S., 40, 1096-1112.

Kuiper, G. P. (1966). Communications Lunar and Planet. Lab., 4, 1, 1-70.

Kuiper, G. P., Arthur, D. W. G., Moore, E., Tapscott, J. W., and Whitaker, E. A. (1960). "Photographic Lunar Atlas". University of Chicago Press, Chicago.

Levin, B. J. (1966a). Proceedings Caltech - JPL Lunar and Planetary Conference (JPL TM 33-266), 61-76, and elsewhere.

Levin, B. J. (1966b). In "The Nature of the Lunar Surface", 267-271. Johns Hopkins, Baltimore, 320 pp.

Linsky, J. L. (1966). Icarus, 5, 606-634

Lipsky, Y. N. (1966). Sky Telescope, 32, 257-260

Low, F. J. (1965). Astrophys. J. 142, 806-808

MacDonald, G. J. F. (1964). Reviews of Geophysics, 2, 467-541.

Majeva, S. V. (1964). Doklady Academii Nauk SSSR, 159, 294-297.

Marcus, A. H. (1964). Icarus, 3, 460-472

Marcus, A. H. (1966a). Monthly Notices Roy. Astron. Soc., 134, 269-274.

Marcus, A. H. (1966b). Icarus, 5, 165-200 and 5, 590-605.

Minnaert, M. (1961). In "Planets and Satellites", 213-248. Kuiper, G. P., and Middlehurst, B.M., Eds., Univ. of Chicago Press, Chicago, 601 pp.

Munk, W. S. (1968). Harold Jeffreys Lecture delivered at Burlington House, 29 March 1968.

Murphey, I. F. (1961). In Proceedings of the Cratering Symposium, Paper G, 1-13. Lawrence Radiation Laboratory, Livermore, California, 434 pp.

Murray, B. C., and Wildey, R. L. (1964). Astrophys. J., 139, 734-750.

NASA (1964). "Ranger VII Atlas. Part I - Camera A", JPL - Cal Tech.

NASA (1965a). "Ranger IX Atlas", JPL - Cal Tech.

NASA (1965b). "Ranger VII Atlas. Part III - Camera P", JPL - Cal Tech.

NASA (1967). "Surveyor III Mission Report", Tech. Report 32-1177, JPL Pasadena, Part I, 194 pp., and Part II (June 1, 1967), 216 pp.

Newell, H., and NASA Team (1966). "Surveyor I Preliminary Report", NASA SP - 126, 39 pp.

Newell, H. E., and NASA Team (1967). "Surveyor III Preliminary Report", NASA SP-146, 159 pp.

Nordyke, M. D. (1961). In Proceedings of the Cratering Symposium, Paper F, 1-14. Lawrence Radiation Laboratory, Livermore, California, 464 pp.

Oetking, P. (1966). J. Geophys. Research, 71, 2505-2513

Olson, S. (1966). American Scientist, 54, 458-464 .

O'Keefe, J. A. (1964). Science, 146, 514-515 .

O'Keefe, J. A. (1966a). In "The Nature of the Lunar Surface", 259-266. Johns Hopkins, Baltimore, 320 pp.

O'Keefe, J. A. (1966b). Science News, 90, 441 .

O'Keefe, J. A., Lowman, P. D., and Cameron, W. S. (1967). Science, 155, 77-79 .

Öpik, E. (1936). "Theory of Formation of Meteor Craters", Acta et Comm. Univ. Tartu, A30; Tartu Observ. Public., 28, No. 6 .

Öpik, E. J. (1951). Proc. Roy. Irish Acad., 54A, 165-199; Armagh Observ. Contrib. No. 6

Öpik, E. J. (1955). Irish Astron. J., 3, 245-248 .

Öpik, E. J. (1956). Irish Astron. J., 4, 84-135; Armagh Observ. Contrib. No. 19

Öpik, E. J. (1958a). Irish Astron. J., 5, 14-36; Armagh Observ. Contrib. No. 24

Öpik, E. J. (1958b). Irish Astron. J., 5, 79-95; Armagh Observ. Contrib. No. 28

Opik, E. J. (1958c). "Physics of Meteor Flight in the Atmosphere". Interscience, New York, 174 pp.

Öpik, E. J. (1960). Monthly Notices Roy. Astron. Soc., 120, 404-411; Armagh Observ. Contrib. No. 29.

Öpik, E. J. (1961a). "Notes on the Theory of Impact Craters". In Proceedings of the Geophysical Laboratory - Lawrence Radiation Laboratory Cratering Symposium, Paper S, 1-28. Milo D. Nordyke, Ed., Lawrence Radiation Laboratory, Livermore, California, 464 pp.

Opik, E. J. (1961b). Astron. J., 66, 60-67

Opik, E. J. (1962a). In "Progress in the Astronautical Sciences", 215-260 S. F. Singer, Ed., North Holland, Amsterdam, 398 pp.

Opik, E. J. (1962b). Planetary Space Sci., 9, 211-244.

Opik, E. J. (1963a). Advances in Astronomy and Astrophysics, 2, 219-262

Opik, E. J. (1963b). Irish Astron. J., 6, 39-40

Opik, E. J. (1963c). Irish Astron. J., 6, 3-11; Armagh Observ. Contrib. No. 38. (1963) Ibidem, 6, 162-164

Opik, E. J. (1964). Irish Astron. J., 6, 279-280.

Opik, E. J. (1965a). Advances in Astronomy and Astrophysics, 4, 301-336.

Öpik, E. J. (1965b). "Particle Distribution and Motion in a Field of Force", in Interactions of Space Vehicles with an Ionized Atmosphere, 3-66, Pergamon Press, Oxford; Armagh Observ. Contrib. No. 52.

Opik, E. J. (1965c). Irish Astron. J. 7, 92-104; Armagh Observ. Leaflet No. 67

Opik, E. J. (1966a). Congres et Colloques de L'Universite de Liege, 37, 523-574.

Opik, E. J. (1966b). Congres et Colloques de l'Universite de Liege, 37, 575-580.

Opik, E. J. (1966c). Irish Astron. J., 7, 141-161; Armagh Observ. Contrib. No. 54

Opik, E. J. (1966d). In "The Nature of the Lunar Surface", 287-291 Johns Hopkins, Baltimore, 320 pp.

Öpik, E. J. (1966e). Science, 153, 255-265.

Öpik, E. J. (1966f). Irish Astron. J., 7, 201-205

Pettengill, G. H., and Henry, J. C. (1962). J. Geophys. Research, 67, 4881-4885

Pettit, E. (1961). In "Planets and Satellites", 400-428. Kuiper, G. P., and Middlehurst, B. M., Eds., Univ. of Chicago Press, Chicago, 601 pp.

Rolsten, R. F., Hopkins, A. K., and Hunt, H. H. (1966). Nature, 212, 495-497.

Rosenberg, D. L., and Wehner, G. K. (1964). J. Geophys. Research, 69, 3307-3308

Ryan, J. A. (1966). J. Geophys. Research, 71, 4413-4425

Saari, J. M. (1964). Icarus, 3, 161-163.

Saari, J. M., and Shorthill, R. W. (1966). Sky Telescope, 31, 327-331.

Schmidt, O. J. (1950). Izvestia Acad. Nauk SSSR, Ser. Fiz., 14, No. 1, 29-45

Senior, T. B. A. (1962). Conference on Lunar Exploration, Paper IX, 32 pp. Va. Polytechnic Institute.

Senior, T. B. A., and Siegel, K. M. (1960). J. of Research National Bureau of Standards, 64 D, 217-229

Shoemaker, E. M. (1963). In "The Moon, Meteorites, and Comets", 301-336. Middlehurst, B. M., and Kuiper, G. P., Eds., Univ. of Chicago Press, Chicago, 810 pp.

Shoemaker, E. M. (1966). In "The Nature of the Lunar Surface", 23-77. Johns Hopkins, Baltimore, 320 pp.

Shoemaker, E. M., Hackman, R. J., and Eggleton, R. E. (1963). Advances in the Astronomical Sciences, 8, 70-89; Plenum Press, New York.

Shorthill, R. W., and Saari, J. M. (1965a). Nature, 205, 964-965.

Shorthill, R. W., and Saari, J. M. (1965b). Science, 150, 210-212.

Shorthill, R. W., and Saari, J. M. (1966). In "The Nature of the Lunar Surface", 215-228. Johns Hopkins, Baltimore, 320 pp

Singer, S. F., and Walker, E. H. (1962). Icarus, 1, 112-120.

Slichter, L. B. (1963). J. Geophys. Research, 68, 4281-4288.

Smith, Bruce G. (1967). J. Geophys. Research, 72, 1398-1399.

Smoluchowski, R. (1966). J. Geophys. Research, 71, 1569-1574.

Sorokin, N. A. (1965). Astronomitcheskij Zhurnal, 42, 1070-1074.

Thompson, T. W., and Dyce, R. B. (1966). J. Geophys. Research, 71, 4843-4853.

Trask, N. J. (1966). J.P.L. Tech. Rep. No. 32-800, pp. 252-263, Pasadena

Troitsky, V. S. (1962). Astron. Zh., 39, 73-78.

Turkevich, A. L., Franzgrote, E. J., and Patterson, J. H. (1967). Science 158, 635-637.

Turkevich, A. L., Patterson, J. H., and Franzgrote, E. J. (1968). Science 160, 1108-1110.

Twersky, W. (1962). J. Math. Phys., 3, 724-734

Urey, H. C. (1960a). Proceedings First Intern. Space Sc. Symposium, 1114-1122, North-Holland, Amsterdam; and elsewhere

Urey, H. C. (1960b). J. Geophys. Research, 65, 358-359; and elsewhere

Urey, H. C. (1965). JPL Tech. Report 32-800, 339-362.

Urey, H. C. (1966). In "The Nature of the Lunar Surface", 3-21. Johns Hopkins, Baltimore, 320 pp.

Walker, E. H. (1966). J. Geophys. Research, 71, 5007-5010

Walker, E. H. (1967). Icarus, 7, 183-187

Watts, C. B. (1963). Astron. Papers Amer. Ephemeris, 17, 1-951.

Watts, R. N. (1967). Sky Telescope, 33, 97

Wattson, R.B., and Danielson, R. E. (1965). Astrophys. J., 142, 16-22.

Wattson, R. B., and Hapke, B. W. (1966). Astrophys. J., 144, 364-368.

Wehner, G. K., Kenknight, C. E., and Rosenberg, D. (1963a). Planetary Space Sci., 11, 1257-1261

Wehner, G. K., Kenknight, C., and Rosenberg, D. L. (1963b). Planetary Space Science, 11, 885-895.

Wesselink, A. J. (1948). Bull. Astron. Institutes Netherlands, 10, 351-363.

Whipple, F. L. (1959). Vistas in Astronautics, 2, 267-272.

Whitaker, E. A. (1966). . In "The Nature of the Lunar Surface", 79-98. Johns Hopkins, Baltimore, 320 pp.

Wildey, R. L., and Pohn, H. A. (1964). Astron. J., 69, 619-634

NOTATIONS

(A) Cratering Symbols

a, b ... fallback parameters; also semi-axes of ellipse

$a^2 = 2\ cm^2$ ... coefficient of surface strength of granular target

B_o ... rim-to-rim diameter of crater

$\frac{1}{2}B$ ... throwout distance from center of crater

d ... spherical equivalent diameter of projectile

$D = B_o/d$ ... the relative crater diameter

F ... coefficient of lateral transmission of penetration (pressure) work against cohesive resistance

H ... rim to bottom crater depth

f_b ... differential fallback fraction

F_b ... integrated fallback fraction

f_s ... coefficient of friction

f_g ... vaporized fraction in central funnel

g ... acceleration of gravity

K_a ... drag coefficient of inertial (hydrodynamic) resistance

K_r ... coefficient of radial momentum transfer

L ... flight distance of ejecta

M ... total cratering mass affected

M_c ... cratering mass crushed

m ... mass load of projectile per unit cross section

$p = x_p/d$, the relative penetration

P, Q ... penetration parameters for granular target

Q ... symbol of central funnel

q ... shock heating per unit mass

R ... equivalent radius of projectile front surface (cross section)

s, s_p ... lateral (crushing) and frontal (compressive) strength of target

s_c ... cohesive component of lateral strength

s_t ... tensile strength

S_c; S_p ... strength parameters for granular target

u ... shock front velocity

u_s ... ultimate (destructive) shock velocity of target

V, V_d, V_p ... total cratering volume affected, and its dynamic and pressure components

V_c ... cratering volume crushed

v, v_o ... ejection velocity from depth and from surface

w_o ... initial impact velocity of projectile

$w_1 = \psi w_o$ ... velocity of entry into granular target as decreased by shock

w_m ... minimum velocity for destruction of projectile

x_o ... depth of penetration of front of projectile below original target surface

x_p ... maximum depth of crater bottom affected

x' ... apparent depth of crater

x_c ... average depth of crushing

y ... fraction of cratering mass inside shock front

y_Q ... fraction of cratering mass in central funnel

z ... zenith angle of incidence or ejection

β, β_o ... angle and maximum angle of ejection relative to normal

347

γ ... angle of incidence of projectile relative to normal

ζ ... density of projectile

ε ... ellipticity of crater

λ ... coefficient of kinetic efficiency (elasticity) at ejection

λ_x, λ_c ... same, at depth x and in central funnel

λ_r ... same, in ricocheting

μ ... mass of projectile

σ ... cross section of projectile

σ_s ... strength of target at secondary ray crater

ρ ... density of target (rock, soil)

(β) Planetary Encounters and Cosmogony Symbols

$A = a/r_p$ relative semi-major axis of orbit

A_p ... total accretion rate (on a satellite)

a ... orbital semi-major axis

a_m, a_1, a_2 ... distance of moon from earth, earth radii

c_1, c_2 ... average specific heat of solid and liquid

D_f ... a distance inside Roche's limit

D_r ... Roche's limit of distance for tidal disruption

e, e_0, e' ... orbital eccentricity

f_m ... melted fraction of cratering material

f_{pg} ... fraction of particles ejected out of the system in gravitational encounters

G ... gravitational constant

H_0 ... pre-melting heat per unit mass

H_f ... heat of fusion

i_e ... inclination of the orbits of two colliding bodies to the resultant orbit

i, i_p, i_c ... orbital inclination

J_m ... rate of mass accretion per unit area

K_p ... coefficient of P_o, or of the average encounter probability

K_t, K_o ... thermal conductivity, and same of compact rock

K_s ... Stefan's radiation constant

L_r ... radial damping length for collision of planetesimals

m, m_o, m_c ... mass load per unit cross section; of pre-planetary ring of planetesimal

m_c' ... linear mass load of planetesimal

N ... number density

N_f ... number of fragments

N_r ... number of fragments in one coherent ring

P_e, P_m ... mathematical expectation of encounter per orbital revolution, and its upper limit

P_o ... average P_e for a random U-vect

Q_o ... rate of black body radiation

R_a ... radius of sphere of gravitational action

R_o ... radius of planet (earth)

R_p and R_3 ... radius of satellite (moon) or planet (earth); and of planetesimal

R_f ... upper limit of radius of fragments surviving tidal breakup

r ... distance from main body (heliocentric, geocentric)

T_s, T_e, T_o ... temperature: subsurface, surface radiative, initial

T_a ... angular deflection parameter

T_m ... temperature of fusion

t_A ... time scale of increase of semi-major axis of accelerated particles

t_a ... time of outward tidal drift of the moon

t_F ... average time of free fall of particle upon satellite

t_i ... period of precession of orbital plane

$t_{\delta\sigma}$ ... damping lifetime of planetesimal in ring at finite inclination

t_r ... radial damping time at $i \sim 0^{\circ}$

t_s ... synodic orbital period

$t(\sigma)$ ... lifetime for encounter at parameter σ

$t(\bar{\pi})$ ... perica of the motion of perigee

$t(\omega)$ ... period of the argument of periastron (perigee, perihelion)

u_0 ... equatorial velocity of rotation

U, U_m ... Jacobian velocity of encounter, in units of circular velocity, and its average.

U_r ... radial component of U

v ... encounter velocity in metric units

v_c ... orbiting circular velocity

v_h ... heliocentric velocity

v ... velocity of escape

w_f ... minimum impact velocity to cause fusion

δ, $\delta_{\oplus}$, δ_{ρ} ... density: of planetesimal, of earth, of moon

Δh ... thickness of lava crust

$\xi(U)$ ... fraction of particles surviving (eluding) physical collisions.

η_m .. mass fraction retained by pre-planetary ring

η_t ... probability of encounter for time interval t

θ, θ_0, θ_{max} ... melted fraction

μ ... mass of "planet" or "satellite" revolving around central body of mass $1-\mu$

μ_1, μ_2 ... masses of two competing accreting nuclei

σ_c ... target radius for physical collision

σ_e ... target radius or encounter parameter (in units of r)

σ_a ... target radius for angular deflection of 90^0

ω ... angular distance of periastron from node, or argument of periastron

ω_c ... orbital angular velocity

ω_r ... angular velocity of rotation

ρ_1, ρ_0 ... space density of particulate matter in pre-planetary ring

(Y) Symbols in Mixed Context

A_a, A_v, A_e, A_o ... ricocheting amplification factors

A_d ... force of cohesion between grains

A_r ... reflectivity at normal incidence

d_g ... diameter of grain

dN/dt d_N/d_t ... number flux

E_1, E_e, E'_m ... transport efficiency

E_f ... statistical erosion (survival) factor of craters
F_i ... meteorite incidence; creation rate of craters
E_h ... downhill flow (of dust, of overlay)

G_g ... fraction of granular target at impact into overlay

G_f, G_v ... gain factors in filling of depression by overlay

H ... depth of depression; also total layer of accreted overlay

H_p, H_s ... impact penetration into overlay

h_r ... height of rim

J ... radial (cratering) momentum flux

J_μ, J_o, J_1, J_2, J_3, J_e ... the six components of the lunar surface cratering (radial) momentum flux in overlay, as well as the symbols of the components themselves: micrometeorites, dustball meteors, Apollo-Meteorites, comet nuclei, Mars asteroids, secondary ejecta. J_G

J_c ... supplementary to preceding overlay-penetrating flux relating to intermediate and large craters: $S = J_c - J_1$

J_r ... total radial momentum in a cratering event

L_d ... electrostatic screening length in plasma

L_e ... effective depth from which radiation is emitted

L_m ... radius of spread of cratering ejecta

L_t ... effective depth of thermal wave in soil

n ... power index in differential frequency function of particle radii (frequency index of radii)

N_a, N_c ... cumulative number of impacts; by Apollo group, by comet nuclei

n_i, n_o, n_c, n_p, n_s ... number of impacts; crater areal density

Q_a ... amplitude of heat content per cm^2 of surface

Q_m, Q_f ... mixing factor of overlay, for past and future

R with proper subindices ... impinging projectile radius

r, r_o ... ejecta particle radius as distinct from R

S ... area

S_o, S_f ... area of crater, area covered by ejecta

t_r ... relative age of craters

t_e, t' ... degradation lifetime of craters, and provisional value

τ_I ... erosion lifetime of rim

t_t ... total degradation lifetime of rimmed craters

t_m ... mixing time of overlay

V_e ... volume of ejecta

v_a, V_e ... velocity of inelastic grain capture; also ricocheting escape velocity from trap

X, X_0, X_1 ... overlay thickness; from small craters; averaged from large craters

Y ... Young's modulus

α ... angle of inclination to horizon

α' ... kinetic parameter for ejecta (cm^{-1})

γ/t ... thermal inertia parameter

ε_i, ε_0 ... dielectric constant, of granular and of compact rock

η ... fraction of momentum retained after penetration of a layer

Θ_a ... surface temperature amplitude

κ ... kinetic thickness of a protective layer

λ_e ... wavelength

μ_1, μ_2, μ_3, μ_0 ... total mass influx from flux components (see J - components)

$d\mu/d\tau$ ... mass flux

ν .. overlapping deletion rate of craters

σ_B ... cumulative crater area coverage per unit time and area

σ_p ... contact area of grains per unit cross section

τ ... fractional area covered by ejecta; also total erosion relaxation time

τ_o, τ_F, τ_f, τ_e, τ_s ... exponential relaxation times in various processes of crater degradation

τ_m ... total supply of overlay accretion time

τ_E ... total degradation time scale (relaxation time)

λ, λ_o ... equivalent thickness of overlay annually displaced by meteorite impact

λ_s ... rock or boulder ablation, cm/year

γ_L ... fraction of λ ejected beyond distance L

ω_e ... negative gain factor around depression

Öpik —

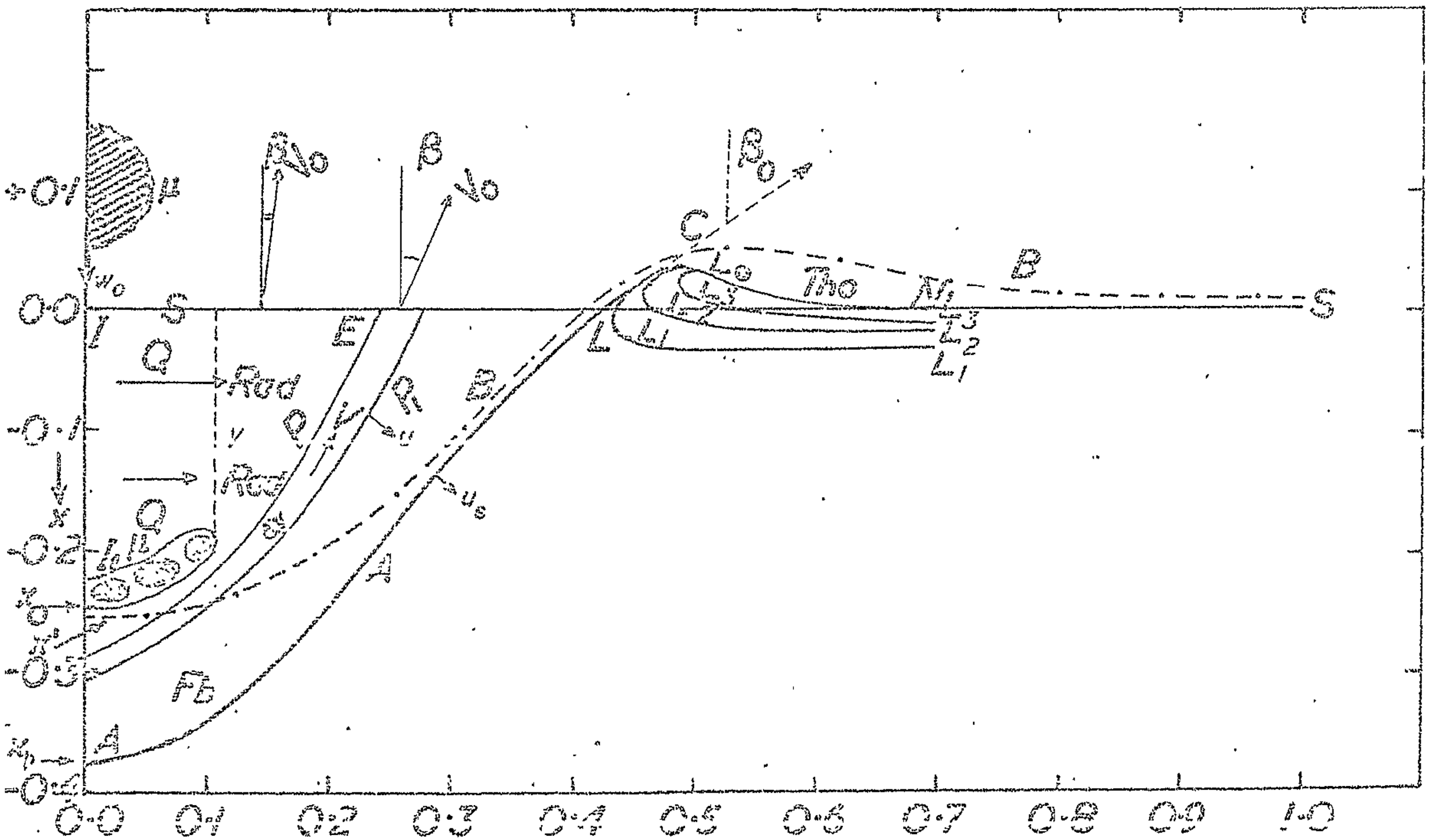
+0·1
0·0
-0·1
-0·2
-0·3
-0·4
0·0
0·1
0·2
0·3
0·4
0·5
0·6
0·7
0·8
0·9
1·0
S
Q
Rad
Rad
E
B
C
B
Tho
S
L
L1
Fb
A

Fig 1

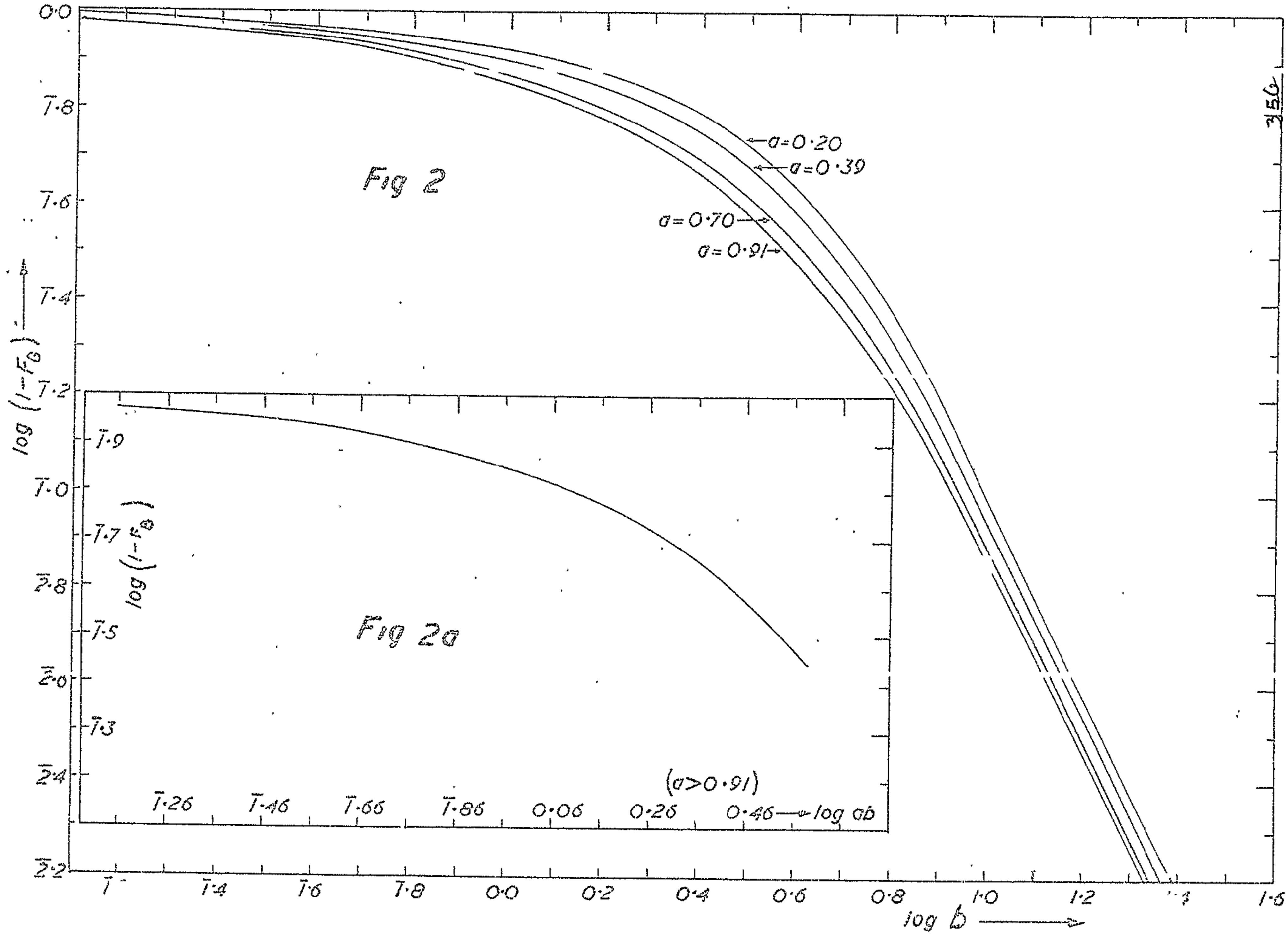

0·0
$\bar{1}$·8
$\bar{1}$·6
$\bar{1}$·4
$\bar{1}$·2
$\bar{1}$·0
$\bar{2}$·8
$\bar{2}$·6
$\bar{2}$·4
$\bar{2}$·2
log $(1-F_G)$
Fig 2
a=0·20
a=0·39
a=0·70
a=0·91
$\bar{1}$·4
$\bar{1}$·6
$\bar{1}$·8
0·0
0·2
0·4
0·6
0·8
1·0
1·2
1·6
log b
$\bar{1}$·9
$\bar{1}$·7
$\bar{1}$·5
$\bar{1}$·3
log $(1-F_G)$
Fig 2a
(a>0·91)
$\bar{1}$·26
$\bar{1}$·46
$\bar{1}$·66
$\bar{1}$·86
0·06
0·26
0·46
log ab

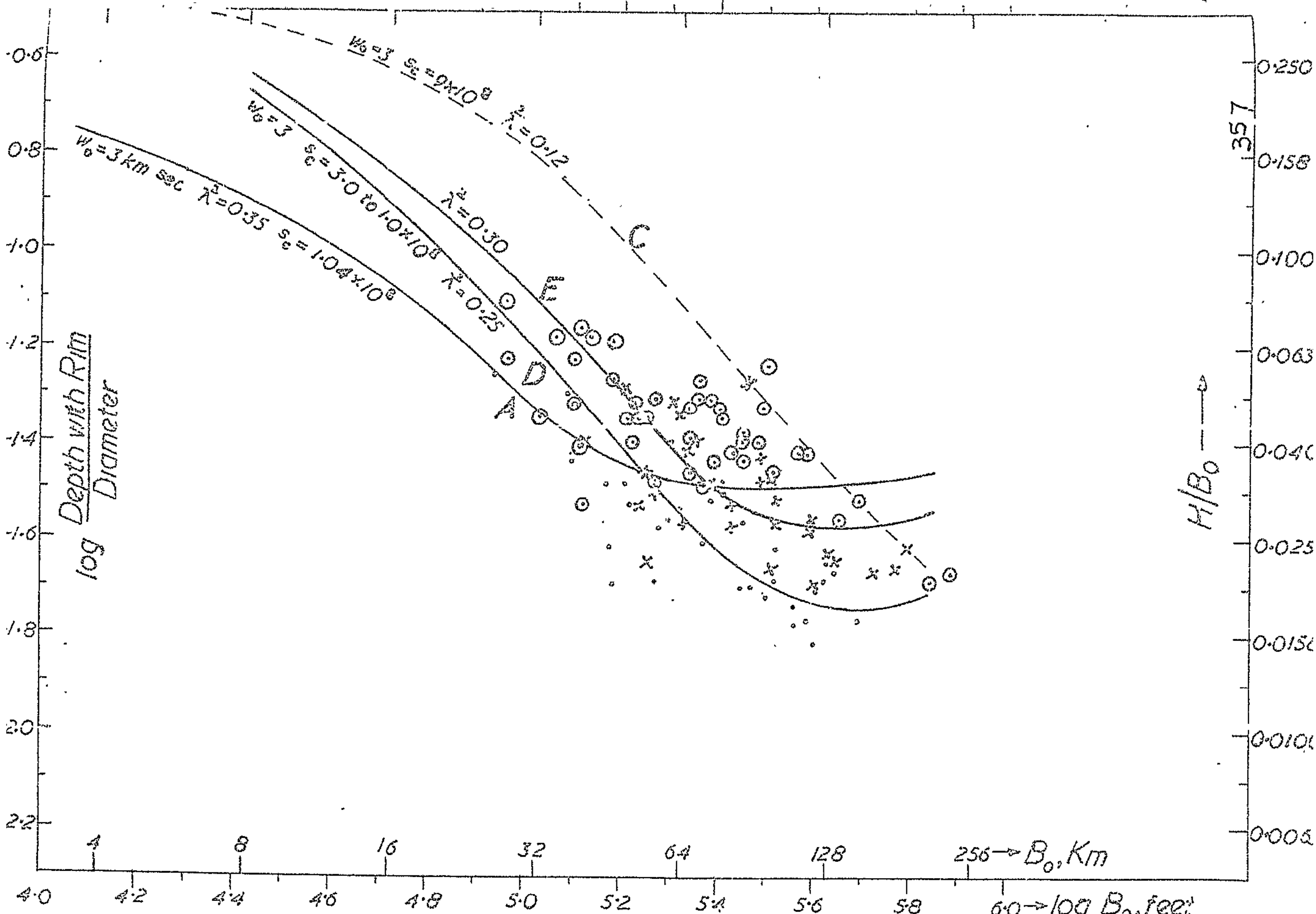
log Depth with Rim / Diameter
H/B₀ →
log B₀, feet
B₀, Km
W₀ = 3 km sec λ² = 0·35 s₀ = 1·04 × 10⁸
W₀ = 3 s₀ = 3·0 to 1·0 × 10⁸
λ² = 0·25
λ² = 0·30
W₀ = 3 s₀ = 9 × 10⁸ λ² = 0·12
A
D
E
C
4·0
4·2
4·4
4·6
4·8
5·0
5·2
5·4
5·6
5·8
6·0
4
8
16
32
64
128
256
0·6
0·8
1·0
1·2
1·4
1·6
1·8
2·0
2·2
0·250
0·158
0·100
0·063
0·040
0·025

Fig 3

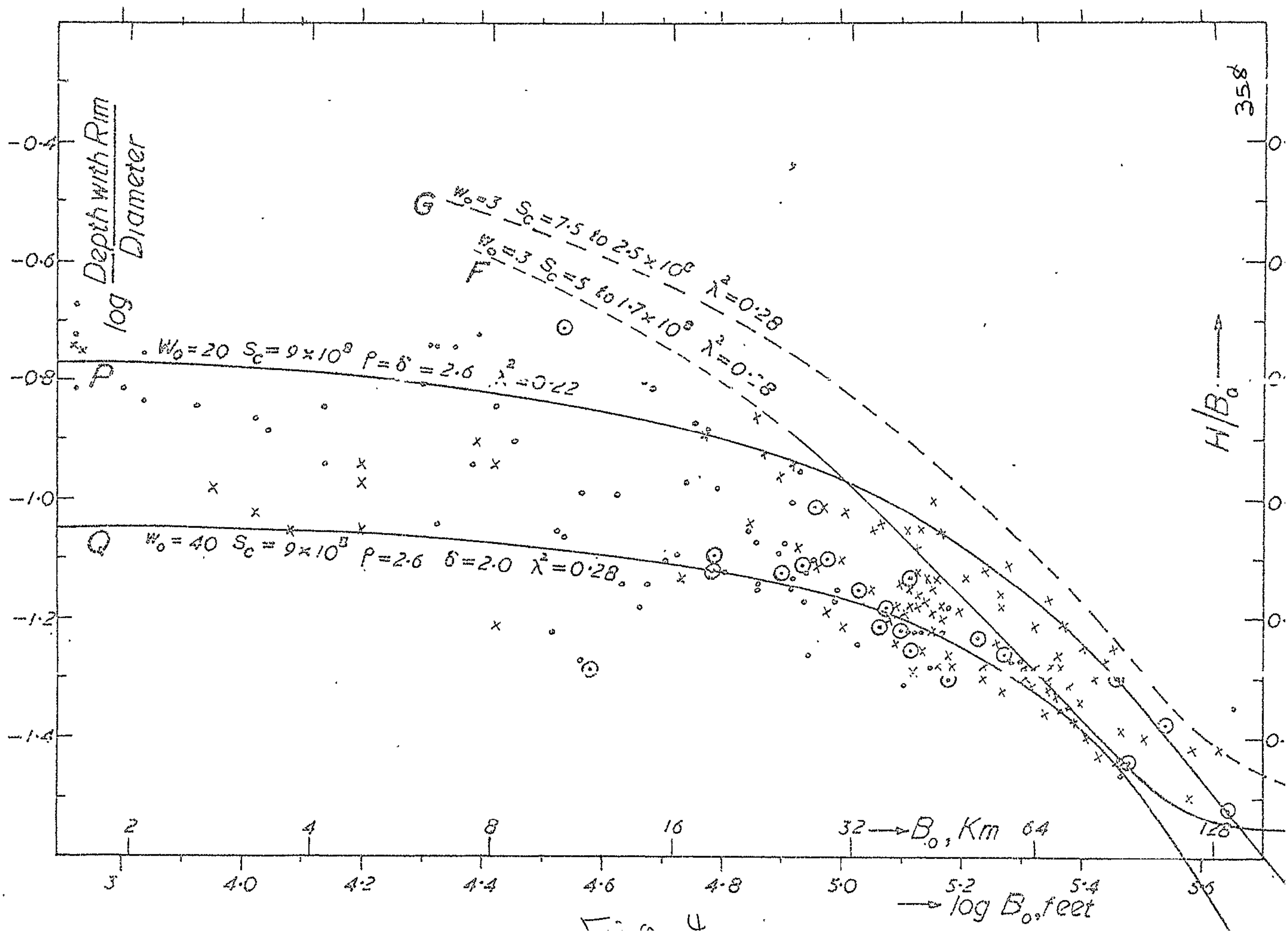

log Depth with Rim / Diameter
H/B₀ →
G W₀=3 S_c=7·5 to 2·5×10⁸ λ²=0·28
F W₀=3 S_c=5 to 1·7×10⁸ λ²=0·28
P W₀=20 S_c=9×10⁸ ρ=δ=2·6 λ²=0·22
Q W₀=40 S_c=9×10⁸ ρ=2·6 δ=2·0 λ²=0·28
32 → B₀, Km
→ log B₀, feet
358

Fig. 5a. (Compare Fig. 5b.)

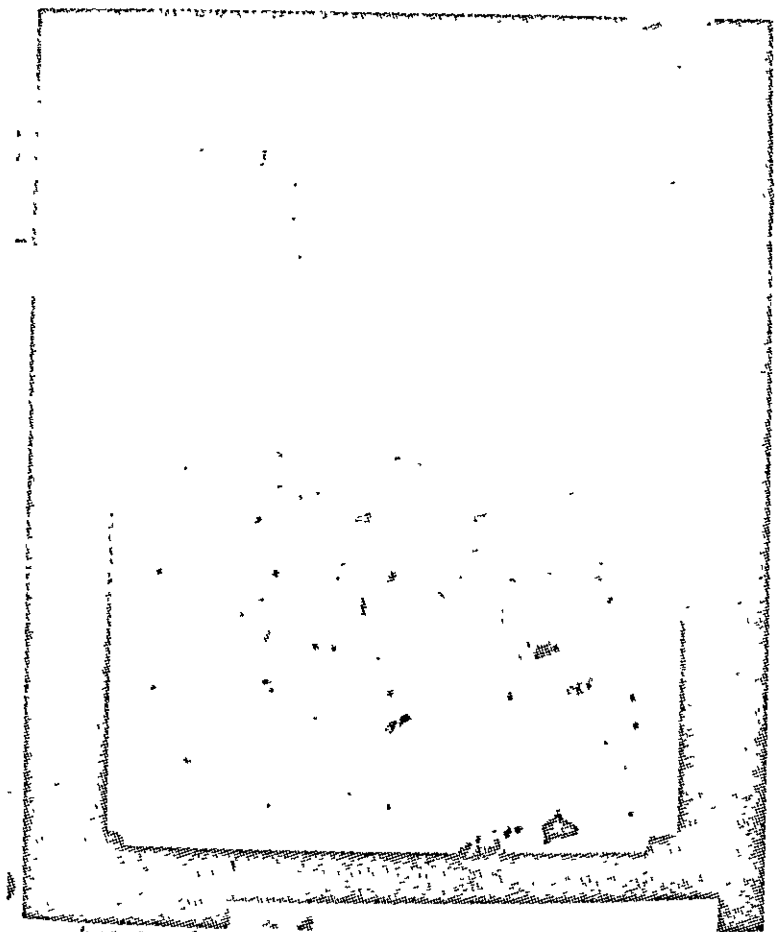

Öpik–Cratering

Fig. 9b. (Compare FIG. 9a)

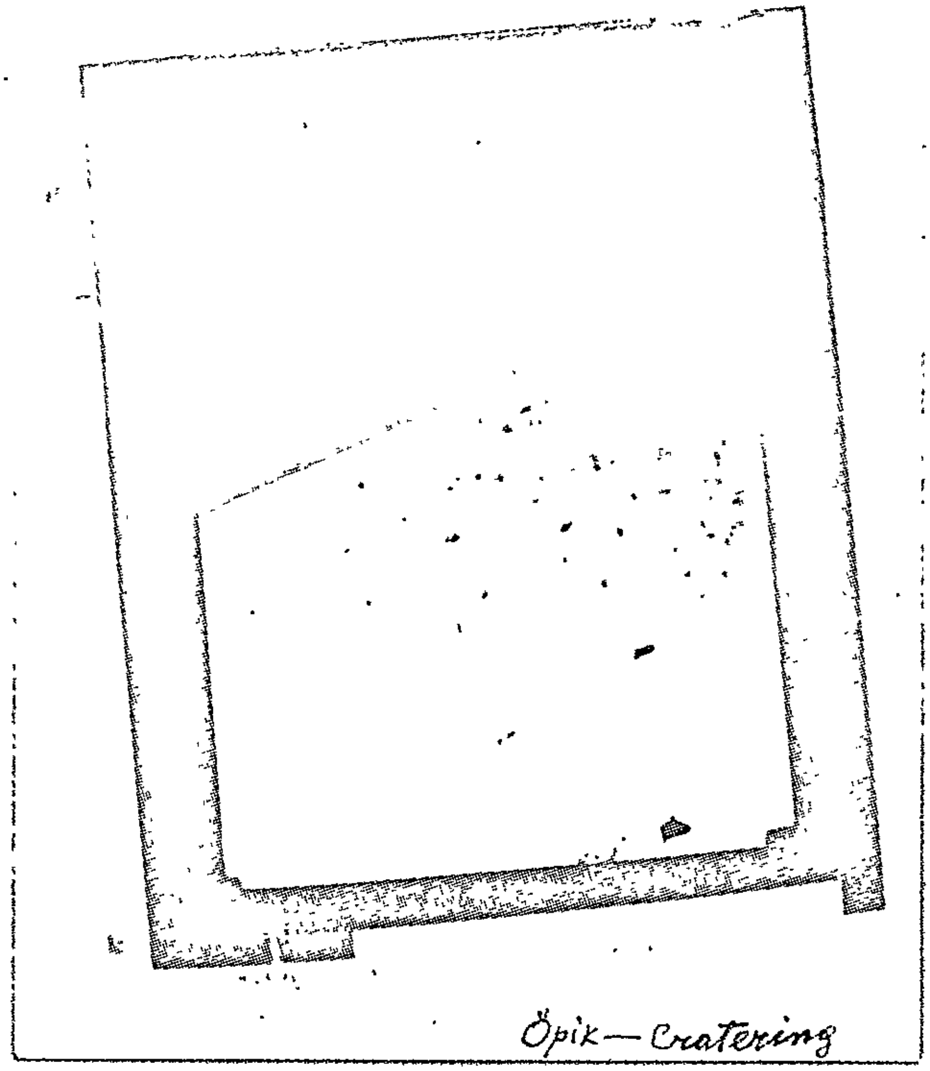

Öpik — Cratering

Ôpiv - Cratering

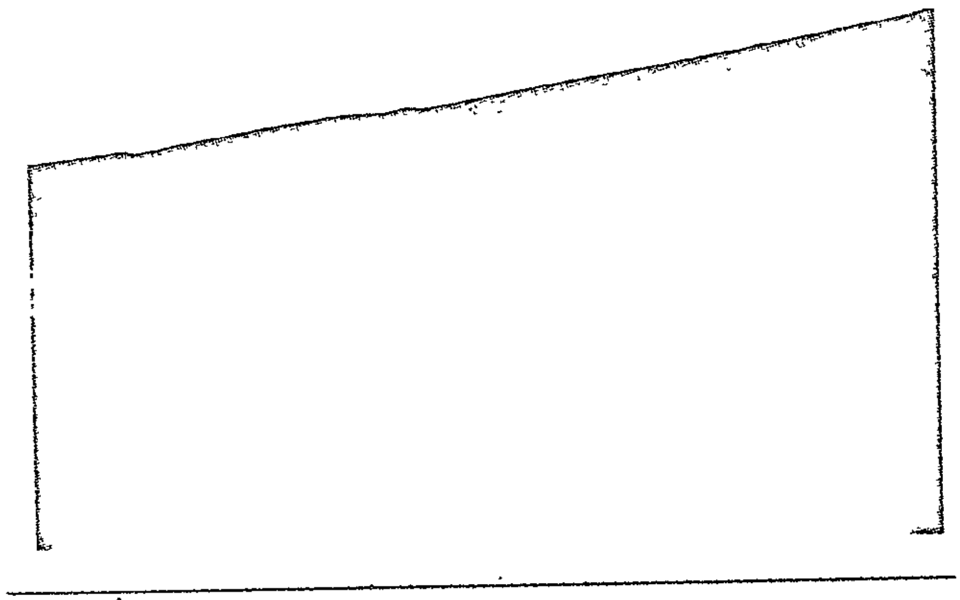

Fig. 7

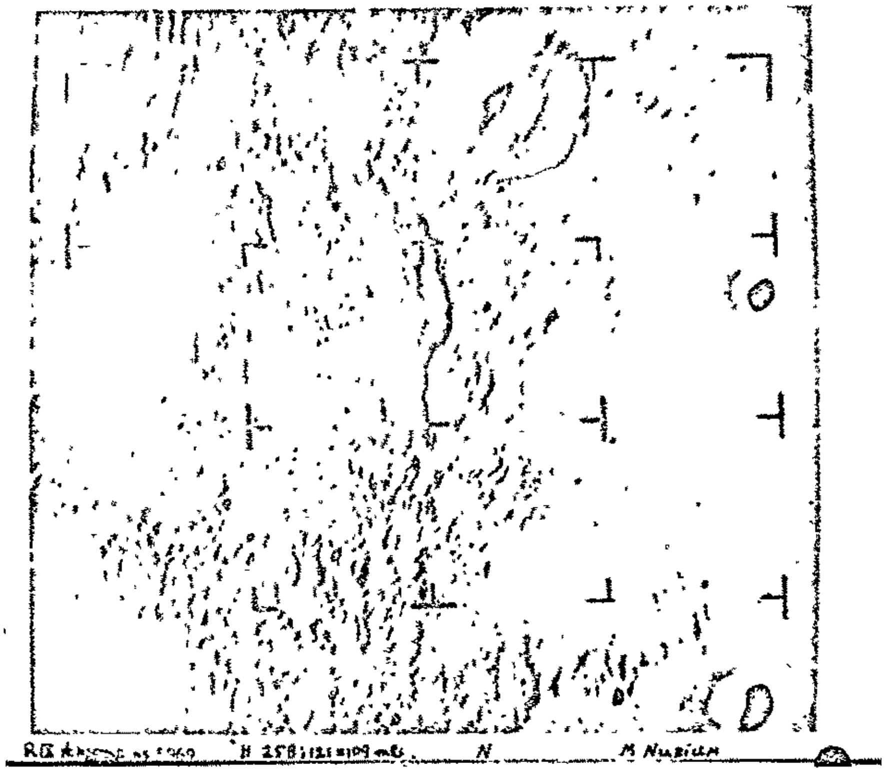

Öpik— Cratering

Fig. 9

Öpik-Cratering

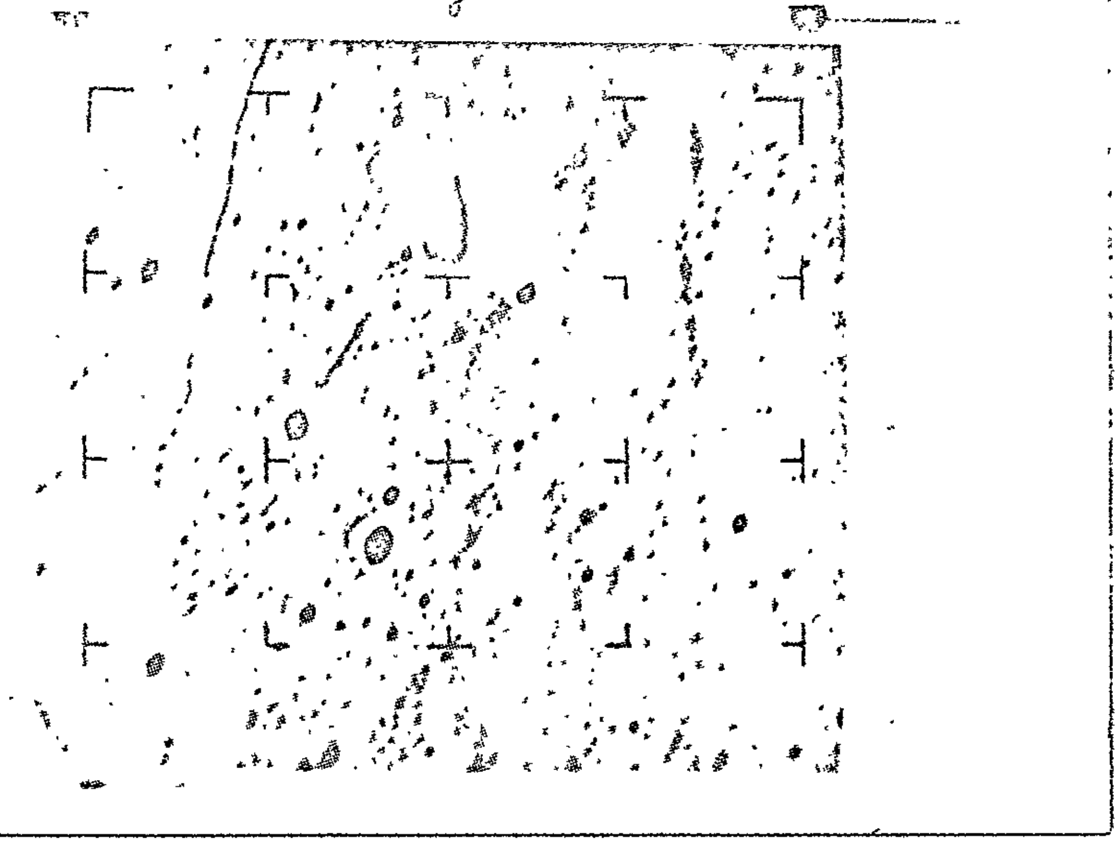

Fig. 9 Öpik-cratering

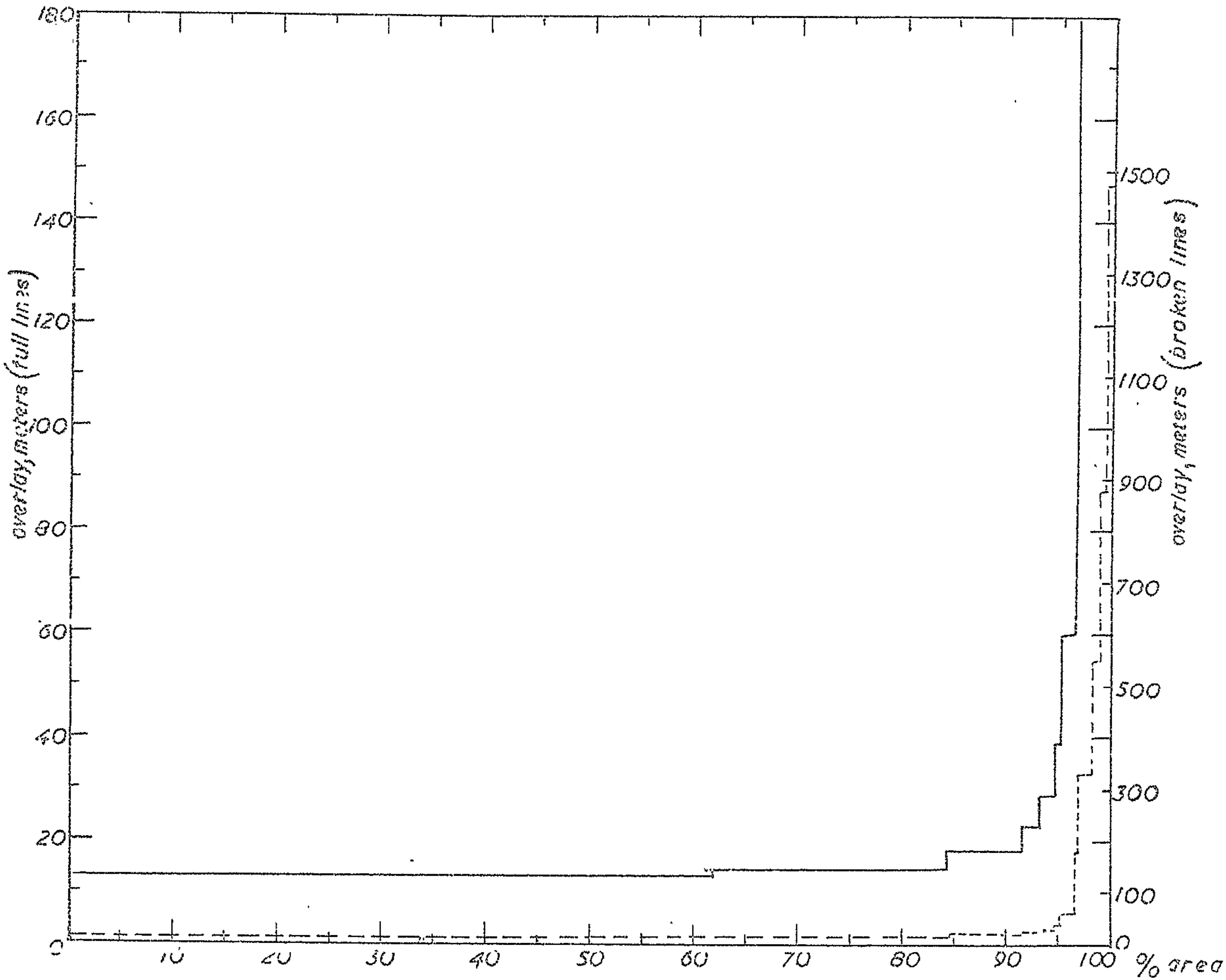

overlay, meters (full lines)
overlay, meters (broken lines)
% area
180
160
140
120
100
80
60
40
20
0
1500
1300
1100
900
700
500
300
100
0
10
20
30
40
50
60
70
80
90
100

Fig 10

365

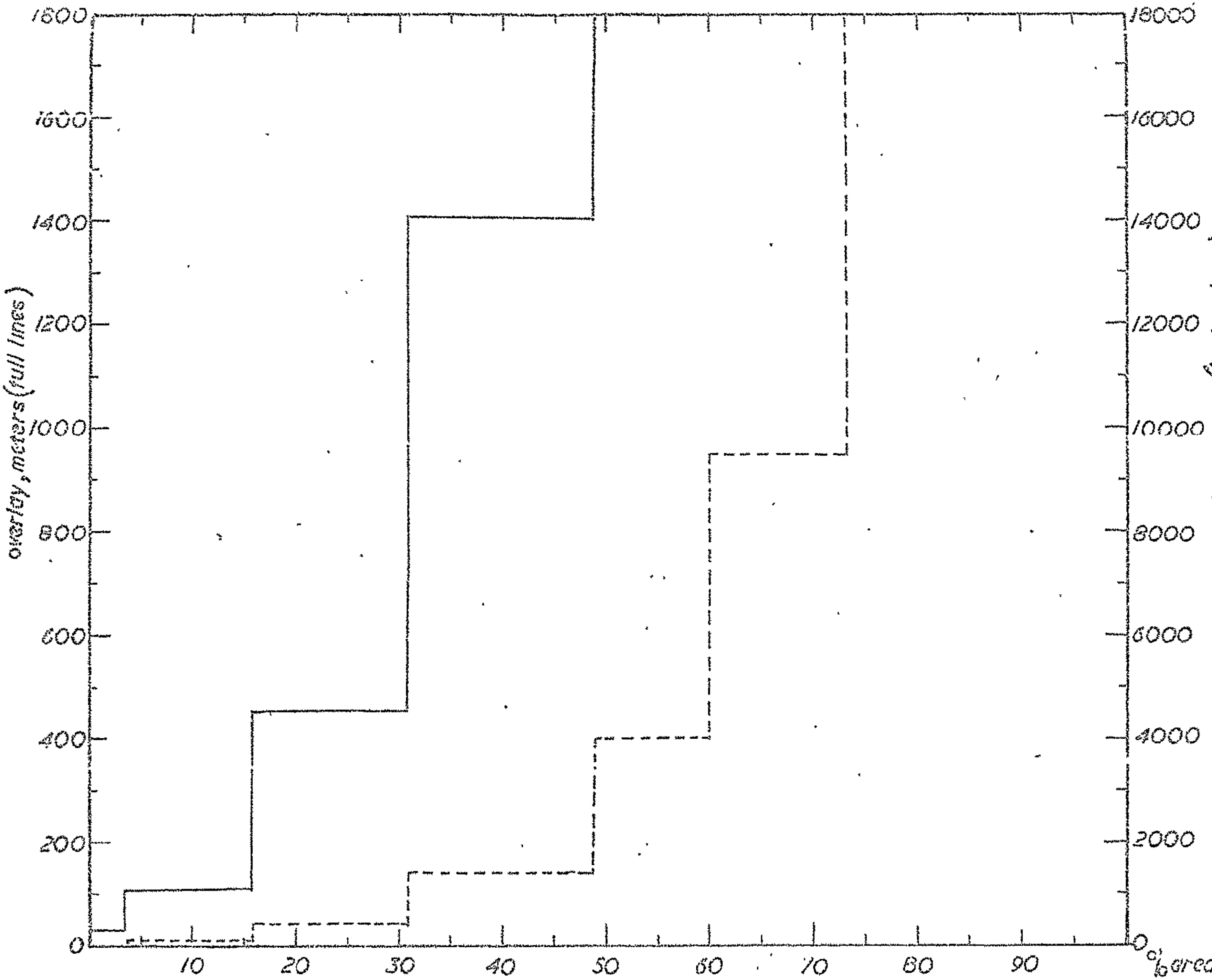

Fig 11

Öbir — Cratering

Fig 12

Öpik—Cratering

Fig. 13

Öpik—Cratering

Fig. 14

Öpik – Cratering

3Ce9

Fig. 15

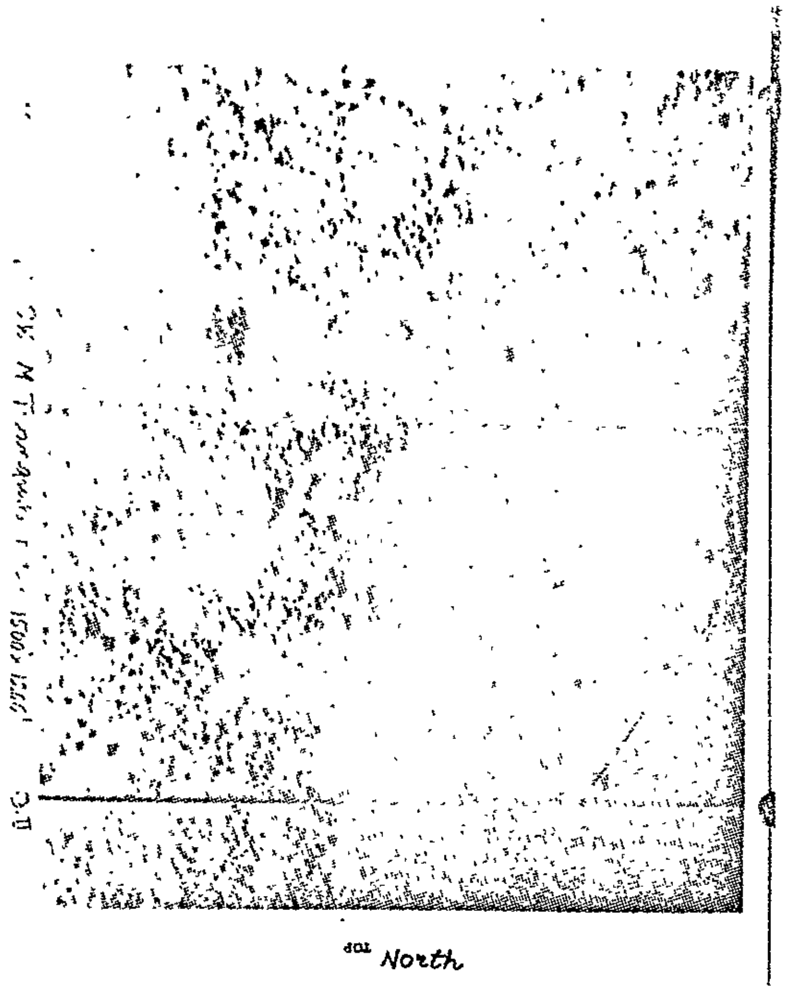

North

Öpik—Cratering

Fig. 16

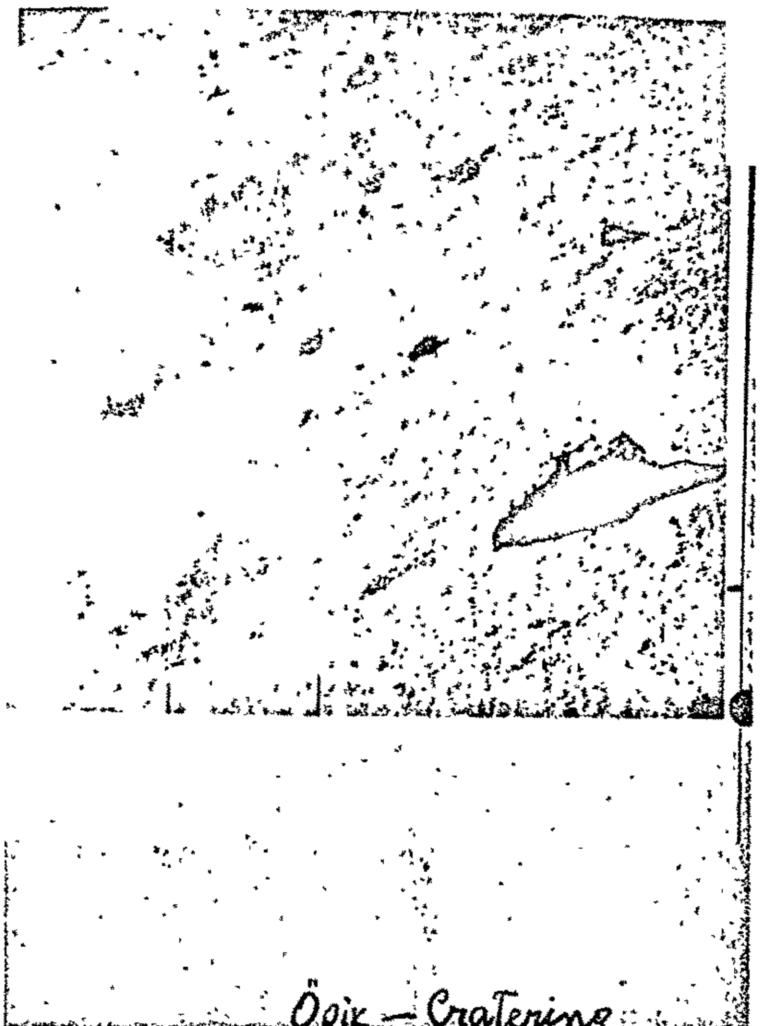

Öpik — Cratering

Fig. 17

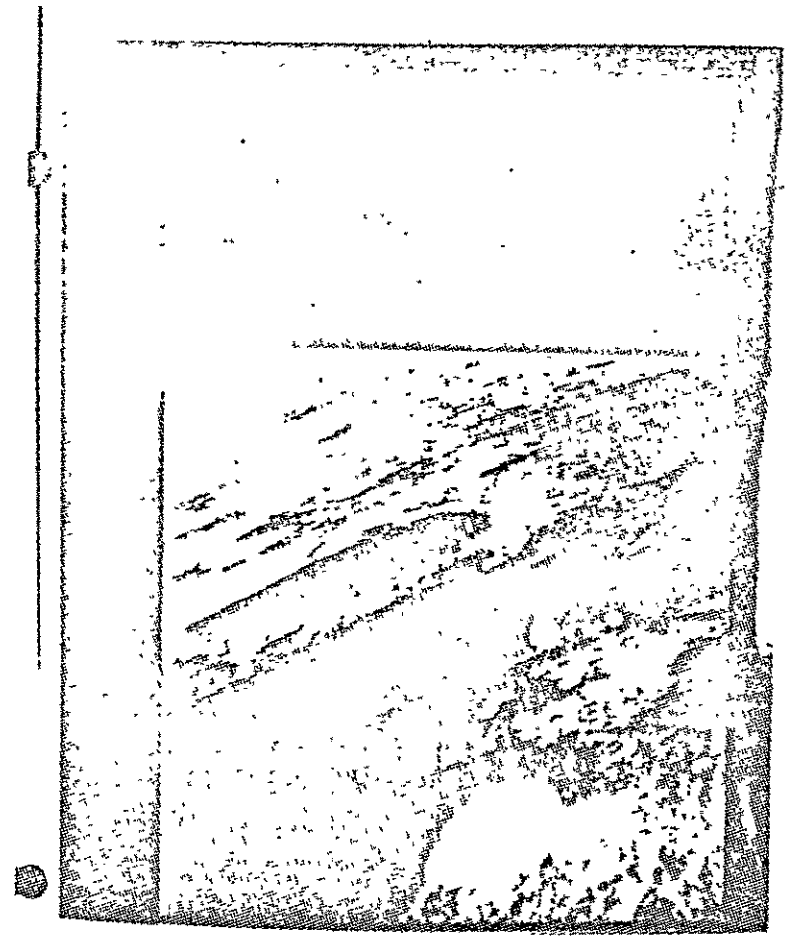

Öpik — Cratering

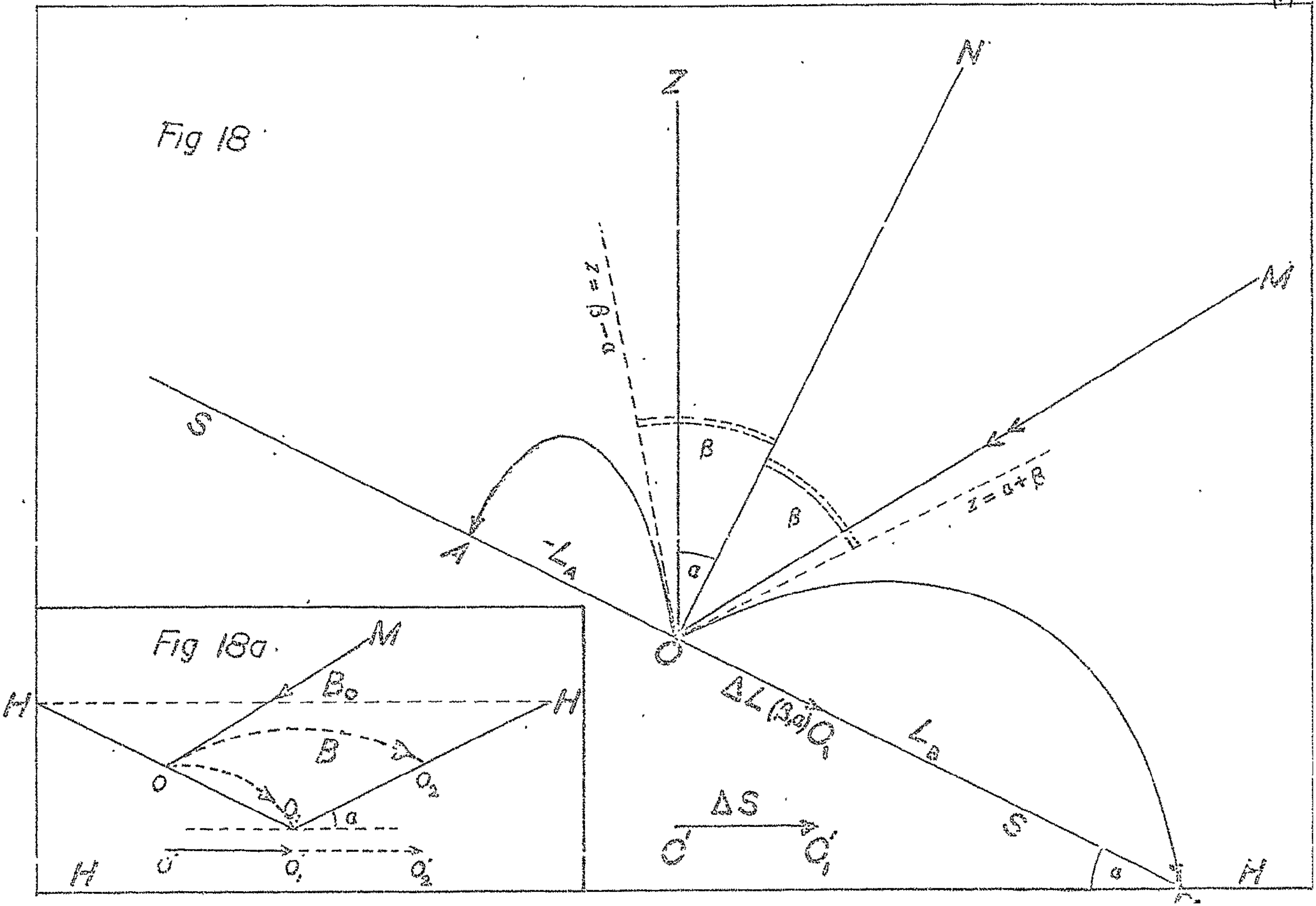

Fig 18

Fig 18a

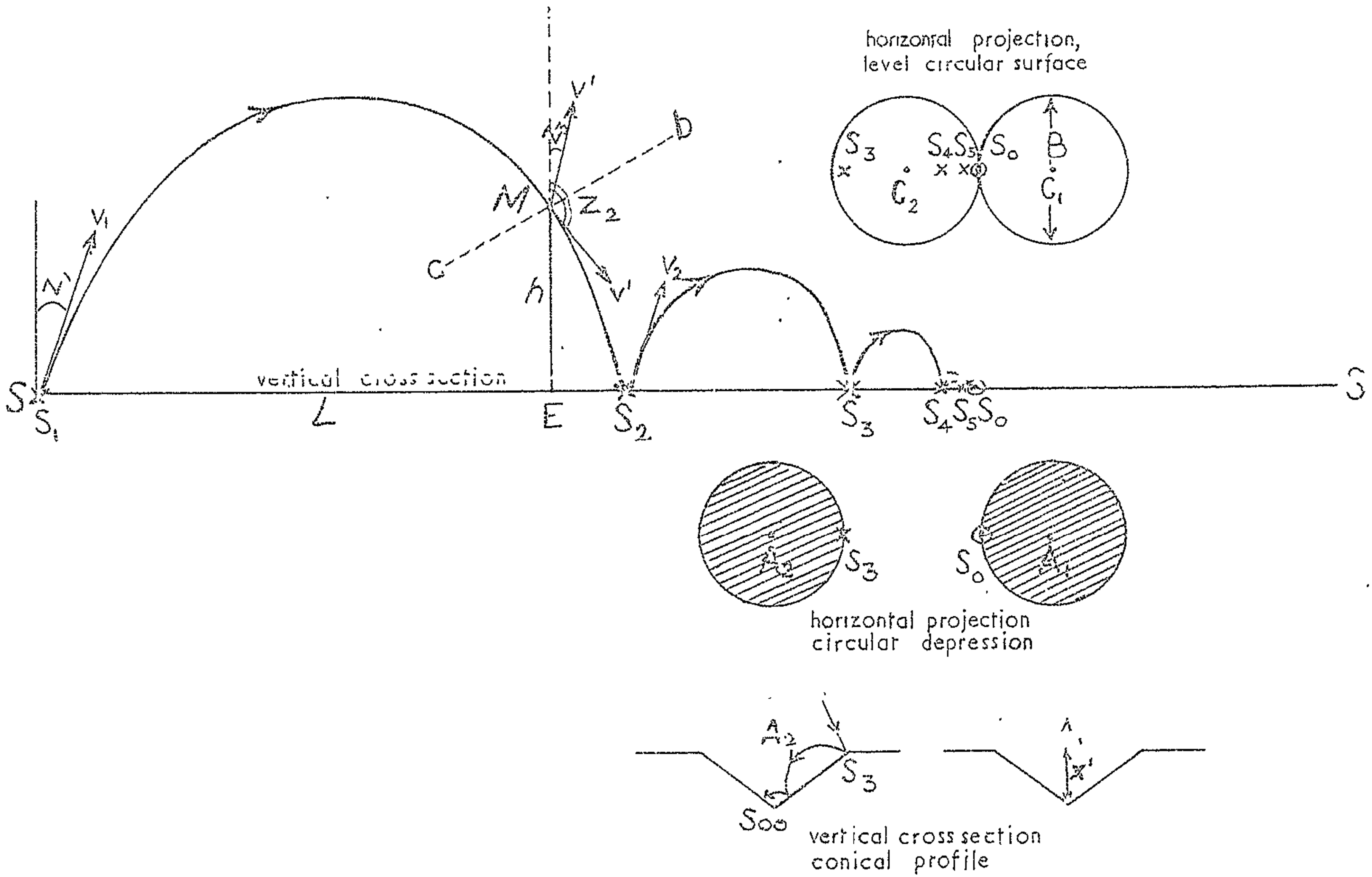

Fig. 19

Öpik—Craters

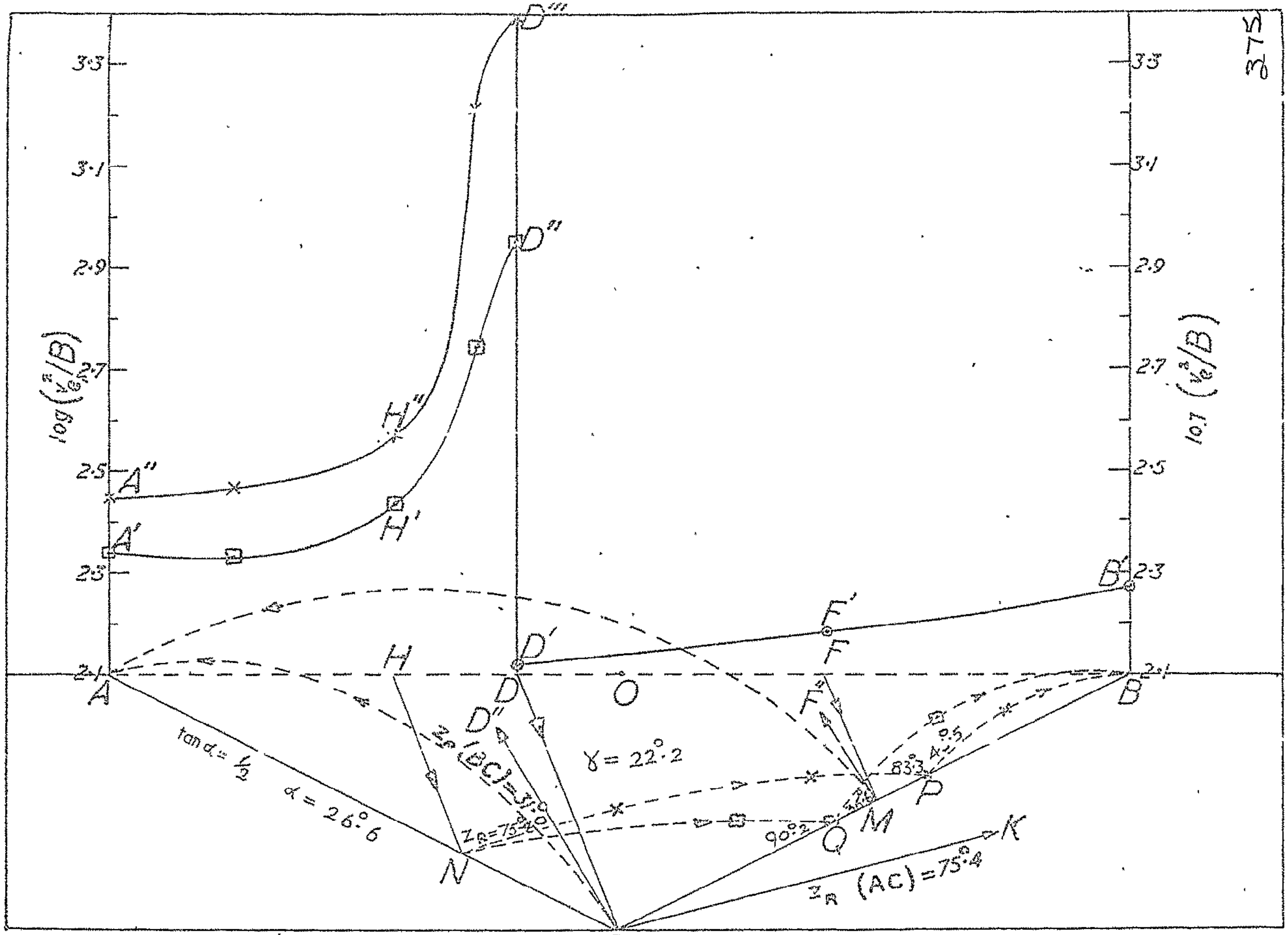

D'''
3·3
3·1
2·9
2·7
2·5
2·3
2·1
D''
H''
H'
A''
A'
B'
F'
D'
H
D
O
F
A
B
tan α = 1/2
α = 26°·6
γ = 22°·2
83°3
M
P
Q
N
K
C
z_R (AC) = 75°·4

Fig 2(

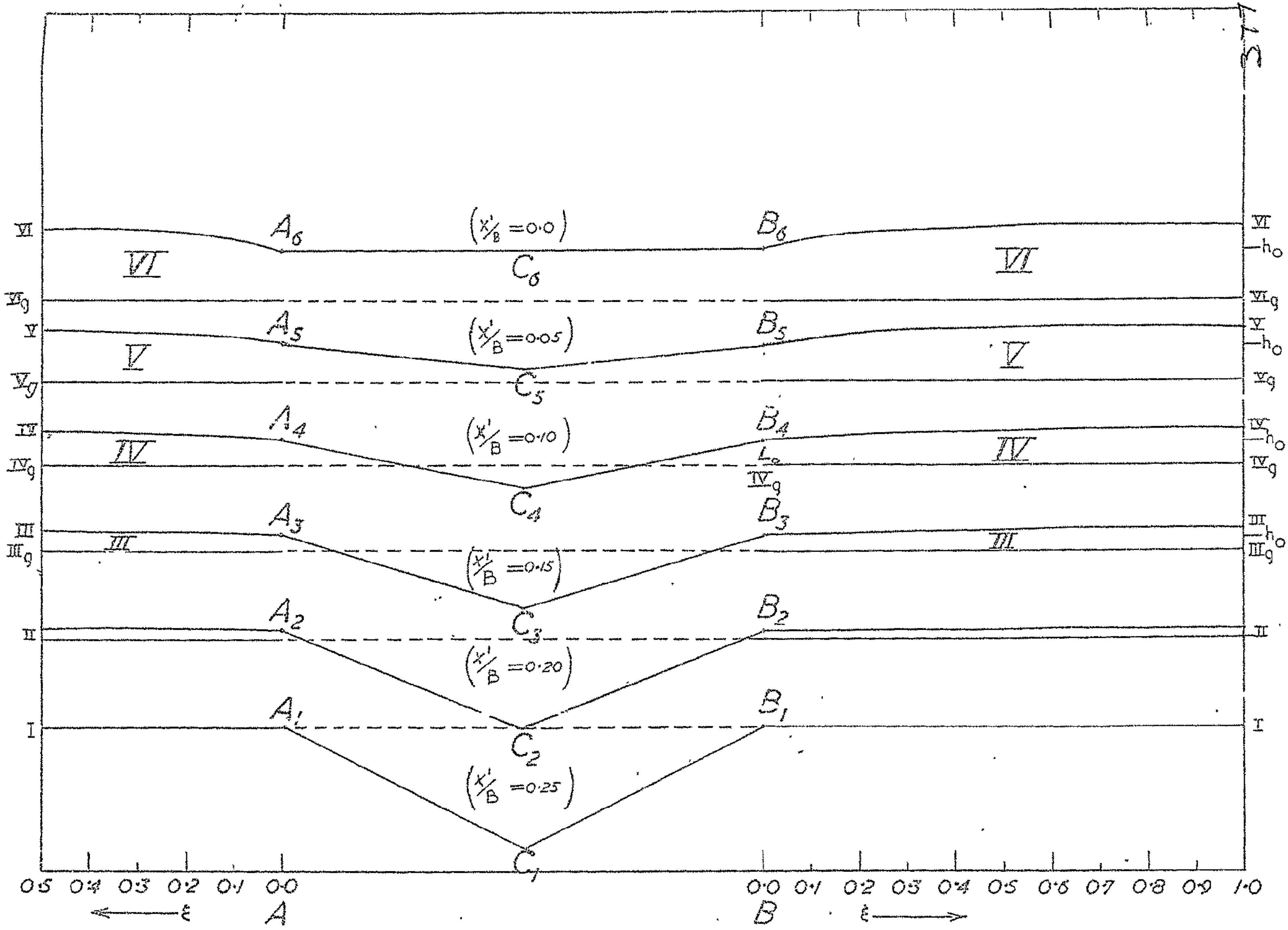
VI
A6
(x'/B = 0·0)
B6
VI
h0
VI
C6
VI
VIg
VIg
V
A5
(x'/B = 0·05)
B5
V
h0
V
V
Vg
C5
Vg
IV
A4
(x'/B = 0·10)
B4
IV
h0
IV
IV
IVg
IVg
IVg
C4
III
A3
B3
III
h0
III
III
IIIg
IIIg
(x'/B = 0·15)
A2
B2
II
C3
II
(x'/B = 0·20)
A1
B1
I
I
C2
(x'/B = 0·25)
C1
0·5 0·4 0·3 0·2 0·1 0·0
0·0 0·1 0·2 0·3 0·4 0·5 0·6 0·7 0·8 0·9 1·0
ε
A
B
ε

Fig 22

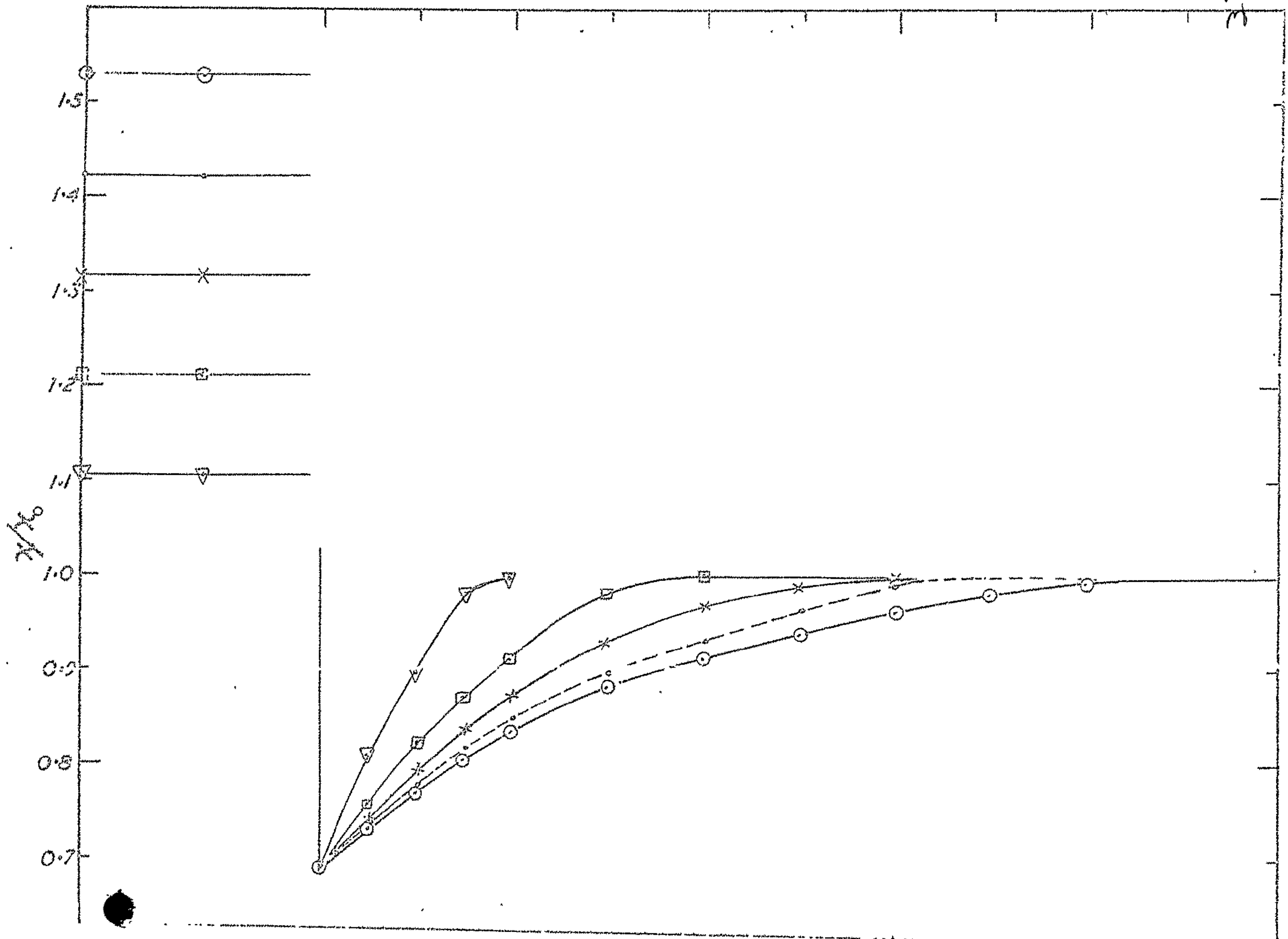

Fig. 21

Fig. 23

Opik—Cratering